Simulation of cavitation erosion by a coupled CFD-FEM approach

Prasanta Sarkar

Communauté
UNIVERSITÉ Grenoble Alpes

THÈSE

Pour obtenir le grade de

DOCTEUR DE LA
COMMUNAUTÉ UNIVERSITÉ GRENOBLE ALPES

Spécialité : **MEP: Mécanique des fluides, Energétique, Procédés**

Arrêté ministériel : 25 mai 2016

Présentée par

Prasanta SARKAR

Thèse dirigée par **Marc FIVEL**

et codirigée par

Giovanni GHIGLIOTTI et **Jean-Pierre FRANC**

préparée au sein du **Laboratoire des Écoulements Géophysiques et Industriels (LEGI)**

dans **l'École Doctorale I-MEP2 : Ingénierie - Matériaux, Mécanique, Environnement, Énergétique, Procédés, Production**

Simulation de l'érosion de cavitation par une approche CFD-FEM couplée

Thèse soutenue publiquement le **5 Mars 2019**,
devant le jury composé de :

M. Jean-Yves BILLARD
Professeur, Institut de Recherche de l'Ecole Navale, Président.

M. Eric GONCALVES DA SILVA
Professeur, Institut Pprime, ISAE-ENSMA, Rapporteur.

M. Christophe CORRE
Professeur, MFAE/LMFA, École Centrale de Lyon, Rapporteur.

M. Marc FIVEL
Directeur de Recherche CNRS, SIMaP, Univ. Grenoble Alpes, Directeur de thèse.

M. Jean-Pierre FRANC
Directeur de Recherche CNRS, LEGI, Univ. Grenoble Alpes, Invité.

M. Giovanni GHIGLIOTTI
Maître de Conférences, LEGI, Univ. Grenoble Alpes, Invité.

Communauté
UNIVERSITÉ Grenoble Alpes

THESIS

For obtaining the grade of

DOCTORATE OF THE

COMMUNAUTÉ UNIVERSITÉ GRENOBLE ALPES

Speciality : **MEP : Fluid Mechanics, Energy, Processes**

Ministerial order : 25 mai 2016

Presented by

Prasanta SARKAR

Thesis directed by **Marc FIVEL**

and co-directed by

Giovanni GHIGLIOTTI and **Jean-Pierre FRANC**

prepared within **Laboratory of Geophysical and Industrial Flows (LEGI)**

in **Doctoral School I-MEP2 : Engineering – Materials, Mechanics, Environment, Energy, Processes, Production**

Simulation of cavitation erosion by a coupled CFD-FEM approach

Thesis defended publicly on **5 March 2019**,
before the jury composed of :

Mr. Jean-Yves BILLARD
Professor, Naval Academy Research Institute, President.

Mr. Eric GONCALVES DA SILVA
Professor, Institut Pprime, ISAE-ENSMA, Reviewer.

Mr. Christophe CORRE
Professor, MFAE/LMFA, École Centrale Lyon, Reviewer.

Mr. Marc FIVEL
Director of Research CNRS, SIMaP, Univ. Grenoble Alpes, Thesis director.

Mr. Jean-Pierre FRANC
Director of Research CNRS, LEGI, Univ. Grenoble Alpes, Invited.

Mr. Giovanni GHIGLIOTTI
Assistant Professor, LEGI, Univ. Grenoble Alpes, Invited.

To Maa and Baba

Acknowledgements

courage does not always roar.
sometimes courage is the quiet voice
at the end of the day saying,
"i will try again tomorrow".
-Mary Anne Radmacher

First, I would like to express my sincere thanks and gratitude to my supervisors, Giovanni Ghigliotti, Marc Fivel and Jean-Pierre Franc for their guidance, support as well as patience throughout this research work. I have the deepest admiration about their passion and interest in my work, insightful discussions and immense knowledge which made enormous contributions to this thesis. I acknowledge their dedication and hard work during the preparation and reviewing of this thesis. I would like to gratefully acknowledge Guillaume Balarac for his scientific suggestions, discreet encouragement of my work as well as for giving me the opportunity to work within the MoST team.

I would like to show my appreciation to Jean-Yves Billard, Eric Goncalves Da Silva and Christophe Corre for accepting to be member of this jury, for dedicating their time in evaluating the work and for their valuable comments.

I want to extend a special thanks to Patrick Begou for his kindness and for patiently helping with the daily struggles with computers and other technical challenges. Patrick's enthusiasm and energy provided a good support system especially during challenging times. I also want to extend a big thanks to Vincent Moureau, Ghislain Lartigue and Pierre Benard from CORIA for the introduction to the vast world of YALES2, scientific guidance and fruitful discussions during our collaboration.

I would like to thank Cecile Cretin who managed my numerous travel and administrative request with utmost kindness, Lafiyatou Emeriaud and Agustina Alessio for their precious help with the administration in LEGI and IMEP2 doctoral school.

I have been fortunate enough to have the opportunity to learn and discuss with Steffen Schmidt who has helped enormously this work with his scientific insight and suggestions. A special thanks to Polina and Daria for giving me a warm welcome at TU Munich during my secondment. I would like to thank Claus-Dieter Ohl and Julien Rapet for welcoming me during my secondment at NTU Singapore and for all the help in performing experiments on bubble dynamics. Thank you Julien for all the fun we had during the sleepless nights we were working together and during my stay in Singapore.

This work would not have been possible without funding from the CaFE project and I extend my special thanks to the project coordinators Manolis Gavaises, Amalia Petrova and Nikolaos Chatziarsenis. Along with them, many thanks to all the

collaborators Magdalena Neuhauser, Rickard Bensow, Tom van Terwisga, Mohamed Farhat, Nikos, Akis, Themis, Marco, Max, Mohammad, Soren and everyone else involved in the project for many wonderful discussions and exciting project meetings.

I would also like to acknowledge my former supervisors, M. Balakrishnan, who is unfortunately no longer with us, S. Nadaraja Pillai and R. Dorairaj from Department of Aerospace Engineering, SRM University, India, S. Ganesan from Gas Turbine Research Establishment, India, Antonio Filippone from University of Manchester, UK and Jacek Malecki from PZL Swidnik Helicopters, Poland for providing me opportunities at different stages and your faith in my abilities.

And of course, a big thanks to friends and (former) colleagues in Grenoble, who made my life as a Ph.D. student most pleasurable - Guillaume Sahut (for all the extended discussions over coffee), Shrey, Yves, Markku, Chakri, Sholpan, Jade, Kaoutar, Richi, Jean-Bastien, Andrey, Manuel, Cyril, Matthieu, Jeremie, Francois, Vincent, Alexandre Sikora, Alexandre Simon, Sylvia, Lucas, Nick, Jan, Nathanael, Guillaume Fromant. Thank you guys for the cordiality and many scientific and non-scientific discussions.

To close this on an emotional note, I must acknowledge all those teachers, professors, staff and students, too numerous to list, at Kendriya Vidyalaya ONGC Agartala, SRM University, University of Manchester and Universite Grenoble Alpes who have educated me over the years. Along with them to many others who have directly or indirectly contributed in shaping my life and career, this effort may serve as a token of gratitude for their efforts.

It is love, however, that truly motivates. It is, therefore, my family: my parents, Chinu and Ashutosh, to whom this thesis is dedicated, my sister Lipika and her family, my friends (and faithful supporters) Pritam, Partha, Jaya, Saurav, Kakali, Plaban, Jhantu, Sumit, Deepraj, Arindam, Sagnik, Puspita, Jayanta, Shubhajit - I want to thank you all for believing in me. Finally, I am grateful to Paula for all the love and constant encouragement, for the patience, for the help with the vast world of Python and for never stopping believing in me even in my lows.

I've been very lucky for being surrounded by such wonderful people in my life.

Prasanta Sarkar
December 2018

This thesis was accomplished within the project CaFE[1] *which has received funding from the European Union Horizon 2020 Research and Innovation programme, Grant Agreement No 642536 under the Marie Skłodowska-Curie Innovative Training Network. A part of the Ph.D. thesis work on experimental bubble dynamics has been conducted in a planned secondment at Nanyang Technological University, Singapore.*

1. http://cafe-project.eu

Contents

Abstract

This research is devoted to understanding the physical mechanism of cavitation erosion in liquid flows on the fundamental scale of cavitation bubble collapse. Cavitation bubbles forms in a liquid when the pressure of the liquid decreases locally below the saturated vapor pressure. The bubbles grow due to low ambient pressure and rapidly collapses when the surrounding liquid pressure increases. As a consequence of collapsing bubbles near solid walls, high pressure impact loads are generated. The primary bubble collapse is accompanied by the emission of shock waves and therefore, the fluid compressibility has to be considered. The pressure loads from primary bubble collapse and shock waves causes plastic deformation and eventually, mass loss in the solid. These pressure loads believed to be responsible for the erosive damages on solid surfaces, are observed in applications like liquid fuel injection, hydrodynamic power generation and marine propulsion. On the other hand, the pressure loads from collapsing bubbles are useful for applications like shock wave lithotripsy, drug delivery and cleaning surfaces. Our numerical approach begins with the development of a compressible solver capable of resolving the cavitation bubbles in the finite-volume code YALES2 employing a simplified homogenous mixture model. In cavitation erosion, the solid wall deforms under the influence of pressure loads from collapsing bubbles. Therefore, the solver is extended to Arbitrary Lagrangian-Eulerian formulation to equip with moving mesh capabilities in order to perform fluid structure interaction simulation. The material response is resolved with the finite element code Cast3M, which allowed us to investigate one-way and two-way coupled fluid-structure interaction simulations between the fluid and solid domains. In one-way coupling, no feedback of solid wall deformation on the fluid is considered whereas in two-way coupling, the feedback of solid wall deformation is considered in the fluid domain. In the end, we draw comparisons between 2D and 3D vapor bubble collapse dynamics and compare them with experimental observations. We estimate the pressure loads on the solid wall from collapsing bubbles and discuss the dynamical events responsible for surface damage. The response of different materials to bubbles collapsing at different distances from the solid wall is also discussed. Finally, we present results from two-way coupled fluid-structure interaction simulations where the damping of pressure loads by different materials is analysed.

Keywords: *cavitation; cavitation erosion; bubble dynamics; computational fluid dynamics; finite element method; fluid-structure interaction; impact pressure load prediction; material characterization*

Résumé

Ce travail de recherche est dédié à la compréhension des mécanismes physiques de l'érosion de cavitation dans un fluide compressible à l'échelle fondamentale de l'implosion d'une bulle de cavitation. Des bulles de cavitation se forment dans un liquide lorsque la pression du liquide chute en dessous de la pression de vapeur saturée. Les bulles grossissent en raison de la faible pression ambiante et s'effondrent rapidement lorsque la pression du liquide environnant augmente. Suite à l'implosion d'une bulle de vapeur à proximité d'une surface solide, des très hautes pressions sont générées. L'effondrement primaire de la bulle s'accompagne de l'émission d'ondes de choc et la compressibilité du fluide doit donc être prise en compte. Les pressions exercées par l'effondrement primaire des bulles et les ondes de choc entraînent une déformation plastique et, éventuellement, le phénomène de perte de masse dans le solide. Ces pressions, considérées responsables de l'endommagement (érosion) des surfaces solides, sont observées dans la plupart des applications telles que l'injection de carburant liquide, la génération de puissance hydrodynamique et la propulsion marine. Notre approche numérique démarre avec le développement d'un solveur compressible capable de résoudre les bulles de cavitation au sein du code volumes finis YALES2 en utilisant un simple modèle de mélange homogène des phases fluides. En érosion par cavitation, la paroi solide se déforme sous l'effet des pressions exercées par les bulles qui s'effondrent. Par conséquent, le solveur est étendu à une approche ALE (Arbitraire Lagrangien Eulérien) qui permet l'utilisation de maillage mobiles afin de réaliser une simulation d'interaction fluide-structure où la domaine fluide suit la déformation de la surface solide. La réponse du matériau solide est calculée avec le code de calcul éléments finis Cast3M, et nous permet de mener des simulations avec un couplage d'abord monodirectionnel, ensuite bidirectionnel, entre le fluide et le solide. Dans le couplage monodirectionnel, aucun retour de déformation de paroi solide sur le fluide n'est pris en compte, alors que dans le couplage bidirectionnel, le retour de déformation de paroi solide est pris en compte dans le domaine du fluide. On compare des résultats obtenus à deux dimensions, puis à trois, avec des observations expérimentales. On discute les chargements de pression generés par l'effondrement des bulles et discutons de la dynamique responsable des dommages en surface. La réponse de différents matériaux pour des implosions de bulle à des différentes distances de la surface est également abordée. Enfin, à travers l'utilisation de simulations avec couplage bidirectionnel entre fluide et solide, on identifie l'amortissement des chargements de pression générés par des différents matériaux.

Mots clés *: cavitation ; érosion de cavitation ; dynamique des bulles ; mécanique des fluides numérique ; méthode des éléments finis ; interaction fluide-structure ; prédiction des pressions d'impact ; caractérisation des matériaux*

Nomenclature

Greek letters

α	Vapor volume fraction	[-]
β_s	Isentropic fluid compressibility	$[m^2/N]$
$\dot{\varepsilon_p}$	Plastic strain rate	$[s^{-1}]$
λ	Thermal conductivity	$[W/(m.K)]$
μ	Dynamic viscosity	$[kg/(m.s)]$
ν	Poisson's ratio	[-]
Ω	Sub-domain of physical space	[-]
$\partial\Omega$	Boundary of sub-domain of physical space	[-]
ρ	Density	$[kg/m^3]$
σ	Stress	$[Pa]$
σ_n	Normal stress	$[Pa]$
σ_v	Cavitation number	[-]
σ_y	Yield strength	$[Pa]$
σ_{VM}	von Mises stress	$[Pa]$
τ	Viscous stress tensor	$[Pa]$
τ_n	Shear stress	$[Pa]$
ε	Total Strain	[-]
ε_e	Elastic Strain	[-]
ε_p	Plastic Strain	[-]
ε_{th}	Thermal Strain	[-]

Latin Letters

Δt	Time step	$[s]$
Δx,Δy,Δz	Characteristic length of mesh element in cartesian coordinates	$[m]$
$\dot{R}$	Bubble interface velocity	$[m/s]$

$\mathcal{E}$	Total energy per unit volume	$[kg/(m \cdot s^2)]$
$\mathcal{I}$	Identity matrix	[-]
$\mathcal{T}$	Traction	$[Pa]$
π	Pi	[-]
A_{ε_p}	Area under plastic deformation	$[m^2]$
c	Speed of sound	$[m/s]$
E	Total energy per unit mass	$[m^2/s^2]$
E	Young's modulus	$[Pa]$
e_s	Internal energy	$[kg \cdot m^2/s^2]$
F	Equivalent nodal force	$[Pa]$
g	Gravitational acceleration	$[m/s^2]$
K	Strength coefficient of material	$[Pa]$
K_e	Elastic stiffness	$[N/m]$
m	Momentum	$[kg/(m^2 \cdot s)]$
n	Strain hardening exponent	[-]
N_{cell}	Total number of cells in the computational domain	[-]
N_{dim}	Dimensions of the computational domain	[-]
N_{iter}	Total number of iterations	[-]
N_{node}	Total number of nodes in the computational domain	[-]
p	Pressure	$[Pa]$
p_v	Vapor pressure	$[Pa]$
P_{ε_p}	Accumulated plastic strain	[-]
$P_{\varepsilon_p}^{max}$	Maximum accumulated plastic strain	[-]
p_{g0}	Partial pressure of non condensable gas inside a bubble	$[Pa]$
p_{wh}	Water hammer pressure	$[Pa]$
Q	Heat flux	$[W/m^2]$
R	Spherical bubble radius	$[m]$
S	Surface tension of the liquid	$[N/m]$
T	Temperature	$[K]$
t	Time	$[s]$
u	Velocity	$[m/s]$
u_d	Displacement	$[m]$

Non-dimensional numbers

γ	Stand-off distance

CFL Courant Friedrichs Lewy

Ma Mach number

Re Reynolds number

Operators

Δ Increment operator

δ Kronecker delta

$\nabla.$ Divergence

∇ Gradient

Subscripts

0 Initial values

max Maximum value of a quantity

min Minimum value of a quantity

g Gas

l Liquid

lv Liquid-vapor

s Solid

v Vapor

Superscripts

$\equiv$ Fourth order tensors

$=$ Second order tensors

$-$ First order tensors (vectors)

n Solution at previous time step

$\star$ Solution at intermediary time step between n & $n+1$

$n+1$ Solution at the end of current time step

T Transpose

Abbreviations

2D Two-dimensional

3D Three-dimensional

AFM Atomic Force Microscope

ALE Arbitrary Lagrangian Eulerian

BC Boundary Condition

BiCGSTAB2 Stabilized Bi-Conjugate Gradient

CaFE Development and experimental validation of computational models for **Ca**vitating **F**lows, surface **E**rosion damage and material loss

CCS Compressible Cavitation Solver

CFD Computational Fluid Dynamics

CLE Cavitation ALE solver

CPS Implicit Compressible Solver

CSM Computational Solid Mechanics

CV Control Volume

DNS Direct Numerical Simulation

DPCG Deflated Preconditioned Conjugate Gradient

EOS Equation of State

FEM Finite Element Method

FSI Fluid Structure Interaction

FVM Finite Volume Method

Grenoble INP Grenoble Institute of Technology (Institut Polytechnique de Grenoble)

HPC High Performance Computing

LEGI Laboratory of Geophysical and Industrial Flows (Laboratoire des Écoulements Géophysiques et Industriels)

LES Large-Eddy Simulation

LHS Left Hand Side

LW Lax-Wendroff

NTU Nanyang Technological University

PDE Partial Differential Equation

RHS Right Hand Side

RK Runge-Kutta

SGS Subgrid-scale

SIMaP Science and Engineering of Materials and Processes (Science et Ingénierie des Matériaux et Procédés)

TUM Technical University of Munich

UGA Université Grenoble Alpes

YALES2 Yet Another LES Solver

Part I

Motivation and Experimental Results

Chapter 1

Cavitation Erosion

1.1 Motivation

The motivation behind this research lies in understanding the physical mechanism of cavitation erosion in compressible liquid flows, with applications in the field of aerospace, hydrodynamics, diesel injectors, mechanical heart valves etc. Cavitation affects the performance and life cycle of a machine by producing surface erosion, unwanted noise and vibrations depending on the duration and extent of the exposure to cavitating flows. Cavitation bubbles form in a liquid when the pressure of the liquid drops below the saturated vapour pressure, causing the bubbles to expand and collapse near solid walls. This bubble collapse mechanism is believed to be causing the surface damage. Considerable research has focused on understanding the physics of bubble formation and collapse near solid boundaries. However to date, a thorough understanding of how bubble collapse relates to surface erosion has been an elusive goal due to the different physical processes of fluids and solids, temporal scales and computational limitations. This research focus on developing a computational model of bubble collapse dynamics close to a solid wall with Fluid-Structure Interaction (FSI) to aid in the development of cavitation erosion prediction tools.

1.2 Cavitation

Cavitation is the appearance of vapor regions (or cavities) inside an initially homogeneous liquid when the pressure decreases locally (Franc 2006, Brennen 1995). Analogous to boiling where water turns into vapor when the temperature reaches the boiling point, in cavitation the phase change from water into vapor takes place when the pressure decreases below its vapor pressure, as shown in the phase diagram in fig. 1.1. In the phase diagram, the liquid and vapor phases are separated by a curve joining the triple point T_r to the critical point C. Crossing this curve is representative of an equilibrium phase change of the fluid at a vapor pressure $p_v(T_f)$ which is a function of temperature T_f. In a simplified consideration, cavitation is similar to boiling except that the driving mechanism is a decrease in pressure at a nearly constant temperature i.e. isothermal process along $p_v(T_f)$. In actual practice, the phase change process needs heat transfer from the surrounding liquid which results in minor decrease in surrounding liquid temperature i.e. non isothermal phase change at $p_v(T_f')$. The difference $T_f - T_f'$ is called thermal delay in cavitation. The formation

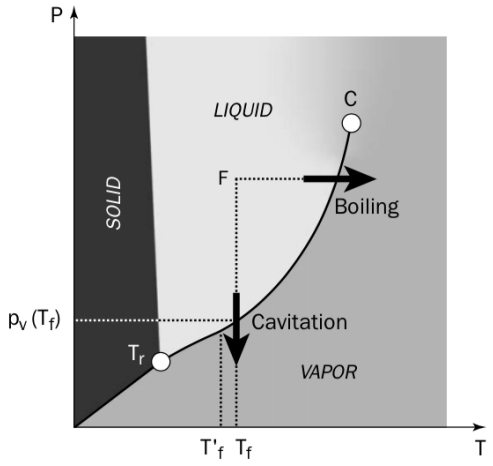

Figure 1.1 – Phase diagram of water (Franc 2006).

of the bubbles or nucleation is however quite complex as pure liquid water is able to sustain pressure below the vapor pressure before the intermolecular bonds break for the formation of cavities. In practice, microscopic dissolved gas or solid impurities, known as cavitation nuclei, act as weak points in the continuum liquid where the cavities grow once the vapor pressure is reached. The pressure decrease is induced by the flow dynamics, the geometry of the solid boundaries, surface roughness or even by shear stresses. An important parameter for classification of cavitating flows is the cavitation number σ_v defined as:

$$\sigma_v = \frac{p_{ref} - p_v(T_{ref})}{\frac{1}{2}\rho_{liq} u_{ref}^2} \tag{1.1}$$

where p_{ref} is the reference pressure and $p_v(T_{ref})$ is the vapor pressure at reference temperature T_{ref}, ρ_{liq} is the liquid density and u_{ref} is the flow velocity at a reference position. The cavitation number defines a ratio of local pressure drop with respect to the reference condition of the flow field and thus a smaller value of σ_v indicates the possibility of cavitation. The location of the reference condition is dependent on the application considered and most often taken at the inlet of the flow domain. The start of cavitation in the flow field is called *cavitation inception* which initiates at some particular σ_v value called the *incipient cavitation number* σ_i. Although it is usual to expect cavitation to initiate at a location where the local pressure drops to vapor pressure p_v with $\sigma_v < \sigma_i$, deviations do exist and liquid flows sometimes are able to sustain cohesion even at lower pressures. Generally, σ_v should be greater than σ_i for non-cavitating flows. Cavitation inception, therefore, is the limiting region between cavitating and non-cavitating flows and depends on parameters such as fluid quality or initial gas content.

Hydrodynamic cavitation in a flowing liquid can be broadly classified into:

- *Transient isolated bubble* : An isolated cavitation bubble appears in a region of low pressure due to rapid growth of existing cavitation nuclei in the liquid. They are carried along the flow and collapse once they enter areas of high pressure.
- *Vortex cavitation*: Cavitation occurs at the low pressure core of a vortex or turbulent wake inside the flow.

- *Sheet cavitation*: These cavities are often formed at the leading edge of solid bodies like propeller blades or hydrofoils, attached to the suction (or low-pressure) side.
- *Cloud cavitation*: Cavitation region consisting of many small cavitation bubbles formed when a sheet cavity periodically oscillates or sheds vapor cavities.
- *Supercavitation*: When the sheet cavity grows with decreasing cavitation number and encloses the entire solid body in a vapor region.

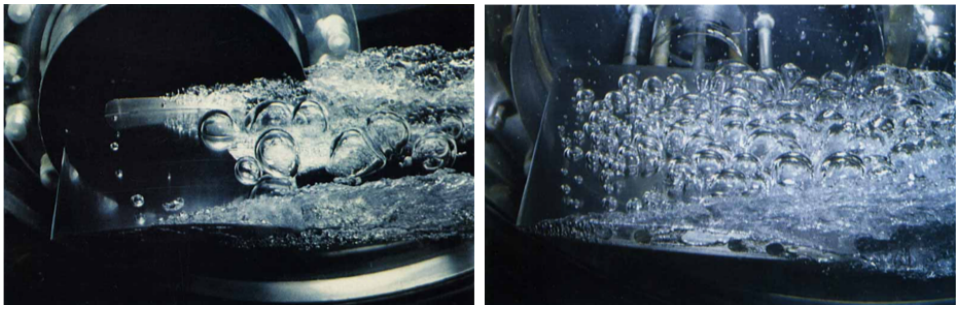

Figure 1.2 – Transient cavitation bubbles on the surface of a hydrofoil, $(left)$ mixed cavitation regime $Re = 10^6$, $\sigma_v = 0.07$, angle of incidence= 1.1°, $(right)$ saturation $Re = 1.1 \times 10^6$, $\sigma_v = 0.08$, angle of incidence= 5° (Briançon-Marjollet 1990).

Figure 1.2$(left)$ shows transient cavitation bubbles on the low-pressure side of a hydrofoil in a mixed cavitation regime and in fig. 1.2$(right)$ shows the downstream part of the hydrofoil saturated (or almost completely covered) with transient bubbles. The bubbles usually collapse near the point of inception or travel downstream with the flow before they collapse. Cavitating regimes on the low pressure sides of hydraulic machines significantly modify the flow and can lead to dramatic drop in performance in addition to vibration and subsequent structural damages. In key applications, unexpected damages and early replacement of the machines can result in huge economic cost. Cavitation is not restricted to water and can occur in any liquid. The diesel injectors of automobiles is one such key area where cavitation inception and erosion is of prime importance. In rocket engines, the liquid fuel and oxidizer are pumped by turbopumps to be injected into combustion chamber. The turbopumps need to be designed to sustain the effects of cavitation and the Space Shuttle Main Engine (SSME) is one such example which experienced many issues during both development and operations due to cavitation. In artificial heart valves also, cavitation can cause blockages and severely affect the functionality risking lives. On the brighter side, cavitation is not only associated with erosion but increasingly considered as a tool for beneficial use as well, such as shock wave lithotripsy (ultrasound shock wave induced disintegration of kidney stones), drug-delivery, microchip cleaning and microfluidics (Lauterborn 2013). Despite more than a century of research, a thorough description of the physical processes of cavitation erosion is still not available. Emphasis has been laid on preventing the initiation of cavitation and where not possible to prevent, minimize the erosive damages. However, an effective prevention strategy and further beneficial exploitation necessitates a deeper understanding of the fundamental physical phenomena in both fluids and solids. This understanding has been pursued in this research with the simplest form of cavitation, the single bubble.

1.3 Literature review

1.3.1 Cavitation Bubble Dynamics

Historically the first scientific study of cavitation is credited to Reynolds 1894, who observed the growth of vapor cavities and subsequent collapse in water flowing through constricted tubes. Later Silverrad 1912 was one of the first to report erosion on the propeller of large cruise boats. Such erosive damages due to low pressure zones generated by the high rotation speed on the propeller blades raised experimental interest in the study of cavitation. Parallely on the theoretical side, Rayleigh 1917 proposed the first model to describe the collapse of an empty spherical bubble in an infinite incompressible, liquid medium with no gravity, surface tension, viscosity, heat or mass transfer. Plesset 1954 adapted and improved the model to take into account surface tension, viscosity and non-condensable gas inside the bubble. This proposed model called the Rayleigh-Plesset equation is given in eq. (1.2), and is still widely used in cavitation studies to determine the temporal evolution of the bubble radius R.

$$\rho\left[R\ddot{R}+\frac{3}{2}\dot{R}^2\right]=p_v-p_\infty+p_{g0}\left(\frac{R_0}{R}\right)^{3\gamma_g}-\frac{2S}{R}-4\mu\frac{\dot{R}}{R} \tag{1.2}$$

Here p_v is the vapor pressure, p_{g0} is the initial partial pressure of the non-condensable gas in the bubble, R_0 is the initial bubble radius, $\dot{R}$ is the bubble interface velocity, γ_g is the adiabatic index of the non-condensable gas, S is the surface tension and μ is the viscosity of the liquid. Many further numerical models were developed for calculating the dynamics of spherical bubble collapse to include the effect of liquid compressibility and gas content. The first numerical solution for bubble collapse and rebound in a compressible liquid medium was proposed by Hickling 1964 which showed the emission of pressure wave at the instant of rebound, propagating outwards from the bubble center. The amplitude of the pressure wave decreases approximately as $1/r$, where r is the radial distance from the bubble center. Further analysis of collapsing bubble dynamics in a compressible liquid medium can be found in Fujikawa 1980 and Prosperetti 1987.

On the dynamics of non-spherical bubble collapse, much of the interest can be traced back to the early work of Naude 1961 and Benjamin 1966. Benjamin 1966 showed successfully that cavitation bubbles do not collapse spherically near solid boundaries. They applied the concept of Kelvin impulse, which is the apparent inertia of the cavitation bubble, to explain the acceleration of a translating cavity during its collapse, coupled with the formation of liquid-jet and formation of bubble vortex ring. A bubble exposed to a pressure gradient experiences a Bjerknes force (translational forces on bubbles in an acoustic field) leading to the motion of the bubble with respect to surrounding liquid. The Kelvin impulse is almost constant during the final stages of bubble collapse. For conservation of this impulse, the velocity of the bubble center has to increase as the bubble size decreases which determines the motion of the bubble. Near a solid wall, it results in increased velocity of the bubble surface located far from the solid wall. This high velocity of the bubble surface far from the wall and its surrounding liquid in comparison to the bubble surface closer to solid wall gives rise to a liquid micro-jet. The velocity of the liquid micro-jet was predicted to be very high, on the order of few hundred m/s, which led to the hypothesis that the liquid-jet piercing the bubble and hitting the solid wall in a non-spherical collapse is the primary cause of cavitation erosion.

Many decades later, this hypothesis is still debatable, nevertheless a much advanced review of liquid micro-jet properties can be found in Obreschkow 2011.

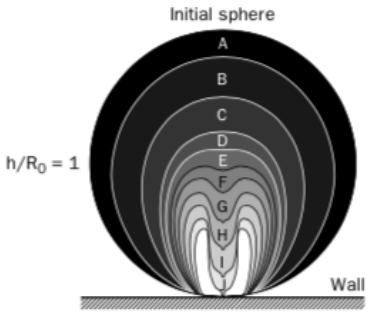

Shape	Time	Velocity (m/s)
A	0.63	7.7
B	0.885	19
C	0.986	42
D	1.013	65
E	1.033	100
F	1.048	125
G	1.066	129
H	1.082	129
I	1.098	128
J	1.119	128

Figure 1.3 – Numerical results from collapse of a bubble close to wall, $R_0 = 1mm, \gamma = 1$. The time is non-dimensionalized time with reference time $R_0\sqrt{\frac{\rho}{p_\infty - p_v}}$ and the velocity is computed on the upper point of the bubble interface near the axis of symmetry (Plesset 1971, image reproduced from Franc 2006).

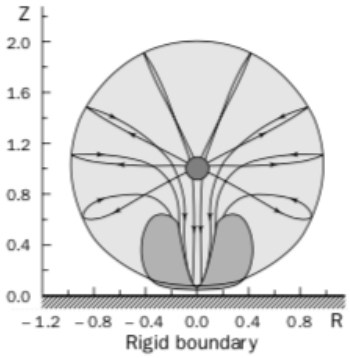

Figure 1.4 – Theoretical calculations for particle path during growth and collapse of a vapor bubble near a wall for $\gamma = 1$ (Blake 1987).

Plesset 1971 numerically predicted the development of liquid jet towards the wall relatively early in the collapse of an initially spherical bubble near a solid wall, long before any compressibility effects could be important. The results of temporal evolution of bubble shape and interface velocity at the bubble upper surface is shown in fig. 1.3. During collapse, a high velocity re-entrant jet is developed, directed towards the solid wall. The velocity of the re-entrant jet increases rapidly while piercing the bubble and hits the solid wall, indicating a possible mechanism of hydrodynamic cavitation erosion. Further insights on the re-entrant jet dynamics were provided by Blake 1987 who presented the particle paths during growth and collapse of the material points on the surface of a vapor bubble for $\gamma = 1$, as shown in fig. 1.4. Here $\gamma = h/R_{max}$ is the non-dimensional stand-off distance where h is the distance between the solid wall and bubble center at the time of formation and R_{max} is the maximum bubble radius. Zhang 2004 performed numerical analysis based on Kelvin Impulse using the boundary integral method to determine the effect

of surface tension on collapsing bubbles near solid wall. They concluded that just before the vapor cavity begins to collapse and the resultant action of Bjerknes force and buoyancy force is small, i.e. when Kelvin impulse is near zero, surface tension can have substantial effects on bubble behaviour such as changing the direction of liquid jet or development of secondary jets. At final stages of collapse, when the action of both the forces are not small (i.e. when the Kelvin impulse acting on the cavity is not near zero), surface tension has no significant effects on bubble behaviour. An additional dimension to the study of this problem appeared when Gibson 1968 showed that the jet formation, direction and intensity are functions of bubble-boundary interaction that can be controlled by changing the character of the boundary impedance. The collapse of bubbles near deformable surfaces was further studied by Gibson 1980, Gibson 1982 and Blake 1987.

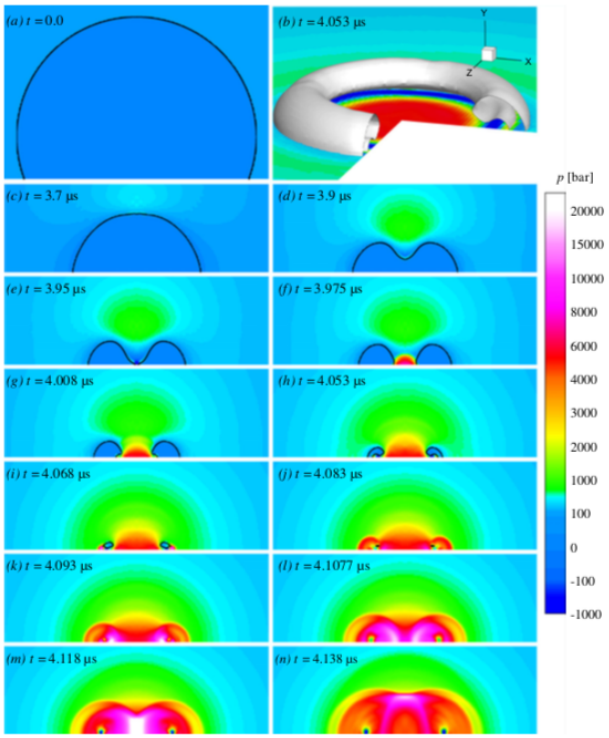

Figure 1.5 – Shape of vapor bubble and pressure field evolution for the collapse of an attached bubble on solid wall, $R_0 = 400\,\mu m$ (Lauer 2012).

Lauer 2012 performed 3D numerical simulations for attached and detached vapor bubbles of initial radius $R_0 = 400\,\mu m$ collapsing near a solid wall at initial liquid pressure of 100 bar. A higher ambient pressure was reported to be relevant in the technical applications of high pressure pumps for liquid-fuel injection system which operates in pressure up to 2500 bar. For a detached vapor bubble at $\gamma = 1.04$, they reported liquid jet velocities of more than $1100\,m/s$ and maximum wall pressure of more than $10,000\,bar$. It was concluded that for a detached vapor cavity at $\gamma = 1.04$ which is collapsing in a liquid at $100\,bar$, the liquid-jet impact has the highest potential for cavitation erosion. The pressure field evolution for an initially attached vapor bubble is shown in fig. 1.5. For an attached cavity at $\gamma = 0.35$, liquid jet could reach velocities up to $900\,m/s$ creating pressures of more than $14,000\,bar$ and further strong shock waves from the collapse of bubbles ring vortex leading to

maximum pressure of $50,000\,bar$. Shock waves are propagating disturbances in the liquid (or any fluid medium) that travels faster than the local speed of sound. The maximum wall pressure obtained by Lauer 2012 for different stand-off distances is shown in fig. 1.6.

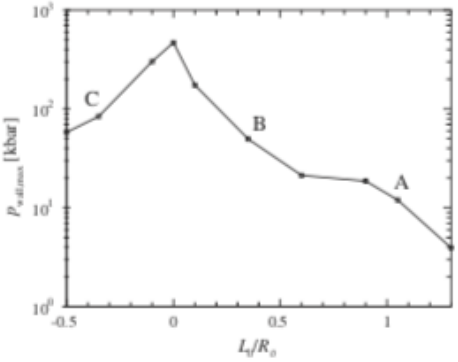

Figure 1.6 – Maximum wall pressure obtained for different stand-off distances (Lauer 2012).

Further insights on numerical simulations of bubble collapse were provided by Müller 2010 who studied the collapse of gas bubbles by considering the liquid-gas phases as single compressible medium characterized by different equation of states and Johnsen 2008, Johnsen 2009 who used a high order shock & interface capturing scheme to simulate gas bubble collapses in water. Hawker 2012 studied shock waves interacting with gas bubbles in liquid medium using front-tracking schemes identifying new dynamical features at the final stages of bubble collapse. They performed full $3D$ and rotationally symmetric simulations to compare spherical and cylindrical bubbles, and reported 40% higher pressure for a spherical bubble compared to a cylindrical one.

Experimental methods were also developed to generate single bubbles on demand, growing and eventually collapsing in a liquid at rest. These single bubbles can be generated by several means by local energy deposition (for example, through a focussed laser beam) or by exciting cavitation nuclei with acoustic pressure, to the point where the bubble grows several times their initial volume. With high speed imaging, it becomes possible to observe phenomena such as the formation of liquid micro-jets at the collapse, or the propagation of shock waves in the liquid. Since experimental bubble dynamics is also a part of this thesis, it will be discussed in chapter 2.

In this review, the discussion has been restricted to some early interest on cavitation bubble dynamics and then to the mechanism of cavitation erosion. Although the early work focused mostly on theoretical and experimental findings, numerical techniques and improved computational resources have added to the understanding of bubble-wall interactions. More on numerical modelling of collapsing bubbles can be found in Best 1992, Wang 2010, on the effect of viscosity in Popinet 2002 and bubble collapse in a flowing liquid with pressure gradient in Tinguely 2013.

1.3.2 Cavitation Erosion

Cavitation erosion has been studied for long, mostly on the macro-scale of sheet and vortex cavitation. Erosion takes place on small, concentrated areas of solid walls exposed to cavitation. The collapse of vapor structures exerts mechanical energy, leading to high stress levels on the solid surface. A detailed review of hydrodynamic cavitation erosion has been reported in Franc 2006, Brujan 2011, Franc 2009 & Franc 2012. A typical experimental observation of mass loss rate with exposure time is shown in 1.7. An initial period with no mass-loss is the so-called incubation period, followed by a progressively increasing mass loss in the acceleration period. It finally reaches a steady state and with further exposure time, experimentally an attenuation period is often reached with decreased erosion rate. Plastic deformation of the material surface in the form of permanent indentation or pitting is a very typical material response during the incubation period in hydrodynamic cavitation.

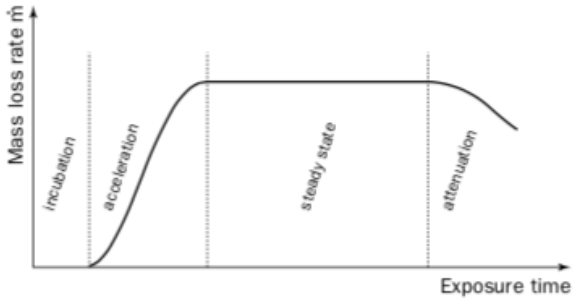

Figure 1.7 – Experimental mass loss rate vs exposure time (Franc 2006).

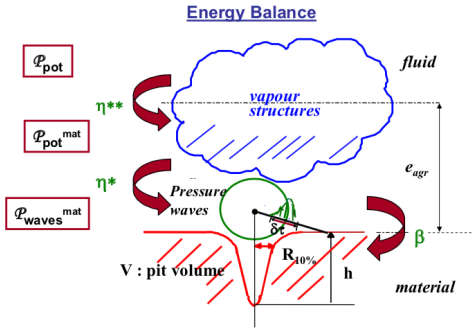

Figure 1.8 – Schematic of erosion model by Fortes-Patella 2004.

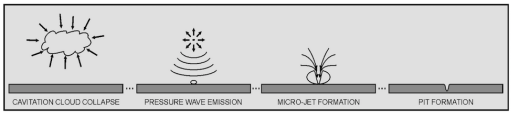

Figure 1.9 – Schematic of erosion model by Dular 2006.

Many cavitation erosion models have been proposed based on the conversion and focusing of the potential energy of vapor cavities in space and time on the material surface by attached vortices. Fortes-Patella 2004 proposed a cavitation

erosion model based on the physical scenario of collapsing vapor structures, emission and propagation of pressure waves from the cavities. The final material damage results from the interaction of pressure waves and neighbouring solid surface shown in fig. 1.8. Dular 2006 suggested an erosion model from collapse of cavitation cloud and emission of shock wave that attenuates as it travels towards the solid surface. The shock wave excites the individual bubbles near the solid surface and the final damage pits are formed from the high velocity liquid jet impacting the solid surface shown in fig. 1.9. A comprehensive review of these erosion models is provided by Van Terwisga 2009.

1.3.3 Fluid-Structure Interaction (FSI)

Material deformation and pitting from cavitation bubble collapse has gained a lot of interest in the recent years. A Fluid-structure Interaction (FSI) study provides insight into different dynamical features of fluid and solid mechanics, connecting the links between cavitation load and surface deformation. One of the approaches adopted is by Roy 2015a, Roy 2015b & Pöhl 2015 to determine the cavitation loads by an inverse FEM approach based on surface pit analysis. This cavitation-induced pressure estimated from the surface pit analysis can be validated with CFD and experimental results, as shown in fig. 1.10. This type of methodology gives detailed

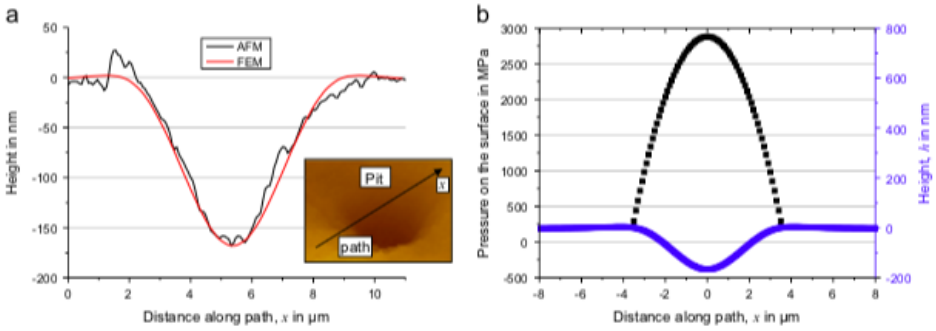

Figure 1.10 – (*left*) Nearly axi-symmetric pit height profile from AFM (experiments) and FEM (simulation), (*right*) numerically predicted pressure distribution on surface and pit height (Pöhl 2015).

insight on material response due to strain rate sensitivity, hardening, damage initiation and failure, as shown in fig. 1.11 from the work of Fivel 2015. But such an analysis requires surface pits as input either from the experiments or CFD simulation. This highlights the need for highly resolved 3D fluid simulations down to the fundamental scale of single bubble collapse.

Also the need for FSI can be highlighted by understanding the effect of impact loads on rigid metallic materials and compliant materials. Reported in Franc 2006, the impact pressure from a high velocity liquid jet on an elastic material can be written as eq. (1.3):

$$\Delta p = \frac{(\rho_l c_l v_l)}{1 + (\rho_l c_l / \rho_s c_s)} \tag{1.3}$$

Two shock waves are created on the impact of liquid jet - one shock propagating in the solid and one shock reflecting back into the liquid. The numerator $\rho_l c_l v_l$ is the water hammer pressure for the liquid jet of velocity v_l on a perfectly rigid wall, $\rho_l c_l$ is

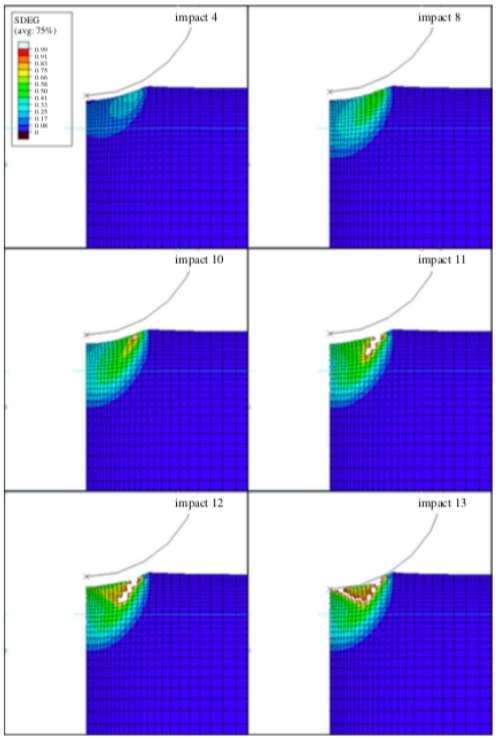

Figure 1.11 – FEM modelling of material fatigue and mass loss after repetitive impacts (Fivel 2015).

the acoustic impedance of liquid and $\rho_s c_s$ is the acoustic impedance of solid, which is related to the Young's modulus E by $\rho_s c_s = \sqrt{\rho_s E}$. The ratio of acoustic impedance $(\rho_s c_s / \rho_l c_l)$ is infinite for a perfectly rigid wall, whereas for a perfectly compliant wall it is zero. Therefore, an elastic wall sees a much smaller impact pressure compared to the rigid wall. The impact pressure vanishes for a fully compliant wall due to the damping effect of the wall.

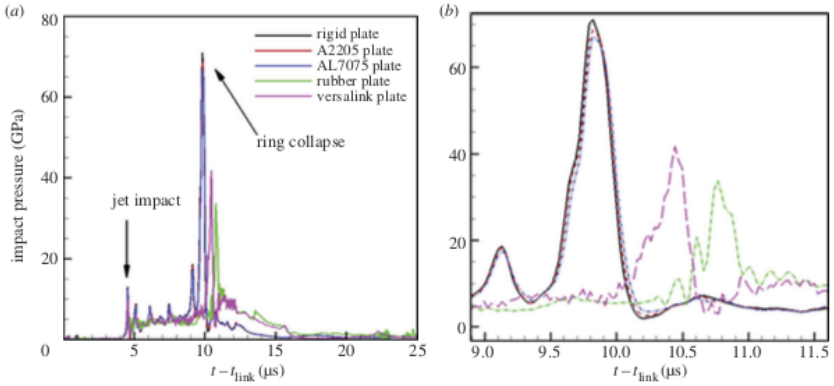

Figure 1.12 – $(left)$ Time evolution of pressure from bubble collapse showing liquid jet and bubble ring collapse, $(right)$ zoom near ring collapse pressure peaks for two rigid and two compliant materials $R_{max} = 2\,mm$, driving pressure $p = 0.1\,MPa$ (Chahine 2015).

Therefore, the logical extension is the FSI study resolving both the fluid and solid dynamics. Some studies have been performed by Hsiao 2014, Choi 2016, Chahine 2016, Paquette 2017 with different numerical approaches. Chahine 2015 reported the pressure peaks shown in 1.12 corresponding to liquid jet impact and bubble ring collapse on the solid wall. The liquid jet penetrates the cavitation bubble from the bubble surface far from the wall and hits the wall. The bubble takes a ring or torus shape after the jet penetration. The bubble ring subsequently collapses on the solid wall accompanied by the propagation of shock waves which were reported in the study. The authors also reported the damping effect on impact pressures seen for rigid and compliant materials.

1.4 Thesis Overview

The aim of this thesis is to investigate the mechanism of cavitation erosion on the fundamental scale of single bubble collapse. For such studies, it is vital to focus on the characteristic features of the bubble collapse and impact pressure peaks on the solid wall. Once a detailed understanding of erosion potential from different dynamical features of a single bubble collapse is achieved, a systematic study to include the effect of the solid material response has to be considered. In this thesis, a FSI methodology has been pursued by combining Computational Fluid Dynamics *(CFD)* and Computational Solid Mechanics *(CSM)* on the scale of single bubble collapse. The effect of material surface deformation on the dynamics of the collapsing cavitation bubble near rigid wall is also pursued.

Initially, the collapse of a vapor bubble surrounded by a liquid is modelled as represented in fig. 1.13, where p_{bubble} is the pressure inside the bubble and p_{liquid} is the surrounding liquid pressure such that $p_{liquid} \gg p_{bubble}$. The vapor bubble

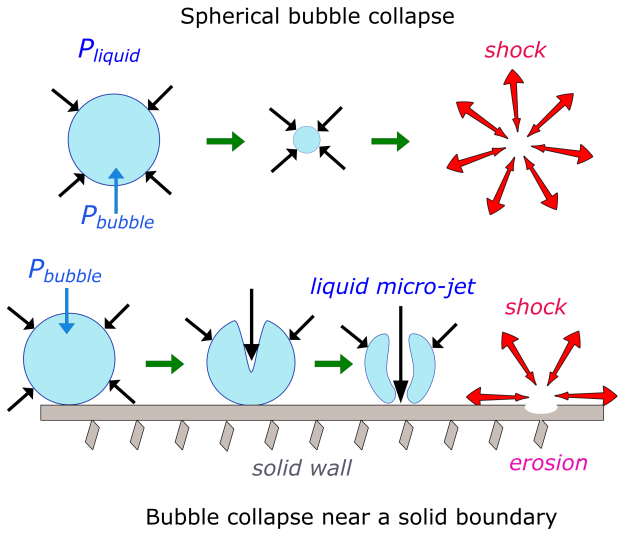

Figure 1.13 – Vapor bubble collapse due to imposed pressure difference $p_{liquid} \gg p_{bubble}$, (top) collapse of an isolated bubble - spherical collapse, (bottom) bubble collapse near a solid wall - non-spherical collapse.

surface starts to shrink towards the center of the bubble due to higher surrounding

liquid pressure with an accelerated liquid flow towards the center. During the final stages of the collapse, a high impulse shock wave is produced and propagated into the surrounding liquid. For an isolated bubble, the collapse is basically spherical and a shock wave forms near the center of the bubble which propagates into the surrounding liquid. For a non-spherical bubble collapse due to its proximity to the solid wall, a liquid re-entrant micro-jet pierces through the bubble surface opposite to the solid wall, accelerating one side of the bubble towards the opposite surface. The liquid jet is directed towards the solid wall and multiple shock waves are emitted due to the impact of the liquid jet with the opposite bubble surface and eventually, the solid wall. This highly dynamical sequence of events along with high amplitude pressure peaks at the solid wall from emitted shock waves and liquid micro-jet needs to be resolved first to predict material response.

The focus initially is to develop the requisite methodology in the CFD solver YALES2 and CSM solver CAST3M to model accurately a 2D bubble collapse and then extend it to a 3D bubble collapse. As observed in experiments on laser-induced bubble dynamics, a collapsing bubble could undergo multiple collapses and rebounds depending on the stand-off distance. A collapsing bubble relatively far from the wall will undergo one or two collapses and rebounds before impacting the solid wall. The flow field during bubble collapse can be assumed to be axisymmetric only in the first bubble collapse. Therefore, axisymmetric computations can only be an intermediate step and there must be full 3D computations for accurate predictions. In the fluid solver the bubble will be resolved with Direct Numerical Simulation (DNS), that is to say that one simulates on a mesh sufficiently fine and with time steps rather reduced so that all the temporal and spatial scales of the flow are taken into account without any sub-grid scale model. The partitioned fluid and solid domains are solved separately with boundary conditions computed from the other domain shown in fig. 1.14. This necessitates the implementation of the fluid mesh deformation

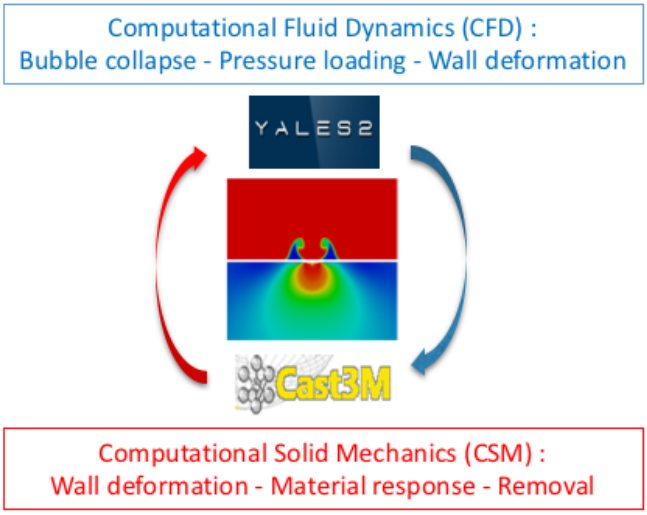

Figure 1.14 – Representation of proposed FSI using CFD-CSM solvers.

procedure into the fluid solver. The Arbitrary Lagrangian-Eulerian (ALE) technique combining the Eulerian and Lagrangian formulations for the deformation of the fluid mesh is implemented into the compressible fluid solver developed as part of this

thesis. ALE provides the ability to maintain high quality meshes near the deformed solid interface, resulting in a more accurate prediction of fluid mechanics.

A *step-wise coupling approach* is employed to couple the CFD and CSM domains in our fluid-structure interaction analysis. The CFD and CSM physical domains are solved separately and sequentially for the entire computational time. Data is extracted independently from each numerical simulation at a coupling interval Δt_{FSI}. The analysis begins with the CFD simulation of bubble collapse (CFD step 1) which provides the surface pressure predictions every Δt_{FSI}. These spatial-temporal pressure evolution is used by the CSM simulation (CSM step 1) as boundary condition to provide the resulting solid response and surface deformation. The spatial-temporal surface deformation predictions are used as input boundary conditions introduced every Δt_{FSI} for the next CFD simulation step (CFD step 2) where the same bubble collapse simulation as CFD step 1 is performed again but with newly introduced boundary conditions. This step is followed by next step of CSM simulation and so on. This cycle of independent but sequential steps of CFD and CSM simulation is continued until convergence is achieved between consecutive CFD and CSM steps on the surface pressure and deformation predictions, as shown in fig. 1.15. A further distinction can be made between one-way and two-way FSI coupling. A one-way coupling involves one CFD simulation step for surface pressure predictions, followed by a single CSM simulation step for resulting surface deformation. No effect of surface deformation is introduced on the collapse dynamics of the bubbles. On the other hand, the two-way coupling is continued until there is an agreement between the resulting surface deformation and the collapse dynamics of the bubble.

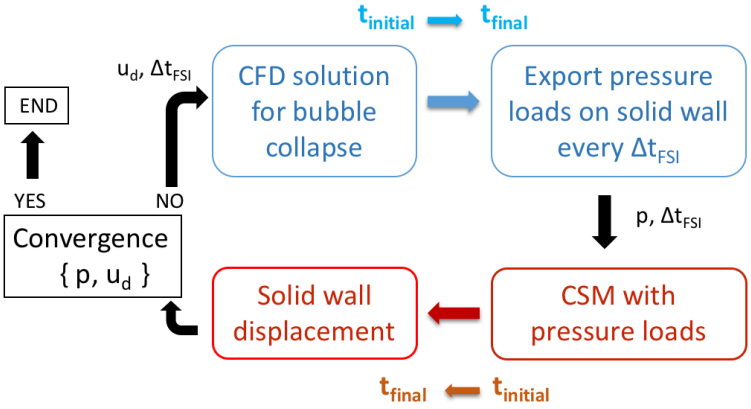

Figure 1.15 – Step-wise FSI methodology.

The computational data in the simulations are exchanged at the boundaries of the physical domain. A step-wise FSI approach requires comparatively less computational development for data exchange and storage between solvers, allowing them to work independently taking advantage of their respective optimizations. Each solver can use its own numerical methods, different spatial resolution at the coupling interface and may even work on different computing machines. Further benefits can be derived by controlling the FSI coupling process for scheduling and frequency of the data exchanges with Δt_{FSI} and exchange of interpolated data through a matching/non-matching physical interface.

An introduction to the numerical solvers is given below:

- **YALES2**
  YALES2 [1](Yet Another Large Eddy Simulation Solver) is a *finite volume method* (FVM) based multi-physics code for a wide range of flow problems developed at CORIA, Rouen (FRANCE) by V.Moureau since 2007. It is currently developed, maintained and available to participating French laboratories of the scientific group SUCCESS [2] including LEGI, Univ. Grenoble Alpes. Dedicated to both incompressible and compressible approach, the code is designed to benefit from massively parallel architectures using several thousands of processors and to manage very large computational grids, which can be composed of up to several billions mesh elements. Figure 1.16 shows the speed-up graph of YALES2 on up to 32768 processors for a weak scaling test case. Weak scaling represents the software performance for an increasing number of processors with increasing mesh resolution at the same time. YALES2 is capable of refining the computational mesh automatically during computations, thus combining the mesh refinement with HPC capability of the code.

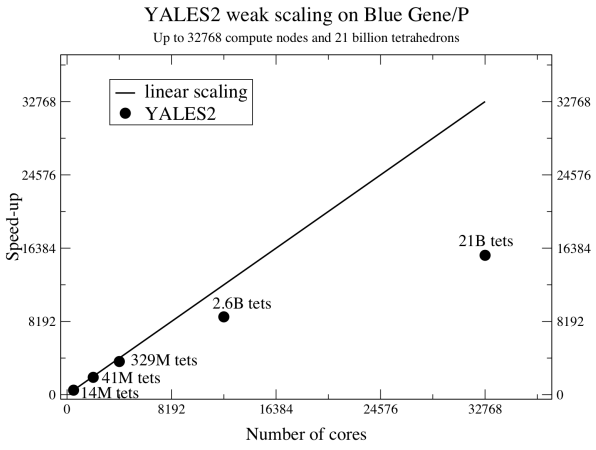

Figure 1.16 – Weak scaling of YALES2 on an IBM BlueGene/P computer (Moureau 2011).

- **Cast3M**
  Cast3M [3] is a tool for numerical simulation of solid mechanics using the *finite-element method* (FEM) for different types of scientific problems. It is developed by the Department of Modelling of the Systems and the Structures (DM2S, Département de Modélisation des Systèmes et Structures), of the French Atomic Energy Commission and Alternative Energies (CEA, Commissariat Français à l'Energie Atomique et aux Énergies Alternatives). The code is written using the *Gibiane* programming language to describe data and operations and *Esope* (extension of fortran 77) to develop the source

1. http://yales2.coria-cfd.fr
2. https://success.coria-cfd.fr
3. http://www-cast3m.cea.fr

code. The code is written entirely in French and perform the pre-processing, calculations and post-processing of thermo-mechanical problems in static and dynamic domains.

This thesis has been organized as follows:

- Chapter 1 discusses the physical aspects of cavitation erosion, motivation, literature review and outlines the thesis overview for this research work.
- Chapter 2 presents results from experimental investigations on the dynamics of laser-generated bubbles and observed surface deformation. Distinguishable differences in dynamics of non-spherical bubbles for different distances from the solid wall and its importance on surface deformation is discussed.
- Chapter 3 introduces the governing equations for fluid flow modelling in CFD. The development of 3D compressible, unsteady solver for cavitation, equipped with ALE capabilities, in YALES2 is described in detail. The physical model of phase-change with equations of state and numerical boundary treatments are discussed.
- Chapter 4 presents the FEM methodology for CSM modelling in the Cast3M solver, to predict solid material response to cavitation impact. The FSI coupling methodology for one-way and two-way coupling is described in detail with their key assumptions.
- Chapter 5 discusses the numerical results for validation of the developed Compressible Cavitation Solver (CCS) and Cavitation ALE Solver (CLE) solvers with test cases such as 1D shock tube, Rayleigh-Plesset model and bubble collapse in a moving computational domain.
- Chapter 6 introduces the simulation results for 2D and 3D bubble collapses near solid wall. The surface pressure peaks associated with different characteristic features of bubble collapse are identified and analyzed.
- Chapter 7 discusses the response of three different solid materials, namely on Aluminum alloy (Al-7075), duplex stainless steel (St A-2205) and Nickel-Aluminum Bronze (NAB) to cavitation impact loads obtained with fluid-structure interaction.
- Chapter 8 discusses the important conclusions from this thesis and summarizes the possible future work.

Chapter 2

Experimental Bubble Dynamics

2.1 Introduction

A thorough understanding of the dynamics of single bubble collapse near solid surfaces is essential to the understanding and development of a computational model to predict cavitation erosion. Experimentally cavitation is initiated in a fluid medium by creating a local decrease in pressure through a mechanical apparatus or acoustic waves. Multiple bubbles usually appear simultaneously in acoustically driven bubble generation systems which could influence the single bubble dynamics investigation. An alternative is local energy deposition in the form of light and heat through laser or spark to initiate the phase change. A short laser pulse is one of the preferred experimental methods for generating a single bubble. It typically involves an optical system focussing the energy from the laser into a small focal volume, causing local heating of the water. The size and shape of the bubbles generated are dependent on the energy of the laser beam, type of laser used, the focussing angle and the laser pulse duration. An overview of the laser generated bubbles and their use in cavitation research, shock wave lithotripsy, shock wave cleaning and other biological applications can be found in Lauterborn 2013, Ohl 1999, Song 2004. When a bubble collapses near a solid wall, a high-speed liquid jet travels towards the surface, accompanied by a localized shock wave emission, and sometimes bright light emission at collapse known as *sonoluminescence*. The liquid micro-jet impact and the shock wave interaction with the solid wall are primarily believed to be responsible for the surface damage. The debate about which of these phenomena causes the most damage is quite old and a long one, but both phenomena are indicative of bubble collapse and surface damage. The entire formation and collapse process occurs on a very small scale with cavitation bubble radius of few millimetres (mm) and a collapse time of few microseconds (μs). Despite the small size of the bubbles and the short duration of the collapse, the pressures generated are very large, approximately in the order of gigapascals (GPa) depending on the operating conditions. Due to such discrepancies between these scales, studying cavitation erosion even for a single bubble collapse is quite challenging with the requirements of high speed cameras, laser system, optical and pressure sensors equipments. On the solid material side, surface pits of few micrometers (μm) are typically observed after bubble collapses. Therefore, a polished solid surface needs to be prepared with residual surface roughness of few nanometers (nm) to detect accurately surface damages from a single

bubble collapse using high resolution optical microscopes.

Much experimental research has been performed to study the interaction of cavitation bubbles with a solid wall like in Lauterborn 1997, Bremond 2006. Most notable of them is by Philipp 1998 who studied the dynamics of laser generated cavitation bubbles in water and the resulting surface damage on a flat aluminum surface. High speed visualization of different dynamical features of collapsing bubbles and surface damage patterns were presented for an aluminum sample at different non dimensional stand-off distance $\gamma = h/R_{max}$, where h is the distance between the solid wall and bubble center at the time of formation and R_{max} is the maximum bubble radius, as shown in fig. 2.1. In the case of a non-spherical bubble, R_{max} is the equivalent radius defined as the radius of a perfectly spherical bubble that would have the same volume as the non-spherical bubble. Philipp 1998 reported maximum surface pit depth corresponding to greatest damage by single bubble collapse for $\gamma \leq 0.3$ and $\gamma = 1.2$ to 1.4 from laser generated single bubble, $R_{max} = 1.45\,mm$ shown in fig. 2.2.

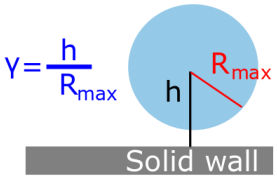

Figure 2.1 – Stand-off distance, $\gamma = h/R_{max}$.

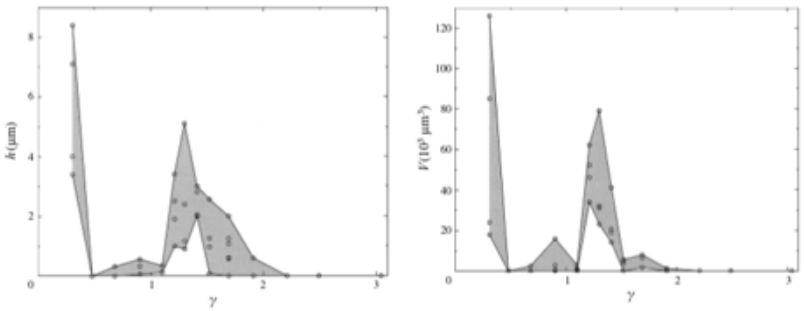

Figure 2.2 – Collapse of single cavitation bubble on an aluminum sample, $(left)$ maximum depth of surface damage produced, $R_{max} = 1.45\,mm$, $(right)$ volume of deformation (Philipp 1998).

Reuter 2017 reported bubble shapes, vortex ring dynamics and time resolved flow field measurements for bubble collapse near solid wall using high speed cameras, hybrid particle imaging velocimetry and particle tracking velocimetry techniques. The authors identified and presented resolved flow field visualizations of two kinds of bubble ring vortices for collapsing bubble near solid wall. First is the wall vortex, where a ring vortex of opposite circulation moves towards the solid wall and subsequently spreads radially over the wall. Second is the free vortex, where a ring vortex that translates into the liquid away from the solid wall. The flow field for a collapsing bubble, $R_{max} = 340\,\mu m$, $\gamma = 1.1$ is shown in fig. 2.3 where the free vortex moving away from solid wall can be seen in the final stages of collapse at $t = 191\,\mu s$.

Shaw 2000, Shaw 2001 recorded pressure stress at the solid surface, particularly during the first collapse using a series of pressure transducers for collapsing laser generated bubbles. Tomita 2002 performed laser induced cavitation bubble collapses near curved surfaces drawing up comparisons for bubble motion and liquid jet ve-

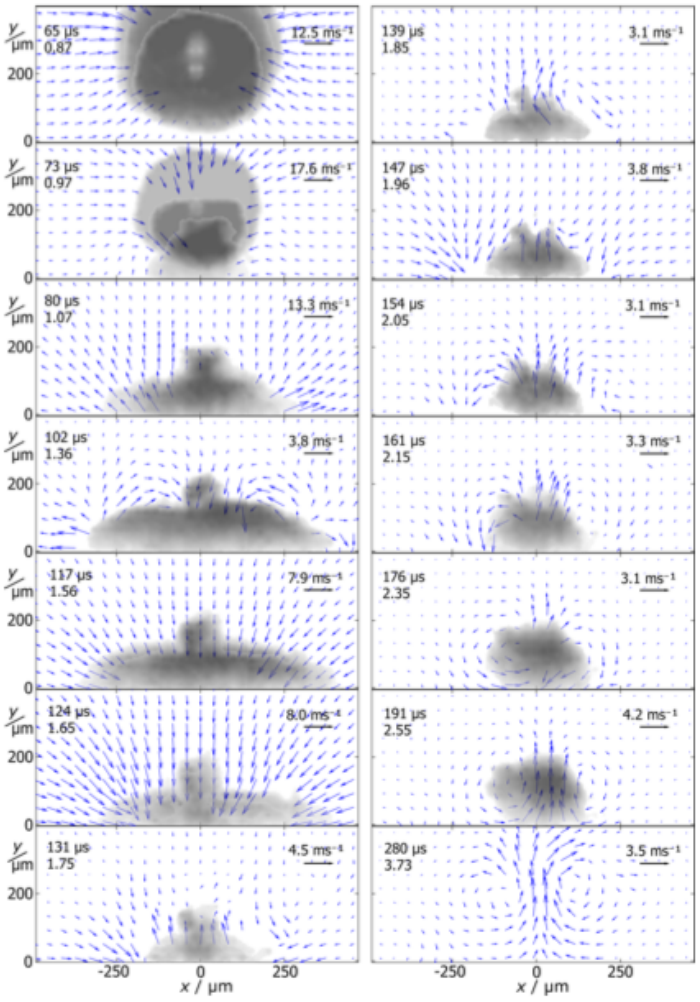

Figure 2.3 – Evolution of velocity field during bubble collapse near a solid wall and development of free vortex $\gamma = 1.1$, $R_{max} = 340\,\mu m$ (Reuter 2017).

locity between curved rigid and flat rigid boundaries. The authors reported higher liquid jet velocity in the case of a curved rigid boundary during bubble collapse, suggesting higher impact pressures near non-flat boundaries. This phenomenon was suggested to be partly responsible for increased mass loss after incubation period in cavitation erosion experiments.

Brujan 2001 investigated the behaviour of laser induced cavitation bubbles near a compliant elastic boundary made of polyacrylamide (PAA) gel with 80% water concentration and elastic modulus $E = 0.25 MPa$, to test its suitability in preventing cavitation erosion. They identified that in elastic boundaries for $\gamma \geq 0.6 \sim 0.7$, the bubble starts collapsing from the bubble surface close to the boundary and the liquid-jet is directed away from the boundary. For $\gamma < 0.6$, the liquid jet is directed towards the boundary with the bubble side far from the boundary collapsing first as shown in fig. 2.4.

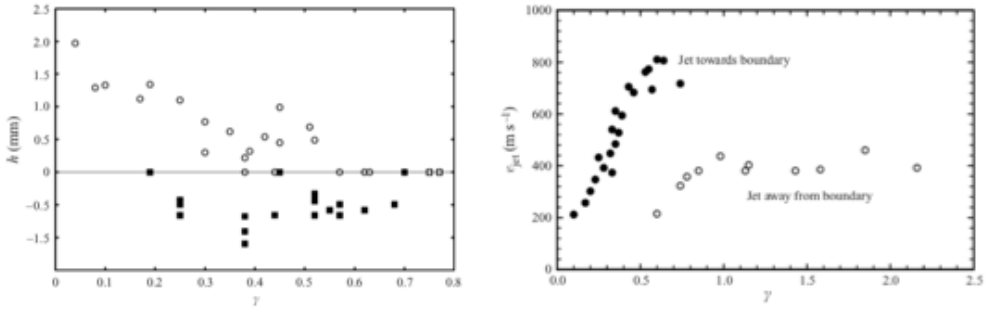

Figure 2.4 – (*left*) Maximum jet velocity and (*right*) penetration depth from liquid jet into a PAA sample for bubble collapsing near elastic boundaries (Brujan 2001).

In the present work, laser generated single and multiple bubble collapses near a flat solid surface are investigated for different γ. We are presenting bubble dynamics at $\gamma = 0.55, 0.87, 1.1, 1.4, 1.7, 2.14$. This research work has been performed at School of Physical and Mathematical Sciences, Nanyang Technological University (NTU), Singapore, with Julien Rapet under the supervision of Prof. Claus-Dieter Ohl (currently Professor at Institute of Physics, Otto-von-Guericke-Universität Magdeburg, Germany) as part of a 2-month secondment of project CaFE. The experimental setup, methodology and some interesting results are presented for collapsing bubbles near aluminum samples in the next sections.

2.2 Experimental Setup

Aluminum is used as the solid wall for the collapsing bubbles. Aluminum is soft, lightweight and can be severely deformed without failure. The tensile strength of pure aluminum is around 90 MPa but this can be increased to over 690 MPa for some heat-treatable alloys. "As-received" pure aluminum sample undergoes work-hardening, also known as cold working, during the production process which involves subjecting the metal to mechanical stress so as to cause a permanent change to the crystalline structure for strengthening a metal. The resulting metal product has improved tensile strength and hardness, but less ductility. Aluminum hardened by cold working can be restored to a soft, ductile condition by annealing which eliminates strain hardening as well as the changes in structure that are the result of cold working. These changes occur in several stages according to the temperature or time during the recovery process. Complete recovery from the effects of cold working is obtained only with re-crystallization which is characterized by the gradual formation and appearance of a microscopically resolvable grain structure. The new structure is largely strain-free with very few, if any, dislocations or imperfections within the grains.

Three different aluminum samples are prepared at SIMaP, Univ. Grenoble Alpes to be used as solid wall for the experiments. The first sample is an aluminum alloy Al-7075-T651 while the second sample is the "as-received" pure aluminum sample from the vendor. The third sample is a specially prepared recovered aluminum, for which recovery process was conducted by heating the "as-received" pure aluminum sample at 560° for 2 hours and letting it cool in room temperature in order to

remove any pre-existing work hardening. The sample surfaces are polished in 6 stage manual and automatic polishers up to 30 nm surface roughness. The samples can be categorized in the order of increasing hardness : Alloy Al-7075 $>$ pure Al $>$ recovered Al.

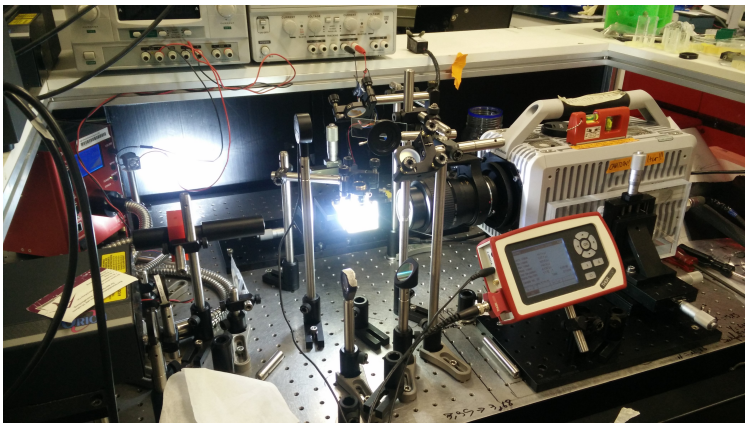

Figure 2.5 – Experimental setup for laser generated bubble collapse near solid wall.

In the experiments, bubbles are nucleated by focusing a laser pulse from a Q-switched Nd:YAG laser (New Wave Research Orion) into a glass cuvette filled with de-gassed distilled water. The laser delivered light pulses of beam diameter 2.75 mm at a wavelength of 532 nm with energies of up to 10 mJ and a pulse duration of 6 ns. The laser beam is first expanded by a plano-concave lens ($f = -35\,mm$) and collimated using a plano-convex lens ($f = 250\,mm$). A 4x microscope objective ($Olympus\ UPlanFL\ N\ 4x/0.13na$) is used to focus the laser beam inside the water as shown in fig. 2.5. During each laser exposure, the pulse energy was measured by reflecting with a glass plate approximately 5% of the laser energy into a pyroelectric energy sensor ($Thorlabs\ ES111C$). The aluminum sample is fixed on the side wall of the glass cuvette and the laser pulse is shot from the top of the cuvette which made the direction of the laser pulse parallel to the solid wall.

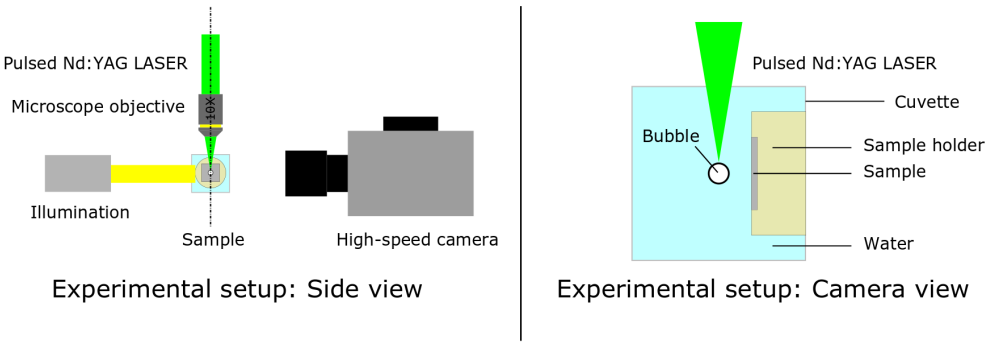

Figure 2.6 – Schematic of the experimental setup for laser generated bubble collapse near solid wall.

The dynamics of the bubble collapses are recorded using a high speed camera ($Photron\ FASTCAM\ SA{-}X2$). The camera offers recording rates up to $13,500\,fps$

at megapixel image resolution with a $12 - bit$ dynamic range and frame rates up to $1,080,000\ fps$ at reduced image resolution with shutter speeds as short as $293\ ns$. A schematic of the experimental setup is shown in fig. 2.6.

The surface deformation is observed under high resolution optical microscope and Atomic Force Microscope (AFM) is used to estimate pit dimensions. The different dynamics of the collapsing bubbles and their salient features are discussed next. For convenience, all the high speed photographic frames of bubble dynamics presented have been rotated 90° to the right so that the solid wall is at the bottom of the presented frame wherever applicable and the laser beam direction is from left to the right of the frames.

2.3 Bubble Dynamics

2.3.1 Isolated Bubble Collapse

An isolated single bubble undergoes nearly symmetrical collapse for most part of its life cycle. After nucleation, the bubble grows and expands to a spherical cavity whose size is dependent on the energy deposited. It is followed by a series of bubble collapses and rebounds. A spherical bubble collapse shows volume pulsations during successive collapse and rebounds which have to be captured at high frame rates to estimate its radial evolution. Energy is continuously converted between different forms as the bubble oscillates in the liquid medium. The gas in the bubble is compressed during collapse along with acoustic emission. Figure 2.7 shows a nearly spherical growth and collapse of a laser generated isolated bubble $R_{max} = 535\ \mu m$, far from the solid wall in water at 200000 fps.

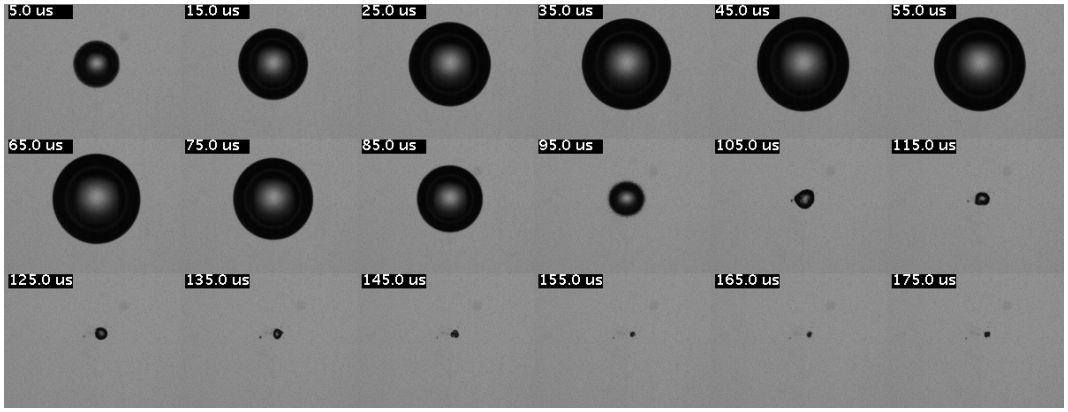

Figure 2.7 – *Left to right, top to bottom*: Isolated bubble undergoing a nearly spherical collapse $R_{max} = 535\ \mu m$, resolution=200000 fps.

Figure 2.8 shows the evolution of bubble radius with time for an isolated bubble having $R_{max} = 420\ \mu m$ at 540000 fps up to three rebound stages. The bubble loses most of its energy after the first symmetrical collapse and undergoes mostly asymmetric oscillatory collapses after. As observed in this experiments and also reported by Vogel 1989, the flow field around an isolated bubble can be assumed to be spherically symmetric only in the first collapse. During rebound, the bubble shape loses spherical symmetry due to instabilities.

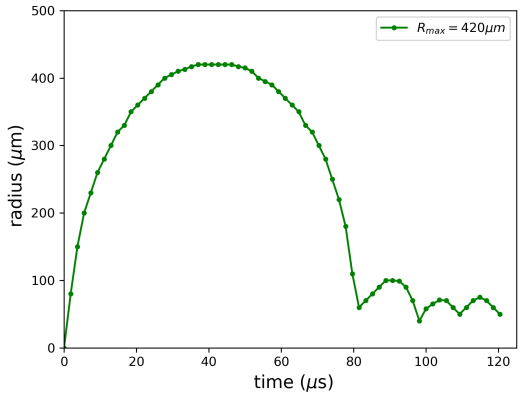

Figure 2.8 – Evolution of bubble radius with time - isolated bubble collapse and rebound $R_{max} = 420\ \mu m$, resolution=540000 fps.

With the presence of some geometric asymmetry in the bubble or its surroundings due to the presence of a solid wall or a pressure gradient, the bubble dynamics changes dramatically with new bubble shapes, motion and characteristic flow field patterns discussed next.

2.3.2 Bubble collapse near solid wall

As mentioned, the stand-off ratio γ affects not only the damage pattern but also the magnitude of the pressure and velocity fields at collapse. A collapsing cavitation bubble near a solid wall leads to the formation of a liquid jet directed towards the wall, piercing the bubble. It leaves behind a toroidal bubble initiating the characteristic torus bubble dynamics with collapse of the toroidal ring that traps the remnant gas and emits shock waves. For convenience from here on, the bubble surface close to the solid wall will be referred as bubble lower surface and bubble surface opposite to the solid wall will be referred as bubble upper surface. Depending on the value γ, the dynamical features of the collapsing bubbles can be classified into four major categories described below.

2.3.2.1 Stand-off $\gamma \leq 0.6 \sim 0.7$

In the case of $\gamma \leq 0.6 \sim 0.7$ the bubble is attached to the solid wall during its growth after nucleation, as seen in fig. 2.9. The bubble collapse initiates with curvature of the bubble upper surface and generation of an inwardly moving flow with decreasing bubble volume. The bubble torus is compressed by the evolving liquid micro-jet from inside and the inward moving flow from outside. The liquid jet piercing through the bubble hits the wall and the bubble collapses on the wall during the first collapse. As it cannot be clearly identified from the images whether a thin liquid film exists in between the wall and expanding bubble, for such small γ, the bubble is considered to be in close contact with the wall. There is no water layer in between the bubble and wall to retard the micro-jet, so it impacts the wall with its maximum velocity. By the time the liquid jet impacts the wall, the bubble volume has shrunk considerably and the remaining volume disintegrates into tiny micro-cavities on the surface seen in fig. 2.9 for a bubble $R_{max} = 400\ \mu m, \gamma = 0.55$.

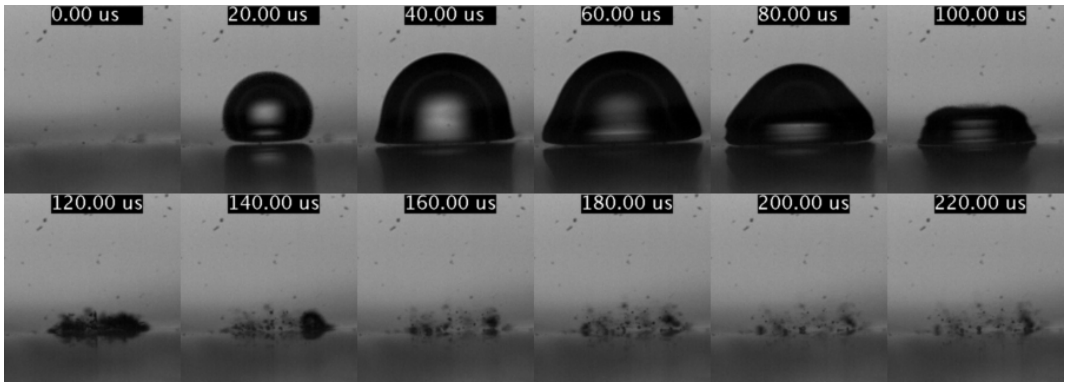

Figure 2.9 – *Left to right, top to bottom* : Liquid micro-jet impacting the solid aluminum surface $R_{max} = 400\,\mu m$, $\gamma = 0.55$, frame size= $1.2 \times 1.4\,mm^2$.

2.3.2.2 Stand-off $0.8 \leq \gamma \leq 1.2$

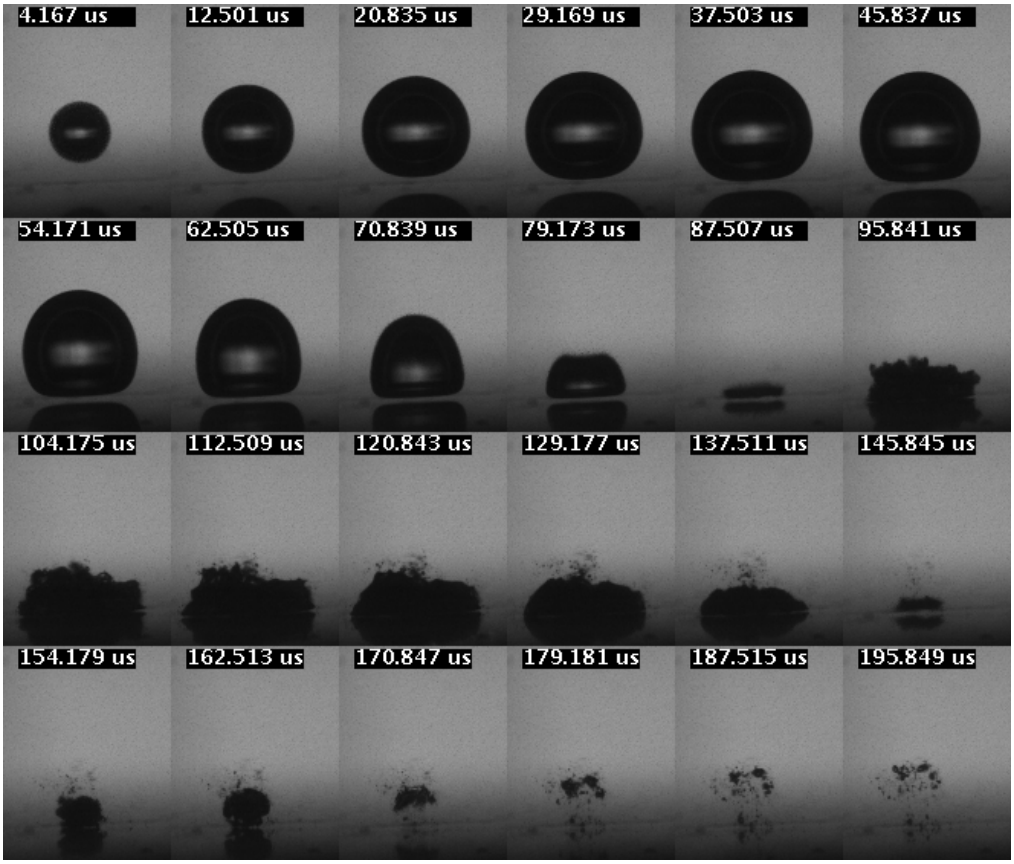

Figure 2.10 – *Left to right, top to bottom* : Collapse of bubble and resulting "splash" effect , presence of liquid film between the bubble and aluminum surface can be observed during the growth and first collapse, $R_{max} = 390\,\mu m$, $\gamma = 0.87$, frame size= $1.1 \times 1.4\,mm^2$.

For $0.8 \leq \gamma \leq 1.2$, the bubble grows very close to the wall. The presence of solid wall flattens the bubble lower surface during its expansion, as seen in fig. 2.10 for a bubble with $R_{max} = 390\,\mu m, \gamma = 0.87$. The presence of a thin water layer can be

observed between the bubble and the wall in the frames. The bubble volume shrinks during the initial stages of collapse with the bubble lower surface remaining more or less flat, as seen from $t = 54.171\ \mu s$ onwards. The first collapse of the bubble volume takes place very close to the wall. The liquid micro-jet piercing the bubble from the bubble upper surface hits the bubble lower surface few moments before the first collapse forming a ring shaped bubble torus.

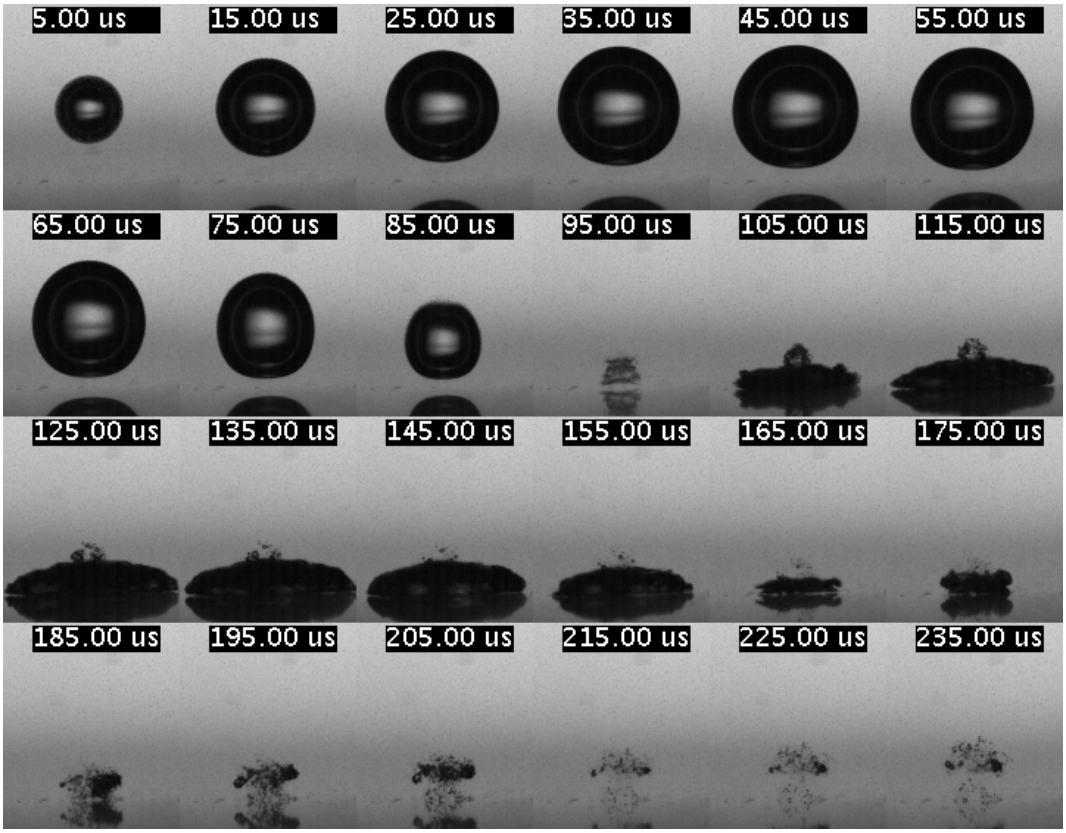

Figure 2.11 – *Left to right, top to bottom*: "splash" effect after the collapse pushes the bubble cavity away from aluminum surface forming a mushroom shaped cavity $R_{max} = 430\,\mu m$, $\gamma = 1.1$, frame size$= 1.2 \times 1.4\,mm^2$.

Two shock waves are expected based on literature, as in Blake 1998, Tong 1999- one jet-induced shock by the impact of liquid jet into bubble lower surface and one bubble-collapse-induced shock wave. The proximity of the wall to the liquid jet produces a radial flow outwards from the jet axis. The bubble rebounds after the first collapse and is carried along the wall by the radially outward moving flow. This outward flowing liquid jet meets the inward flowing inertial flow induced by the collapsing bubble. The collapse between the inward induced flow and outward liquid jet pushes the thin bubble cavity in a direction opposite to that of the liquid jet. In the final stages a splash is projected with the bubble cavity repelled from the wall in a mushroom shaped cloud and disintegrating into tiny micro-bubbles away from the wall, as seen from $t = 162.513\ \mu s$ in fig. 2.10. This effect is most commonly known as the *splash* effect, representing the migration of the bubble torus into water in a direction perpendicular to the wall. Similar dynamical behaviour has been observed for a bubble having $R_{max} = 430\,\mu m$, $\gamma = 1.1$, as in fig. 2.11 with bubble growth near

the wall and less flattening of bubble lower surface due to the increased distance from the wall. The mushroom shaped cavity can be seen at $t = 175\ \mu s$ onward and the collapse sequence observed is similar to what was described previously in fig. 2.10 for bubble at $\gamma = 0.87$.

2.3.2.3 Stand-off $1.2 \leq \gamma \leq 2.1$

The bubble for $1.2 \leq \gamma \leq 2.1$ undergoes the first collapse away from the wall as the collapse takes place farther away from the solid wall. The first collapse of the bubble proceeds almost spherically except for the last stages where the bubble attains an oval shape seen in fig. 2.12 for a bubble with $R_{max} = 730\ \mu m$, $\gamma = 1.4$ and in fig. 2.13 for a bubble with $R_{max} = 535\ \mu m$, $\gamma = 1.7$.

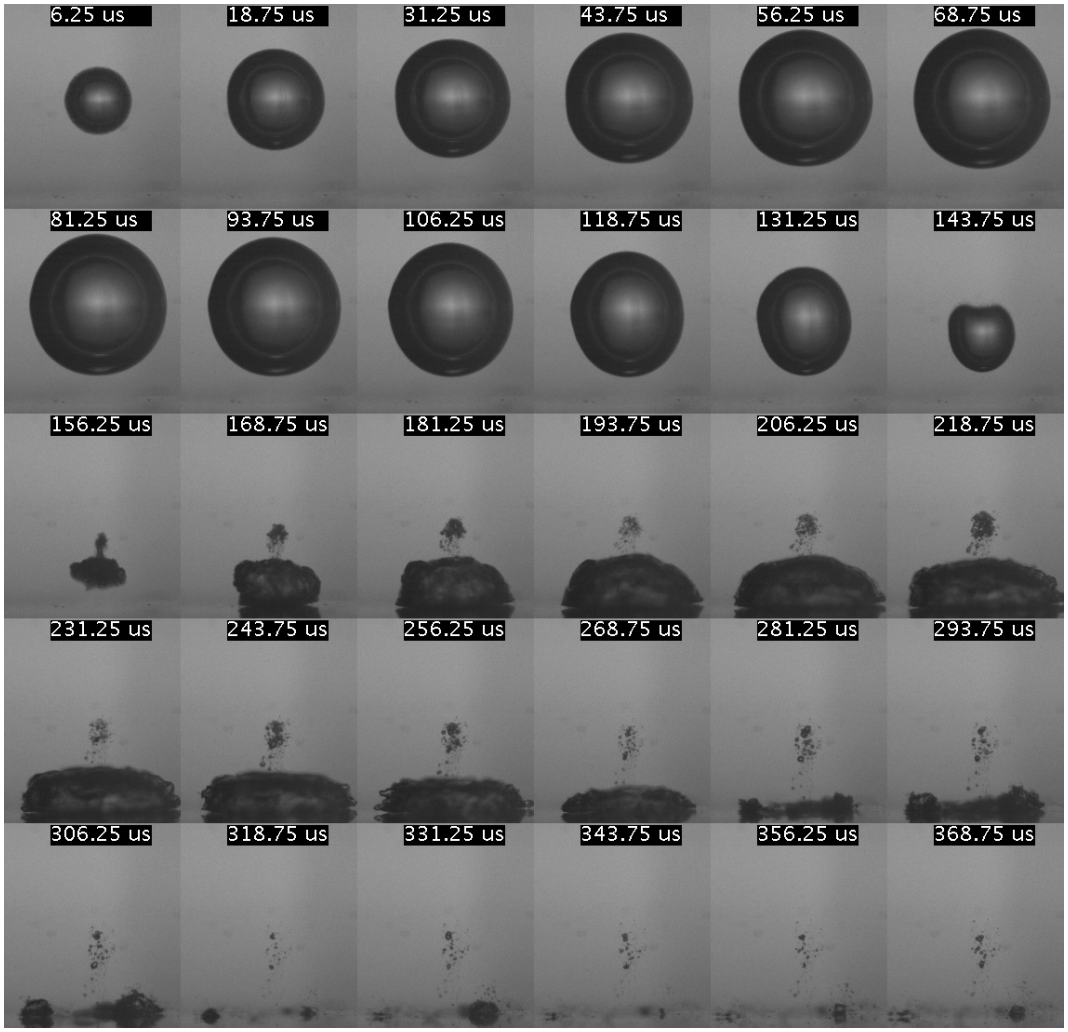

Figure 2.12 – *Left to right, top to bottom* : Collapse of bubble torus and formation of tiny micro-bubbles on aluminum surface $R_{max} = 730\ \mu m$, $\gamma = 1.4$, frame size= $1.9 \times 2.2\ mm^2$.

The liquid micro-jet pierces the bubble from the upper surface and the bubble rebounds after the first collapse seen in fig. 2.12 at $t = 143.75\ \mu s$ and $t = 168.75\ \mu s$ respectively. The liquid micro-jet passing through the bubble center gives rise to an

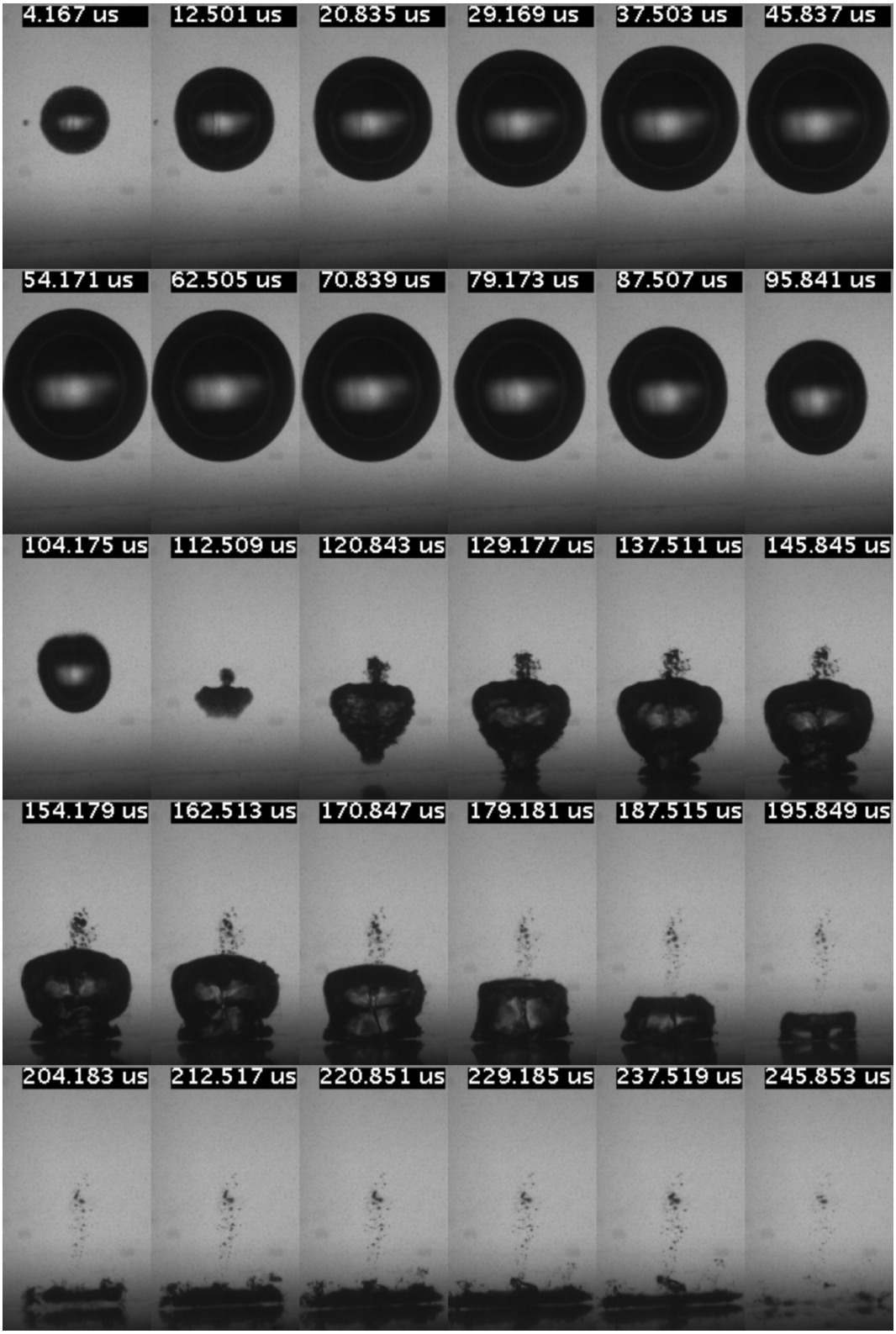

Figure 2.13 – *Left to right, top to bottom* : Elongated bubble torus and liquid micro-jet dissipating into surface micro-bubbles $R_{max} = 535\,\mu m$, $\gamma = 1.7$, frame size$= 1.1 \times 2\,mm^2$.

enlarged bubble torus which grows to its maximum size due to the rebound energy from the first collapse. The liquid micro-jet is retarded by the water layer between the bubble and the wall, more so in the case of $\gamma = 1.7$ than $\gamma = 1.4$. The liquid micro-jet has to travel a longer distance to the solid wall due to increased distance in the case of $\gamma = 1.7$ giving rise to a funnel-shaped bubble after rebound seen at $t = 120.843\,\mu s$ & $t = 129.177\,\mu s$ in fig. 2.13. This horizontally moving bubble torus impacts on the radially outward flowing liquid jet along the wall from the bubble center and disintegrates into tiny micro-bubbles. Such a disintegration of bubble torus into tiny micro-bubbles leads to simultaneous violent collapse of many tiny bubbles along the ring, each possibly emitting smaller jets and/or shock waves.

Another interesting feature of such collapses is the "counter-jet", also reported by Vogel 1989, seen from $t = 156.25\,\mu s$ in fig. 2.12 and from $t = 112.509\,\mu s$ in fig. 2.13 at the bubble upper surface. A protrusion can be observed over the flat bubble upper surface, produced by emitted shock waves during bubble rebound around the axis of symmetry. This bubble fragment for most part stays stationary around its origin of generation and disintegrates locally indicating the absence of any vortex flow in the wall perpendicular direction.

2.3.2.4 Stand-off $\gamma > 2.1$

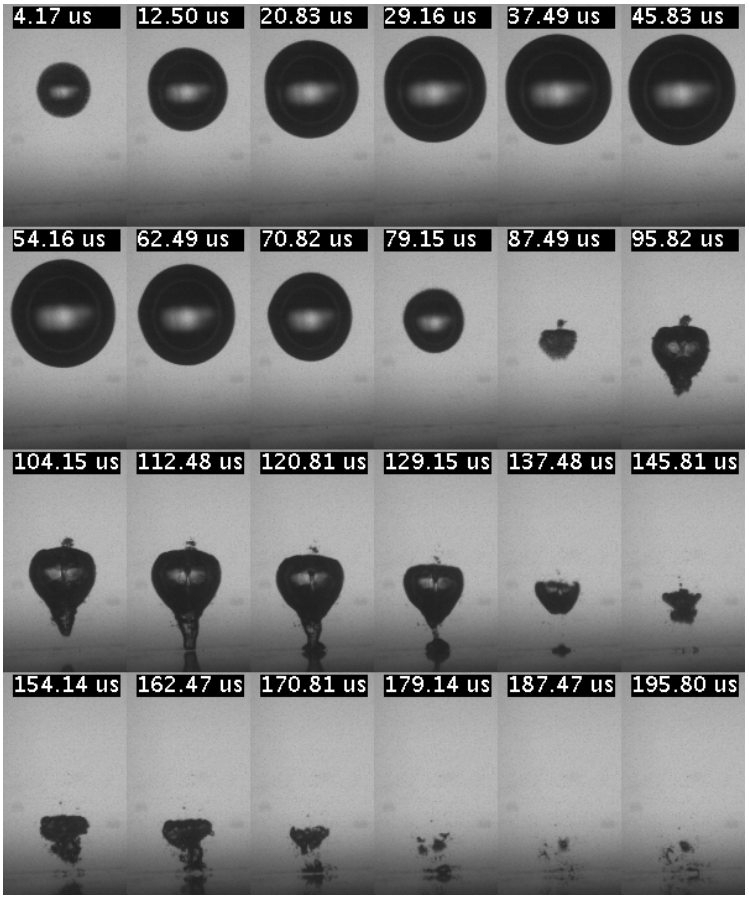

Figure 2.14 – *Left to right, top to bottom* : Bubble torus and liquid micro-jet retarded by liquid layer between the surface and collapsing bubble $R_{max} = 430\,\mu m$, $\gamma = 2.14$, frame size$= 1.0 \times 1.8\,mm^2$.

For $\gamma > 2.1$ in fig. 2.14, a thin liquid micro-jet is formed from the bubble upper surface after the first collapse as the asymmetric effect of the solid wall on the bubble is small. The elongated liquid jet is retarded by the thick water layer between the bubble and the wall. The jet detaches seen at $t = 129.15\,\mu s$ from the funnel shaped main bubble torus as the bubble proceeds for the second collapse and rebound at $t = 154.14\,\mu s$ before it reaches the wall. By the time the bubble cavity reaches the wall, it has lost most of its energy during collapse and rebound cycle. Only a small fragment of the bubble attaches itself to the wall and collapses.

2.4 Surface Deformation

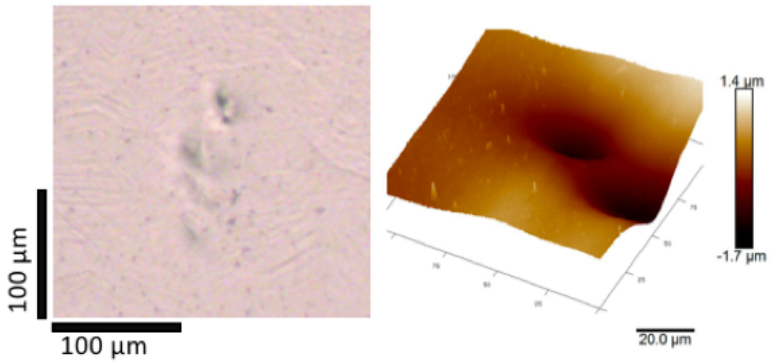

Figure 2.15 – Surface deformation on recovered aluminum sample, distinct surface pits due to liquid micro-jet impact $R_{max} = 400\,\mu m$, $\gamma = 0.55$, $(left)$ surface under a high resolution optical microscope after 10 bubble collapses, frame size $= 250 \times 250\,\mu m^2$, $(right)$ AFM scan of pits, scan size $= 110 \times 110\,\mu m^2$.

Distinct surface deformation patterns are observed in the recovered aluminum sample from the laser generated bubble collapse experiment. For collapsing bubbles at $\gamma = 0.55$, indentation pits are observed under an optical microscope on the recovered aluminum surface after 10 bubble collapses, as shown in fig. 2.15*(left)*. Since the bubbles grow and collapse attached to the solid surface, the pits are associated to the liquid-jet impact on the solid surface. The surface deformations are characterized with an AFM and the maximum pit depth is found to be $1.7\,\mu m$ shown in fig. 2.15*(right)*. The darker shades in the AFM scans represent the surface deformations and dotted-white line, if present, shows the probe used to characterize the pit dimensions. In fact, there are two kinds of surface pits observed-first are the shallow pits and second are the deeper pits, which can be seen as the two top-most pits on fig. 2.15*(left)* and also in fig. 2.15*(right)*. The shallow pit depth is of about $600\,nm$ and pit radius of about $20\,\mu m$ shown in fig. 2.16.

The deeper pits are of depth more than $1\,\mu m$ usually, with maximum pit depth of $1.7\,\mu m$ and pit radius of about $20\,\mu m$ shown in fig. 2.17. The two pits seen in fig. 2.17 that are close to each other and partially overlapping with each other are most likely produced by individual single bubble collapse. The bubble position relative to the wall moved slightly due to interaction with the induced flow from the passing laser beam and therefore, the spreading occurred in the surface deformation.

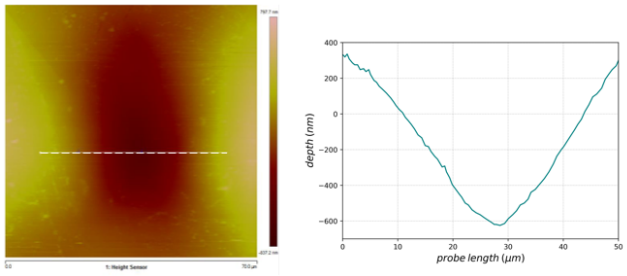

Figure 2.16 – Indentation pit of depth 600 nm and pit radius of about 20 μm, scan size $= 70 \times 70\ \mu m^2$

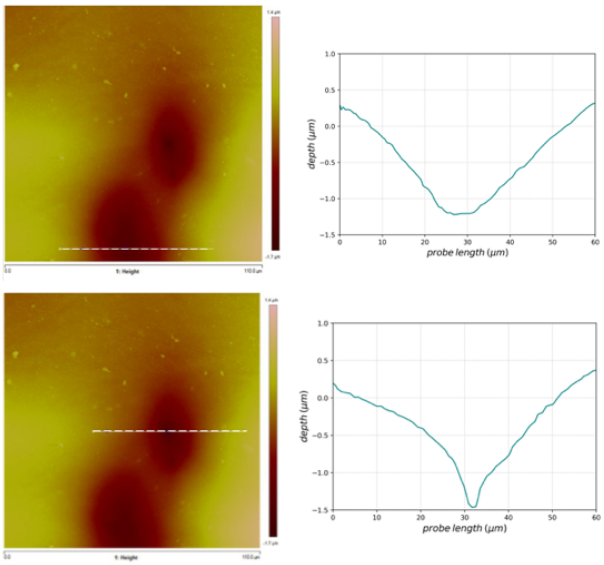

Figure 2.17 – Indentation pit of depth more than 1 μm and pit radius of about 20 μm, scan size $= 110 \times 110\ \mu m^2$.

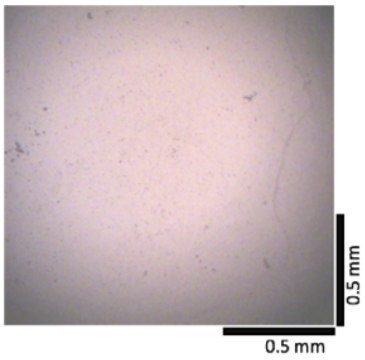

Figure 2.18 – Recovered aluminum surface after 10 bubble collapses, no visible surface deformation due to rebounding bubble cavity from "splash" effect $R_{max} = 430\ \mu m$, $\gamma = 1.1$ frame size $= 1.5 \times 1.5\ mm^2$.

No corrective measures could be taken due to the lack of experience in using such experimental setup and relatively short duration of the experimental campaign.

The "splash" effect and disintegration of the bubble torus into tiny micro-bubbles away from the sample surface produced no visible surface deformation seen in fig. 2.18 for the recovered aluminum sample after 10 bubble collapse of maximum bubble radius $R_{max} = 430\,\mu m$, $\gamma = 1.1$. The spreading of the bubble cavity on the sample surface before the "splash" has no resulting effect on it indicating the absence of any jet or shock wave on the solid surface.

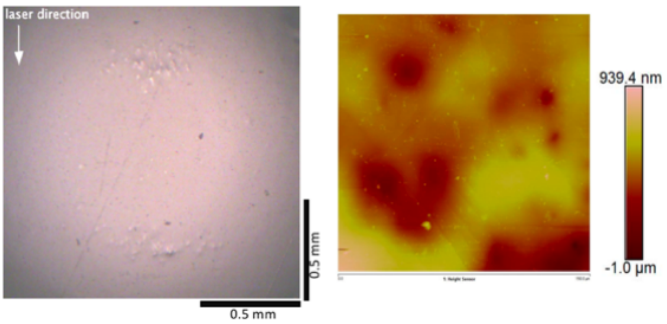

Figure 2.19 – Circular damage pattern after 100 repetitive bubble collapses due to collapsing bubble torus and micro-bubbles $R_{max} = 730\,\mu m$, $\gamma = 1.4$, $(right)$ recovered aluminum sample under optical microscope, frame size $= 1.5 \times 1.5\,mm^2$, $(right)$ AFM scan of top surface pits, scan size$= 150 \times 150\,\mu m^2$.

In the case of $\gamma = 1.4$, a circular damage pattern is observed on the recovered aluminum surface with multiple tiny pits along the periphery of the bubble torus ring for 100 repeated bubble collapses of maximum radius $R_{max} = 730\,\mu m$ seen in fig. 2.19*(left)*. The collapse of tiny micro-bubbles from the disintegrated bubble torus at $\gamma = 1.4$ is responsible for the pits along the periphery of the bubble torus ring. Maximum surface pits are aligned along the laser direction indicating the interaction of the induced flow from the passing laser beam on the tiny micro-bubble collapse. A surface scan of dimension $150 \times 150\,\mu m^2$ of the pits on the top of fig. 2.19*(left)* are shown in fig. 2.19*(right)*. The pit dimensions from micro-bubbles are shown in fig. 2.20. Most of the pit depths are about $600\,\mu m$ with maximum pit depth of $1\,\mu m$ and in general, smaller pit radius in comparison to the attached bubble case. The collapsing tiny micro-bubbles along the bubble torus ring on the solid surface possibly generates strong shock waves. It is still not clear if the liquid-jet velocity from such tiny micro-bubble collapse might be high enough for pit formation.

Very insignificant surface deformation is observed on the much harder pure aluminum sample seen in fig. 2.21 whereas no visible deformation could be seen in the aluminum Alloy Al-7075 in fig. 2.22 from the bubbles generated in the present investigation. The experiment on pure aluminum with 5 bubble collapse in fig. 2.21 did produce surface deformation on the sample surface. The deformation is spread out in a much larger surface area in comparison to bubble radius and therefore, difficult to evaluate.

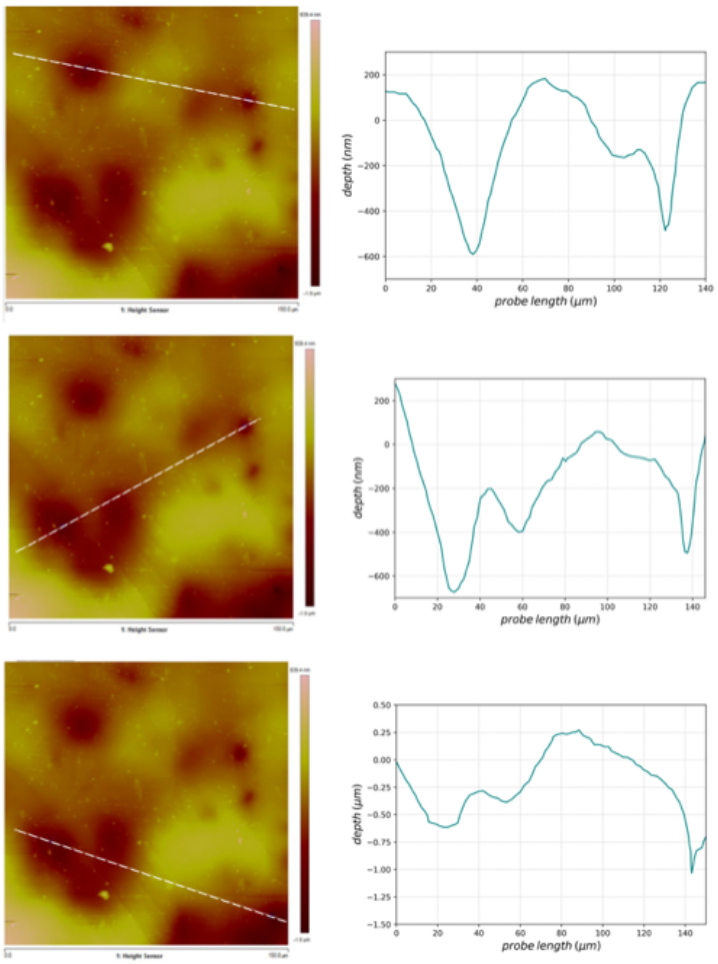

Figure 2.20 – AFM scan and pit shapes from tiny micro-bubble collapse, scan size= $150 \times 150\,\mu m^2$.

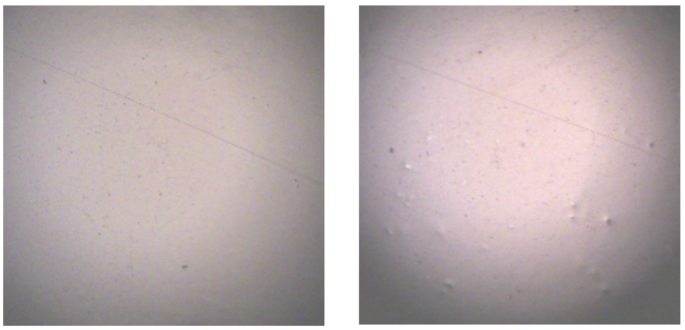

Figure 2.21 – Surface deformation on pure aluminum sample after 5 bubble collapse $R_{max} = 600\,\mu m$, $\gamma = 1.4$, $(left)$ before, $(right)$ after, frame size $= 1.5 \times 1.5\,mm^2$.

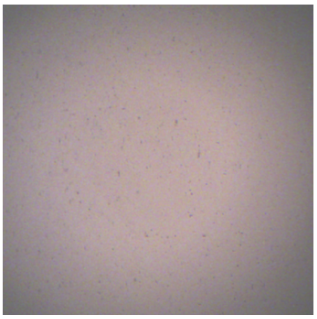

Figure 2.22 – No surface deformation on Al-7075 from detached bubble collapse, frame size $= 1.5 \times 1.5\, mm^2$.

2.5 Summary & Discussion

Surface pits and a circular damage pattern for collapsing bubble at $\gamma = 0.55$ and $\gamma = 1.4$ respectively is identified from the experiments. Surface deformation is dominated by the impacting liquid jet for attached bubbles on the solid wall, whereas tiny surface micro-bubbles from detached bubbles are found to cause significant surface deformation as well. The important observation is that the bubble cavities produce surface damage when they are attached to the solid wall although the mechanism and type of damage may vary. The work done by Philipp 1998 with bubbles of $R_{max} = 1.45\, mm$ is quite extensive and thorough and the present results qualitatively agree with their observations depicted in fig. 2.23 reporting damage for $\gamma \leq 0.6$ and $\gamma = 1.2$ to 1.4. The difference in the pit depth are due to smaller bubble size produced in our experiment. The absence of considerable surface damage on

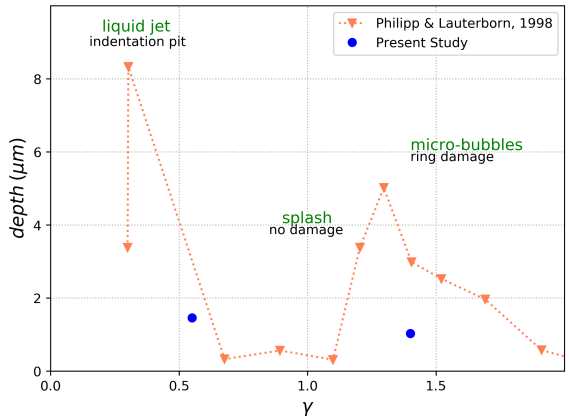

Figure 2.23 – Comparison of γ range for observed surface damage in the present experiments and Philipp 1998.

the pure aluminum and Alloy Al-7075 can be attributed to small size of the bubbles generated in our experiment. Comparatively, much larger bubbles would have to be generated with much more local energy deposition on the solid wall. It was attempted although the experimental setup used produces deviations in bubble shape and size, and often creates multiple bubbles when the deposited energy is increased. An improvement in the optics was required and not pursued due to limitation in time.

Part II

Numerical Approach

Chapter 3

Computational Fluid Dynamics

3.1 Introduction

In this chapter, a broad introduction to the physical modelling of fluid flow is presented. As a starting point, the governing equations for a fully compressible flow is introduced, followed by a presentation of the unique algorithm for compressible flows implemented in the CFD solver YALES2. It will be followed by the introduction of the solver developed for cavitation and FSI in this thesis.

3.2 Basic equations of fluid mechanics

Considering the flow of a fluid, the equations describing its motion are the conservation laws for mass, momentum and energy. These equations are derived based on the continuum hypothesis which states that a flow can be characterized by means of continuous functions of the spatial coordinate vector $\bar{x}$ and of time t, like the velocity $\bar{\mathbf{u}}(\bar{x}, t)$ and the mass density $\rho(\bar{x}, t)$. This idealization accurately describes the macroscopic behaviour of a flow. The continuous functions represent the average over a volume which is small with respect to the spatial variation of the flow but large compared to the distance between molecules.

3.2.1 Conservation of mass

The mass conservation equation in its integral form can be expressed as

$$\frac{\partial}{\partial t}\int_{\Omega} \rho \, dV = -\int_{\partial\Omega} (\rho\bar{\mathbf{u}}) \cdot \bar{\mathbf{n}} \, dS \tag{3.1}$$

In eq. (3.1), Ω represents a fixed control volume in an Eulerian framework and $\partial\Omega$ denotes its boundaries, ρ is the density, $\bar{\mathbf{u}}$ is the velocity vector and $\bar{\mathbf{n}}$ is the outward normal vector. This can be interpreted as the change of mass with time for any sub-domain Ω of a fluid flow is due to mass flux across its boundaries $\partial\Omega$. Applying the Gauss' divergence theorem to RHS leads to the following formulation

$$\int_{\Omega} \left(\frac{\partial \rho}{\partial t} + \nabla \cdot (\rho\bar{\mathbf{u}}) \right) dV = 0 \tag{3.2}$$

Since eq. (3.2) is valid for any volume Ω, the volume integration can be set aside and a local relationship is obtained called the continuity equation in eq. (3.3).

$$\frac{\partial \rho}{\partial t} + \nabla \cdot (\rho \bar{\mathbf{u}}) = 0 \tag{3.3}$$

3.2.2 Conservation of momentum

The integral form of momentum conservation equation is represented in eq. (3.4) derived from Newton's second law which states that the rate of change of momentum of a body equals the net force exerted on that body. The second term in RHS of eq. (3.4) is the stress tensor representing the contribution of surface forces whereas the last term represents the volumetric forces. The stress tensor is comprised of two components, $p\bar{\bar{\mathcal{I}}}$ representing the normal stresses due to the pressure p, where $\bar{\bar{\mathcal{I}}}$ is the identity matrix and $\bar{\bar{\tau}}$, that is the deviatoric stress tensor.

$$\int_\Omega \frac{\partial \rho \bar{\mathbf{u}}}{\partial t}\, dV = -\int_{\partial\Omega} ((\rho \bar{\mathbf{u}}) \otimes \bar{\mathbf{u}}) \cdot \bar{\mathbf{n}}\, dS + \int_{\partial\Omega} (-p\bar{\bar{\mathcal{I}}} + \bar{\bar{\tau}}) \cdot \bar{\mathbf{n}}\, dS + \int_\Omega \rho \bar{\mathbf{g}}\, dV \tag{3.4}$$

For a *Newtonian* fluid where there is a linear relationship between stress and strain-rate, $\bar{\bar{\tau}}$ can be written as:

$$\bar{\bar{\tau}} = \mu \left(\nabla \bar{\mathbf{u}} + (\nabla \bar{\mathbf{u}})^T - \frac{2}{3} (\nabla \cdot \bar{\mathbf{u}}) \bar{\bar{\mathcal{I}}} \right) \tag{3.5}$$

Applying on eq. (3.4) the Gauss' divergence theorem, we obtain eq. (3.6)

$$\int_\Omega \left(\frac{\partial \rho \bar{\mathbf{u}}}{\partial t} + \nabla \cdot (\rho \bar{\mathbf{u}} \otimes \bar{\mathbf{u}}) \right) dV = \int_\Omega \left(-\nabla p + \nabla \cdot \bar{\bar{\tau}} + \rho \bar{\mathbf{g}} \right) dV \tag{3.6}$$

whose validity for any control volume Ω allows us to write its local form

$$\frac{\partial \rho \bar{\mathbf{u}}}{\partial t} + \nabla \cdot (\rho \bar{\mathbf{u}} \otimes \bar{\mathbf{u}}) = -\nabla p + \nabla \cdot \bar{\bar{\tau}} + \rho \bar{\mathbf{g}} \tag{3.7}$$

This eq. (3.7) is called the momentum equation, historically also referred as the *Navier-Stokes* equation. In recent practice and in this thesis, the *Navier-Stokes* equations refer to the entire set of conservation equations for mass, momentum and energy.

3.2.3 Conservation of energy

The total energy E of the fluid is defined as the sum of internal (thermal) energy (e_s) and kinetic energy ($\frac{1}{2}\bar{\mathbf{u}}^2$), for which the following integral formulation holds

$$\begin{aligned} \int_\Omega \frac{\partial \rho E}{\partial t}\, dV = -\int_{\partial\Omega} (\rho E \bar{\mathbf{u}}) \cdot \bar{\mathbf{n}}\, dS + \int_{\partial\Omega} ((-p\bar{\bar{\mathcal{I}}} + \bar{\bar{\tau}}) \cdot \bar{\mathbf{u}} - \bar{Q}) \cdot \bar{\mathbf{n}}\, dS \\ + \int_\Omega \rho \bar{\mathbf{g}} \cdot \bar{\mathbf{u}}\, dV \end{aligned} \tag{3.8}$$

Equation (3.8) relates the energy transported by the flow to the work done on the fluid by the environment. Q is the heat flux defined by the Fourier law as $Q = -\lambda \nabla T$, where λ is the thermal conductivity and T is the temperature. In a similar way as continuity and momentum equations, the energy equation can be represented for

any control volume Ω and into a partial differential equation (PDE) as eq. (3.9) & (3.10) respectively.

$$\int_\Omega \left(\frac{\partial \rho E}{\partial t} + \nabla \cdot (\rho E \bar{\mathbf{u}}) \right) dV = \int_\Omega \left(-\nabla \cdot (p\bar{\mathbf{u}}) + \nabla \cdot (\bar{\bar{\tau}}\bar{\mathbf{u}}) + \nabla \cdot (\lambda \nabla T) + \rho \bar{\mathbf{g}} \cdot \bar{\mathbf{u}} \right) dV \quad (3.9)$$

$$\frac{\partial \rho E}{\partial t} + \nabla \cdot (\rho E \bar{\mathbf{u}}) = -\nabla \cdot (p\bar{\mathbf{u}}) + \nabla \cdot (\bar{\bar{\tau}}\bar{\mathbf{u}}) + \nabla \cdot (\lambda \nabla T) + \rho \bar{\mathbf{g}} \cdot \bar{\mathbf{u}} \quad (3.10)$$

3.2.4 Navier-Stokes Equations

The second order PDE's derived from eqs. (3.1), (3.4) and (3.8) forms the system of conservation equations also known as the *Navier-Stokes* equations. The gravitational forces are neglected in the purview of this thesis.

$$\frac{\partial \rho}{\partial t} + \nabla \cdot (\rho \bar{\mathbf{u}}) = 0 \quad (3.11)$$

$$\frac{\partial \rho \bar{\mathbf{u}}}{\partial t} + \nabla \cdot (\rho \bar{\mathbf{u}} \otimes \bar{\mathbf{u}}) = -\nabla p + \nabla \cdot \bar{\bar{\tau}} \quad (3.12)$$

$$\frac{\partial \rho E}{\partial t} + \nabla \cdot (\rho E \bar{\mathbf{u}}) = -\nabla \cdot (p\bar{\mathbf{u}}) + \nabla \cdot (\bar{\bar{\tau}}\bar{\mathbf{u}}) + \nabla \cdot (\lambda \nabla T) \quad (3.13)$$

3.2.5 Fluid compressibility and Mach number

Before moving further, an important aspect about fluid compressibility and its effect on the numerical modelling of fluid flows is discussed. The dimensionless quantity describing the ratio of convective velocity u to the speed of sound c, is the Mach number:

$$Ma = \frac{u}{c} \quad (3.14)$$

Often the convective velocities occurring in flows are rather small compared to the speed of sound, which can be expressed as Mach number tending towards zero. This does not mean that the convective velocity $u = 0$ but that $u << c$ or $c \to \infty$. In terms of physics, it represents the propagation of small, isentropic disturbances like pressure waves at the speed of sound which is much faster than the advection of the flow. In such a scenario, no pressure and density fluctuations are created due to differences in velocity field and the flow is assumed incompressible. The mathematical nature of the governing equations is elliptical where the pressure waves propagate at an infinite speed and prohibits the occurrence of acoustics in the flow field. Consequently, the time step size of a numerical simulation is limited by the Courant-Friedrichs-Lewy (CFL) condition in eq. (3.15) which determines the distance travelled by information during one time step.

$$CFL = v \frac{\Delta t}{\Delta x} = |u| \frac{\Delta t}{\Delta x} \quad (3.15)$$

v is the highest velocity at which information is transported within the simulation i.e. $v = |u|$ since no acoustic occurs, Δt is the given time step and Δx is the mesh size. For an adiabatic and reversible process, isentropic compressibility of a fluid element of volume V can be defined as

$$\beta_s = -\frac{1}{V} \left(\frac{\partial V}{\partial p} \right)_s \quad (3.16)$$

where p is the pressure acting on the surface of the fluid element. Considering V as the specific volume of the fluid element and rewriting eq. (3.16) using the density ρ of the fluid gives

$$\beta_s = \frac{1}{\rho}\left(\frac{\partial \rho}{\partial p}\right)_s \tag{3.17}$$

Fluids undergoing density variations due to an imposed pressure field are characterized as compressible. Compared to gases, liquids have very low compressibility and it is reasonable to treat liquids as incompressible for certain applications. Nevertheless, for resolving acoustic wave propagation, it is required to treat all fluid components as compressible, where the finite propagation speed of the waves is defined by the speed of sound c. This isentropic speed of sound relationship is therefore

$$c_s = \sqrt{\frac{1}{\rho\beta_s}} = \sqrt{\left.\frac{\partial p}{\partial \rho}\right|_s} \tag{3.18}$$

The compressible set of governing equations are hyperbolic in nature and any fluctuation is transported at the speed of sound, so $v = |u + c|$. The relationship between Courant-Friedrichs-Lewy condition with acoustic propagation CFL_{acou} for compressible flow and convective CFL for incompressible flow is expressed as:

$$\begin{aligned} CFL_{acou} =& v\frac{\Delta t}{\Delta x} = |u + c|\,\frac{\Delta t}{\Delta x} = \frac{u\Delta t}{\Delta x}\,\left(1 + \frac{1}{Ma}\right) \\ &\Rightarrow CFL_{acou} = CFL\,\left(1 + \frac{1}{Ma}\right) \\ &\Rightarrow CFL_{acou}\,\left(\frac{Ma}{Ma+1}\right) = CFL \end{aligned} \tag{3.19}$$

Considering for example a flow simulation at $Ma = 0.5$ gives a CFL_{acou} which is 33% of the convective CFL. Thus the time step of a simulation derived from the $min(CFL, CFL_{acou})$ will be limited by the CFL_{acou} condition. For a cavitation bubble collapse in liquid water with $c = 1483\, m/s$, the Mach number stays small for major part of the simulation and approaches 1 only during the final stages of bubble collapse. An explicit treatment of the time step will lead to very small time steps and larger computation time for such simulations. Thus, the solver's design down to the algorithmic level has an effect on the capability to resolve such problems efficiently.

3.3 YALES2 code

YALES2 is a versatile numerical code based on *finite volume method* (FVM). The code consists of many different solvers for varied multi-physics fluid dynamical problems. A review of the existing Implicit Compressible Solver algorithm is provided next before describing the two new solvers developed in this thesis.

3.3.1 Implicit Compressible Solver (CPS)

Implicit Compressible Solver (CPS) has been developed by Moureau 2007 for ideal gas flows employing a pressure based semi-implicit algorithm to remove CFL_{acou}

constraints for all Mach numbers. In this *prediction-correction* algorithm, flow convection and acoustics are separated based on the characteristic splitting of the compressible *Navier-Stokes* equations. The eigenvalues of the 1D compressible *Navier-Stokes* equations corresponding to two acoustic waves i.e $(u+c)$,$(u-c)$ and pure advection (u) are split into two steps

$$\begin{pmatrix} u+c \\ u-c \\ u \end{pmatrix} = \begin{pmatrix} u \\ u \\ u \end{pmatrix} + \begin{pmatrix} c \\ -c \\ 0 \end{pmatrix} \tag{3.20}$$

The first part of the RHS corresponds to the pure advection of the flow whereas the second part is the isentropic propagation of acoustic waves. The solver algorithm extends this decomposition to the 3D *Navier-Stokes* equations, ensuring that the algorithm extends towards a density-based compressible solver when the CFL_{acou} tends towards zero. A density based solver methodology refers to the solution of the coupled system of governing equations where fluid velocity is obtained from the momentum conservation equations, density from the mass conservation equation and pressure is determined from the equation of state. The algorithm developed on the idea of fractional-step method of Kim 1985 for incompressible flows tends towards a classical low-Mach number projection scheme of Chorin 1968 when the Mach number tends to zero. This removes the need for numerical preconditioning like approach typical for density based solvers at very low Mach numbers.

3.3.2 Time advancement - characteristics based fractional step method

The main idea of the time advancement method of CPS is to perform an operator splitting on the governing eq. (3.11), (3.12) and (3.13). For a vector of conservative variables $\phi = (\rho, \mathbf{m}, \mathcal{E})^T$, where ρ is the density, $\mathbf{m} = \rho\mathbf{u}$ is the momentum, $\mathcal{E} = \rho E$ is the total energy, the splitting can be expressed as:

$$\frac{\partial \phi}{\partial t} = \mathcal{F}_c(\phi) + \mathcal{F}_v(\phi) + \mathcal{F}_a(\phi) \tag{3.21}$$

where $\mathcal{F}_c, \mathcal{F}_v$ and $\mathcal{F}_a$ represents the convective,viscous and acoustic parts:

$$\mathcal{F}_c(\phi) = \begin{pmatrix} -\mathbf{u}\cdot\nabla\rho \\ -\mathbf{u}\cdot\nabla\mathbf{m} \\ -\mathbf{u}\cdot\nabla\mathcal{E} \end{pmatrix} \tag{3.22}$$

$$\mathcal{F}_v(\phi) = \begin{pmatrix} 0 \\ \nabla\cdot\tau \\ \nabla\cdot(\lambda\nabla T) + \nabla\cdot(\tau\mathbf{u}) \end{pmatrix} \tag{3.23}$$

$$\mathcal{F}_a(\phi) = \begin{pmatrix} -\rho(\nabla\cdot\mathbf{u}) \\ -\mathbf{m}(\nabla\cdot\mathbf{u}) - \nabla p \\ -\mathcal{E}(\nabla\cdot\mathbf{u}) - \nabla\cdot(p\mathbf{u}) \end{pmatrix} \tag{3.24}$$

The algorithm is split into a prediction step followed by a correction step for the conservative variables, as detailed in the next sections.

3.3.2.1 Prediction

The prediction step solves for the convective and viscous part of eq. (3.21). However setting the acoustic part contribution to zero introduces large splitting errors and hence a constant acoustic part is added as a source term proposed by Roger 2016 as in eq. (3.25).

$$\phi^{\star} = \phi(t) + \int_{t}^{t+\Delta t} (\mathcal{F}_c(\phi(\tau)) + \mathcal{F}_v(\phi(\tau)) + \mathcal{F}_a(\phi(t))) \, d\tau \tag{3.25}$$

A characteristic analysis of the system of equations of this step shows that the eigenvalues are equal to the convective propagation speed $\mathbf{u}$ and the step is only limited by the convective CFL stability condition, independently of Mach number. Equations (3.26) & (3.27) show the generic form of *Navier-Stokes* equations for the prediction step for $\phi \in (\rho, \mathbf{m}, \mathcal{E})$.

$$\frac{\phi^{\star} - \phi^{n}}{\Delta t} + \nabla \cdot \left(\tilde{\phi} \mathbf{u}^{n} \right) - D_{\phi} = \left(\tilde{\phi} - \phi^{n} \right) \nabla \cdot \mathbf{u}^{n} \tag{3.26}$$

$$\begin{pmatrix} D_{\rho} \\ D_{\mathbf{m}} \\ D_{\mathcal{E}} \end{pmatrix} = \begin{pmatrix} 0 \\ -\nabla p^{n} + \nabla \cdot \tau^{n} \\ -\nabla \cdot (p^{n} \mathbf{u}^{n} + \tau^{n} \mathbf{u}^{n} + \lambda \nabla T^{n}) \end{pmatrix} \tag{3.27}$$

ϕ^{n} is the value of ϕ before time advancement i.e. from the previous time step, $\phi^{\star}$ is the value computed at the end of the prediction step and $\tilde{\phi}$ is the value computed at different steps of the time integration scheme. The terms D_{ρ}, $D_{\mathbf{m}}$ & $D_{\mathcal{E}}$ are the explicit pressure and diffusion contributions, evaluated only at the beginning of the time step. The LHS of (3.26) represents a classical explicit discretization of the compressible *Navier-Stokes* equations which is solved with TFV4A temporal scheme described in section 3.4.2. The RHS on the other hand is proportional to the local dilatation (divergence of velocity) and is intended to remove the acoustics from the prediction step. For a low Mach number flow, this term tends towards zero and is only present for highly compressible flows.

The equation of state is solved next to estimate the pressure $p^{\star}$ and $T^{\star}$ from $\phi^{\star}$ to close the system of equation at the end of prediction step.

3.3.2.2 Helmholtz Equation

Before correcting the conservative variable $\phi \in (\rho, \mathbf{m}, \mathcal{E})$ in the second step, a Helmholtz equation is solved to obtain the pressure variation $\delta p = p^{n+1} - p^{\star}$ in eq. (3.28). The equation is derived by taking the divergence of momentum equation during the correction step in eq. (3.34) and using the continuity equation from the prediction step in eq. (3.26) to remove the unknown momentum $\mathbf{m}^{n+1}$. Thus, a discrete mass conserving equation for the corrected pressure p^{n+1} and pressure variation δp is obtained.

$$\nabla \cdot \nabla \delta p - \nabla \cdot \left(\frac{\delta p \, \mathbf{u}^{\mathrm{n}}}{c^2 \Delta t} \right) - \frac{\delta p}{c^2 \Delta t^2} = \nabla \cdot \nabla \left(p^{n} - p^{\star} \right) + \frac{\rho^{\star} - \rho^{n}}{\Delta t^2} + \frac{1}{\Delta t} \nabla \cdot (\mathbf{m}^{\star}) \tag{3.28}$$

The Helmholtz equation can be transformed into a linear system, the matrix being solved implicitly with Stabilized Bi-Conjugate Gradient (BiCGSTAB2) linear solver (Vantieghem 2011). The second term on the LHS represents the influence of local

flow on the acoustics. The second and third term in LHS are negligible for low Mach number flows and the Helmholtz equation with negligible acoustic presence tends towards a variable density Poisson equation. It can then be resolved with a dedicated efficient linear solvers like Deflated Preconditioned Conjugate Gradient (DPCG), as discussed in Roger 2016.

3.3.2.3 Correction

The governing equations for the correction step are obtained after removing eq. (3.26) from the full set of *Navier-Stokes* equations in eq. (3.11),(3.12) and (3.13). The splitting between the prediction-correction step can be derived for any conservative variable ϕ as:

$$\begin{aligned} \phi^{n+1} =& \phi^n + (\phi^\star - \phi^n) + \left(\phi^{n+1} - \phi^\star\right) \\ \Rightarrow \phi^{n+1} =& \phi^n + \delta\phi^{conv} + \delta\phi^{acous} \\ \Rightarrow \phi^{n+1} =& \phi^\star + \delta\phi^{acous} \end{aligned} \tag{3.29}$$

A temporal integration on the resulting equation after splitting resolves the acoustic influence on the set of conservative variable $\phi \in (\rho, \mathbf{m}, \mathcal{E})$, taking into account the presence of acoustic source term in the prediction step.

$$\phi^{n+1} = \phi^\star + \int_t^{t+\Delta t} \mathcal{F}_a(\phi^*(\tau)) - \mathcal{F}_a(\phi(t))d\tau \tag{3.30}$$

The speed of sound expression at constant entropy can be written as:

$$c^2 = \left.\frac{\partial p}{\partial \rho}\right|_s \tag{3.31}$$

which can link the temporal variations of pressure and density in the purely isentropic correction step as:

$$\frac{\partial \rho}{\partial t} = \frac{1}{c^2}\frac{\partial p}{\partial t} \tag{3.32}$$

$$\Rightarrow \frac{p^{n+1} - p^\star}{\Delta t} = c^2 \frac{\rho^{n+1} - \rho^\star}{\Delta t} \tag{3.33}$$

Thus, the variation of $\phi \in (\rho, \mathbf{m}, \mathcal{E})$ during the correction step can be expressed in terms of pressure variation in eq. (3.34) with the source term $S_\rho, S_\mathbf{m} \& S_\mathcal{E}$ defined in eq. (3.35).

$$\frac{\phi^{n+1} - \phi^\star}{\Delta t} - \frac{\phi^n}{\rho^n (c^n)^2}\frac{\delta p}{\Delta t} = S_\phi \tag{3.34}$$

$$\begin{pmatrix} S_\rho \\ S_\mathbf{m} \\ S_\mathcal{E} \end{pmatrix} = \begin{pmatrix} 0 \\ -\nabla \delta p \\ -\nabla \cdot (\delta p \mathbf{u}^n) \end{pmatrix} \tag{3.35}$$

An important point to note in eq. (3.34) is that the speed of sound denoted by c^n is computed only once at the beginning of the time-step for the entire prediction-correction algorithm. The final algorithm for time advancement can be expressed as fig. 3.1.

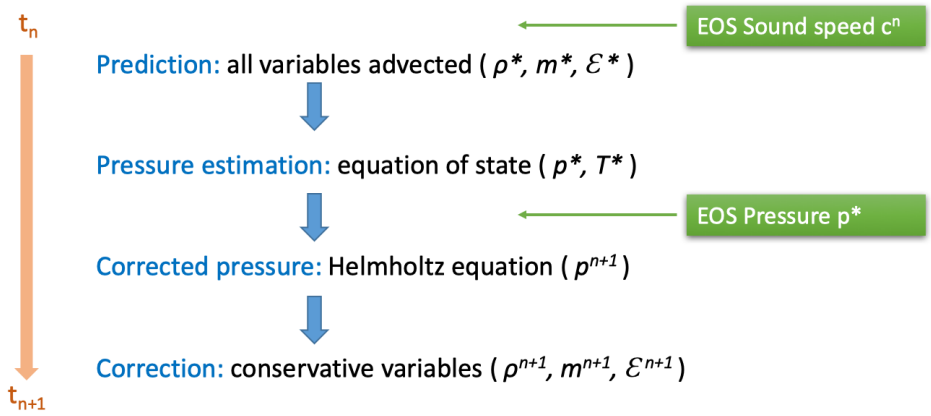

Figure 3.1 – Schematic of CPS algorithm- estimation of sound speed and pressure from equation of state (in green).

3.4 Compressible Cavitation Solver (CCS)

In this thesis, a new solver in YALES2 called Compressible Cavitation Solver (CCS) for hydrodynamics and cavitation research is developed. The new solver is developed based on the numerical algorithm of the CPS solver, thus taking advantage of the inherent numerics and efficiency due to no time step constraints from CFL_{acou} limitation. The solution domain is solved in a FVM framework by dividing the total volume into small *control volumes* (CV). Discretization in space & time is performed on the integral conservation equation over this CV. The weak form or so-called integral form of the compressible *Navier-Stokes* equations allows to model discontinuities like shock waves and phase boundaries in a cavitating flow. The numerical algorithm is shown in section 3.3.2 where the time advancement is performed based on the characteristic splitting of the compressible *Navier-Stokes* equations. The prediction-correction algorithm of CCS solves for the purely convective part of governing equations explicitly in the first step with a constant acoustic source term for $\phi \in (\rho, \mathbf{m}, \mathcal{E})$ as in eq. (3.36), (3.37) & (3.38). The speed of sound c^n is computed before starting the time advancement to obtain the time step from CFL_{acou}.

$$\frac{\rho^\star - \rho^n}{\Delta t} + \nabla \cdot (\tilde{\rho}\mathbf{u}^n) - (\tilde{\rho} - \rho^n)\nabla \cdot \mathbf{u}^n = 0 \tag{3.36}$$

$$\frac{\mathbf{m}^\star - \mathbf{m}^n}{\Delta t} + \nabla \cdot (\tilde{\mathbf{m}} \otimes \mathbf{u}^n) - (\tilde{\mathbf{m}} - \mathbf{m}^n)\nabla \cdot \mathbf{u}^n = -\nabla p^n + \nabla \cdot \tau^n \tag{3.37}$$

$$\frac{\mathcal{E}^\star - \mathcal{E}^n}{\Delta t} + \nabla \cdot \left(\tilde{\mathcal{E}}\mathbf{u}^n\right) - \left(\tilde{\mathcal{E}} - \mathcal{E}^n\right)\nabla \cdot \mathbf{u}^n = -\nabla \cdot (p^n \mathbf{u}^n) + \nabla \cdot (\tau^n \mathbf{u}^n) + \nabla \cdot (\lambda \nabla T^n) \tag{3.38}$$

At the end of the prediction step, the equation of state is used to estimate the pressure $p^\star$. It is worth noting here that the solver is specifically developed for modelling cavitating flows in liquid water, which are modeled with a barotropic equation of state described in section 3.4.5. A barotropic assumption implies that the pressure is only a function of density $p = f(\rho)$. Therefore, the evolution of energy equation and by virtue of it, the evolution of temperature is decoupled from the system of governing equations. Thus in the prediction step for liquid water,

only eq. (3.36) & (3.37) are advanced in time with TFV4A time integration scheme described in section 3.4.2. A fourth-ordered centered scheme is used for spatial discretization, as detailed in section 3.4.1. It is important to highlight here that for an ideal gas flow simulation in CCS, the energy eq. (3.38) & (3.42) are included into the system of governing equations solved.

Another modification introduced in the algorithm is to update the speed of sound c^* at the end of the prediction step based on the advected density field. This is especially important for multiphase flows where the different phases/components of the fluid can have varying orders of speed of sound. The computation of speed of sound from the advected density at each CV is important near phase boundaries i.e. interfaces. Thus in the correction step, the subsequent pressure field computation will have the correct speed of sound of the fluid phase from the temporal evolution of density, most importantly near fluid interfaces.

The Helmholtz equation is solved next implicitly with the BiCGSTAB2 (Vantieghem 2011) linear solver for the pressure variation $\delta p = p^{n+1} - p^\star$ in eq. (3.39) the properties of which at both high and low Mach flows have already been discussed with eq. (3.28).

$$\begin{aligned} \nabla \cdot \nabla \left(p^{n+1} - p^\star\right) - \nabla \cdot \frac{\mathbf{u}^n}{(c^*)^2 \Delta t} \left(p^{n+1} - p^\star\right) - \frac{p^{n+1} - p^\star}{(c^*)^2 \Delta t^2} \\ = \nabla \cdot \nabla \left(p^n - p^\star\right) + \frac{\rho^\star - \rho^n}{\Delta t^2} + \frac{1}{\Delta t} \nabla \cdot \left(\rho^\star \mathbf{u}^\star\right) \end{aligned} \tag{3.39}$$

In the correction step the pressure variation is used to express the variations of the conserved variables in eq. (3.40) & (3.41) obtaining the updated field of ρ^{n+1} & $\mathbf{m}^{n+1}$.

$$\frac{\rho^{n+1} - \rho^\star}{\Delta t} - \frac{1}{(c^*)^2} \frac{\delta p}{\Delta t} = 0 \tag{3.40}$$

$$\frac{\mathbf{m}^{n+1} - \mathbf{m}^\star}{\Delta t} - \frac{\mathbf{u}^n}{(c^*)^2} \frac{\delta p}{\Delta t} = -\nabla \left(\delta p\right) \tag{3.41}$$

$$\frac{\mathcal{E}^{n+1} - \mathcal{E}^\star}{\Delta t} - \frac{E^n}{(c^*)^2} \frac{\delta p}{\Delta t} = -\nabla \cdot \left(\delta p \, \mathbf{u}^{\mathrm{n}}\right) \tag{3.42}$$

The equation of state is introduced again in the CCS algorithm at the end of the correction step. This is again to enforce strict agreement between pressure and density in the phase interfaces for cavitating flows. The discontinuities in the orders of magnitude of density and speed of sound at the interface between vapor and liquid regions can often give rise to numerical oscillations in the pressure field. A situation may arise where the corrected p^{n+1} and ρ^{n+1} do not satisfy the equation of state in specific regions of phase interface. The solution of the equation of state implementation at the end of the time advancement removes such oscillations and corrects the pressure $p^{(n+1)_c}$ from the updated density ρ^{n+1} using the equation of state.

In the context of the developed solver CCS in the present work, the following contributions to the algorithm are provided for cavitating flows (also represented in fig. 3.2):

- Decoupling of temperature and energy evolution from the system of equations, through the implementation of a barotropic model ($p = f(\rho)$).
- Estimation of updated speed of sound at the end of prediction step.

- Updated speed of sound used for corrected pressure in Helmholtz equation and variation of density and velocity fields.
- Updated pressure from corrected density field in the correction step to satisfy equation of state at the end of temporal loop.

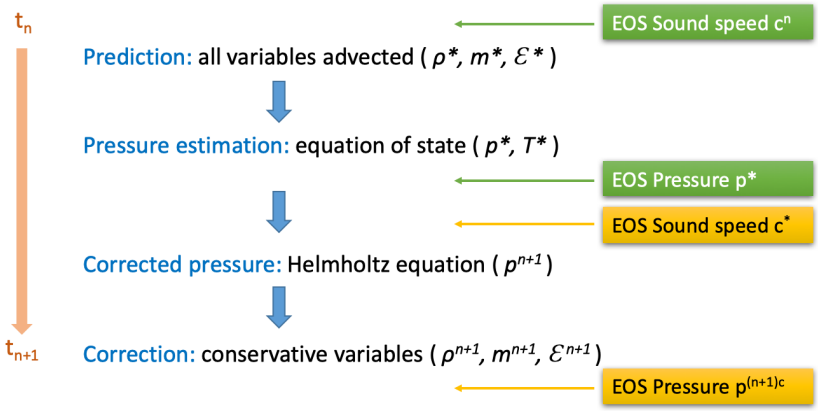

Figure 3.2 – Schematic of CCS algorithm- estimation of intermediate sound speed and corrected pressure from equation of state (in yellow).

3.4.1 Spatial discretization

In a FVM, a computational domain is defined and filled with a set of non-overlapping polygons (in 2D) or polyhedra (in 3D) called the mesh. These constituting bricks of the mesh can be referred as *mesh elements*, their vertices as *nodes*, mesh element interfaces as *faces* and intersection of two interfaces as *edges*. A badly designed mesh can give rise to large numerical errors, therefore destroying the physical content of simulation. The building block of FVM is the *control volume* (CV) over which the integral of the conservation equation is discretized. For example integrating the momentum equation eq. (3.6), neglecting gravity forces, on a polyhedra control volume Ω, bounded by a number of faces n_f gives eq. (3.43).The surface integral expresses that the variation of momentum in the CV Ω is due to the transport of momentum to or from the neighbouring CV, through its boundaries. Thus the volume and surface integral in eq. (3.43) is expressed as a combination of values of the variables at specific locations within the control volume and its neighbours.

$$\begin{aligned}\int_\Omega \frac{\partial \rho\bar{\mathbf{u}}}{\partial t}\, dV &= \int_\Omega \left(-\nabla\cdot(\rho\bar{\mathbf{u}}\otimes\bar{\mathbf{u}}) - \nabla p + \nabla\cdot\bar{\bar{\tau}} \right) dV \\ &= \int_{\partial\Omega} \left(-(\rho\bar{\mathbf{u}}\otimes\bar{\mathbf{u}}) - p\bar{\bar{\mathcal{I}}} + \bar{\bar{\tau}} \right)\cdot\, dS \\ &= \sum_i^{nf} \int_{S_i} \left(-(\rho\bar{\mathbf{u}}\otimes\bar{\mathbf{u}}) - p\bar{\bar{\mathcal{I}}} + \bar{\bar{\tau}} \right)\cdot\, dS\end{aligned} \tag{3.43}$$

For a given mesh, there exists two common approaches to construct the CV's. In *cell-centered* methods, the mesh elements are the CV on which the solution for the

integral form of the conservation laws are obtained. In YALES2, the other approach called the *vertex-centered* is used, where the CV is created centered around the nodes of the elements. The CV is the median dual cell built up out of a number of subtriangles (denoted *subtri*) in 2D and subtetrahedron (denoted *subtet*) in 3D shown in fig. 3.3. In 2D, the subtri is the surface delimited by the node, the midpoint of element edge connected to the node and the barycenter of the mesh element shown in fig. 3.3(b). The CV's of the boundary nodes are closed by attributing portions of the boundary mesh elements to their respective nodes. The total volume of the nodal CV, also called the *nodal volume* V_{node} is computed as the sum of the volume of its subtris/subtets.

$$V_{node} = \frac{1}{n_{dim}} \sum_{st} X_{st} \cdot S_{st} \tag{3.44}$$

where S_{st} is the normal vector on the subtri face opposing the node, X_{st} is the vector connecting the node and midpoint of the element edge to define st and for the closed surface of the CV, it is normally $\sum_{st} S_{st} = 0$. Some variables are needed to be known on the CV surface to compute the surface integral of the *Navier-Stokes* equations. Therefore distinct portions of the CV surface are assigned to *pairs* of nodes (Π_{ij}, say for nodes i & j) and the surface integral is the summation over the *pairs* connected to the node of the CV in consideration. A detailed description of the construction of CV stencil and spatial discretization can be found in the doctoral thesis of Vantieghem 2011. To compute the average over the CV for the unsteady

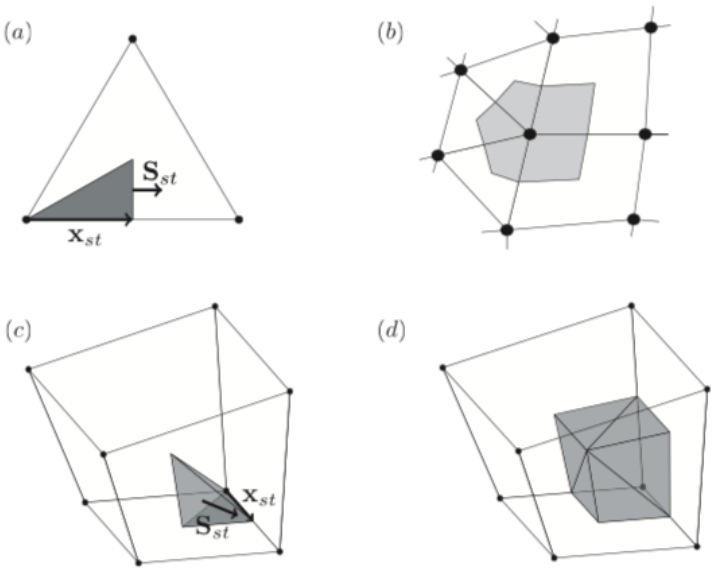

Figure 3.3 – Control volume representation for spatial discretization: (a) Subtri of a node pair for a triangular element (b) CV of a node in a mesh (c) Subtri of an edge-mesh face in a hexahedron (d) Exterior triangles of all subtetrahedra showing the contribution node CV for hexahedral element (Vantieghem 2011).

term in eq. (3.43), the volume integral for ϕ can be expressed as a Taylor expansion for the CV node i with the length scale Δ associated with CV size in eq. (3.45)

$$\int_\Omega \phi \, dV = \int_\Omega \left(\phi|_i + (\nabla\phi)|_i \cdot (\mathbf{x} - \mathbf{x_i}) + \mathcal{O}(\Delta^2) \right) \, dV \tag{3.45}$$

The average of ϕ is approximated over the CV by its nodal value in eq. (3.46)

$$\int_{\Omega} \phi \, dV \approx V_i \phi|_i \tag{3.46}$$

which is only first order for a generic mesh but is second order if the center of mass (or barycenter) of the CV where ϕ is approximated, is located at the node position (*i.e.* $\mathbf{x} = \mathbf{x_i}$) seen in eq. (3.45). Therefore for a locally uniform mesh, discretization errors can be reduced by avoiding large size jumps between adjacent mesh elements.

In the centered scheme, the gradient of a scalar field ϕ at a node i is expressed as:

$$\nabla \phi|_i = \frac{1}{V_i} \sum_{j \in \pi(i)} \frac{\phi|_i + \phi|_j}{2} \bar{\mathbf{n}}_{ij} \tag{3.47}$$

whereas the divergence for a vector field $\mathbf{u}$ at the node is the weighted sum of contributions from neighbouring nodes written for pairs of nodes Π_{ij} as:

$$\nabla \cdot \mathbf{u}|_i = \frac{1}{V_i} \sum_{j \in \pi(i)} \frac{\mathbf{u}|_i + \mathbf{u}|_j}{2} \cdot \bar{\mathbf{n}}_{ij} \tag{3.48}$$

Here V_i is the nodal volume associated with node i, $\bar{\mathbf{n}}_{ij}$ is the normal vector for CV of node i along the element edge between the pair nodes Π_{ij}. Both the ∇ and $\nabla\cdot$ operators are second order, computed from the second order Taylor expansion around node i. A successive application of both the operators to compute the Laplacian Δ will bring up the infamous *checkerboard problem* of numerical discretization that decouples the odd and even numbered nodes and cannot represent the Laplacian accurately. The problem and its resolution has also been discussed in detail by Vantieghem 2011 by approximating the integral of $\nabla^2 \phi dV$ on a CV as a sum of integrals of $\nabla\phi \cdot dS$ on the faces of CV. This involves approximation of $\nabla\phi$ on the normal of a face for complicated non-orthogonal mesh. Finally the Laplacian of a scalar field in a node is

$$\Delta p|_i = \frac{1}{V_i} \sum_{j \in \pi(i)} w_{ij} \left(p|_j - p|_i \right) \tag{3.49}$$

where w_{ij} is a element pair coefficient computed in the discretization stencil.

A fourth-ordered centered scheme also exist for which a deconvolution is necessary. It refers to expression of the nodal values as a function of the volume averages calculated at the barycenter of the CV. These nodal values are then used to compute fluxes between adjacent CV's. It is obvious that the barycenter of CV and mesh nodes do not coincide for a complex unstructured mesh and thus the deconvolution consists of computing components of gradient vector and Hessian matrix. This is not discussed here and readers are encouraged to refer to the doctoral thesis of Kraushaar 2011, Malandain 2013 and Vantieghem 2011 for details on construction of higher order discrete operators. For example, the divergence of a vector field for the fourth-ordered centered scheme is

$$\nabla \cdot \mathbf{u}|_i = \frac{1}{V_i} \sum_{j \in \pi(i)} \left(\frac{\mathbf{u}|_i + \mathbf{u}|_j}{2} + \Delta_{ij} \frac{\nabla \cdot \mathbf{u}|_i - \nabla \cdot \mathbf{u}|_j}{6} \right) \bar{\mathbf{n}}_{ij} \tag{3.50}$$

where Δ_{ij} is the length of the element edge connecting nodes i & j. In general higher order centred space discretization schemes are oscillatory in nature. In the

regions of numerical discontinuities like shock waves, the application of such schemes results in non-physical, spurious oscillations. Their combination with RK methods can become unstable and stabilizing measures need to be taken. Three strategies are possible:

1. Numerical viscosity in spatial and temporal discretization.
2. Adding artificial viscosity.
3. High-order filtering of solution fields.

3.4.2 Time integration

The time integration scheme TFV4A, developed by Kraushaar 2011, has been used to advance the solution in time from t_n to an instant $t_{n+1} = t_n + \Delta t$, where Δt is the time step used. This fourth-order scheme is explicit in nature, which only uses the known solution at t_n. The scheme is based on the idea of blending the low storage, explicit, fourth-order Runge-Kutta (called RK4 henceforth) with a Lax-Wendroff-type scheme, where the in-built numerical diffusion in the temporal scheme can be adjusted with a parameter κ. In RK4, a successive iterative computation is carried out to determine the updated variable field ϕ^{n+1}, where $\mathcal{C}$ is the discretized spatial operator.

$$\begin{aligned}
\phi^1 &= \phi^n - \frac{1}{4}\Delta t\mathcal{C}(\phi^n, p^n) \\
\phi^2 &= \phi^n - \frac{1}{3}\Delta t\mathcal{C}(\phi^1, p^n) \\
\phi^3 &= \phi^n - \frac{1}{2}\Delta t\mathcal{C}(\phi^2, p^n) \\
\phi^{n+1} &= \phi^n - \Delta t\mathcal{C}(\phi^3, p^n)
\end{aligned} \tag{3.51}$$

A Two-step Runge-Kutta (TRK) family of schemes can be designed by combining each two steps of RK4 as follows, where $\mathcal{C}^2$ represents the discretized spatial operator applied twice $\mathcal{C}^2(\phi, p) = \mathcal{C} \circ \mathcal{C}(\phi, p)$:

$$\begin{aligned}
\phi^2 &= \phi^n - \frac{1}{3}\Delta t\mathcal{C}(\phi^n, p^n) + \frac{1}{12}\Delta t^2\mathcal{C}^2(\phi^n, p^n) \\
\phi^{n+1} &= \phi^n - \Delta t\mathcal{C}(\phi^n, p^n) + \frac{1}{2}\Delta t^2\mathcal{C}^2(\phi^2, p^n)
\end{aligned} \tag{3.52}$$

A Lax-Wendroff-type (LW) scheme is TTG4A (Two-step Taylor Galerkin, fourth order) proposed in Quartapelle 1993 which in operator notation is expressed as:

$$\begin{aligned}
\phi^2 &= \phi^n - \frac{1}{3}\Delta t\mathcal{C}(\phi^n, p^n) + \frac{1}{12}\Delta t^2\mathcal{D}^2(\phi^n, p^n) \\
\phi^{n+1} &= \phi^n - \Delta t\mathcal{C}(\phi^n, p^n) + \frac{1}{2}\Delta t^2\mathcal{D}^2(\phi^2, p^n)
\end{aligned} \tag{3.53}$$

Here, the new operator $\mathcal{D}$ is the discretization operator of the LW diffusion term and is the only different term in the RK and LW-type schemes. Therefore by combining the RK4 and LW-type scheme, the fourth-ordered TFV4A scheme is obtained:

$$\begin{aligned}
\phi^{(2)} &= \phi^n - \kappa\frac{1}{3}\Delta t\mathcal{C}(\phi^n, p^n) + (1-\kappa)\frac{1}{12}\Delta t^2\mathcal{C}^2(\phi^n, p^n) + \kappa\frac{1}{12}\Delta t^2\mathcal{D}^2(\phi^n, p^n) \\
\phi^{n+1} &= \phi^n - \kappa\Delta t\mathcal{C}(\phi^n, p^n) + (1-\kappa)\frac{1}{2}\Delta t^2\mathcal{C}^2(\phi^2, p^n) + \kappa\frac{1}{2}\Delta t^2\mathcal{D}^2(\phi^2, p^n)
\end{aligned} \tag{3.54}$$

The parameter κ allows to adjust the amount of numerical diffusion in the time integration scheme. The RK4 scheme is obtained for $\kappa = 0$ whereas LW-type diffusive TTG4A scheme is obtained for $\kappa = 1$. As mentioned previously, the use of central space discretization are oscillatory by nature. The use of numerical diffusion reduces the high frequency numerical dispersion arising from spatial discretization while preserving the initial dispersion of the physics. This in turn provides a time integration scheme which is stable in a large spectrum of CFL condition with adjustable numerical diffusion.

TFV4A can be considered as adding LW-type diffusion term in the second and fourth steps of the classical RK4 scheme. This scheme has been used for all the simulations in this thesis with $\kappa = 0.2$.

3.4.3 Boundary Conditions

Appropriate initial and boundary conditions (BC) need to be applied on the computational domain to solve the system of *Navier-Stokes* equations. The different boundary conditions available in CCS solver are:

- **Outlet** BC - Subsonic outflow where the total pressure is defined.
- **Inlet** BC - Subsonic inflow with prescribed flow velocity.
  Due to pressure wave propagation and strong transient behaviour of the flow, the boundaries should allow the control of different waves that cross the boundaries. To handle this, YALES2 uses the classical Navier- Stokes Characteristic Boundary Conditions (NSCBC) proposed by Poinsot 1992, which are applied on flow Inlets and Outlets. The NSCBC conditions are imposed at the end of the correction step when both the convective and acoustic transports have been performed.
  In this thesis, the NSCBC conditions have been extended in the CCS solver for all types of fluid such as liquid water and ideal gas. It means NSCBC equipped Inlets and Outlets can be used for any type of fluid in CCS solver which is not the case in CPS solver where NSCBC are hard coded for an ideal gas.
- **Wall** (also called **No-Slip wall**) - Solid walls with normal pressure gradient equal to zero. Both normal and tangential velocity at the wall are zero ($v_n = v_\tau = 0$).
  Supports the development of boundary layers due to viscous effects. Imposed in the prediction step of the solver, leading to acoustically reflecting BC.
- **Slip-wall** - Similar to No-Slip wall except viscous effects on the wall are negligible. Normal velocity is zero but tangential velocity not equal to zero ($v_n = 0, v_\tau \neq 0$).
  In viscous flows, the **Slip-wall** BC is similar to **Symmetry** BC and can be applied as symmetry surfaces.
- **Periodic** - Rotationally or translationally periodic boundaries.

3.4.3.1 Navier- Stokes Characteristic Boundary Conditions (NSCBC)

Compressible fluid flow simulations are complicated, more so due to the need for boundary conditions with low dispersion errors and to avoid numerical instabilities and spurious wave reflections at the computational boundaries. An appealing technique to specify boundary conditions for such hyperbolic systems is to define

relationships based on characteristic lines for different waves crossing the boundary. The Navier-Stokes Characteristic Boundary Conditions (NSCBC) by Poinsot 1992 are used for subsonic inlet and outlet boundaries. The method consists of expressing the inviscid *Navier-Stokes* equations as characteristic equations at the domain exits. The conservative system of characteristic equations for density, pressure and velocity components $\phi \in (\rho, p, u_1, u_2, u_3)$ at the exits are as follows:

$$\begin{aligned}
\frac{\partial \rho}{\partial t} + \frac{1}{c^2}\left(L_2 + \frac{1}{2}(L_5 + L_1)\right) &= 0 \\
\frac{\partial p}{\partial t} + \frac{1}{2}(L_5 + L_1) &= 0 \\
\frac{\partial u_1}{\partial t} + \frac{1}{2\rho c}(L_5 - L_1) &= 0 \\
\frac{\partial u_2}{\partial t} + L_3 &= 0 \\
\frac{\partial u_3}{\partial t} + L_4 &= 0
\end{aligned} \tag{3.55}$$

where $L_i^{'}s$ are the characteristic wave amplitudes crossing the boundary, associated with each $\lambda_i^{'}s$, the propagation velocity of each characteristic wave. The characteristic velocities are:

$$\begin{aligned}
\lambda_1 &= u_1 - c, \\
\lambda_2 = \lambda_3 = \lambda_4 &= u_1, \\
\lambda_5 &= u_1 + c
\end{aligned} \tag{3.56}$$

In fig. 3.4, a computational domain with subsonic inlet at $x_1 = 0$ and outlet at $x_1 = L$ is shown. λ_1 and λ_5 are the velocities of sound waves travelling in negative and positive x_1 direction respectively, λ_2 is the convective velocity whereas λ_3 and λ_4 are the velocities at which u_2 and u_3 are advected by the flow in the x_1 direction. It is important to note that waves are only assumed to travel in the normal direction at the boundaries, which needs to be carefully considered while designing domain exits for the flow.

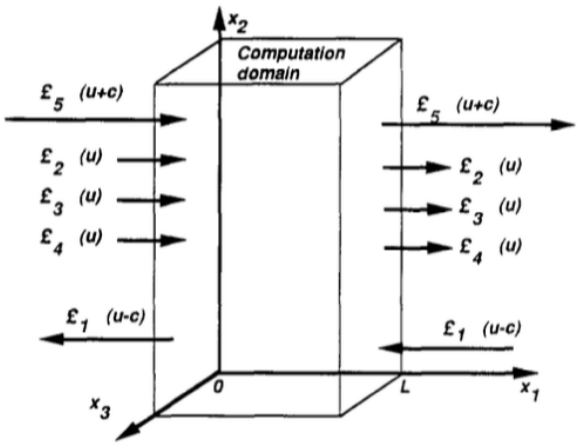

Figure 3.4 – Waves entering and leaving the computational domain through an inlet plane at $x_1 = 0$ and an outlet plane $x_1 = L$ for a subsonic flow (Poinsot 1992).

The wave amplitudes value $L_i^{'}s$ can be defined in terms of flow variables at the boundary of the domain.

$$\begin{aligned} L_1 &= \frac{\partial p}{\partial x_1} - \rho c \frac{\partial u_1}{\partial x_1} \\ L_2 &= c^2 \frac{\partial \rho}{\partial x_1} - \frac{\partial p}{\partial x_1} \\ L_3 &= \rho c \frac{\partial u_2}{\partial x_1} \\ L_4 &= \rho c \frac{\partial u_3}{\partial x_1} \\ L_5 &= \frac{\partial p}{\partial x_1} + \rho c \frac{\partial u_1}{\partial x_1} \end{aligned} \tag{3.57}$$

The role of NSCBC in our viscous multi-dimensional simulations is to determine unknown flow variables from the wave amplitude variation at the boundaries by resolving the local one-dimensional inviscid system in eq. (3.55). Along with known $L_i^{'}s$ for outgoing waves, the physical incoming wave amplitudes could be defined to be solved with eq. (3.55) to compute all unknown variables at the boundaries. Depending on the boundary type, physical incoming wave amplitudes can be estimated.

- **Subsonic outlet** - Most of the waves are moving out of the domain, so can be easily estimated except for L_1 which is expressed as a function of the reference pressure at the boundary p_{ref} in eq. (3.58). If the outlet pressure p is not close to p_{ref}, an incoming wave will enter the domain in order to bring the pressure value back to p_{ref}. Its mechanical analogy with a spring cannot be ignored, with the pressure relaxation constant $p_{relax} = 0$ will give *"perfectly non-reflecting"* conditions, although it will not impose the desired pressure p on the boundary.

$$L_1 = 2p_{relax}(p - p_{ref}) \tag{3.58}$$

- **Subsonic Inlet** - With four incoming waves entering the domain whose amplitude can be defined as eq. (3.59). Here $u_{1,relax}$, $u_{2,relax}$, T_{relax} are the normal velocity, tangential velocity and temperature relaxation constant used to recover the reference values inside the domain.

$$\begin{aligned} L_1 &= -2u_{1,relax}\rho c(u_1 - u_{1,ref}) \\ L_2 &= T_{relax}\rho\gamma r(T - T_{ref}) \\ L_3 &= u_{2,relax}\rho c(u_2 - u_{2,ref}) \\ L_4 &= u_{2,relax}\rho c(u3 - u_{3,ref}) \end{aligned} \tag{3.59}$$

3.4.4 Artificial Viscosity

A nonlinear artificial viscosity proposed by Cook 2004, based on the high-order derivative of the strain rate tensor is used to damp spurious oscillations near discontinuities. A mesh dependent artificial viscosity μ_{artif} is added to the momentum and energy equations, defined as

$$\mu_{artif} = C_\mu \rho \left(\Delta x\right)^r \overline{\left|\frac{\partial^r u}{\partial x^r}\right|} \tag{3.60}$$

where Δx is the mesh spacing, $\overline{|\ |}$ is a Gaussian filter applied to the absolute value to ensure a smooth and positive μ_{artif}. C_μ is a model constant called the artificial viscosity constant and r is a user-specified integer called the artificial viscosity order and is set to 4 wherever applicable in this thesis. A high-resolution numerical scheme will have μ_{artif} damp only the wavenumbers close to the Nyquist wavenumber, $\pi/\Delta x$. Setting $\mu_{artif} \propto \partial^r u/\partial x^r$ imparts a high wavenumber bias to the artificial viscosity μ_{artif}.

A shock wave in a solution domain is represented by a discrete discontinuity in pressure and velocity fields. These numerical discontinuities correspond to the largest wavenumbers in terms of Fourier analysis. A sufficiently high r, will make μ_{artif} important near the shock waves and close to zero in the rest of the flow.

3.4.5 Cavitation Model

The system of compressible *Navier-Stokes* equations is coupled with the equations of state (EOS) to close the system of governing equations. A *single fluid* or widely called homogenous mixture model is used to treat the two-phase cavitating flow. A single fluid model treats the cavitating flow as a mixture of two fluids of varying density and are quite popular in cavitation studies, for example Goncalves 2009, Goncalves 2010 and Egerer 2013. A homogenous mixture of liquid and vapor is assumed in two phase regions, with vapor volume fraction $\alpha = \Omega_v/\Omega$ in a control volume Ω. The volume average density ρ in the two phase region is expressed by the linear combination of liquid density ρ_l and vapor density ρ_v in eq. (3.61).

$$\rho = \alpha\rho_v + (1-\alpha)\,\rho_l \tag{3.61}$$

The model assumes local kinematic equilibrium between phases which implies same local velocity for both phases and thermodynamic equilibrium which implies the phase change is infinitely fast, isentropic and in mechanical equilibrium. This allows us to distinguish the different phases in the model - pure liquid water with $\alpha = 0$ and a two phase liquid-vapor mixture region separated from the pure liquid by $\rho_{sat,l}$ in eq. (3.62).

$$\alpha = \begin{cases} 0 & ,\rho \geq \rho_{sat,l} \\ \frac{\rho_{sat,l} - \rho}{\rho_{sat,l} - \rho_{sat,v}} & ,\rho < \rho_{sat,l} \end{cases} \tag{3.62}$$

Here, $\rho_{sat,l}$ and $\rho_{sat,v}$ are the liquid and vapor densities at the saturation point, respectively. In literature, homogenous mixture models have been used to resolve large vapor structures like cavitating vortices or bubble clouds as well as single bubbles. It does not require any empirically computed mass transfer term between the liquid and vapor phases. However since no interface is reconstructed in the model, the surface tension effects are neglected.

The different phases are defined by equations of state which are barotropic, meaning that the pressure is a function of the fluid density only. These equations are used in the solver to evaluate analytically the pressure p from the density ρ calculated by the continuity equation. Since the cavitation model is assumed to be barotropic, the energy equation is decoupled from the system of governing equation in CCS for liquid water. In fact, the energy equation is solved, but the evolution of energy and temperature has no effect on the two phase flow modelling. The two phase liquid-vapor mixture region is considered without the presence of any condensable

gas. The pure liquid phase is modelled with the modified Tait's equation of state in eq. (3.63), with the fitted model constants B and N given in table 3.1.

$$p = (p_{sat} + B)\left(\frac{\rho}{\rho_{sat,l}}\right)^N - B, \text{ if } \alpha = 0 \tag{3.63}$$

In the two phase mixture region, phase transition is modelled following an isentropic

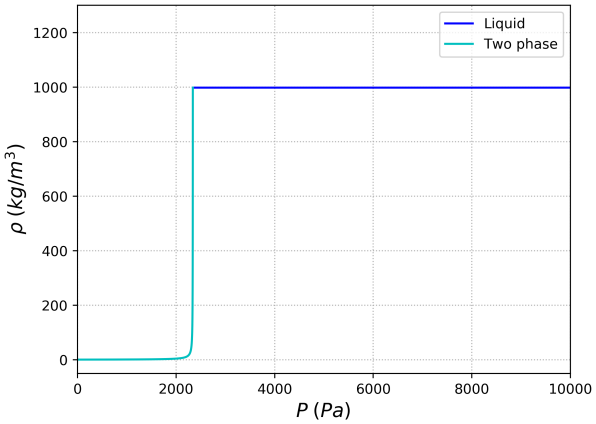

Figure 3.5 – Density vs pressure evolution in the cavitation model.

path in the phase diagram proposed by Egerer 2013 in eq. (3.64), where the model constant C and saturation properties are taken at a reference temperature $T_{ref} = 293.15\,K$, listed in table 3.1. The equilibrium pressure-density evolution following an isentropic path in the phase diagram is shown in fig. 3.5.

$$p = p_{sat} + C\left(\frac{1}{\rho_{sat,l}} - \frac{1}{\rho}\right), \text{ if } 0 < \alpha < 1 \tag{3.64}$$

A consistent speed of sound based on eq. (3.18) is used for the pure liquid as follows:

$$c = \sqrt{(p_{sat} + B)\ N\ \frac{(\rho)^{N-1}}{(\rho_{sat,l})^N}}, \text{ if } \alpha = 0 \tag{3.65}$$

The speed of sound in the homogenous two-phase mixture decreases dramatically as the fluid is not composed of a single liquid phase anymore. This huge decrease in speed of sound at the phase interface, plotted in fig. 3.6 as "Barotropic two phase", makes the flow locally supersonic as soon as cavitation appears, and could give rise to spurious numerical oscillations at the interface. As the purview of this thesis is the collapse of cavitation bubbles and resulting pressure wave propagation in the liquid medium, a constant speed of sound is implemented in the two-phase cavitation region shown in fig. 3.6 as "Two phase". In our numerical simulations, the shock waves propagating in the pure liquid are resolved accurately and shock propagation speed in the two-phase cavitation region is not important. The shock propagation in the two phase region inside the bubble propagates at a constant speed of sound of $1483.3\,m/s$, obtained from the $\rho_{sat,l}$ at $293.15\,K$ in eq. (3.66). The model constants used in the cavitation model are summarized in table 3.1.

$$c = \sqrt{(p_{sat} + B)\ N\ \frac{(\rho_{sat,l})^{N-1}}{(\rho_{sat,l})^N}}, \text{ if } 0 < \alpha < 1 \tag{3.66}$$

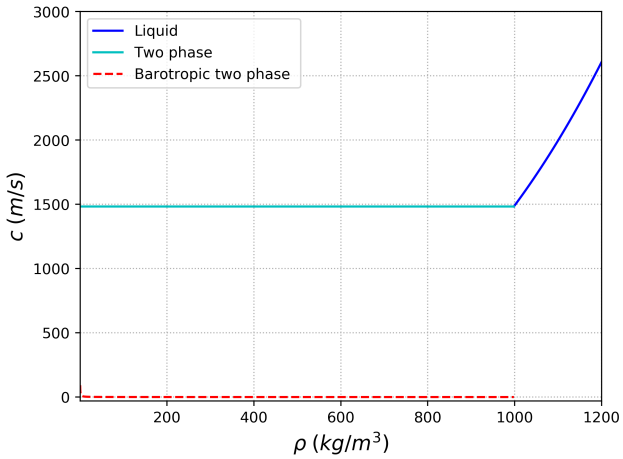

Figure 3.6 – Speed of sound vs density evolution in the cavitation model.

Property	Value	Unit
p_{sat}	2340	Pa
$\rho_{sat,l}$	998.1618	kg/m^3
$\rho_{sat,v}$	0.01731	kg/m^3
$\mu_{sat,l}$	1.002×10^{-3}	$Pa \cdot s$
$\mu_{sat,v}$	9.727×10^{-6}	$Pa \cdot s$
C	1468.54	$Pa \cdot kg/m^3$
N	7.132	–
B	3.078×10^8	Pa
T_{ref}	293.15	K

Table 3.1 – Saturation properties of water.

$$\mu = (1-\alpha)\left(1+\frac{5}{2}\alpha\right)\mu_{sat,l} + \alpha\,\mu_{sat,v}, \text{ if } 0<\alpha<1 \tag{3.67}$$

For viscous calculations, a constant liquid viscosity $\mu_{sat,l}$ is used for pure liquid phase whereas the implemented dynamic viscosity for the liquid-vapor mixture is similar to Egerer 2013 using eq. (3.67) shown in fig. 3.7. The effective viscosity for liquid-vapor mixture is modelled as a quadratic law with a maximum in the two phase region following the model proposed in Beattie 1982. The dynamic viscosity varies with the vapor volume fraction α in the two phase region. For a single bubble collapse, the effect of such viscosity model is not substantial as the vapor volume fraction inside the bubble is approximately constant. In the case of large cavitating vortices or bubble clouds, such dynamic viscosity model accounts for fully immersed small vapor bubbles in a liquid which in turn account for subgrid effects of fully immersed non-resolved vapor structures.

Finally, it is worth mentioning that as seen in fig. 3.5, there is a steep decrease in density (as well as pressure) at the phase interface in our cavitation model. This restricts the choice of numerical time step Δt in our two-phase simulations as too big a time step leads to instability in the time advancement scheme. We do not

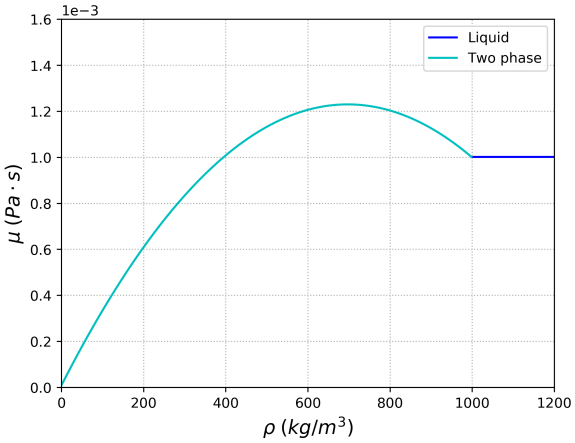

Figure 3.7 – Dynamic viscosity vs density evolution in the cavitation model.

define a different stability criteria for this and instead choose a time step with much smaller CFL to ensure stability of the numerical scheme.

3.4.6 Bubble initialization

In the single-fluid cavitation model, a bubble is initialized with a hyperbolic tangent function which assumes a continuous evolution of density through the interface given in eq. (3.68). Here Δx is the computational mesh spacing and d_f is a distance function defined in eq. (3.69), x_i is the spatial coordinate, *center* is the desired coordinate of the bubble center, R_0 is the initial bubble radius, ρ_v is the liquid-vapor mixture density & ρ_l is the liquid density. The pressure at initialization is obtained depending on ρ_v and ρ_l from eq. (3.63) & (3.64).

$$\rho_{init} = \rho_v + \left(\frac{\rho_l}{2} + \frac{\rho_l}{2} \times \tanh\left(\frac{d_f}{\Delta x} \right) \right) \tag{3.68}$$

$$d_f = \sqrt{\sum_{i=1}^{ndim} (x_i - center)^2} \; - \; R_0 \tag{3.69}$$

In fig. 3.8, the initialization of bubble of radius $R_0 = 500\ \mu m$ is shown in 1D with the bubble center at the *origin*, $\rho_v = 10\ kg/m^3$ and $\rho_l = 1000\ kg/m^3$. From thermodynamic considerations, we cannot obtain pure vapor phase i.e. $\alpha = 1$ in an isentropic phase change from liquid to vapor. Physically, cavitation leads to local cooling of the surrounding liquid as it provides the the latent heat of evaporation. In an isothermal process, the temperature during phase change is kept constant by allowing heat transfer with the surrounding which increases the entropy during vaporization. In an isentropic phase change, temperature is not kept constant with heat transfer and temperature decreases along the isentropic path. Therefore, the isentropic phase transition model terminates at the triple line in the phase diagram within the two-phase region and complete vaporization of the liquid is not possible. The thermodynamic equations of state employed are not valid for temperature below the triple line and the maximum amount of vapor produced is limited by the point where the liquid-vapor isentrope terminates in the triple line. Based on our initial

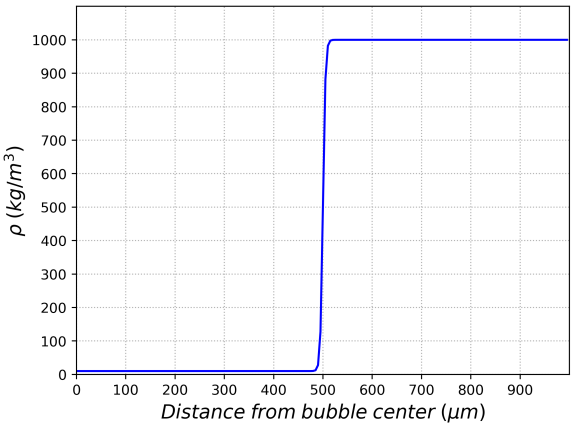

Figure 3.8 – 1D representation of bubble radius initialization.

conditions $T_{ref} = 293.15\,K$ and $p_{sat} = 2340\,Pa$, the maximum vapor volume fraction is limited to $\alpha_{max} = 0.9993$.

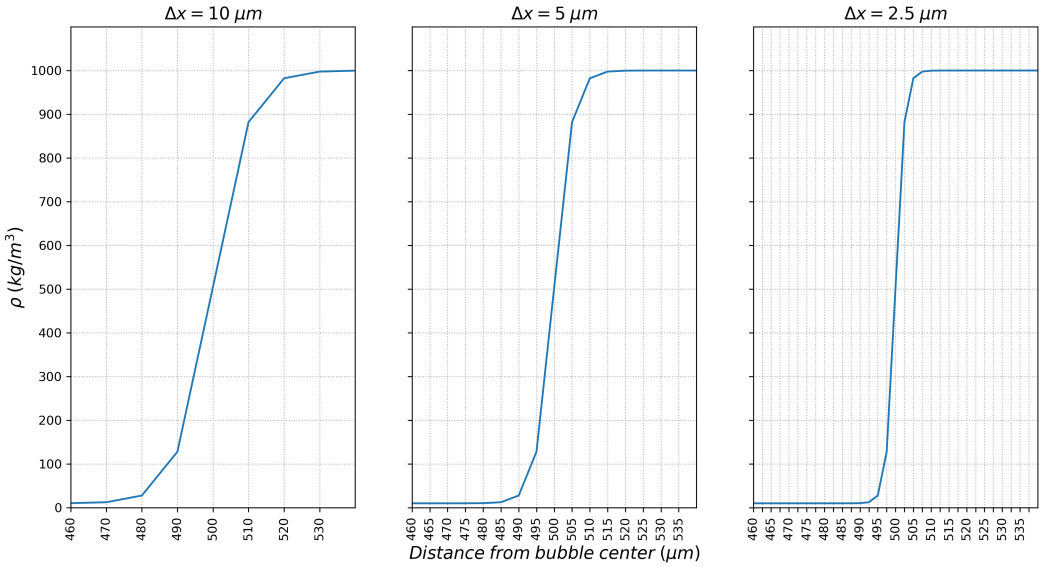

Figure 3.9 – 1D representation of bubble radius initialization for different mesh spacing of Δx=10, 5, 2.5 μm.

In our bubble collapse modelling, we take the liquid-vapor mixture density $\rho_v = 10\ kg/m^3$ so that the pressure inside the bubble is $p_v = 2194\ Pa$, close to the saturation pressure p_{sat}. The value of $\rho_l = 1000\ kg/m^3$ in fig. 3.8 corresponds to ambient liquid pressure of about $4\,MPa$ at initialization. The value ρ_l and ρ_v can be adjusted to match desired initial conditions. The bubble radius in eq. (3.68) is independent of the mesh spacing with the bubble interface defined at $\rho_l/2$ which corresponds to $500\,kg/m^3$ in the present example. Figure 3.9 shows the 1D plot for bubble initialization for different mesh resolution of $\Delta x = 10,\ 5,\ 2.5\,\mu m$, where the $R_0 = 500\,\mu m$ for all different mesh resolution.

3.5 Cavitation ALE Solver (CLE)

In cavitation erosion, the solid wall deforms under the influence of high-intensity pressure loads from collapsing bubbles. The numerical simulation of such coupled FSI problem requires the distortion of both fluid and solid computational domains. To accomplish this, the CCS solver needs to be extended in a numerical framework that not only allows to delineate fluid phase interfaces accurately, but can also provide continuous fluid-structure domain with moving boundaries. Neither the Eulerian nor the Lagrangian formulations are optimal for the entire domain due to their respective limitations. The Eulerian formulation widely used in fluid mechanics has a computational mesh fixed in space, with the continuum (materials modeled as a continuous mass) moving with respect to the mesh. Although the continuum motion relative to the mesh can be handled easily with some complexity in resolving the transport of the material, it cannot resolve FSI interface motion since the mesh is fixed in space. The Lagrangian formulation mainly used in solid mechanics is the one where the mesh moves with the material, allowing ease in resolving material interfaces accurately but frequent re-meshing is required to handle large distortions of the computational domain. For such cases, Arbitrary Lagrangian Eulerian (ALE) formulation is quite attractive and has been implemented with CCS solver algorithm as a new solver called the Cavitation ALE Solver (CLE) in YALES2. ALE combines the best features of both the approaches and allows for the movement of nodes of the computational mesh with the continuum in normal Lagrangian manner or to be held fixed in Eulerian manner or, more importantly, in any intermediate way. An ALE-equipped fluid mesh can conform to the Lagrangian mesh deformation of the solid at the fluid-structure interface which is a convenient framework for the FSI problem of bubble collapse. Since the ALE mesh moves relative to the material in the flow domain, similar transport terms to the existing Eulerian formulation of the CCS solver exist. Therefore, implementation of ALE formulation will benefit from many of the implemented algorithms. CLE solver can be used to model compressible simulations of realistic complex geometries like rotor-stator stages in aeronautics or hydraulic turbines, deformable walls in bio-mechanical flows.

3.5.1 ALE formulation

The motion of individual nodes of a computational mesh with its associated material particle motion is shown in fig. 5.16 for Eulerian, Lagrangian and ALE frameworks. In the Eulerian, the computational nodes are fixed and the material particles move with respect to them. In the Lagrangian framework, each individual node follows the motion of its associated material particle. In the ALE formulation, the individual nodes can be moved in some specified way with respect to the material particle, thus offering more freedom in moving the computational mesh. The original development of ALE is credited to, among others, Hirt 1974 and an in-depth introduction to the mathematical framework is given in Donea 2004.

The Lagrangian framework uses the material configuration R_X following the material particles in the computational domain. The motion of the material particles relates the material coordinates X to the spatial coordinates x in time t. There are no convective effects in Lagrangian calculations and the material derivative is a simple time derivative. In the Eulerian framework, the spatial configuration x is employed dissociating the mesh nodes from the material particles. The conservation

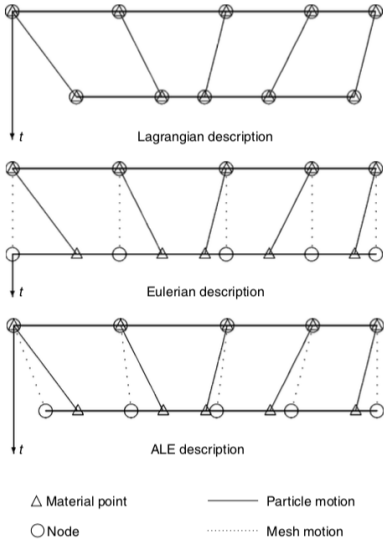

Figure 3.10 – 1D Lagrangian, Eulerian and ALE mesh node motion with associated material particle motion (Donea 2004).

equations are framed for the spatial coordinate x and time t, with the material velocity $\bar{\mathbf{u}}$ at a given mesh node describing the velocity of the material particle with the considered node at the considered time t. For any scalar physical quantity f, the well-known relationship between the material and spatial time derivative can be written in eq. (3.70). It represents that the variation of the physical quantity for a given material particle is the local variation plus a convective term accounting for the relative motion between the spatial and material framework.

$$\left.\frac{\partial f}{\partial t}\right|_X = \left.\frac{\partial f}{\partial t}\right|_x + \bar{\mathbf{u}} \cdot \nabla f \tag{3.70}$$

In ALE a third domain called the referential framework R_χ is introduced with reference coordinates χ. The one-to-one transformations between the material, spatial and referential framework are shown in fig. 3.11. The mapping ϕ defines a configuration in the spatial coordinate x depending on material particle X and time t. The referential domain R_χ is mapped into the material R_X and spatial R_x domain by ψ and Φ respectively.

The fundamental relationship between the material, referential time derivative and spatial gradients with the help of the domain mapping can be expressed as (the full derivation can be found in Donea 2004):

$$\left.\frac{\partial f}{\partial t}\right|_X = \left.\frac{\partial f}{\partial t}\right|_\chi + \left.\frac{\partial f}{\partial t}\right|_x \cdot \bar{\mathbf{w}} = \left.\frac{\partial f}{\partial t}\right|_\chi + \bar{\mathbf{w}} \cdot \nabla f \tag{3.71}$$

Here $\bar{\mathbf{w}}$ is the convective velocity, defined as the relative velocity between the material velocity $\bar{\mathbf{u}}$ and the mesh velocity $\dot{\mathbf{x}}$ such that $\bar{\mathbf{w}} = \bar{\mathbf{u}} - \dot{\mathbf{x}}$. Equation (3.71) represents the time derivative of the physical quantity f for a given particle , i.e. its material derivative which is expressed as its local derivative in a fixed reference coordinate χ plus a convective term $\bar{\mathbf{w}}$ between the material and the reference spatial coordinates.

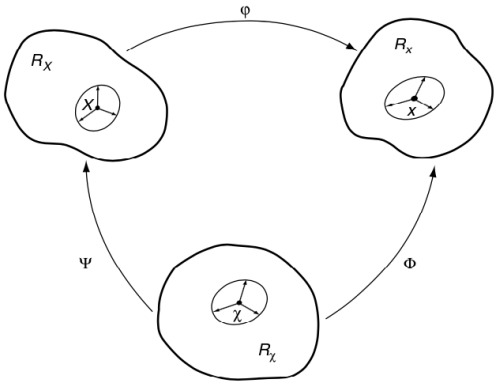

Figure 3.11 – One to one transformation between the material domain, spatial domain and the referential domain for ALE (Donea 2004).

3.5.2 Governing equation for CLE

The ALE form of fully compressible *Navier-Stokes* equations is obtained by replacing the material velocity $\bar{\mathbf{u}}$ by the convective velocity $\bar{\mathbf{w}} = \bar{\mathbf{u}} - \dot{\mathbf{x}}$ shown in eq. (3.72), (3.73) & (3.74).

$$\frac{\partial \rho}{\partial t} + \nabla \cdot (\rho \bar{\mathbf{w}}) = 0 \tag{3.72}$$

$$\frac{\partial \rho \bar{\mathbf{u}}}{\partial t} + \nabla \cdot (\rho \bar{\mathbf{u}} \otimes \bar{\mathbf{w}}) = -\nabla p + \nabla \cdot \bar{\bar{\tau}} \tag{3.73}$$

$$\frac{\partial \rho E}{\partial t} + \nabla \cdot (\rho E \bar{\mathbf{w}}) = -\nabla \cdot (p \bar{\mathbf{u}}) + \nabla \cdot (\bar{\bar{\tau}} \bar{\mathbf{u}}) + \nabla \cdot (\lambda \nabla T) \tag{3.74}$$

The right-hand side of the equations has a form similar to the classical Eulerian form of *Navier-Stokes* equations presented in section 3.2.4 whereas the mesh movement is reflected on the left hand side of the governing equations. Setting $\bar{\mathbf{w}} = 0$ (*i.e.* $\dot{\mathbf{x}} = \bar{\mathbf{u}}$) gives the classical Lagrangian description whereas $\bar{\mathbf{w}} = \bar{\mathbf{u}}$ (*i.e.* $\dot{\mathbf{x}} = 0$) recovers the Eulerian description. The temporal scheme TFV4A has to be recast in an ALE formulation with prescribed mesh movement at each sub-step of the time integration scheme to satisfy the Geometry Conservation Law (GCL) as well as numerical stability conditions. Geometry Conservation Law states that, independently of the mesh motion, the numerical scheme has to preserve the state of a uniform flow. The CFL and CFL_{acou} are then expressed in terms of the convective velocity $\bar{\mathbf{w}}$:

$$CFL = |\bar{\mathbf{w}}| \, \frac{\Delta t}{\Delta x} \tag{3.75}$$

$$CFL_{acou} = |\bar{\mathbf{w}} + c| \, \frac{\Delta t}{\Delta x} \tag{3.76}$$

3.5.3 Fractional step algorithm for CLE

A characteristic splitting of the *Navier-Stokes* equations in ALE form in eq. (3.72), (3.73) & (3.74) is outlined to achieve the fractional step method of time advancement. Equations (3.77), (3.78) and (3.79) are solved for $\phi \in (\rho, \mathbf{m}, \mathcal{E})$ in the prediction step with the convective velocity $\tilde{\mathbf{w}} = \tilde{\mathbf{u}} - \dot{\mathbf{x}}$. The mesh velocity $\dot{\mathbf{x}}$ can be determined explicitly or implicitly by solving an equation for the node displacement

for specific boundary conditions. The time integration is carried out with TFV4A scheme with the mesh being displaced only during the prediction step discussed in section 3.5.4.

$$\frac{\rho^\star - \rho^n}{\Delta t} + \nabla \cdot (\tilde{\rho}\tilde{\mathbf{w}}) - (\tilde{\rho} - \rho^n)\,\nabla \cdot \tilde{\mathbf{w}} = 0 \tag{3.77}$$

$$\frac{\mathbf{m}^\star - \mathbf{m}^n}{\Delta t} + \nabla \cdot (\tilde{\mathbf{m}} \otimes \tilde{\mathbf{w}}) - (\tilde{\mathbf{m}} - \mathbf{m}^n)\,\nabla \cdot \tilde{\mathbf{w}} = -\nabla p^n + \nabla \cdot \tau^n \tag{3.78}$$

$$\frac{\mathcal{E}^\star - \mathcal{E}^n}{\Delta t} + \nabla \cdot \left(\tilde{\mathcal{E}}\tilde{\mathbf{w}}\right) - \left(\tilde{\mathcal{E}} - \mathcal{E}^n\right)\nabla \cdot \tilde{\mathbf{w}} = -\nabla \cdot (p^n \mathbf{u}^n) + \nabla \cdot (\tau^n \mathbf{u}^n) + \nabla \cdot (\lambda \nabla T^n) \tag{3.79}$$

The computational mesh reaches the final position of the time step at the end of the prediction step and a fixed mesh exists at this stage. The Helmholtz eq. (3.80) is solved over this fixed mesh with BiCGSTAB2 linear solver for the pressure variation δp. The pressure variation δp is used to correct the conserved variables $\phi \in (\rho, \mathbf{m}, \mathcal{E})$ in the correction step with eq. (3.81), (3.82) & (3.83).

$$\begin{aligned} \nabla \cdot \nabla \left(p^{n+1} - p^\star\right) - \nabla \cdot \frac{\mathbf{w}^*}{(c^*)^2 \Delta t}\left(p^{n+1} - p^\star\right) - \frac{p^{n+1} - p^\star}{(c^*)^2 \Delta t^2} \\ = \nabla \cdot \nabla \left(p^n - p^\star\right) + \frac{\rho^\star - \rho^n}{\Delta t^2} + \frac{1}{\Delta t}\nabla \cdot (\rho^\star \mathbf{w}^\star) \end{aligned} \tag{3.80}$$

$$\frac{\rho^{n+1} - \rho^\star}{\Delta t} - \frac{1}{(c^*)^2}\frac{\delta p}{\Delta t} = 0 \tag{3.81}$$

$$\frac{\mathbf{m}^{n+1} - \mathbf{m}^\star}{\Delta t} - \frac{\mathbf{w}^*}{(c^*)^2}\frac{\delta p}{\Delta t} = -\nabla (\delta p) \tag{3.82}$$

$$\frac{\mathcal{E}^{n+1} - \mathcal{E}^\star}{\Delta t} - \frac{E^n}{(c^*)^2}\frac{\delta p}{\Delta t} = -\nabla \cdot (\delta p\ \mathbf{u}^{\mathrm{n}}) \tag{3.83}$$

The algorithm is similar to CCS where an intermediate speed of sound c^* is computed from the advected ρ^* and p^*. An equation of state at the end of the correction step gives a consistent $p^{(n+1)_c}$ and ρ^{n+1} at the end of the time step. The CLE solver is equipped with the same discretization schemes, boundary conditions and cavitation model as CCS solver to model cavitation bubble collapse.

3.5.4 Time integration for CLE

The time integration in TFV4A is coupled with movement of mesh nodes and advancement of CV in the prediction step. The convective flux $\tilde{\mathbf{w}} = \tilde{\mathbf{u}} - \dot{\mathbf{x}}$ has to be determined with the displaced CV at each step of time integration. As mentioned in section 3.4.2, TFV4A is classical RK4 scheme with LW-type diffusion term in the second and fourth steps. A classical time integration between t^n and t^{n+1} with a time step Δt for the transport term is in eq. (3.84) where RHS contains the viscous fluxes and pressure gradients.

$$\int_{t^n}^{t^{n+1}} \frac{\partial}{\partial t} \int_{\Omega(t)} \phi \partial\Omega\, dt + \int_{t^n}^{t^{n+1}} \int_{\Omega(t)} \nabla \cdot (\phi(\mathbf{u} - \dot{\mathbf{x}}))\partial\Omega\, dt = RHS \tag{3.84}$$

The sub-step of the time integration at $t^i = t^n + \Upsilon_i \Delta t$, for a classical RK4 with coefficient $\Upsilon_i = [1/4, 1/3, 1/2, 1]$ is shown in eq. (3.85).

$$\begin{aligned} &\phi^n = \phi^0, \\ &\phi^i = \phi^n \frac{\Omega^n}{\Omega^i} - \Upsilon_i \frac{\Delta t}{\Omega_i} \int_{\Omega(t)} \nabla \cdot (\phi^{i-1}(\mathbf{u}^{i-1} - \dot{\mathbf{x}}^{n+1}))\partial\Omega, \ for\ i = 1, 2, 3, 4 \\ &\phi^* = \phi^4 \end{aligned} \tag{3.85}$$

Here, ϕ^* is the predicted variable field, Ω^n is the nodal volume V_{node} at time t^n and Ω^i is the V_{node} at time t^i. The mesh movement coefficient (Chnafa 2014) at each sub-step of the time integration has been derived in such a way that the numerical scheme satisfies a discrete Geometry Conservation Law (GCL) as in eq. (3.86):

$$\Omega^i - \Omega^n = -\Upsilon_i \Delta t \int_{\Omega(t)} \nabla \cdot \dot{\mathbf{x}}^{n+1} \partial\Omega, \ for\ i = 1, 2, 3, 4 \tag{3.86}$$

3.6 Summary

The numerical strategy for modelling compressible fluid flow in the *finite volume* framework has been described. The developed CCS solver for cavitating flows is presented with numerical schemes, boundary conditions and implemented cavitation model. The solver is intended to be coupled with a solid solver to model the fluid-structure interaction problem of a cavitation bubble collapsing near a solid boundary. To do this, CCS solver has been extended with ALE capabilities in the CLE solver.

As per our knowledge, characteristics-based fractional step method for compressible *Navier-Stokes* equations in ALE form implemented in the CLE solver and its integration with TFV4A type scheme has never been presented before.

Chapter 4

Solid Mechanics and Fluid-Structure Interaction

4.1 Introduction

The role of solid mechanics computations is to predict the stress and displacements of a deformable body subjected to the action of forces in equilibrium. The solid material response and surface deformation prediction from impacting cavitation loads are carried out with the finite element based solver Cast3M. A brief review of the equilibrium equations in solid mechanics is presented along with the methodology for FEM computations and introduction of material constitutive laws. The proposed methodology for step-wise fluid-structure interaction is discussed next for one-way and two-way coupling of fluid-solid domain.

4.2 Equilibrium equations of solid mechanics

The equilibrium equations are generalized Newton's second law of motion which states that the rate of change of linear momentum would be equal in magnitude and direction to the net applied force. In principle, we look at the conservation of linear and angular momentum of a deformable solid body subjected to surface and body forces. The surface forces arise by virtue of contact of the body with its surroundings. The surface force component along the normal direction is the normal stress σ_n and the magnitude of the component acting parallel to the surface plane is the shear stress τ_n. The body forces denoted by $\bar{f} = \rho\bar{g}$ are the action of a distance force whose magnitude depends on the mass of the body, for example gravitational force, and $\bar{g}$ is the body force per unit mass whereas ρ is the density. The conservation of linear momentum from the forces acting on an arbitrary volume of material V within a solid is

$$\int_V \rho \frac{D\bar{v}}{Dt} dV = \int_S \bar{\mathcal{T}} dS + \int_V \bar{f} dV \tag{4.1}$$

$$\int_V \rho\bar{a} dV = \int_S \bar{\bar{\sigma}} \cdot \bar{n} dS + \int_V \bar{f} dV \tag{4.2}$$

where $\bar{\mathcal{T}}$ is the internal traction acting on the surface S with normal $\bar{n}$ that bounds the volume V, $\frac{D}{Dt}$ is the Lagrangian time derivative, $\bar{u}_d$ is the displacement vector in

the material coordinates, $\bar{v} = \frac{D\bar{u}_d}{Dt}$ and $\bar{a}$ are the material velocity and acceleration respectively. The internal traction $\bar{\mathcal{T}}$ on a surface is related to the Cauchy stress tensor $\bar{\bar{\sigma}}$ with eq. (4.3), where $\bar{n}$ is the outward normal vector.

$$\bar{\mathcal{T}} = \bar{\bar{\sigma}} \cdot \bar{n} \tag{4.3}$$

Assuming mass to be conserved for any unit material volume and if the stress field is continuously differentiable within the body, the equilibrium equation for *linear momentum balance* arising from the force equilibrium of the unit volume can be expressed as:

$$\nabla \cdot \bar{\bar{\sigma}} + \bar{f} = \rho \bar{a} \tag{4.4}$$

The equilibrium equation for *angular momentum balance* specifies that the rate of change of angular momentum must be equal to the net applied moment on the body. Assuming that this moment is generated only by the surface forces, this condition requires the Cauchy stress tensor to be symmetric $\bar{\bar{\sigma}} = \bar{\bar{\sigma}}^T$, where $()^T$ denotes the transpose.

Therefore,the global equilibrium equations from linear and angular momentum hold if and only if the local conditions in eq. (4.5) hold at each point in the body, at every instant during motion.

$$\begin{aligned} \nabla \cdot \bar{\bar{\sigma}} + \bar{f} &= \rho \bar{a}, \\ \bar{\bar{\sigma}} &= \bar{\bar{\sigma}}^T. \end{aligned} \tag{4.5}$$

In component form at any position y_j in the deformed solid, we can write the conservation equation below using the Einstein notation i.e.summation is performed over repeated indices.

$$\frac{\partial \sigma_{ij}}{\partial y_j} + f_i = \rho a_i, \;\; \sigma_{ij} = \sigma_{ji}, \;\; \mathcal{T}_i = \sigma_{ij} n_j \tag{4.6}$$

4.2.1 The principle of virtual work

The principle of virtual work forms the basis for the finite element method in solid mechanics. Considering a smooth virtual displacement $\delta\bar{u}_d^*$ at each point of a deformable solid subjected to a loading. The loading induces a stress $\bar{\bar{\sigma}}$ that satisfies the angular momentum balance equation $\bar{\bar{\sigma}} = \bar{\bar{\sigma}}^T$ together with a traction $\bar{\mathcal{T}}$ applied to the solid boundary. The principle of virtual work then expresses the partial differential equation for linear momentum balance in an equivalent integral form, much suited for computational solution.

$$\int_V \bar{f}\, \delta\bar{u}_d^*\, dV + \int_S \bar{\mathcal{T}}\, \delta\bar{u}_d^*\, dS = \int_V \rho\, \bar{a}\, \delta\bar{u}_d^*\, dV + \int_V \bar{\bar{\sigma}} : \bar{\bar{\varepsilon}}^*\, dV \tag{4.7}$$

The associated strain field can be defined as:

$$\bar{\bar{\varepsilon}}^* = \frac{1}{2}(\nabla\bar{u}_d^* + \nabla(\bar{u}_d^*)^T) \tag{4.8}$$

Equation (4.7) can be grouped into three separate parts, LHS terms being the external virtual work by the traction vector on the surface and body forces during virtual displacement $\delta\bar{u}_d^*$. The first term in RHS is the virtual kinetic energy whereas the second term in RHS is the internal virtual work associated with the virtual strain field $\bar{\bar{\varepsilon}}^*$. A stress field $\bar{\bar{\sigma}}$ that satisfies the virtual work equation in eq. (4.7) for

all virtual displacements $\delta\bar{u}_d^*$ must satisfy the boundary condition $\bar{\mathcal{T}} = \bar{\bar{\sigma}} \cdot \bar{n}$ and linear momentum balance equation. The equilibrium equations are independent of the material considered and simply Newton's law of motion, stating that in the absence of acceleration all of the forces acting on a body must balance. In applying the virtual work principle for deformable bodies, the strain energy of the body is expressed in terms of displacements and then the virtual work principle is used to determine those displacements.

4.2.2 Finite Element Methodology

Finite Element Method (FEM) is a numerical technique for solving a wide range of complex physical phenomena, particularly those exhibiting geometrical and material non-linearities in physical and engineering sciences. Non linearities can arise from different phenomena such as non linearity of the material like plasticity in metallic materials, shocks and impacts at structural interfaces or fluid-elastic forces from fluid-structure interaction. The premise of the methodology is very simple, starting with decomposition of a continuous computational domain into discrete continuous regions or finite elements shown in fig. 4.1. This reduces the continuum problem with infinite number of unknowns to one with a finite number of unknowns at specified points called *nodes*. A finite number of parameters determine the behaviour of finite number of elements that make up the complete continuum domain. An assembly of individual element-level solution is obtained, which is equivalent to the response of the complete continuum domain to a particular set of boundary conditions. The main feature of FEM is that with such piece-wise approximation of physical fields on finite elements, a good precision can still be derived even with simple approximating functions.

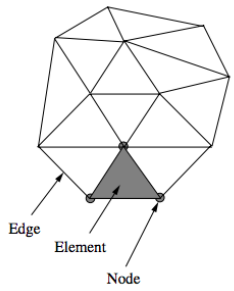

Figure 4.1 – Finite element mesh with elements, edge and nodes (Lewis 2004).

In general the main steps in FEM starts with discretization of the continuum domain into finite elements and selection of appropriate interpolation functions to interpolate the field variable over the element. The next step involves forming the matrix equation for the individual finite element relating the unknown nodal values to other parameters. The local element equations are assembled with defined element connectivity's in order to find the global system of equations for the computational domain. The boundary conditions and loads are applied at this stage and the global equation system is solved for sought field variable like nodal displacement. Subsequently, secondary variables like strains and stresses can be computed from the nodal displacement. The functions employed to represent the nature of the solution within each element are called *interpolation functions* or *shape functions*. They are used to determine the value of the field variable within an element by interpolating the nodal values. Polynomial type functions are used with the degree of the polynomial depending on the number of nodes assigned to the element shown in fig. 4.2. In the present thesis, two-dimensional quadrilateral finite elements with four edges and 8 nodes are used for transient dynamic analysis with quadratic approximation of the field variable within an element.

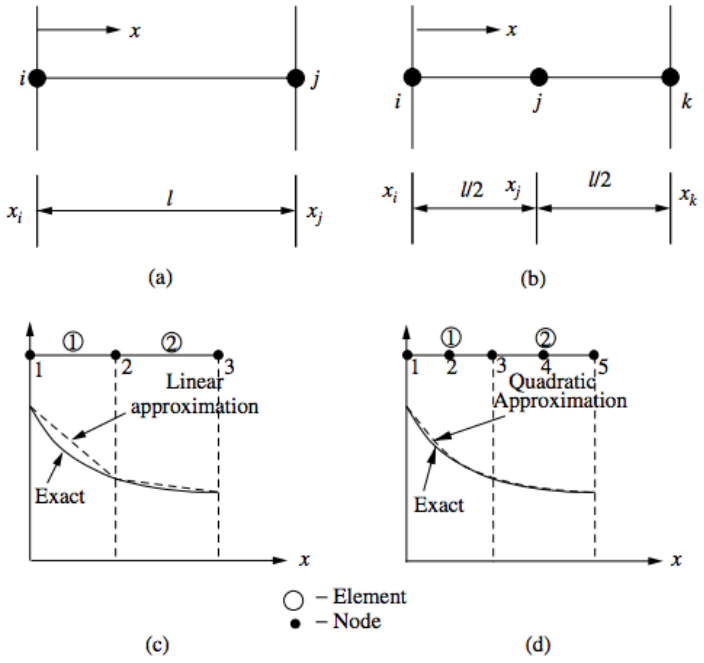

Figure 4.2 – 1D finite element (a) Linear (b) Quadratic (c) Linear approximation (d) Quadratic approximation of field variable (Lewis 2004).

4.3 Material constitutive law

The response of the solid material can be broadly classified into elastic and plastic. An elastic response is of reversible type where a body's original shape and size is recovered when an applied load is removed. The state of stress in the body depends only on the current strain. A linear elastic response is a reversible and non-dissipative type of material response where there is no conversion of mechanical energy to other forms of energy, say heat energy.

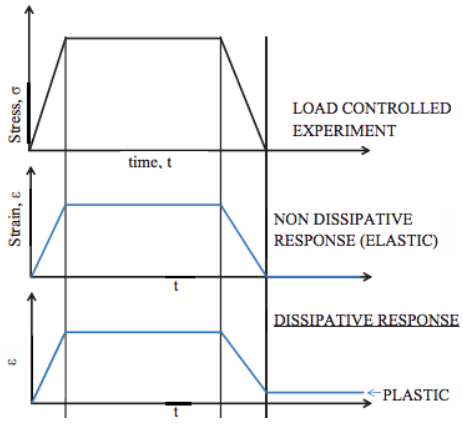

Figure 4.3 – Elastic and plastic response to an applied load (Lewis 2004).

A plastic response is a dissipative type of response in which there is conversion of mechanical energy to other forms of energy. By virtue of the process being dissipative, the stress at an instant would depend on the history of the deformation. When a material deforms plastically, it does not return back to its original shape when unloaded. The process is irreversible and there would be a permanent deformation. A typical representation of an linear elastic and perfectly plastic response is shown in fig. 4.3 under a controlled load experiment.

In this thesis, we considered three materials, namely aluminum alloy (Al-7075),

duplex stainless steel (St A-2205) and nickel-aluminum-bronze (NAB) to estimate the material response. These materials are chosen due to the availability of material characteristics in Roy 2015c for our numerical modelling. The materials are assumed to be homogenous, isotropic and thermal effects are neglected. The stress and strain inside a continuous elastic material can be expressed as :

$$\bar{\bar{\sigma}} = \bar{\bar{\bar{\bar{C}}}} : \bar{\bar{\varepsilon}} \tag{4.9}$$

which is the analogous of Hooke's spring law where $\bar{\bar{\sigma}}$ and $\bar{\bar{\varepsilon}}$ are the second order stress and strain tensor, and $\bar{\bar{\bar{\bar{C}}}}$ is the 4^{th} order stiffness tensor. The strain tensor can be expressed in terms of displacement as $\bar{\bar{\varepsilon}} = \frac{1}{2}(\nabla \bar{u}_d + \nabla(\bar{u}_d)^T)$.

Material	$\rho\,[kg/m^3]$	$E\,[GPa]$	ν	$\sigma_y\,[MPa]$	$K\,[MPa]$	n
Al-7075	2810	71.9	0.33	500	312	0.29
St A-2025	7805	186	0.30	560	917	0.51
NAB	7580	122	0.32	300	1205	0.56

Table 4.1 – Material density, Young's modulus, Poisson's ratio and compressive properties at strain rate 1.0 s^{-1} (Roy 2015c).

The material constitutive law expressed in eq. (4.10) is used where an isotropic elastic-plastic solid deforms according to linear elastic equations when loaded below the yield strength σ_y, but deforms plastically if yield is exceeded. The plastic deformation is governed by the hardening law, known as *Ludwik equation* which expresses the strain hardening as a function of plastic strain ε_p only. The constants K is the strength coefficient, n is the strain hardening exponent, E is the Young's modulus and the total strain can be decomposed into elastic ε_e and plastic ε_p strain.

$$\sigma = \begin{cases} E\varepsilon_e & \text{, if } \sigma < \sigma_y \\ \sigma_y + K\varepsilon_p^n & \text{, if } \sigma > \sigma_y \end{cases} \tag{4.10}$$

Figure 4.4 shows the behaviour for Al-7075 with distinct elastic and plastic regime

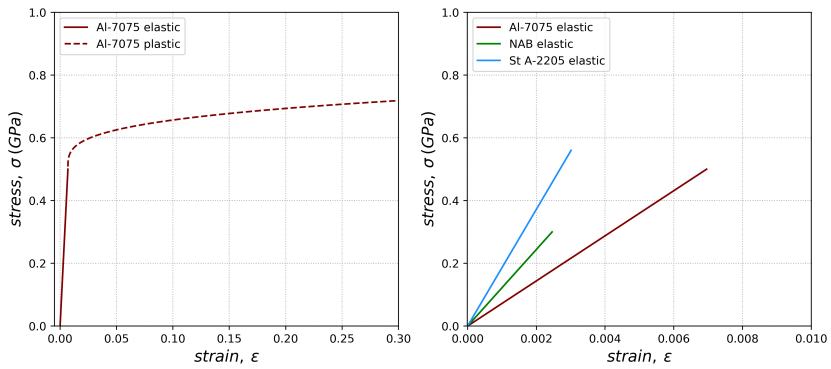

Figure 4.4 – Stress-strain curve at strain rate 1.0 s^{-1}, $(left)$ Al-7075 showing the elastic and plastic regime separated by the yield strength σ_y, $(right)$ elastic regime for Al-7075, St A-2205 and NAB.

governed by the linear and power law between stress and strain respectively, separated by σ_y. The plot also shows the distinct elastic behaviour for all the materials.

Data for material properties and yield strength summarized in table 4.1, are taken from Roy 2015c which were obtained with compression test at strain rate 1.0 s^{-1}. The material behavior for Al-7075, St A-2205 and NAB are shown together in fig. 4.5.

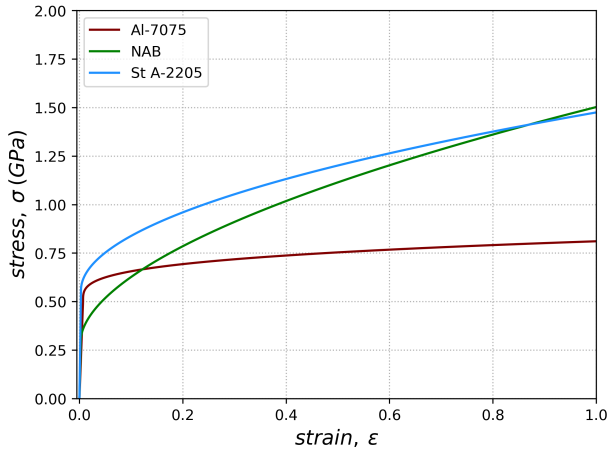

Figure 4.5 – Stress-strain curves for Al-7075, St A-2025 and NAB at strain rate 1.0 s^{-1}.

An important parameter that we will use in our discussion is the von Mises stress σ_{VM} written in eq. (4.11). It is used to determine whether an isotropic and ductile metal will yield when subjected to a complex loading conditions. The von Mises stress σ_{VM} is a scalar computed from the stress tensor and can be compared with the yield strength σ_y of the material which is another scalar. A material is said to starting to yield when $\sigma_{VM} \geq \sigma_y$.

$$\sigma_{VM} = \sqrt{\frac{1}{2}[(\sigma_{xx} - \sigma_{yy})^2 + (\sigma_{yy} - \sigma_{zz})^2 + (\sigma_{zz} - \sigma_{xx})^2 + 6(\sigma_{xy}{}^2 + \sigma_{xz}{}^2 + \sigma_{yz}{}^2)]} \tag{4.11}$$

Another important parameter is the accumulated plastic strain P_{ε_p} which characterizes the changes in the mechanical characteristics of material during the deformation hardening. It can be defined as the measure of the length of the flow trajectory in the plastic strain space written as eq. (4.12).

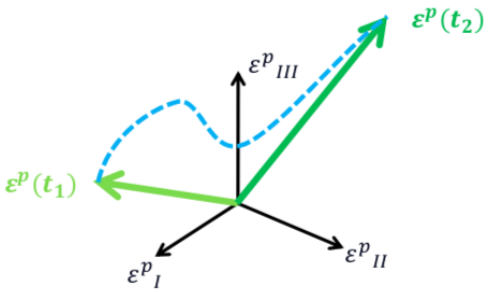

Figure 4.6 – Accumulated plastic strain P_{ε_p} (Di Paola 2017a).

$$P_{\varepsilon_p}(t) = \int_0^t \dot{P}(\tau)d\tau$$
$$\dot{P} = \sqrt{\frac{2}{3}\dot{\bar{\bar{\varepsilon}}}^p : \dot{\bar{\bar{\varepsilon}}}^p} = \sqrt{\frac{2}{3}\dot{\varepsilon}^p_{ij}\dot{\varepsilon}^p_{ij}} \tag{4.12}$$

A further extension could be the implementation of Johnson-Cook (JC) plasticity model given in eq. (4.13) ignoring the thermal softening part, to express the hardening behaviour of solid material with strain rate effect. Although not considered in this thesis, strain rate effect is an important factor and is expected to be very high in cavitation erosion.

$$\sigma = (\sigma_y + K\varepsilon_p^n)\left(1 + C\, ln(\frac{\dot{\varepsilon_p}}{\dot{\varepsilon_0}})\right) \tag{4.13}$$

In eq. (4.13), $\dot{\varepsilon_p}$ is the plastic strain rate and $\dot{\varepsilon_0}$ is the reference strain rate at which σ_y, K, n have been estimated and C is the strain rate sensitivity parameter. At reference strain rate $\dot{\varepsilon_p} = \dot{\varepsilon_0}$, we have $ln\frac{\dot{\varepsilon_p}}{\dot{\varepsilon_0}} = 0$ and a *Ludwik equation* type relationship is obtained where the strain hardening is only a function of plastic strain ε_p.

Strain rate sensitivity reduces the pit depth in erosion damages, resulting in less volume of the material affected by hydrodynamic impact in high strain rate sensitive material in comparison to less strain rate sensitive material. As per Roy 2015c, St A-2205 has the maximum strain rate sensitivity whereas the Al-7075 has the minimum strain rate sensitivity of all the considered materials. It is suggested that a material with higher yield strength as well as higher strain rate sensitivity would offer greater resistance to cavitation erosion.

4.4 Cast3M Methodology

Cast3M is a partial differential equations solver with the finite element method. It is based on an object oriented programming language *Gibiane* and provides a complete package with pre-processing, solver and post-processing capabilities. In cavitation erosion, on one hand, the pressure loading varies over time and on the other hand, the importance of the forces of inertia has to be considered. Therefore, the dynamic response of the solid has to be predicted. The deterministic implicit solver PASAPAS has been used to solve the non-linear dynamic solid mechanics problem in this thesis. Considering a static non-linear problem of small deformation on a domain Ω, the equilibrium equation, constitutive law and small deformation assumption gives:

$$\nabla \cdot \bar{\bar{\sigma}} + \bar{f} = 0 \tag{4.14}$$

$$\bar{\bar{\sigma}} = \bar{\bar{\bar{\bar{C}}}} : \bar{\bar{\varepsilon_e}} = \bar{\bar{\bar{\bar{C}}}} : (\bar{\bar{\varepsilon}} - \bar{\bar{\varepsilon_p}}) \tag{4.15}$$

$$\bar{\bar{\varepsilon}} = \frac{1}{2}(\nabla \bar{u}_d + \nabla(\bar{u}_d)^T) \tag{4.16}$$

The total strain tensor is expressed in terms of elastic and plastic strain:

$$\bar{\bar{\varepsilon}} = \bar{\bar{\varepsilon_e}} + \bar{\bar{\varepsilon_p}} \tag{4.17}$$

The spatial discretization by finite element method provides a system of equations to solve as:

$$\nabla \cdot \bar{\bar{\sigma}} = \bar{F} \tag{4.18}$$

Here $\bar{\bar{\sigma}}$ is the stress in the elements and $\bar{F}$ is the equivalent nodal force vector. Using eq. (4.15), we can express the nodal displacement vector $\bar{U}$ at the nodes of an element taking into account the influence of plasticity as:

$$\bar{\bar{K}}_e \cdot \bar{U} = \bar{F} + \nabla \cdot (\bar{\bar{\bar{\bar{C}}}} : \bar{\bar{\varepsilon}}_p) \tag{4.19}$$

Here $\bar{\bar{K}}_e$ is the elastic stiffness matrix. On introduction of inertial and viscous effect, the dynamic problem can be expressed as:

$$\bar{\bar{M}} \cdot \ddot{\bar{U}} + \bar{\bar{D}} \cdot \dot{\bar{U}} + \nabla \cdot \bar{\bar{\sigma}} = \bar{F} \tag{4.20}$$

where $\dot{\bar{U}}$ and $\ddot{\bar{U}}$ are the nodal velocity and acceleration vectors, $\bar{\bar{M}}$ is the mass matrix and $\bar{\bar{D}}$ is the damping matrix. The eq. (4.20) can be interpreted as the static equilibrium equation with added inertial forces $(-\bar{\bar{M}} \cdot \ddot{\bar{U}})$ and viscous forces $(-\bar{\bar{D}} \cdot \dot{\bar{U}})$. This equation is resolved in Cast3M for the prediction of deformation of solid from the temporal evolution of stresses on cavitation bubble collapse.

The main steps in the PASAPAS procedure for solving a thermo-mechanical problem incrementally in time are: initialization and update of the parameters, loop on the time steps, resolution of thermo-mechanical problem and convergence test, saving of results etc. In PASAPAS architecture, UNPAS procedure is used to resolve mechanical problems and TRANSNON for solving thermal problems. Since we are only interested in the mechanical behaviour, convergence of solution is only validated in the UNPAS procedure and no thermo-mechanical convergence is validated in PASAPAS. Finally, it should be noted that during computations, it is possible to access the computation and introduce time dependent boundary conditions using the procedure PERSO1. The time dependent pressure loads are introduced in the PERSO1 procedure which is used as the boundary condition for the next time step. The PASAPAS procedure used for solving the dynamic mechanical problem in this thesis is shown in fig. 4.7.

The UNPAS procedure for mechanical calculations is based on minimization of residuals at each mechanical step. At the beginning of each UNPAS step, a residual imbalance is computed between the external applied forces F^{ext} and internal forces F^{int}, representing the current state of the solid. The difference between these two forces at each node is called the residual $R_i = F^{ext} - F_i^{int}$. The estimation of displacement at the next time step begins from this residual $\Delta U_{i+1} = \bar{\bar{K}}_e^{-1} R_i$, where $\bar{\bar{K}}_e$ is the elastic stiffness matrix at the beginning of the step. The new stresses $\bar{\bar{\sigma}}_{i+1}$ and strains $\bar{\bar{\varepsilon}}_{i+1}$ are calculated which gives us the updated internal state of the solid F_{i+1}^{int}. The new residual is estimated as $R_{i+1} = F^{ext} - F_{i+1}^{int}$. The procedure then uses a convergence loop to determine the increment of solution that minimizes the residual to the convergence criterion i.e. if $\|R_{i+1}\| \leq PRECISION$. The iteration ends if convergence is reached else the step is repeated with incremental displacement until convergence is reached. Here we have introduced the basic steps for solid mechanics calculations for understanding of our modelling approach. An extensive description of the methodology can be found at Di Paola 2017b and Paquette 2017.

In our 2D computation, we assume a state of plane strain for the solid. The plane strain assumption imposes a strain state at a material particle such that non-zero

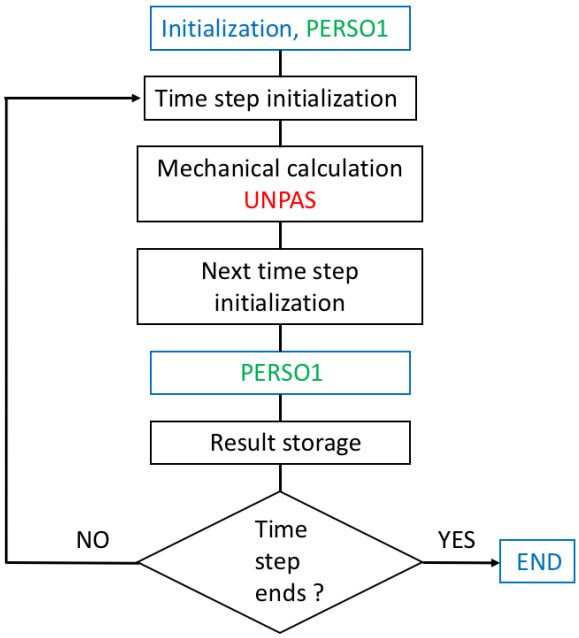

Figure 4.7 – Mechanical calculation with PASAPAS procedure (Di Paola 2017b).

strain components act only in one plane. The x-y plane is the one in which the strains are non-zero and dimension of the solid in the z-direction is much larger than in the x and y directions. The fully three dimensional strain matrix reduces to a two dimensional one as a result since $\varepsilon_{xz} = \varepsilon_{yz} = \varepsilon_{zz} = 0$.

$$\begin{pmatrix} \varepsilon_{xx} & \varepsilon_{xy} & \varepsilon_{xz} \\ \varepsilon_{yx} & \varepsilon_{yy} & \varepsilon_{yz} \\ \varepsilon_{zx} & \varepsilon_{zy} & \varepsilon_{zz} \end{pmatrix} \Rightarrow \begin{pmatrix} \varepsilon_{xx} & \varepsilon_{xy} \\ \varepsilon_{yx} & \varepsilon_{yy} \end{pmatrix} \tag{4.21}$$

4.5 FEM mesh

The computational domain of size $1 \times 2.5\, mm^2$, mesh with 9850 elements and 29065 nodes with the corresponding boundary conditions used for FEM simulation are shown in fig. 4.8. The FSI interface is the boundary on which the pressure loads from cavitation bubble collapse will be applied and is resolved with 801 nodal points. Only one-half of the problem is simulated taking advantage of the symmetry axis. The other two boundaries are equipped with wave absorption characteristics which allows the propagation of elastic waves through the boundary in transient dynamic computations. The FRONABS procedure in Cast3M is used to create absorbing boundaries composed of viscous damping to prevent wave reflection on the edge of the computational mesh. The LYSMER type of boundary absorption is used to absorb all the energy of waves with normal incidence on the boundary. The displacement of FEM nodes at the boundaries equipped with wave absorption is not constrained in the 2D plane i.e. X and Y direction. Therefore, the computational domain represents only a region of interest of a very large solid material. The computational mesh, generated in Cast3M, halves the number of finite elements used in successive layers with increasing distance from the interface, using a mesh

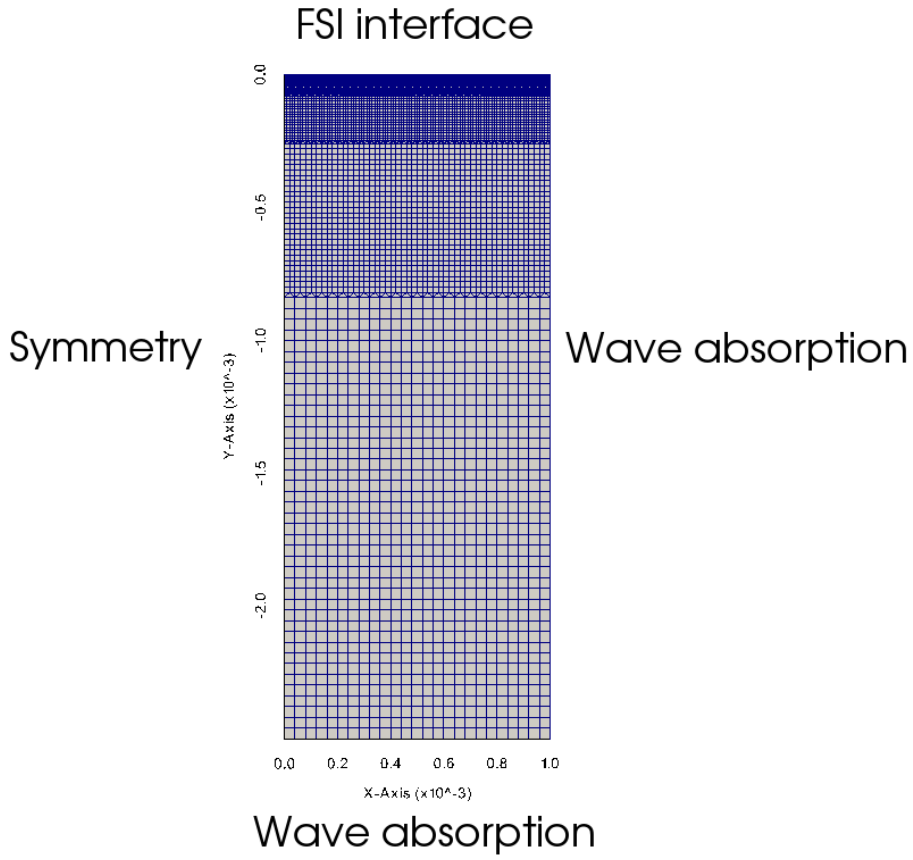

Figure 4.8 – Boundary conditions and mesh used for FEM simulations.

generation methodology devised in the doctoral thesis of Paquette 2017. Such a methodology provides the flexibility to use finer elements near the interface whereas larger element size can be used away from the interface. More information on the FEM mesh is provided in Appendix B.

4.6 Fluid-Structure Interaction

In fluid-structure interaction (FSI) problems, solid structures interact with the surrounding fluid flow. FSI has become increasingly popular as well as sophisticated with advances in computer technology. Broadly classified into *monolithic* and *partitioned* approach, the distinction is based on the mathematical framework for the system of equations for the entire problem. The monolithic approach treats the fluid and solid mechanics in the same mathematical framework of single system of equations and are solved in a unified algorithm. On the other hand, the partitioned approach also known as the staggered approach, used in this thesis, treats the fluid and solid independently with respective numerical algorithms and interfacial conditions are used to exchange information between fluid and solid solutions. Two solvers deal respectively with the fluid and solid mechanics equations and exchange information at the interfaces. The partitioned approach allows for different time steps for the fluid and solid that could be optimized to resolve the different time scales of the two domains. The challenge is, however, to coordinate the algorithms

to achieve accurate and efficient fluid-structure interaction solution with minimal code modification. We present two types of partitioned FSI methodology described below.

4.6.1 One-way Fluid-Structure Interaction

The first one is a simple uncoupled analysis called the *one-way* fluid-structure interaction. The fluid domain is modelled alone by assuming a rigid boundary in place of the solid. To this end, a purely CFD solver is used which computes the pressure distribution $p(\bar{x}, t)$ as a function of space $\bar{x}$ and time t along the fluid solid interface for the entire time duration of interest. Next, the computed pressure $p(\bar{x}, t)$ is used in a separate calculation as boundary condition to load a deformable solid resolved with the CSM solver. This in return gives the time-dependent response of the solid to the applied loads, as represented in fig. 4.9. The bubble collapse

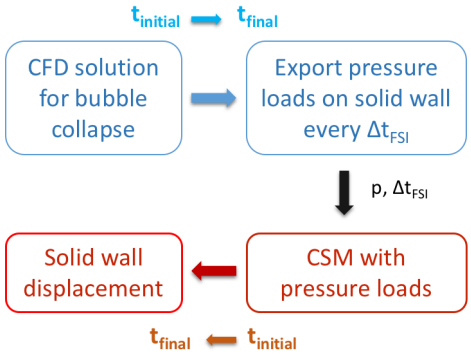

Figure 4.9 – One-way FSI procedure.

dynamics, in this thesis, is solved with the semi-implicit CFD algorithm from initial time $t_{initial}$ to final time t_{final} with the pressure loads on the solid wall extracted at equally spaced time intervals Δt_{FSI}. Let this be referred as CFD step 1. The pressure loads are then used as a time-dependent boundary condition to advance the CSM computation from $t_{initial}$ to t_{final} in CSM step 1. Only one step of CFD and CSM computations are performed and this provides the solid state at the end of the entire simulation as well as during the transients of the bubble collapse.

However, it is obvious that this procedure introduces some approximations as the feedback of solid deformation on the fluid pressure is totally neglected. Therefore, it is possible that under some circumstances, the "true" solid response would be different, nevertheless this provides at least a first-attempt solution of such a complex problem.

4.6.2 Two-way Fluid-Structure Interaction

To introduce the fluid-structure coupling effects in the fluid domain, a two-way coupled analysis is required where the solid wall deformation affects the subsequent fluid dynamics. Two way fluid-structure interaction in a partitioned approach can be further classified into *loosely* and *strongly* coupled. In a loosely coupled algorithm, data exchange on the interface is done only once per time step in a sequentially staggered manner without any convergence loop between fluid and solid solutions.

Such an approach usually suffers from time lag between the fluid and solid solutions. On the other hand, a strongly-coupled partitioned approach typically involves an iterative staggered scheme to ensure convergence between the fluid and solid solutions at each coupling time step. Several fluid and solid computations are performed at every time step, until convergence is obtained between the solutions. Such a scheme increases the complexity of the implementation of FSI as well as the computational cost at each time step.

In our analysis, we implement a *step-wise coupled approach* between the CFD and CSM domain which is an intermediate approach between uncoupled and strongly coupled FSI approach. In our *step-wise coupled approach*, CFD step 1 provides the initial estimates of pressure loads from $t_{initial}$ to t_{final} at every Δt_{FSI} for a rigid boundary which is used to compute the solid wall deformation in CSM step 1. Next the time-dependent solid wall displacement at every Δt_{FSI} is introduced into a new fluid simulation from $t_{initial}$ to t_{final}, denoted by CFD step 2. The pressure loads determined after introducing the FSI coupling effects are introduced next into the CSM step 2. This step-wise iterative loop is repeated until convergence of pressure p and solid wall displacement u_d is established between successive CFD and CSM step shown in fig. 4.10.

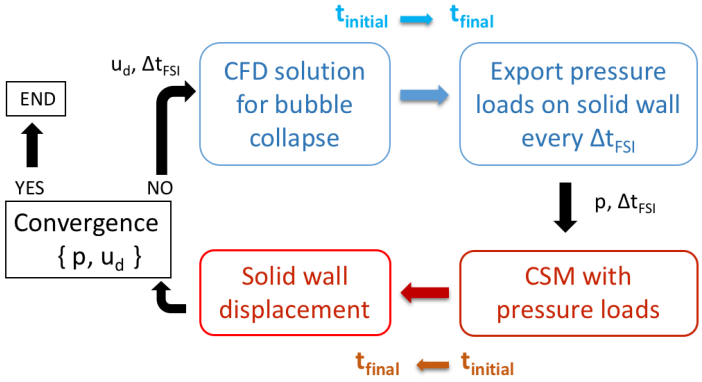

Figure 4.10 – Step-wise two-way FSI procedure.

The continuity between the fluid and solid computational domain is maintained thanks to the flexibility offered by Arbitrary-Lagrangian-Eulerian(ALE) formulation implemented in CLE solver allowing the fluid mesh to deform in response to Lagrangian formulation based solid deformations. If only the pressure acting normal to the solid surface contributes to the surface forces, the fluid and solid equations can be coupled by imposing the following boundary conditions on the interface Γ:

$$\begin{aligned} \bar{\bar{\sigma}} \cdot \bar{n} &= -p\bar{n} \\ u_d^S &= u_d^F \end{aligned} \tag{4.22}$$

Here u_d^F is the ALE displacement field of the fluid, u_d^S is the displacement field of the solid, p is the pressure, $\bar{n}$ is the outward normal vector, $\bar{\bar{\sigma}}$ is the solid stress tensor. These boundary conditions states that the surface forces in the solid interface are in equilibrium with those on the fluid side of Γ. Overall, such coupled FSI algorithm provides a much better approximation of the physical problem compared to an uncoupled approach.

4.7 Summary

In this chapter we introduced the fundamental principles of linear and angular momentum equilibrium applied to a deformable solid along with a brief overview of FEM and Cast3M solver methodology. The material constitutive law governing the behaviour of the considered material, aluminum alloy (Al-7075), duplex stainless steel (St A-2205) and nickel-aluminum-bronze alloy (NAB) along with solid computational domain has been introduced. Finally, the simplified approach for one-way and two-way step-wise fluid structure interaction simulation is presented. Such an FSI approach has been used in this thesis to predict the material response.

Part III

Numerical Results

Chapter 5

Solver Validation

5.1 Introduction

In this chapter, we present validation studies of the numerical solvers. First the proposed changes in the time advancement algorithm of the Compressible Cavitation Solver (CCS) is validated using the shock tube test case with ideal gas in section 5.2. We will discuss the numerical strategies employed to reduce numerical oscillations in our simulations. It is then extended to validate the cavitation modelling with spherical bubble collapse away from solid wall in 2D and 3D and compared with the analytical solution in section 5.3 & 5.4. Finally, the ALE implementation in the Cavitation ALE (CLE) solver is validated against the CCS solver presented in section 5.5.

5.2 Shock-Tube

The fundamental idea of a shock tube consists of a long tube closed at its end and divided into two equal regions by a thin diaphragm shown in fig. 5.1. Each region is filled with a gas of different thermodynamic variables of pressure and density. The region with the highest pressure is called the driven section of the tube whereas the low pressure region is the working section. The fluid is at rest initially and the sudden breakdown of the diaphragm generates a high speed flow which propagates into the working section. In the perspective of this thesis, the interest in studying the shock tube validation test case is threefold. Fundamentally, it offers an interesting framework to introduce some basic notions about nonlinear hyperbolic systems of PDE's. Numerically, this problem constitutes, with its exact solution known, a difficult test case for any numerical method dealing with discontinuous solutions. Finally, it serves as a validation benchmark to compare the developed solver with an existing solver.

Considering the shock tube in fig. 5.1, we define the left part with p_L, ρ_L & u_L as the driven section, whereas the right part is the working section with properties $p_R < p_L$, ρ_R and u_R. The tube is assumed to be filled with an ideal gas having a ratio of specific heat coefficients $\gamma = 1.4$. At time $t = 0$ when the diaphragm is opened, the fluid tends to equalize the pressure in the tube. The gas at high pressure region expands through an expansion wave and flows into the working section. This expansion wave is a continuous process and takes place inside a well-defined region

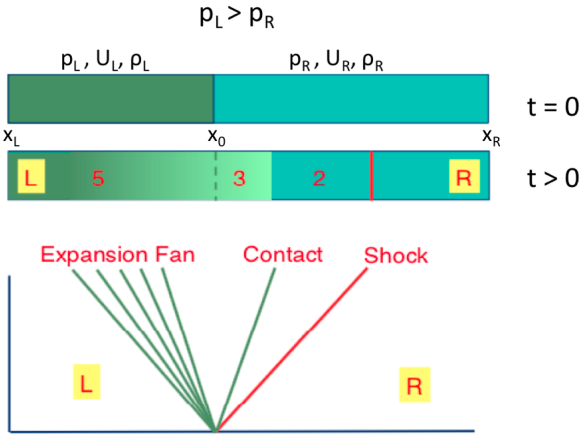

Figure 5.1 – Shock tube test case representation.

$$\begin{bmatrix} p_L \\ \rho_L \\ u_L \end{bmatrix} = \begin{bmatrix} 100000\ Pa \\ 1\ kg/m^3 \\ 0\ m/s \end{bmatrix} \begin{bmatrix} p_R \\ \rho_R \\ u_R \end{bmatrix} = \begin{bmatrix} 10000\ Pa \\ 0.125\ kg/m^3 \\ 0\ m/s \end{bmatrix}$$

Table 5.1 – Initial conditions in the shock tube.

that propagates to the left with its width growing with time. The compression of the low-pressure gas in the working section generates a shock wave propagating to the right of the tube. The expanded gas is separated from the compressed gas by a contact discontinuity which is a fictitious membrane traveling to the right at constant speed. The solution of this problem has been derived analytically for an ideal gas, see Sod 1978 and compared with 1D solution of existing CPS and developed CCS solver for validation.

The initial conditions of the gas in the tube for our 1D test case are summarized in table 5.1. The Euler equations are solved, meaning that there is no fluid viscosity or artificial viscosity considered. The tube boundaries on left and right are at $X_L = 0m$ & $X_R = 1m$ with the initial diaphragm at $X_0 = 0.5m$ at $t = 0ms$. The solutions are obtained with a fourth-order spatial and time integration scheme with $CFL = 0.15$ and $CFL_{acou} = 0.3$ in a $1\ m$ long tube. The time step $\Delta t = 4.3 \times 10^{-8}\ s$ is limited by the CFL_{acou} condition and solutions are compared at final time of $t = 0.5\ ms$. The 1D numerical solutions are compared for two mesh resolutions with 10^3 points ($\Delta x = 1\ mm$) & 10^4 points ($\Delta x = 100\ \mu m$) in the tube.

5.2.1 Implicit Compressible Solver (CPS)

Initially we look into the solution from the CPS solver. As mentioned previously, centered schemes coupled with RK-type time integration schemes produce non-physical spurious oscillations in the solution especially near numerical discontinuities. Artificial viscosity model, although useful, has not been found always sufficient in highly dynamical cases like bubble collapse, where local oscillations develop and grow over time making the simulations unstable. Therefore, filtering of

the solution variables based on volume-weighted averaging with a Gaussian-type smoothing has been employed. Such high order filtering has been found useful in order to stabilize numerical simulations. Figure 5.2 shows the 1D shock tube analytical and numerical solution at $t = 0.5\,ms$ & $\Delta x = 100\,\mu m$ without any filtering. The solution clearly shows spurious oscillations for pressure, density and velocity.

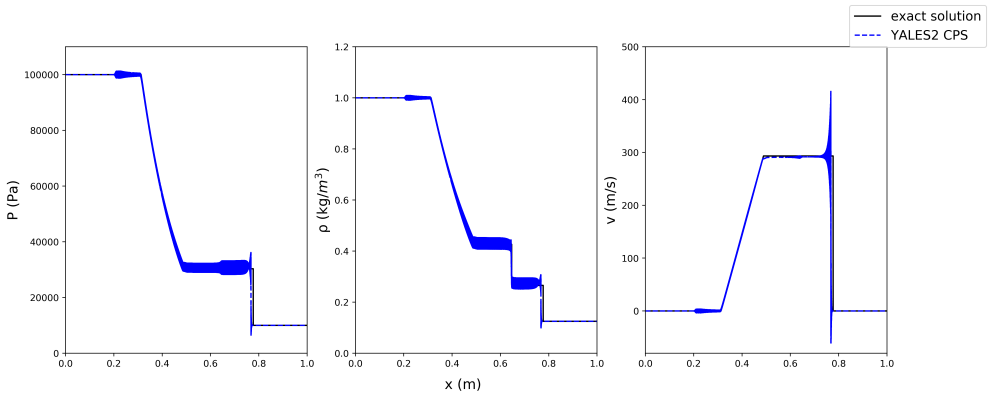

Figure 5.2 – Numerical oscillations from centred difference scheme near discontinuities in CPS solver, without the use of any filtering.

Two different filtering strategies are employed, one filtering of the pressure field, denoted by $FILTER\_PRESSURE$ ($\overline{|\,|}_p$) and another filtering of the density field, denoted by $FILTER\_DENSITY$ ($\overline{|\,|}_\rho$). The $\overline{|\,|}_p$ and $\overline{|\,|}_\rho$ represents the volume weighted Gaussian smoothing of the pressure and density fields respectively. Figure 5.3 shows the effect of pressure filtering $\overline{|\,|}_p$ and density filtering $\overline{|\,|}_\rho$ on the solution for a coarse mesh of $\Delta x = 1\,mm$ in the CPS solver. The pressure filtering $\overline{|\,|}_p$ gives a very close solution to the analytical result whereas density filtering $\overline{|\,|}_\rho$ affects the solution accuracy especially near the discontinuities.

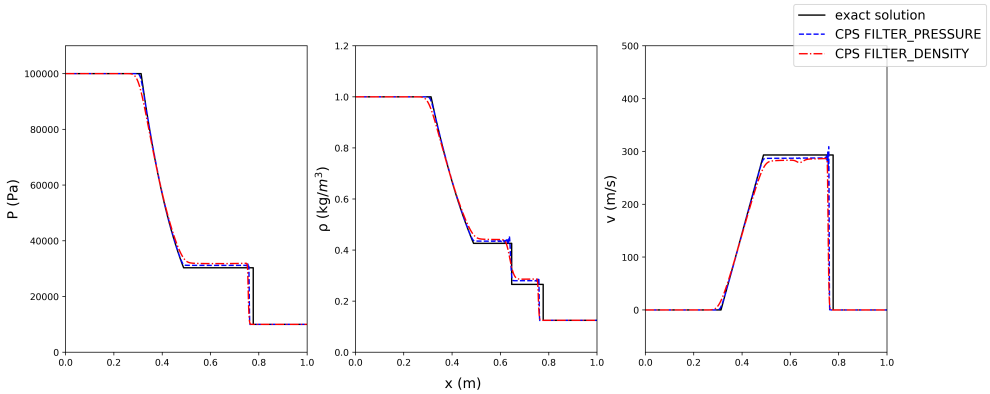

Figure 5.3 – Effect of pressure and density filtering in CPS with coarse mesh $\Delta x = 1\,mm$.

With a finer mesh of $\Delta x = 100\,\mu m$ in fig. 5.4, the pressure filtering $\overline{|\,|}_p$ gives similar results as the coarse mesh solution. However, the density filtering $\overline{|\,|}_\rho$ solution improves with the finer mesh resolution providing results closer to pressure filtering $\overline{|\,|}_p$ near discontinuities. It is important to note that the oscillation in pressure

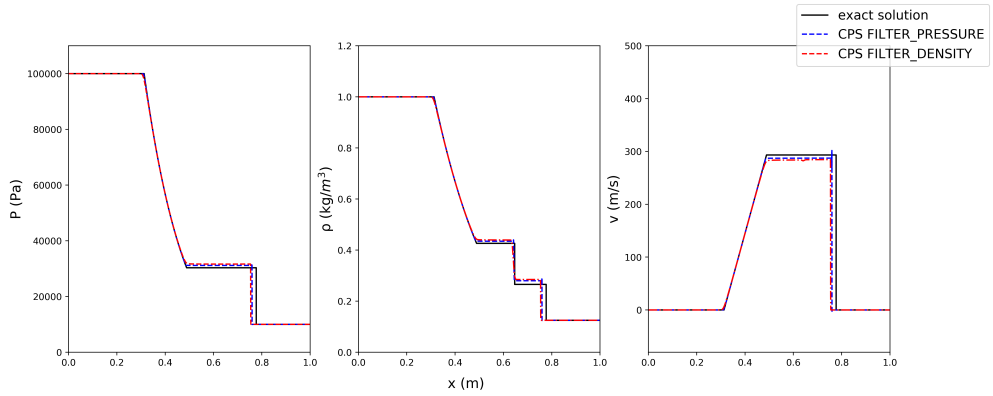

Figure 5.4 – Effect of pressure and density filtering in CPS with fine mesh $\Delta x = 100\,\mu m$.

field is linked to the density oscillations. The density is advected with the continuity equation whereas the pressure is computed from the density field using the equations of state.

5.2.2 Compressible Cavitation Solver (CCS)

In comparison, the CCS solver with the centered scheme also produces spurious oscillations near discontinuities without any filtering, although relatively of smaller amplitudes in comparison to CPS seen in fig. 5.5 due to the proposed changes in the time advancement algorithm of CCS, as discussed in section 3.4. Similar effects of the pressure filtering $\overline{|\,|}_p$ and density filtering $\overline{|\,|}_\rho$ on the coarse mesh and fine mesh solutions are visible in fig. 5.6 & 5.7.

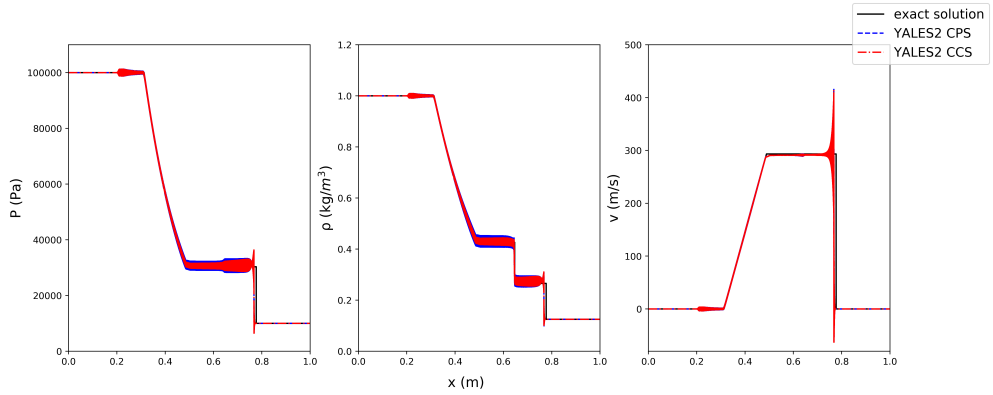

Figure 5.5 – Numerical oscillations from centred difference scheme near discontinuities in CPS and CCS solver.

At this point in the discussion, it is important to state that based on different test cases, the need for both pressure filtering $\overline{|\,|}_p$ and density filtering $\overline{|\,|}_\rho$ has been identified for stable numerical simulations. The pressure filtering $\overline{|\,|}_p$ does not affect the simulation accuracy and can be used throughout the simulation. The density filtering $\overline{|\,|}_\rho$ on the other hand affects the temporal convergence of the solution and its overuse can change the dynamical features of the solution. The solution accuracy

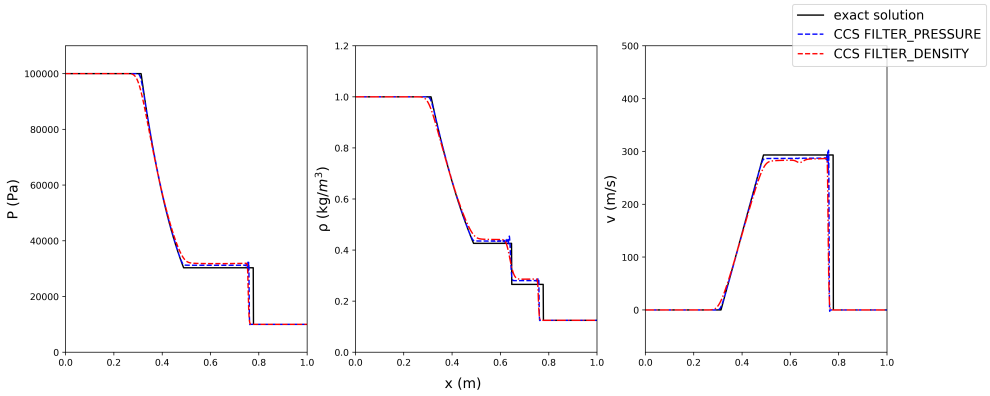

Figure 5.6 – Effect of pressure and density filtering in CCS with coarse mesh $\Delta x = 1\,mm$.

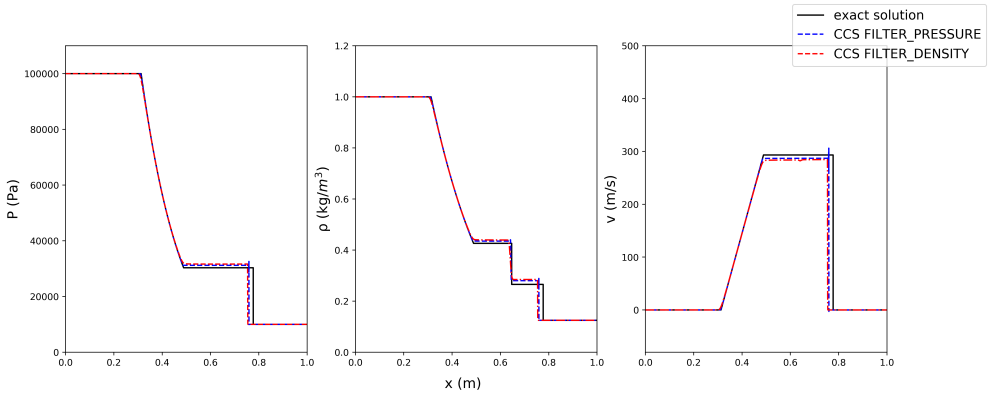

Figure 5.7 – Effect of pressure and density filtering in CCS with fine mesh $\Delta x = 100\,\mu m$.

dependence of density filtering $\overline{|\,|}_{\rho}$ on the mesh resolution has been highlighted with coarse and fine mesh previously. It is difficult to identify such a fine mesh size as it depends on the resolution of the discontinuity, dynamical features and length scale of the problem considered. To circumvent this in CCS, we implemented a strategy to use density filtering $\overline{|\,|}_{\rho}$ in such a way to eliminate its effect on the solution accuracy. The strategy denoted by $ISOLATED\_FILTERING$ ($\overline{|\,|}_{\rho,iso}$) uses the previously described density filtering $\overline{|\,|}_{\rho}$ every specified number of iterations or physical time in a simulation. This in effect allows the local spurious oscillations to grow nominally for certain physical time and then the density filtering $\overline{|\,|}_{\rho}$ is applied.

Figure 5.8 & 5.9 shows the effect of isolated filtering $\overline{|\,|}_{\rho,iso}$ on the results of the 1D shock tube. As can be seen, the isolated filtering $\overline{|\,|}_{\rho,iso}$ of the density field gives a much more accurate representation of the exact solution as compared to the conventional density filtering $\overline{|\,|}_{\rho}$. The effect of the isolated filtering $\overline{|\,|}_{\rho,iso}$ is much more profound for a coarse mesh compared to a fine mesh seen in fig. 5.8. This isolated filtering $\overline{|\,|}_{\rho,iso}$ strategy has been found to have no adverse effect on the solution accuracy although the iteration or physical time frequency of isolated filtering $\overline{|\,|}_{\rho,iso}$ has to be determined depending on the problem in consideration. An isolated filtering $\overline{|\,|}_{\rho,iso}$ based on user-specified number of iterations has been

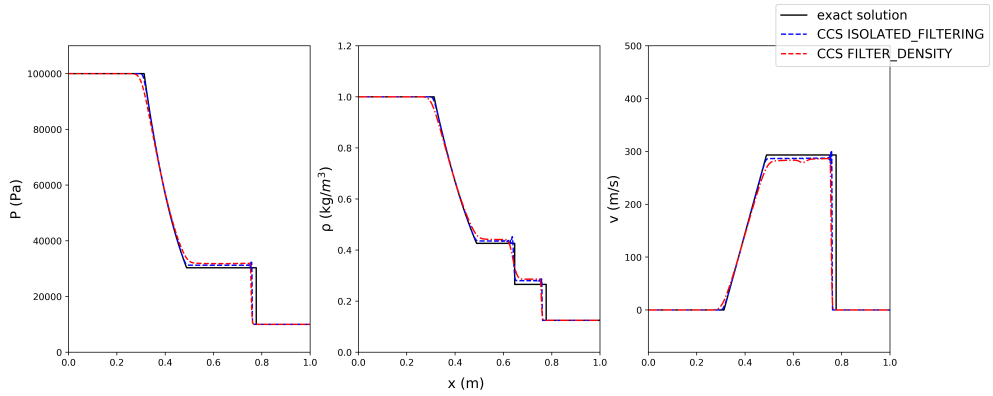

Figure 5.8 – Effect of isolated filtering of density in CCS coarse mesh $\Delta x = 1\,mm$.

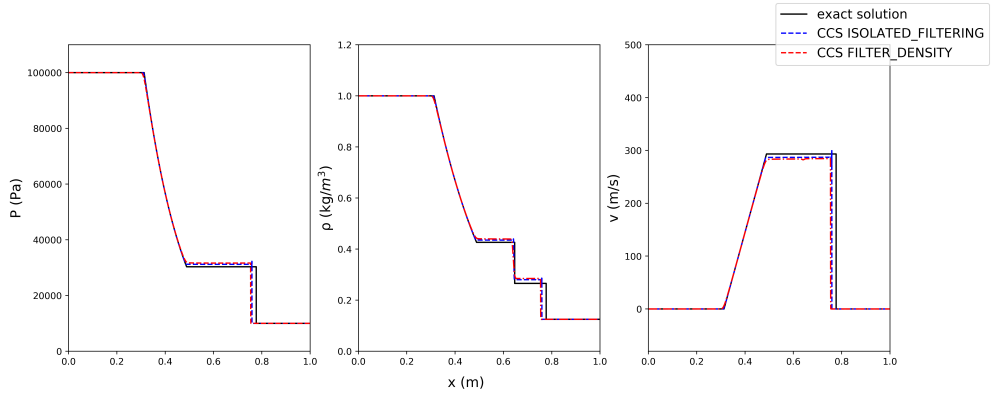

Figure 5.9 – Effect of isolated filtering of density in CCS fine mesh $\Delta x = 100\,\mu m$.

chosen in this thesis, as it ensures less filtering when the time step is large in a CFL controlled simulation. This strategy of isolated filtering $\overline{|\,|}_{\rho,iso}$ after specified number of numerical iterations and pressure filtering $\overline{|\,|}_{p}$ at every iteration has been used for all numerical simulations in this thesis. After validating the CCS solver for a compressible flow, it is validated next for two-phase cavitating flow with 2D (cylindrical) and 3D (spherical) bubble collapse cases.

5.3 2D Rayleigh Collapse

The spherical bubble collapse away from a solid wall is validated in 2D by considering a radial collapse of a circular bubble. The continuity equation in a cylindrical coordinate system (r, θ, z) can be written in terms of radial velocity v in eq. (5.1) with the assumption of axisymmetric motion.

$$\frac{1}{r}\frac{\partial}{\partial r}(rv) = 0 \tag{5.1}$$

The radial velocity can then be expressed as eq. (5.2) on applying the boundary condition $r = R(t)$ on the bubble surface where $\dot{R}$ is the time derivative of bubble radius $R(t)$ with respect to time t.

$$v(r,t) = \frac{\dot{R}R}{r} \tag{5.2}$$

Substituting eq. (5.2) in the Euler equation in eq. (5.3) and integrating between the bubble interface R at vapor pressure p_v and at any position of domain boundary R_b kept at pressure $p(R_b, t)$ gives eq. (5.4),

$$-\frac{1}{\rho}\frac{\partial p}{\partial r} = \frac{\partial v}{\partial t} + v\frac{\partial v}{\partial r} \tag{5.3}$$

$$(R\ddot{R} + \dot{R}^2)ln\frac{R_b}{R} - \frac{\dot{R}^2}{R}\left(1 - \frac{R^2}{R_b^2}\right) = \frac{p_v - p(R_b, t)}{\rho} \tag{5.4}$$

which is the Rayleigh equation in 2D. It is important to note that in eq. (5.4) R_b cannot be taken as infinite to assume a pressure condition applied at infinity due to the logarithmic singularity in the equation. Therefore, a finite cylindrical domain of radius R_b is taken to compute the evolution of a 2D bubble collapsing under the influence of pressure p at the boundary.

The numerical simulation is done with a circular domain in the $x-y$ coordinate, which is assumed to extend infinitely in z direction. We present results for two domain boundaries located at a distance of $R_b = 17R_0$ and $R_b = 25R_0$ from the bubble center where R_0 is the initial bubble radius. A $1/4^{th}$ symmetrical domain is also considered in the case of domain boundary $R_b = 17R_0$, reducing the computational domain by virtue of using two symmetrical planes shown in fig. 5.10. The symmetrical planes are defined using the slip-wall boundary conditions, whose equivalency has been explained in section 3.4.3. Outlet BC with NSCBC is used on the domain external boundaries to impose a pressure condition on the boundaries. The bubble is resolved with uniform mesh resolution of $\Delta x = 5\,\mu m$ in a sub-domain around the bubble, after which a growth ratio has been applied to reduce the computational mesh size in the rest of the domain. Details of the mesh and computational time is given in the Appendix B & C.

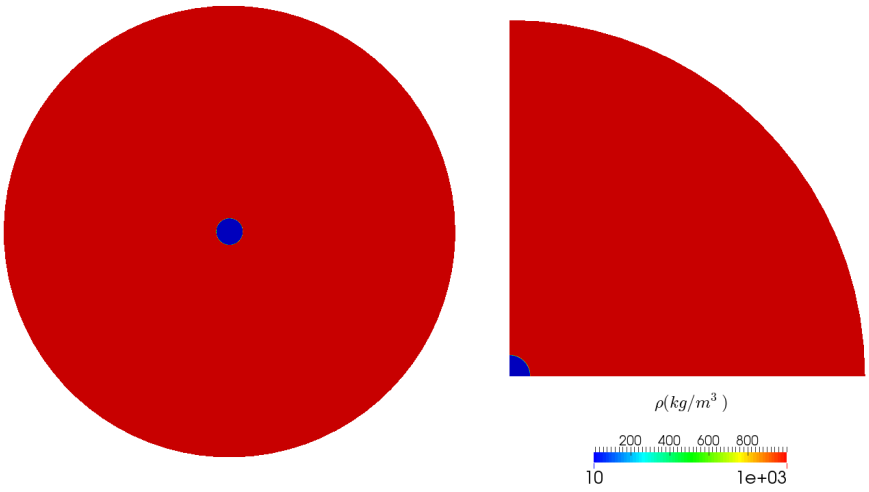

Figure 5.10 – Full vs $1/4^{th}$ domain for 2D Rayleigh collapse.

The numerical results for 2D vapor bubble collapse of $R_0 = 500\,\mu m$, $\alpha = 0.99$ at pressure $p_v = 2194\,Pa$, surrounded by liquid pressure $p = 10\,MPa$, $\alpha = 0$ is compared with the analytical result in fig. 5.11. The analytical result is derived for

a vapor pressure $p_v = 2194\,Pa$ and for two different boundary location $R_b = 17R_0$ and $R_b = 25R_0$ to match the corresponding numerical set up. The bubble is resolved with 100 cells along its radius for both the full and $1/4^{th}$ symmetrical test case. The time step Δt is of the order of $5\,ns$ derived from the limiting $CFL = 0.01$ and $CFL_{acou} = 1$. As mentioned in section 3.4.5, the small value of limiting $CFL = 0.01$ is chosen not only due to the convective flow stability criteria. Such a limiting CFL ensures numerical stability of the time advancement scheme in our cavitation modelling. As seen in fig. 3.5, there is a steep decrease in density at the phase interface in our cavitation model and too big a time step Δt could lead to instability in the numerical simulations. A small limiting CFL ensures stability of the numerical scheme due to considered cavitation model, for which a different stability criteria has not been defined.

The non-dimensionalized temporal evolution of bubble radius R plotted is resolved every $0.05\,\mu s$ except the last three points which are resolved at every $0.25\,\mu s$. The analytical and numerical result in the plot are non-dimensionalized using the initial bubble radius R_0 and collapse time measured from analytical solution, referred in this case as $t_{rayleigh} = 8.75\,\mu s$ for $R_b = 17R_0$ case and $t_{rayleigh} = 9.3\,\mu s$ for $R_b = 25R_0$ case. The numerical results give reasonable agreement with the analytical results, specifically the total duration of the bubble collapse is captured well for the case of $R_b = 17R_0$. There is some deviation in the predicted bubble radius in our numerical simulation compared to analytical result. This is attributed to numerical approximation error in the transported density field, specifically for the curved bubble interface transport in the 2D cartesian mesh. The numerical bubble radius is estimated from the evolving area (since in 2D) with the bubble interface defined at $\alpha = 0.5$ while the vapor volume fraction α is depended on the transported density. For both the cases, the bubble collapse is faster in the numerical case in comparison to the analytical solution, which is due to the difference in the initial pressure evolution in the surrounding liquid. The bubble in the numerical set up is surrounded by uniform liquid pressure of $10\,MPa$ from the bubble interface to the domain boundary. The analytical Rayleigh solution assumes a bubble in equilibrium with surrounding liquid pressure kept close to vapor pressure p_v while the domain boundaries are at higher pressure $p(R_b, t)$.

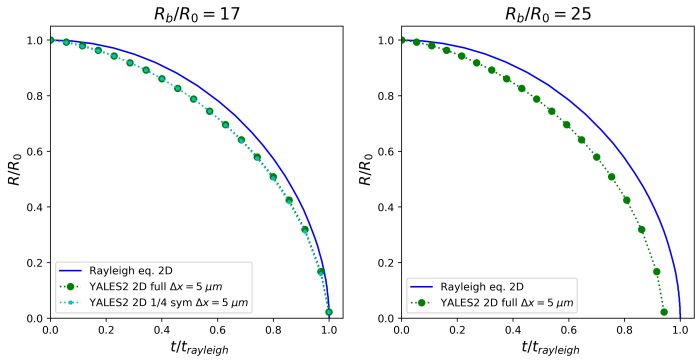

Figure 5.11 – 2D Rayleigh collapse comparison for $R_b = 17R_0$ ($t_{rayleigh} = 8.75\,\mu s$) & $R_b = 25R_0$ ($t_{rayleigh} = 9.3\,\mu s$). Initial bubble radius $R_0 = 500\,\mu m$.

5.4 3D Rayleigh-Plesset Validation

As already mentioned in Chapter 1, the spherical bubble collapse away from the wall has been studied theoretically by many researchers. The 3D Rayleigh-Plesset model introduced in eq. (1.2) governing the growth and collapse dynamics of a spherical bubble is presented here again in eq. (5.5). The derivation of the equation can be found in Franc 2006.

$$\rho\left[R\ddot{R}+\frac{3}{2}\dot{R}^2\right]=p_v-p_\infty+p_{g0}\left(\frac{R_0}{R}\right)^{3\gamma_g}-\frac{2S}{R}-4\mu\frac{\dot{R}}{R} \tag{5.5}$$

A simplified analytical model considering the liquid as incompressible, no liquid viscosity, absence of gravity, non-condensable gas content and surface tension can be written as eq. (5.6).

$$(R\ddot{R}+\frac{3}{2}\dot{R}^2)=\frac{p_v-p_\infty(t)}{\rho} \tag{5.6}$$

Numerically, a vapor bubble of $R_0 = 500\mu m$ initially is considered at $t = 0$ which

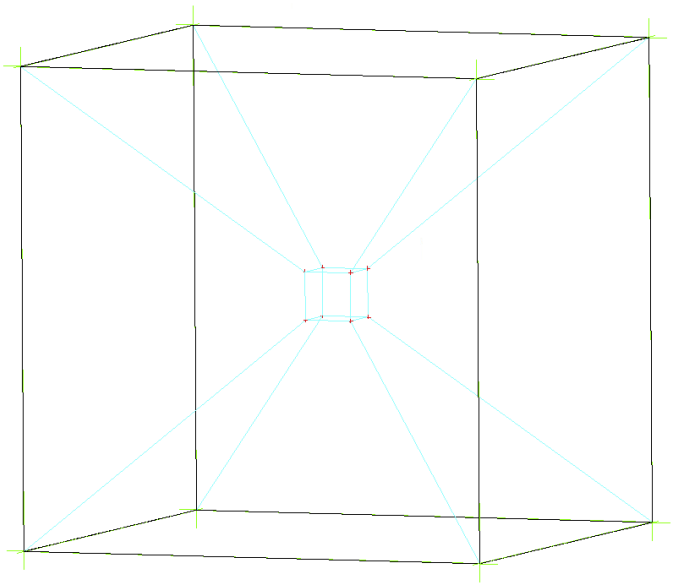

Figure 5.12 – Full computational domain for 3D Rayleigh-Plesset comparison.

will start to collapse when the surrounding liquid is initialized with pressure $p_\infty > p_v$ while p_∞ is held constant at domain boundaries. Theoretically from eq. (5.6) the temporal evolution of the bubble radius R, where $\dot{R}$ is the interface velocity and $\ddot{R}$ is the acceleration of the bubble surface, can be compared with the numerical solution. The theoretical collapse time of the spherical bubble is known as the Rayleigh time, $t_{rayleigh}$.

$$t_{rayleigh}\cong 0.915R_0\sqrt{\frac{\rho}{p_\infty-p_v}} \tag{5.7}$$

A cubic computational domain shown in fig. 5.12 is used for the 3D comparison where the numerical boundaries are located 10 radius distance ($10R_0$) away from the bubble center in all dimensions. A $1/8^{th}$ symmetrical domain shown in fig. 5.13 with symmetrical planes along $x-y-z$ planes is also used for comparison using the slip wall BC, which reduces the computational domain size and cost compared to a

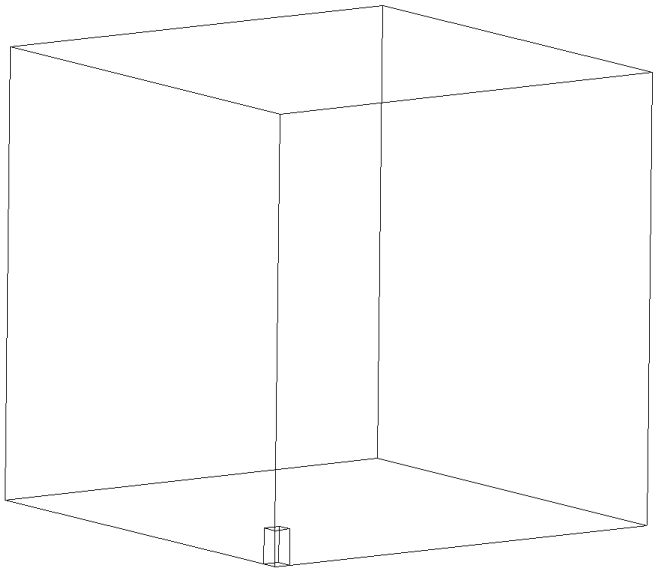

Figure 5.13 – $1/8^{th}$ symmetric computational domain for 3D Rayleigh-Plesset comparison.

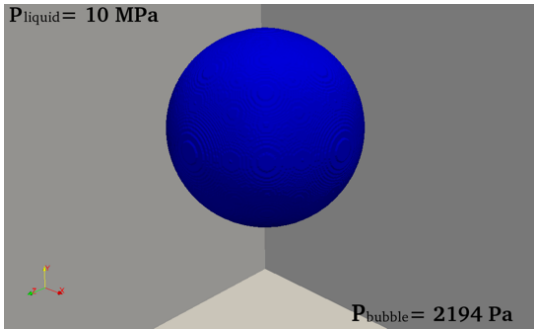

Figure 5.14 – Vapor bubble iso-surface of $\alpha = 0.5$, $R_0 = 500\,\mu m$, $p_\infty = 10\,MPa$.

full domain simulation. The bubble is spatially resolved with 100 cells in the initial bubble radius R_0, whereas the external numerical boundaries are treated as Outlet with NSCBC condition to impose constant pressure. The bubble interface is defined by $\alpha = 0.5$ shown in fig. 5.14 and the vapor volume fraction varies from $\alpha = 0$ in the pure liquid to $\alpha = 0.99$ inside the bubble. The vapor bubble is initialized with $p_v = 2194\,Pa$ whereas the ambient liquid pressure is at $10\,MPa$. The time step for the resolved problem is based on $CFL = 0.01$ and $CFL_{acou} = 1$ condition and the total simulated collapse is completed within the $t_{rayleigh} = 4.53\,\mu s$.

The comparison of the numerical bubble collapse by the compressible cavitation solver and theoretical Rayleigh-Plesset collapse is shown in fig. 5.15. The plot shows the evolution of the bubble radius with respect to time, both normalized by initial bubble radius R_0 and $t_{rayleigh}$ respectively. The solid line is the solution obtained from Rayleigh-Plesset analytical equation with $p_v = 2194\,Pa$, $p_\infty = 10\,MPa$ and the dots represent the numerical simulation results. A reasonably good agreement between the results is obtained overall. The numerical bubble collapses a little faster than the analytical solution, although the discrepancy in collapse time decreases with $1/8^{th}$ symmetrical domain. The discrepancy in the results could be attributed to

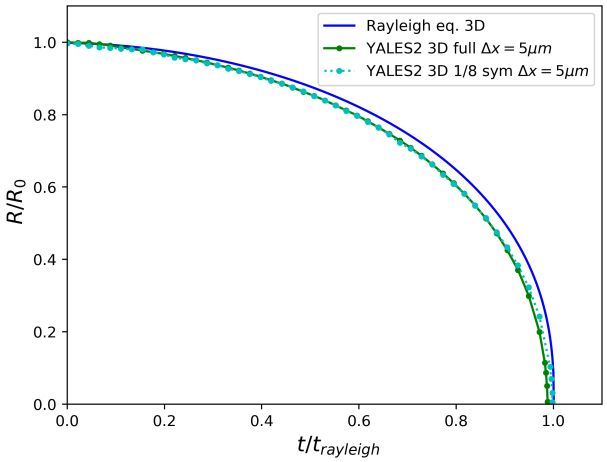

Figure 5.15 – 3D Rayleigh Plesset validation $R_0 = 500\,\mu m$, $t_{rayleigh} = 4.53\,\mu s$.

the decrease in spatial resolution of the bubble volume towards the end of collapse and resolution of curved bubble interface in a 3D cartesian grid using a single fluid cavitation model.The overall agreement in the presented results demonstrates the ability of the developed numerical solver to predict the dynamics of a single bubble collapse effectively.

5.5 ALE Validation

The Cavitation ALE (CLE) solver developed as an extension of the CCS solver with ALE mesh movement capabilities is validated next. A simple 2D test case is devised with a vapor bubble of $R_0 = 100\,\mu m$ in the center of a square domain of dimension $2 \times 2\,mm^2$. The computational domain is discretized with a cartesian mesh of 800×800 cells. The bubble is initialized with a vapor volume fraction $\alpha = 0.99$, $p_v = 2194\,Pa$ surrounded by a uniform liquid pressure of $100\,MPa$. The external boundaries of the square domain are treated as Outlet with NSCBC conditions in order to impose constant pressure $p = 100\,MPa$.

Two simulations are compared for validation, one stationary mesh case for a fixed domain in space where the bubble collapse is numerically solved with the CCS solver. Another moving mesh case, where the computational domain is moving along the positive x-direction with a constant imposed mesh velocity of $250\,m/s$ shown in fig. 5.16. The moving mesh simulation with the CLE solver aims to demonstrate the background moving mesh has no effect on the dynamical evolution of the bubble.

Both the simulations are resolved with $CFL = 0.05$ and $CFL_{acou} = 1$ for a total physical time of $500\,ns$. The computational domain in the moving mesh case moves a total distance of $0.125\,mm$ in the positive x-direction. The mesh resolution in both the computational domain is $\Delta x = 2.5\,\mu m$, which gives a time step $\Delta t \approx 0.1\,ns$ in the stationary case whereas $\Delta t \approx 0.01\,ns$ in the moving mesh case. Figure 5.16 & 5.17 show the temporal evolution of the density field and the spatial position of domain for the two cases considered at different physical times. The bubble in the moving mesh stays in the expected physical space, collapsing under the influence of surrounding liquid pressure while the computational mesh moves in the background.

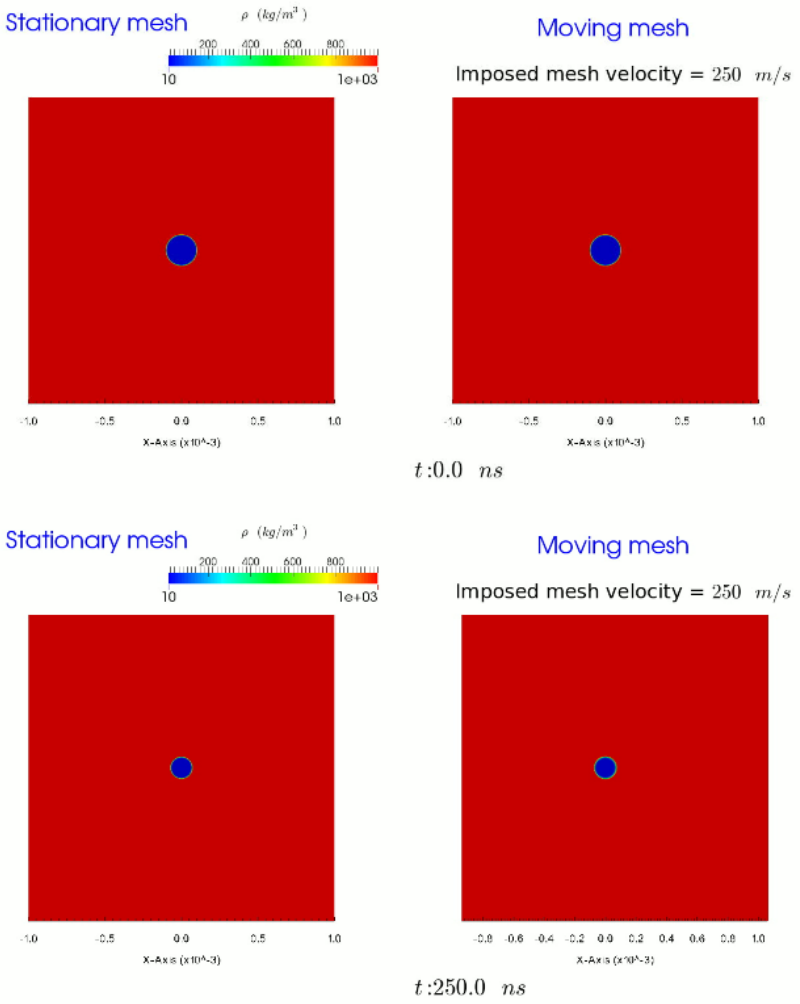

Figure 5.16 – Temporal evolution of 2D bubble collapse $R_{max} = 100\ \mu m$, $p_\infty = 100\ MPa, t = 0\ \&\ 250 ns$ - stationary vs moving domain.

A non-dimensionalized temporal evolution of the bubble radius is plotted in fig. 5.18 for the stationary and moving domains. The bubble radius for both cases gave very good agreement for most part of the simulation except towards the end of the collapse. In the final stages of collapse, the resolution for the bubble volume decreases as the bubble volume shrinks and computational cells resolving the bubble radius decreases. On top of it, we imposed a very high mesh velocity in the domain for our test case which explains the deviations in the final stages. For the bubble collapse FSI problem of interest, only a very small region of the computational mesh near the fluid-solid interface would only encounter relatively high mesh velocity during wall deformation. The test case with such high mesh velocity demonstrates the capability of CLE solver to resolve the flow dynamics with high velocity of moving mesh with relative accuracy and without affecting the underlying fluid dynamics.

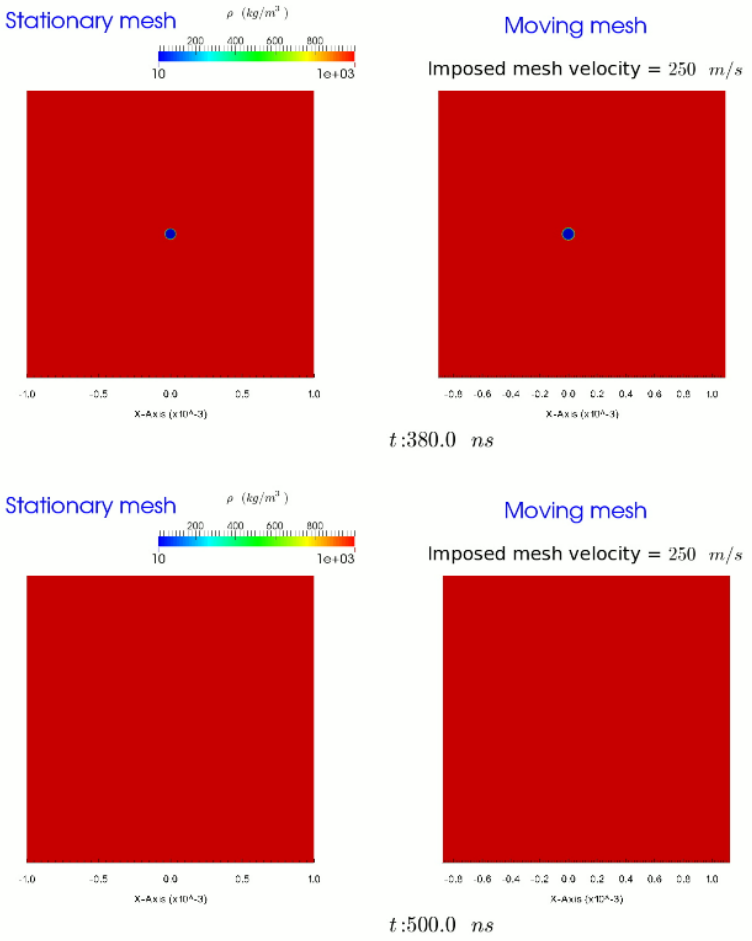

Figure 5.17 – Temporal evolution of 2D bubble collapse $R_{max} = 100\,\mu m$, $p_\infty = 100\,MPa, t = 380\,\&\,500ns$ - stationary vs moving domain.

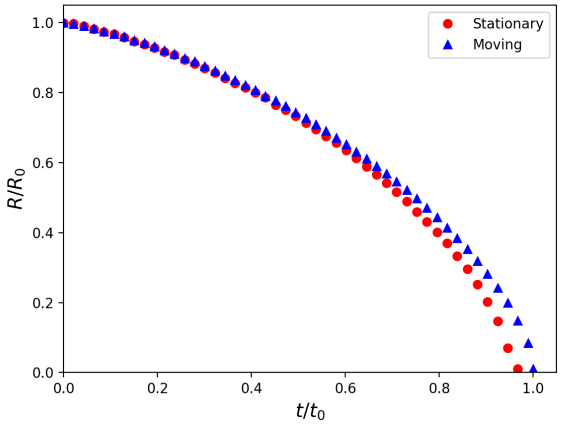

Figure 5.18 – Radius evolution during 2D bubble collapse $R_{max} = 100\,\mu m$, $p_\infty = 100\,MPa$ - stationary vs moving domain.

5.6 Summary

The fluid solver CCS developed for cavitation is validated for compressible flows with the 1D shock tube test case and compared with the existing CPS solver. The implementation and accuracy of high order filtering technique has been discussed for resolving the highly dynamical cases of bubble collapse near solid boundaries. The CCS solver is validated for cavitation studies with the 2D Rayleigh and 3D Rayleigh-Plesset analytical model. The CLE solver is then used to simulate a 2D bubble collapse in a moving domain and results are validated against a bubble collapse in a stationary domain with the CCS solver. The solid mechanics solver Cast3M and methodology used for predicting material response has been validated in the doctoral thesis of Paquette 2017 and hence not presented here.

Chapter 6

Bubble Collapse

6.1 Introduction

In this chapter, the dynamics of bubbles collapsing near solid walls are presented. The bubble collapses are non-spherical due to the presence of the wall. The dynamics for collapsing vapor bubbles are investigated for two different scenarios: liquid pressure-induced collapse and a shock-induced collapse. Comparisons on damage caused by collapsing bubbles driven by these different mechanisms has been a topic of interest, for example see Johnsen 2009. A liquid pressure-induced collapse refers to bubble collapse driven by ratio between the pressure of the water and that of bubble which is assumed at approximately vapor pressure. A shock-induced collapse refers to vapor bubble collapse induced by a shock wave propagating over the bubble. For both these scenarios, planar 2D bubble collapses at different distances from a planar solid wall are presented first. The shock-induced bubble collapse is also extended to three-dimensions followed by a demonstration of a 3D bubble cloud simulation. In all numerical simulations, the evolution of bubble shape, effect of liquid jet, shock wave propagation upon collapse and wall pressure are quantified and reported.

6.2 Liquid Pressure-Induced Collapse

We begin our investigation of the collapse of a vapor bubble near a solid wall with the computational domain shown in fig. 6.1, which will be referred from here on as domain $40R_0$. The initial vapor bubble radius is $R_0 = 500\ \mu m$ and we take advantage of symmetries by simulating only one-half of the 2D bubble. The outlet boundaries are located at $40R_0$ and are equipped with NSCBC conditions for wave treatment. The bubble is initially resolved with 100 computational cells giving $\Delta x = \Delta y = 5\ \mu m$ and grid stretching is applied on the far field of the domain, shown in Appendix B. The test case setup used is similar to one used by Lauer 2012 for numerical simulation of vapor bubble collapse of radius $R_0 = 400\ \mu m$, with 100 computational cells in the bubble radius and domain boundaries at $25R_0$.

Initially both fluids are at rest:

$$\begin{aligned} &vapor:\ \rho = 10\ kg/m^3,\ p = 2194\ Pa, \\ &water:\ \rho = 1038.3\ kg/m^3,\ p = 100\ MPa. \end{aligned} \tag{6.1}$$

where the corresponding pressures are determined from the specified densities using the equations of state in section 3.4.5. Most experimental studies on bubble collapse like Philipp 1998 or our experimental setup in Chapter 2 consider laser generated bubbles in glass cuvette at atmospheric conditions. On the other hand, higher ambient liquid pressure is relevant for industrial applications like liquid fuel injectors (operating pressure levels up to 250 MPa as reported in Lauer 2012) or even high-pressure pumps where the bubbles are collapsing under very high operating liquid pressure. Therefore, we assume the vapor density of 10 kg/m^3 which gives a corresponding pressure of 2194 Pa very close to the liquid saturation pressure $p_{sat} = 2340\,Pa$ whereas the ambient liquid pressure is assumed to be at 100 MPa.

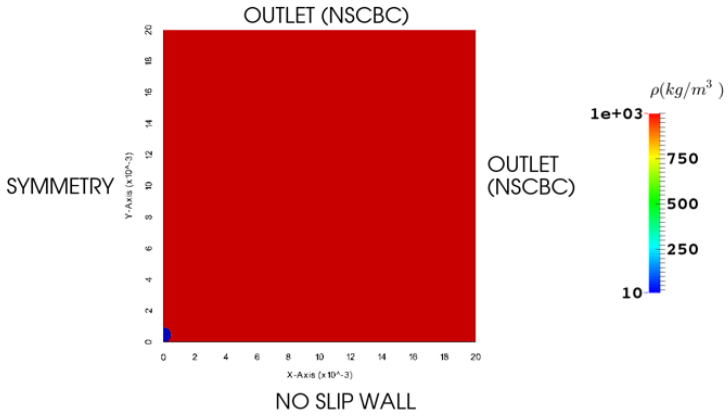

Figure 6.1 – Computational domain for 2D bubble collapse, domain boundary $40R_0$, domain size $= 20 \times 20\,mm^2$.

To quantify the effects of liquid jet and bubble collapse on resulting wall pressure for detached and attached bubbles, different wall positions are considered with respect to initial bubble radius R_0. As mentioned previously in Chapter 2, for non spherical bubble shapes like attached bubbles which grow and collapse being very close or in contact with the solid wall, the equivalent maximum radius R_{max} is relevant. Here R_{max} is the radius of a perfectly spherical bubble that would have the same volume as the non-spherical bubble. For an attached bubble, the solid wall cuts the bubble at the lower hemisphere resulting in decreased bubble volume V_{max}, which gives different equivalent radius R_{max} at different stand-off distances γ. On the other hand, a detached bubble grows nearly spherical due to increased distance from the wall and its volume V_0 is not effected by the position of the wall. To simply highlight the order of decrease in R_{max} and V_{max} for 3D bubbles in our numerical modelling with decreasing γ, we list them in table 6.1. Similarly in 2D, the order of decrease in bubble surface area is more relevant which are summarized in table 6.2.

The vapor bubbles initialization in 2D at different positions with respect to the solid wall are shown in fig. 6.2 for different stand-off distances $\gamma = 0.5, 0.8, 0.9, 1.4$. Data are mirrored about the Y-axis for visualization and the solid wall is located at the bottom of the frames. The solid wall is rigid i.e. has infinite impedance from which all waves are completely reflected. The numerical parameters for the fluid simulations are detailed next. The simulations are carried out with the semi-implicit CLE solver with a limiting $CFL = 0.01$ and $CFL_{acou} = 0.5$ giving a time-step Δt

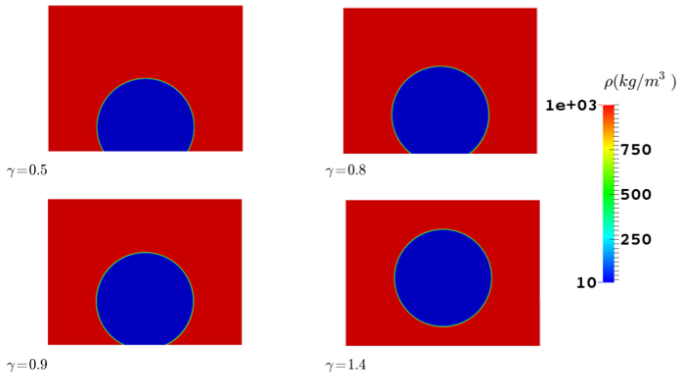

Figure 6.2 – Bubble position for different stand-off $\gamma = 0.5$, 0.8, 0.9, 1.4, solid wall at the bottom of the frame.

γ	$R_{max}(\mu m)$	V_{max}/V_0
1.4	500	1
0.9	498	0.99
0.8	495	0.97
0.5	472	0.84

Table 6.1 – Equivalent radius R_{max} and volume V_{max} for 3D bubbles, $V_0 = 0.5236\, mm^3$ is the volume of a spherical bubble of $R_0 = 500\, \mu m$.

γ	$R_{max}(\mu m)$	A_{max}/A_0
1.4	500	1
0.9	495	0.98
0.8	487	0.95
0.5	449	0.8

Table 6.2 – Equivalent radius R_{max} and area A_{max} for 2D bubbles, $A_0 = 0.785\, mm^2$ is the area of a 2D bubble of $R_0 = 500\, \mu m$.

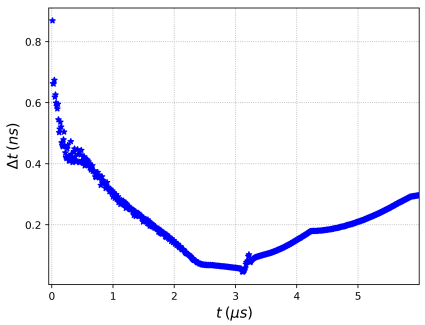

Figure 6.3 – Time step Δt evolution for 2D bubble collapse computation,$\gamma = 0.9$, domain $40R_0$.

smaller than 1 ns for the entire simulation shown in fig. 6.3. It has been already discussed that the small value of limiting CFL is to ensure numerical stability of the time advancement scheme in our cavitation modelling where the fluid density decreases steeply at the phase interface. The smallest Δt of about 0.05 ns is during the most dynamical part of bubble collapse, when the liquid jet velocity is very high and multiple shock waves propagate in the domain. The isentropic cavitation model for evolution of pressure, speed of sound and dynamic viscosity detailed in section 3.4.5 is used to model the two-phase flow. A 4^{th} order artificial viscosity model described in section 3.4.4 with a artificial viscosity constant of 0.1 is used, along with the $ISOLATED\_FILTERING$ ($\overline{|\ |}_{\rho,iso}$), described in section 5.2.2, every 40 iteration step and pressure smoothing by $FILTER\_PRESSURE$ ($\overline{|\ |}_{p}$), described in section 5.2.1, at every iteration. It is important to mention again that the smoothing and filtering steps are needed for solution stability and have been extensively tested to have little impact on the solution. Details about the computational time are given in Appendix C.

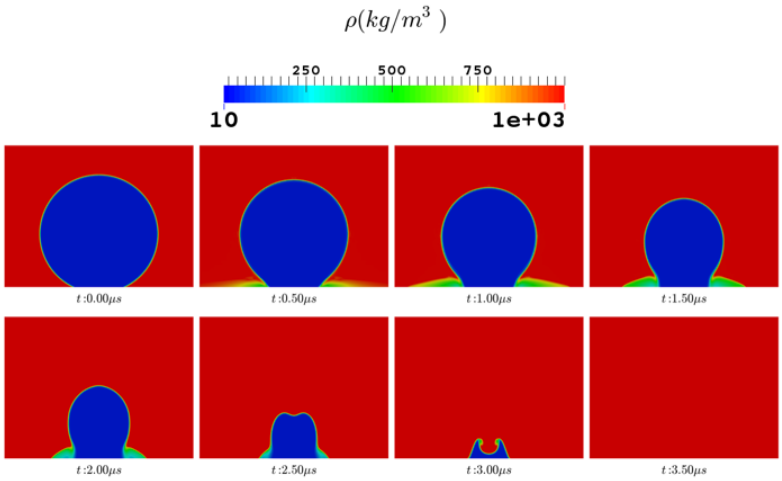

Figure 6.4 – Temporal evolution of density field during liquid pressure-induced attached bubble collapse near solid wall, $\gamma = 0.9$, $R_{max} = 495\,\mu m$, $p = 100\,MPa$, case $P0.9$, frame size = $1.5 \times 1.5\,mm^2$.

The temporal evolution of density field during the collapse of a vapor bubble at $\gamma = 0.9$, $R_{max} = 495\ \mu m$ is shown in fig. 6.4. The contour presents a zoomed in view of the bubble and not the entire computational domain. Similar to our analysis in Chapter 2, the bubble surface close the solid wall will be referred as bubble lower surface and bubble surface opposite to the solid wall be referred as bubble upper surface. The vapor bubble starts to shrink under the influence of ambient liquid pressure and in the final stages of collapse, a liquid jet is formed piercing the bubble from the bubble upper surface. The bubble interface remains well defined during such complex collapse phase. The liquid jet impacts the solid wall after a physical time of 3 μs and the 2 remaining bubbles (corresponding to a bubble torus in 3D) subsequently collapses on the solid wall. There is an appearance of secondary cavitation seen at $t = 0.5\,\mu s$ in the region where the bubble interface is attached to the solid wall. This is primarily due to the barotropic cavitation model, that needs to be initialized with a pressure jump across the bubble interface and thus, initiates an expansion wave that travels from the interface into the water when

the numerical simulation begins similar to the shock tube test case in section 5.2. Upon interaction of expansion wave with the wall, the water pressure in this region decreases as compared to the rest of the domain. This generates the secondary cavitation region and changes the contact angle of the bubble interface with the wall. Similar observation has been made in the literature, for example see Lauer 2012. This region decreases as the bubble collapse progresses in time and disappears during the most dynamical stages seen at $t = 3\mu s$ where the liquid jet is approaching the solid wall.

To quantify the wall pressure and relate it to the bubble dynamics, we will look into the temporal evolution of pressure in fig. 6.6. The plot shows two curves, one is the evolution of pressure p_{F00} on the wall at the axis of symmetry, denoted by a point $F00$ in fig. 6.5. The second curve corresponds to the temporal evolution of maximum pressure on the solid wall, denoted by $p_{max-wall}$. It should be noted that physical position of p_{F00} is fixed which is not the case for $p_{max-wall}$. The other point in fig. 6.5 is $F10$ located on the solid wall at a distance of 1 mm from the axis of symmetry. Before

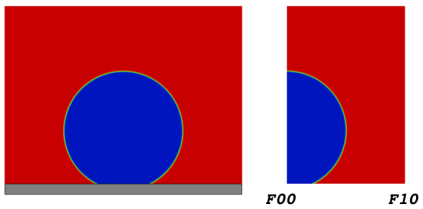

Figure 6.5 – Location of probe points on the solid wall- points $F00(x, y) = (0, 0)$ and $F10(x, y) = (0.001, 0)$.

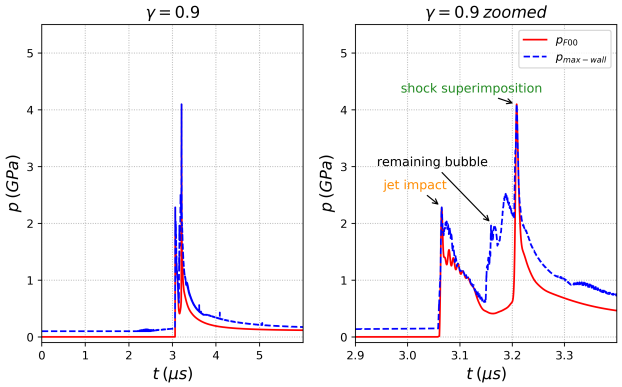

Figure 6.6 – Temporal evolution of pressure at point $F00$ and maximum pressure $p_{max-wall}$, $\gamma = 0.9$, case $P0.9$, $(left)$ entire simulation time, $(right)$ zoomed on the dynamical pressure peaks.

discussing the pressure peaks observed in fig. 6.6, it is worth mentioning that in the most dynamical region of the bubble collapse between time $t = 3\,\mu s$ and $t = 3.5\,\mu s$, the pressure peaks are located between point $F00$ and $F10$, in the 1 mm length of solid wall from the symmetry axis seen in fig. 6.7. For convenience later on, we will refer to the test case of vapor bubble at $\gamma = 0.9$ collapsing under the influence of 100 MPa ambient water pressure as case $P0.9$.

The pressure seen in fig. 6.6 is explained with the contours of numerical Schlieren ($\nabla\rho$), pressure and velocity presented in fig. 6.8 and fig. 6.9. There are three major dynamical events coinciding with the pressure peaks observed in fig. 6.6. The first pressure peak corresponds to liquid jet impact on the solid wall where the maximum velocity of the liquid jet is 900 m/s. The pressure load induced on the wall from

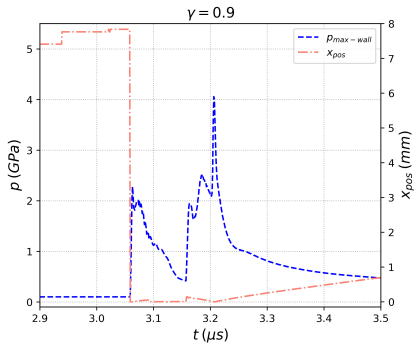

Figure 6.7 – Maximum pressure at the solid wall $p_{max-wall}$ and its location on the wall as a function of distance from the axis of symmetry i.e point $F00$, $\gamma = 0.9$, case $P0.9$.

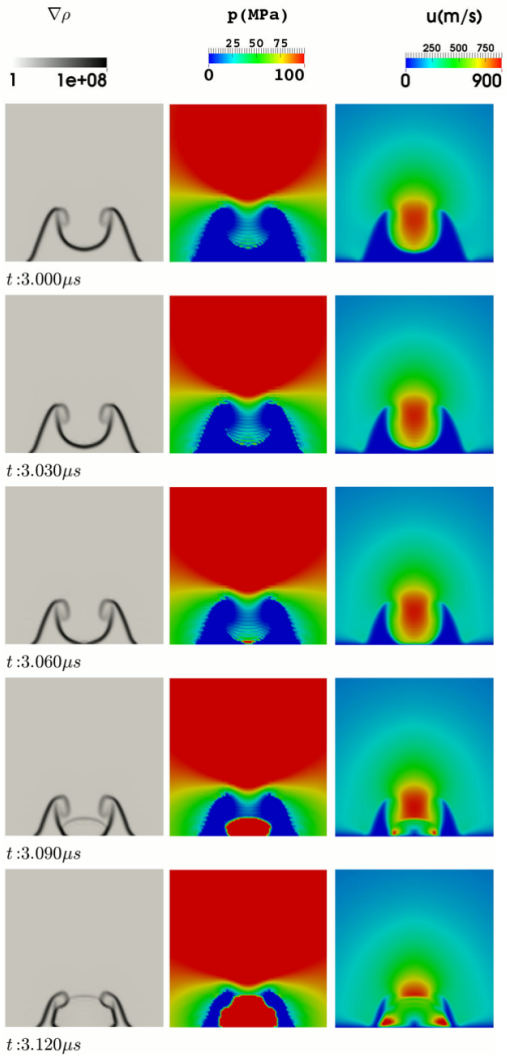

Figure 6.8 – Contour showing - $(left)$ numerical Schlieren, $(center)$ pressure and $(right)$ velocity field during liquid jet impact, $\gamma = 0.9, R_{max} = 495\mu m, p = 100MPa$, case $P0.9$, frame size $= 500 \times 500\ \mu m^2$.

the liquid jet impact is the water hammer pressure expressed with the expression $p_{wh} = \rho\, c\, u_{jet}$, where ρ is the density, c is the speed of sound and u_{jet} is the liquid jet velocity at impact. The water hammer pressure p_{wh} is the pressure on a flat solid surface exerted by a water column with a flat surface. Since the flatness of the liquid jet tip varies with the bubble collapse dynamics, the efficiency of the collapse i.e. water hammer impact pressure would depend on the liquid jet characteristic. The maximum pressure peak on the wall during this event is computed to be 2.2 GPa at $t = 3.063\ \mu s$ at point p_{F00} i.e. at the bubble symmetry axis. The water hammer pressure p_{wh} magnitude depends on the local flow condition with density $\rho = 1350\ kg/m^3$ corresponding to speed of sound $c = 3300\ m/s$ and flow velocity $u_{jet} = 500\ m/s$ at the point of impact. A strong shock wave is emitted on the liquid jet impact on the wall, which will be referred to as water hammer shock seen at $t = 3.09\ \mu s$ in fig. 6.8. The water hammer shock propagates radially from the wall into the fluid domain whereas the liquid jet due to the presence of the solid wall travels outwards along the solid wall from the jet axis. This simultaneous effect of the outward flowing liquid jet and shock wave starts to collapse the remaining bubble (2D equivalent of a 3D torus) still attached to wall, seen at $t = 3.12\ \mu s$ in fig. 6.8.

The remaining bubble starts collapsing next under the influence of outward moving liquid flow and shock wave from the bubble center. The remaining bubble is also influenced by the inward movement of the surrounding flow induced by the collapsing bubble. The remaining bubble collapse seen at $t = 3.15\ \mu s$ in fig. 6.9 gives the second pressure peak 2.4 GPa at $t = 3.19\ \mu s$ located at a distance from the bubble symmetry axis. The remaining bubble collapses in two separate stages, the top part away from the wall collapses first due to the influence of outward moving liquid flow. The velocity of this outward moving liquid flow is higher away from the wall due to fluid viscosity induced boundary layers. The remaining bubble part attached to the wall collapse few moments later and this collapse of remaining bubble in parts gives out two shock waves seen at $t = 3.18\ \mu s$ in fig. 6.9. We will further look into the dynamics of remaining bubble collapse in detail in the next section.

The shock waves from the collapse of the remaining bubble travels along the wall radially. The superimposition at the bubble symmetry axis of the two shock waves generated by the collapse of two remaining bubbles in 2D, gives the third pressure peak at $t = 3.206\ \mu s$ of 4 GPa. This amplified pressure region from shock wave superimposition at the bubble symmetry axis represents a strong compression of the liquid in the center region, which can be seen at $t = 3.21\ \mu s$ in fig. 6.9. The evolution of solid wall pressure between points $F00$ and $F10$ at different time instants is plotted in fig. 6.10. An important observation to note is the shock wave after the superimposition at $t = 3.206\ \mu s$ travels along the wall away from the bubble symmetry axis towards the domain boundaries, attenuating in magnitude with increasing distance. Such observations in 3D, of liquid jet induced and bubble torus collapse induced pressure peaks on the solid wall has been reported in the literature, for example Chahine 2015 with which we attain a qualitative agreement on the bubble dynamics.

Similar dynamics and pressure peaks are observed at reduced $\gamma = 0.5$ and $\gamma = 0.8$ in fig. 6.11. The collapse of the vapor bubbles takes place sooner in time due to reduced bubble volume for $\gamma = 0.5$ & 0.8. Figure 6.12 shows the similarity in collapsing bubble shapes for numerical simulation of vapor bubble at $\gamma = 0.5$ and experimental observations at $\gamma = 0.55$. We obtain a very good agreement in the

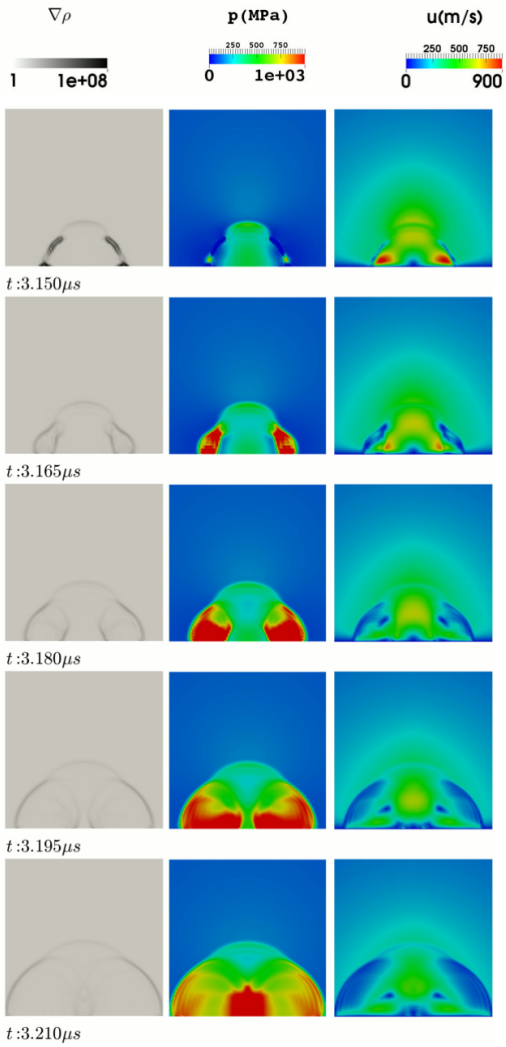

Figure 6.9 – Contour showing - (*left*) numerical Schlieren, (*center*) pressure and (*right*) velocity field on remaining bubble collapse and shock wave superimposition $\gamma = 0.9$, $R_{max} = 495\ \mu m$, $p = 100\ MPa$, case $P0.9$, frame size $= 500 \times 500\ \mu m^2$.

bubble shapes between the experiment and our 2D simulation. We impose a spherical shape for the bubble interface at initialization, whereas it can be seen in experimental image at $t = 40\ \mu s$ that a bubble does not grow spherically so close to the wall. The asymmetric effect of the wall makes the bubble grow comparatively wider in the bubble lower surface as compared to the bubble upper surface. Numerically we capture this effect seen at $t = 1.80\ \mu s$ where the bubble collapse initiates with curvature of the bubble upper surface and generation of an inwardly moving flow with decreasing bubble volume. The liquid jet piercing through the bubble hits the wall and the bubble collapses on the wall during the first collapse. It is important to note that the experimental image is for the growth and collapse of bubble at atmospheric condition and total duration of the physical process is more than $t = 100\ \mu s$. On the other hand, the 2D numerical simulation only considers the collapse under surrounding liquid pressure of $p = 100\ MPa$ where the bubble is initialized at maximum size $R_{max} = 449\ \mu m$ at $t = 0\ s$.

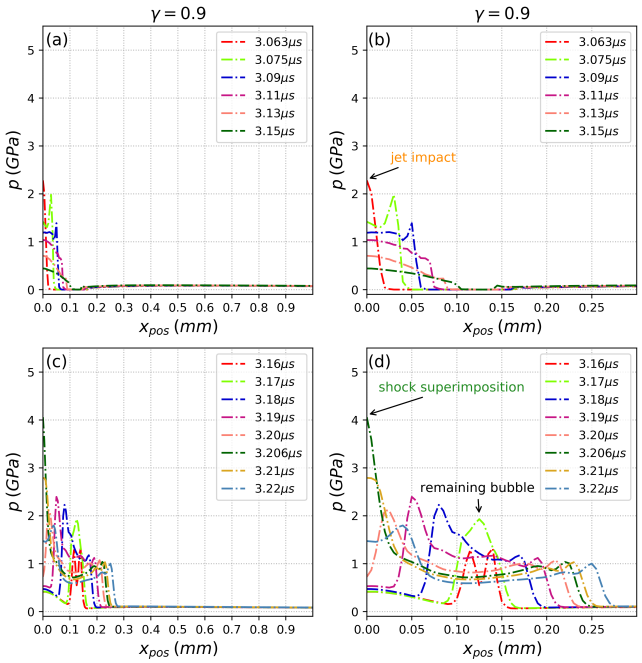

Figure 6.10 – Pressure plots on the solid wall between points $F00$ and $F10$ at different time instants $\gamma = 0.9$, case $P0.9$.

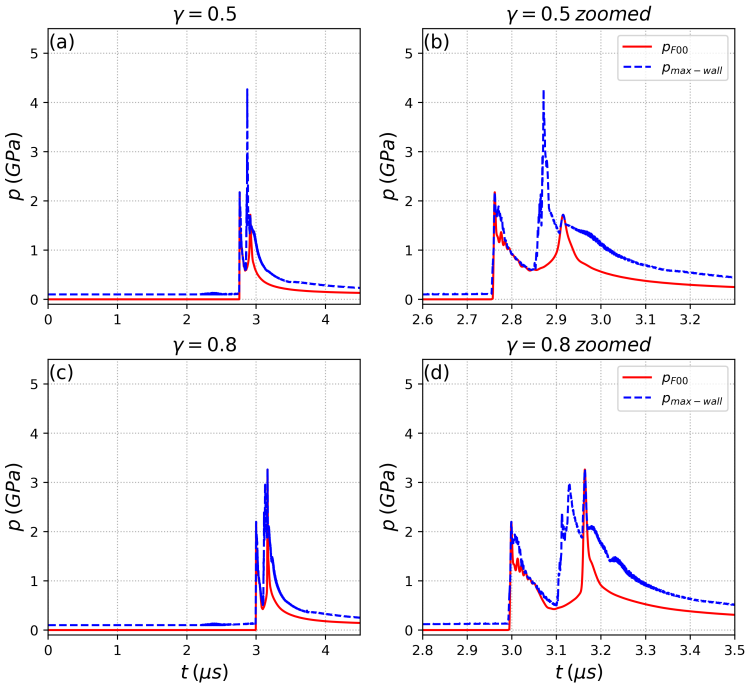

Figure 6.11 – Pressure evolution at p_{F00} and $p_{max-wall}$ for (top) $\gamma = 0.5$ and $(bottom)$ $\gamma = 0.8$, $(left)$ entire simulation time, $(right)$ zoomed on the dynamical pressure peaks.

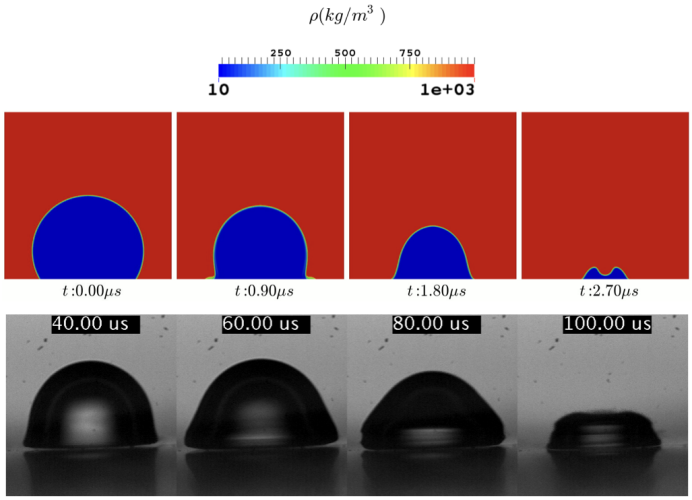

Figure 6.12 – Collapsing bubble shape (*top*) 2D numerical simulation $\gamma = 0.5$, $R_{max} = 449\,\mu m$, $p = 100\,MPa$, (*bottom*) experimental bubble collapse in atmospheric condition $\gamma = 0.55$, $R_{max} = 400\,\mu m$.

The first pressure peak from the liquid jet impact at the bubble symmetry axis gives water hammer pressure p_{wh} similar to $\gamma = 0.9$. There are two important observations to make here. The second pressure peak from the remaining bubble collapse at an offset from bubble symmetry axis, increases in magnitude for $\gamma = 0.5$ and $\gamma = 0.8$ in comparison to $\gamma = 0.9$. It can be seen clearly in the zoomed (right) plots in fig. 6.11 that the second peak of $p_{max-wall}$ increases for decreasing γ. On the other hand, the third pressure peak resulting from the shock superimposition at the bubble symmetry axis decreases with decreasing γ. We explain this with the different shapes of remaining bubble at an offset from bubble symmetry axis seen in fig. 6.13 for $\gamma = 0.8$ and in fig. 6.14 for $\gamma = 0.5$. For smaller $\gamma = 0.5$, the remaining bubble is short and flatter in y-direction, with the collapse much closer to the solid wall. The collapse of the remaining bubble induced by the high pressure surrounding liquid, very close to the wall results in a very high intensity pressure load on the wall. On the other hand for higher $\gamma = 0.8$, the remaining bubble is thin and long with collapse taking place in parts. The top part at a distance from the wall collapses first followed the part attached to the wall. The effect of liquid compressibility on the different remaining bubble shapes determine the magnitude of pressure peaks observed on the wall.

The numerical simulation of vapor bubble collapse at $\gamma = 0.8$ is used for spatial and temporal convergence validation presented in fig. 6.15. The vapor bubble simulations with the current mesh resolution of $\Delta x = \Delta y = 5\,\mu m$ is validated against a numerical simulation of spatial resolution $\Delta x = \Delta y = 2.5\,\mu m$. The simulations gave results with a relative difference of 0.9 % between the pressure peaks for both cases. Therefore, a mesh resolution of $\Delta x = \Delta y = 5\,\mu m$ has been found adequate for such investigations. Validation studies on temporal convergence of the CFL-controlled numerical simulation with time steps shown in fig. 6.3 and with a fixed time step of $0.05\,ns$ and $0.025\,ns$ provided similar bubble dynamics and pressure peaks with relative difference of 0.8 % and 0.3 % respectively, in the dynamical region $3 < t < 3.5\,\mu s$ presented in fig. 6.15.

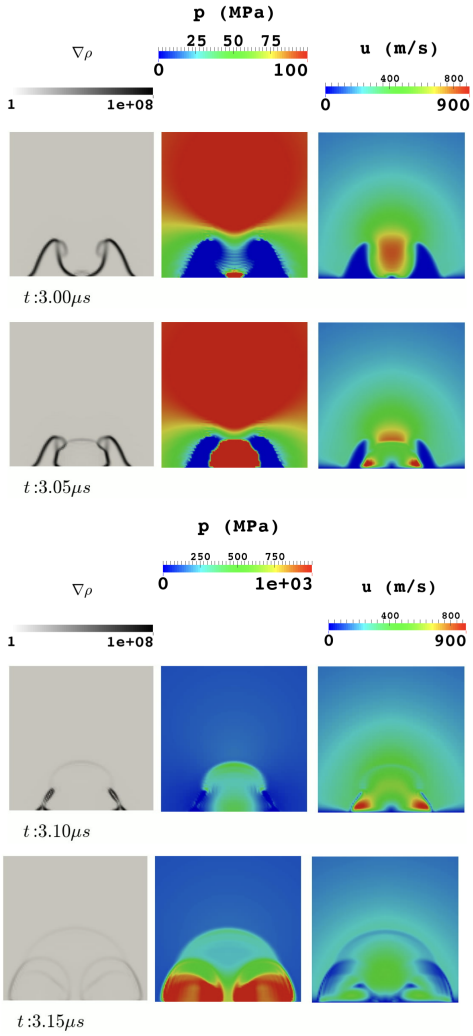

Figure 6.13 – Contour showing - (*left*) numerical Schlieren, (*center*) pressure and (*right*) velocity field on remaining bubble collapse and shock wave superimposition $\gamma = 0.8$, $R_{max} = 487\,\mu m$, $p_\infty = 100\,MPa$, frame size $= 500 \times 500\,\mu m^2$.

Another interesting investigation is made to test a reduced computational domain size taking advantage of the NSCBC wave treatment at the domain outlets. As from the experience in this thesis and based on literature, bubble collapse dynamics is very sensitive to domain boundaries and imposed boundary conditions. A reduced computational domain of size $10R_0 \times 5R_0$ is considered, for convenience we will refer to it as domain $10R_0$. The domain size reduces 4 times along x-axis and 8 times along y-axis in a cartesian coordinate system shown in fig. 6.16 as compared to the previous domain $40R_0$. The imposed boundary conditions are similar to what has been used in the larger domain $40R_0$ presented in fig. 6.1. It has been mentioned in section 3.4.3.1 that the propagation of wave on the NSCBC equipped boundaries is treated only in the boundary normal direction. A double domain length in the positive x-direction in comparison to y-direction has been considered primarily for two reasons. A spherical wave originating in the domain center, near the dynamical bubble region, will become planar due to increased wave front radius from expansion as it approaches the corner between the two outlet boundaries. Secondly, any numerical artifacts, if present, at

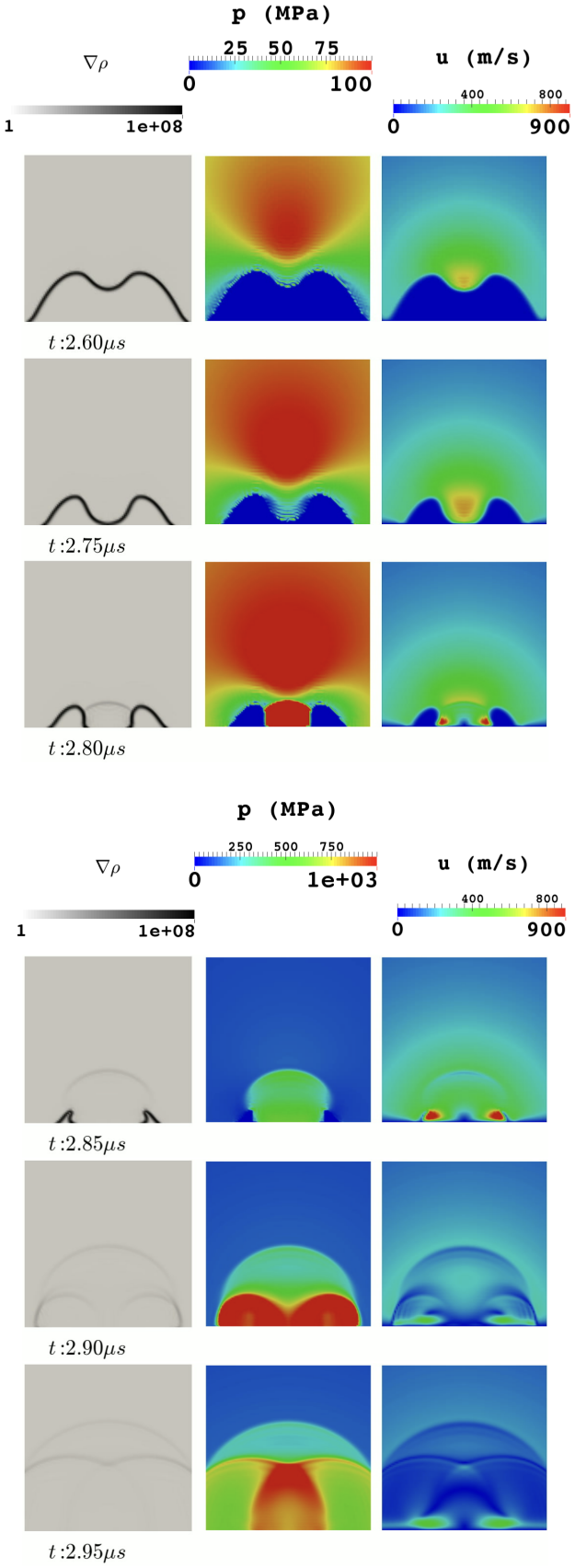

Figure 6.14 – Contour showing - (*left*) numerical Schlieren, (*center*) pressure and (*right*) velocity field on remaining bubble collapse and shock wave superimposition $\gamma = 0.5$, $R_{max} = 449\ \mu m$, $p_\infty = 100\ MPa$, frame size $= 500 \times 500\ \mu m^2$.

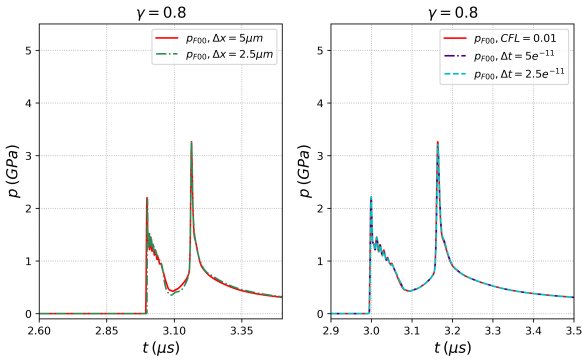

Figure 6.15 – Plot showing $(left)$ spatial and $(right)$ temporal convergence of the numerical solution at p_{F00}, $\gamma = 0.8$.

the corner between the outlets will stay away from the center of the domain. A comparison of pressure peaks between the larger domain $40R_0$ and smaller domain $10R_0$ for the test case $P0.9$ provided similar dynamical features and agreement in results within errors of $\Delta t = 0.025\%$ and $\Delta p = 1.9\%$ presented in fig. 6.17. From here on for all our presented fluid simulations in 2D, we used the reduced computational domain.

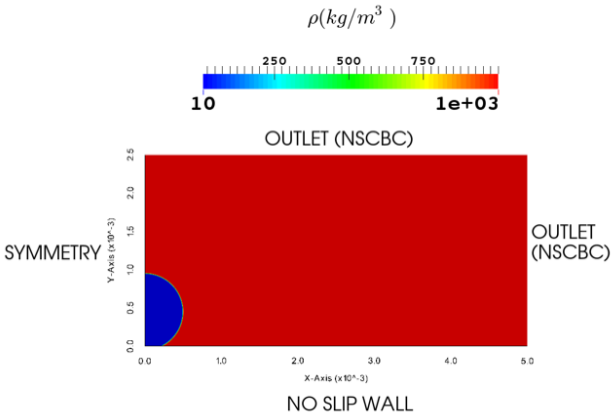

Figure 6.16 – Reduced computational domain for 2D bubble collapse - domain boundary $10R_0 \times 5R_0$, domain size $= 5 \times 2.5\, mm^2$.

Finally, on the numerical simulation of detached vapor bubbles collapsing under ambient liquid pressure presents new set of challenges. As mentioned previously during our discussion on appearance of secondary cavitation in fig. 6.4, the interaction of expansion waves with solid walls leads to the generation of secondary cavitation along the wall. A travelling expansion wave leads to decrease in pressure (as well as temperature, if considered) in a computational domain. In our numerical setup due to the chosen initialization of the bubble with a barotropic model, an expansion wave is generated. Since the initial liquid pressure ($p = 100\, MPa$) is very high, the drop in density and pressure across the expansion wave is very high too. Therefore, when the expansion wave hits and reflects from the wall, secondary cavitation is created near the wall due to localized decrease in pressure. A detached bubble collapse is

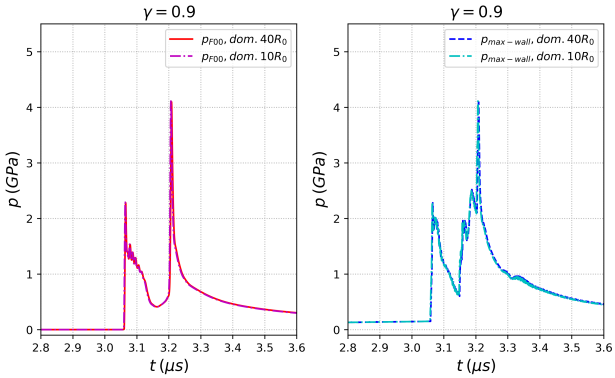

Figure 6.17 – Plot showing agreement of results for domain size $40R_0$ and reduced computational domain size $10R_0 \times 5R_0$, $\gamma = 0.9$, $(left)$ P_{F00}, $(right)$ $p_{max-wall}$.

characterized by the generation of a shock wave from the bubble center which travels towards and hits the solid wall. In the presence of secondary cavitation region near the wall, the shock wave amplitude travelling to the wall is retarded and cannot reproduce the physical state accurately as shown in fig. 6.18 for $\gamma = 1.4$.

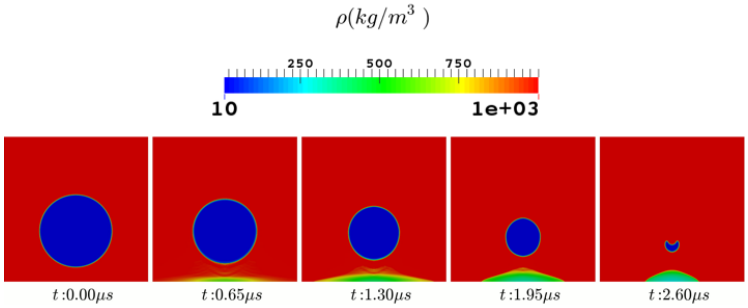

Figure 6.18 – Temporal evolution of density field during liquid pressure-induced detached bubble collapse near solid wall - appearance of expansion wave driven secondary cavitation near the solid wall, $\gamma = 1.4$, $R_{max} = 500\ \mu m$, $p = 100\ MPa$, frame size $= 2 \times 2\ mm^2$.

To circumvent such problem, an alternative is the shock-induced collapse where the collapse of the vapor bubble is induced by an impacting shock wave. In such a setup, the vapor bubble is initialized in liquid at atmospheric pressure ($0.1\ MPa$) and is impacted by a high amplitude shock wave to initiate the bubble collapse. Interesting to note is that the expansion wave would be generated even in such a setup. Since the pressure ratio between the ambient liquid pressure and vapor pressure is comparatively smaller, the decrease in density and pressure across the expansion wave is very small and secondary cavitation will not develop. Ideally if a liquid pressure-induced collapse is numerically simulated at atmospheric condition, the pressure drop across expansion wave is insignificant and the secondary cavitation will not occur. In real technical applications with higher ambient liquid pressure driving the bubble collapse, the secondary cavitation effect has to be considered. Next we will present the results on shock-induced detached and attached vapor bubble collapse.

6.3 Shock-Induced Collapse

In the shock-induced collapse, we use the same computational setup and numerical parameters described in the previous section. We will present 2D and 3D collapse dynamics for attached ($\gamma = 0.9$, $R_{max} = 495\,\mu m$) and detached ($\gamma = 1.4$, $R_{max} = 500\,\mu m$) vapor bubble surrounded by water at atmospheric pressure. A shock front is initiated at a distance of $2\,mm$ from the solid wall and initially both fluids are at rest:

$$\begin{aligned} &vapor:\ \rho = 10\,kg/m^3,\ p = 2194\,Pa, \\ &water:\ \rho = 998.2\,kg/m^3,\ p = 101,325\,Pa. \end{aligned} \tag{6.2}$$

6.3.1 2D Bubble Collapse

6.3.1.1 Attached bubble ($\gamma = 0.9$)

The vapor bubble is attached to the solid wall and the distance between the bubble center and shock front is $1.55\,mm$. On initialization, a shock front of $50\,MPa$ hits the bubble upper surface at $t = 0.68\,\mu s$. After the shock impact, the bubble upper surface flattens initiating its motion towards the shock propagation direction. The bubble starts to deform after the shock impact and a part of the shock front is partially reflected back as an expansion wave in the computational domain. The shock front finally hits the solid wall at $t = 1.3\,\mu s$ and is reflected back in the domain. The temporal evolution of a shock-induced attached bubble dynamics is shown in fig. 6.19. The left half of each frame shows the density contour whereas the right half shows the pressure contour. At $4.2\,\mu s$, the bubble surface area has shrunk to approximately $\frac{1}{20}^{th}$ of the initial bubble size and a liquid jet is formed from the bubble upper surface. For convenience later on, this test case of shock-induced attached bubble at $\gamma = 0.9$ will be referred as case $SH0.9$.

The pressure peaks on the solid wall represented in fig. 6.9 show similar dynamical features of collapse as the liquid pressure-induced collapse. There are three major pressure peaks, each representing an important characteristic of the bubble collapse. The first peak of $1.97\,GPa$ at $4.294\,\mu s$ is the water hammer pressure p_{wh} due to the liquid jet impact on the solid wall. The local flow condition at the moment of collapse in the impact location is density $\rho = 1300 kg/m^3$, speed of sound $c = 3000 m/s$ and jet velocity $500\,m/s$, giving a theoretical water hammer pressure of $1.95\,GPa$ exhibiting a very good agreement with our estimation. This illustrates very high pressure and velocities are achieved in the liquid during collapse. The liquid jet impact produces a shock wave, referred as water hammer shock, at the point where the liquid jet hits the wall. This is also consistent with the dynamics presented previously in the liquid pressure-induced collapse. The magnitude of the water hammer pressure p_{wh} is about 10% lower in shock-induced collapse in comparison to liquid pressure-induced collapse in our investigation. This can be attributed to the decrease in bubble collapse driving pressure in shock-induced collapse. The driving pressure in shock-induced collapse is about $50\,MPa$ in comparison to the driving pressure of $100\,MPa$ in liquid pressure-induced collapse.

The second pressure peak of $2.52\,GPa$ on the solid wall at $t = 4.423\,\mu s$ is due to the remaining bubble collapse at an offset of $0.1\,mm$ from the bubble symmetry axis. The pressure evolution at different time instants on the solid wall is shown in fig. 6.21. This shock wave emitted from the remaining bubble collapse travels

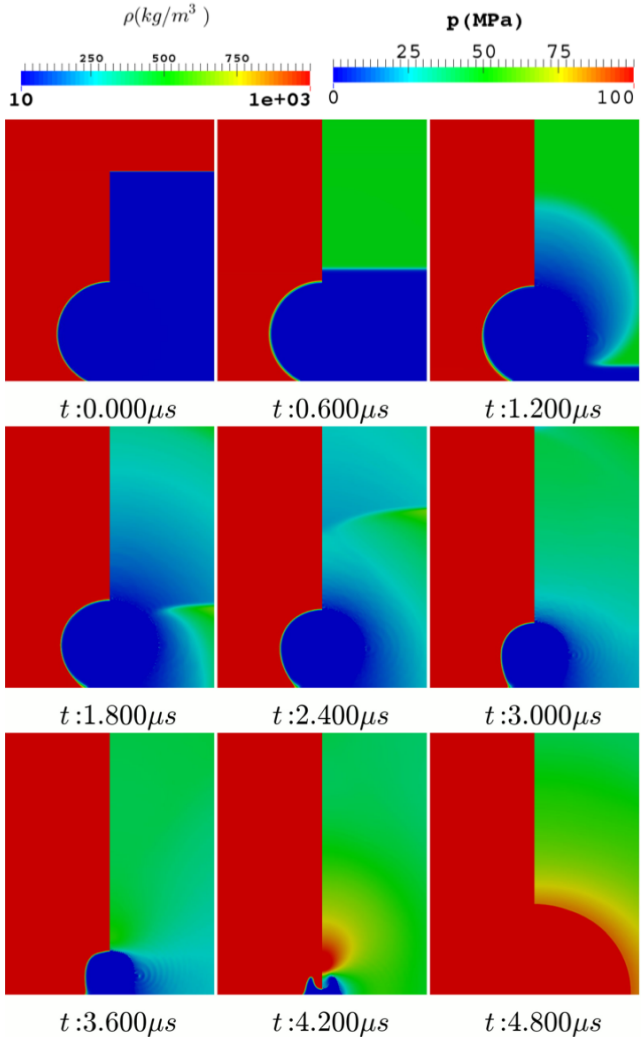

Figure 6.19 – 2D attached bubble: $(left)$ density and $(right)$ pressure contour on each frame showing temporal evolution of a shock-induced 2D bubble collapse, $\gamma = 0.9$, $R_{max} = 495\ \mu m$, $p = 0.1\ MPa$, $p_{shock} = 50\ MPa$, case $SH0.9$, frame size $= 2 \times 2.5\ mm^2$.

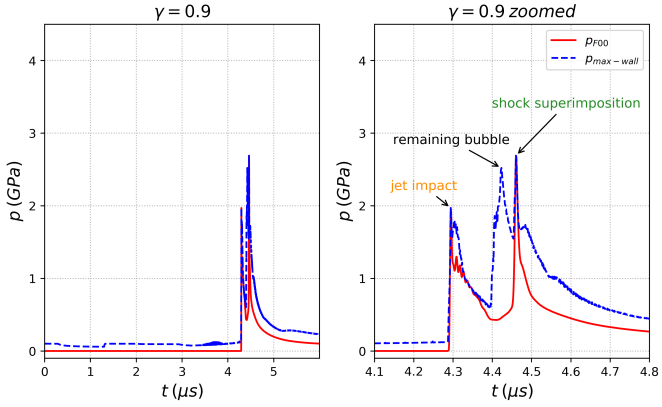

Figure 6.20 – 2D attached bubble: pressure peaks at p_{F00} and $p_{max-wall}$ on the solid wall for shock-induced collapse, $\gamma = 0.9$, case $SH0.9$.

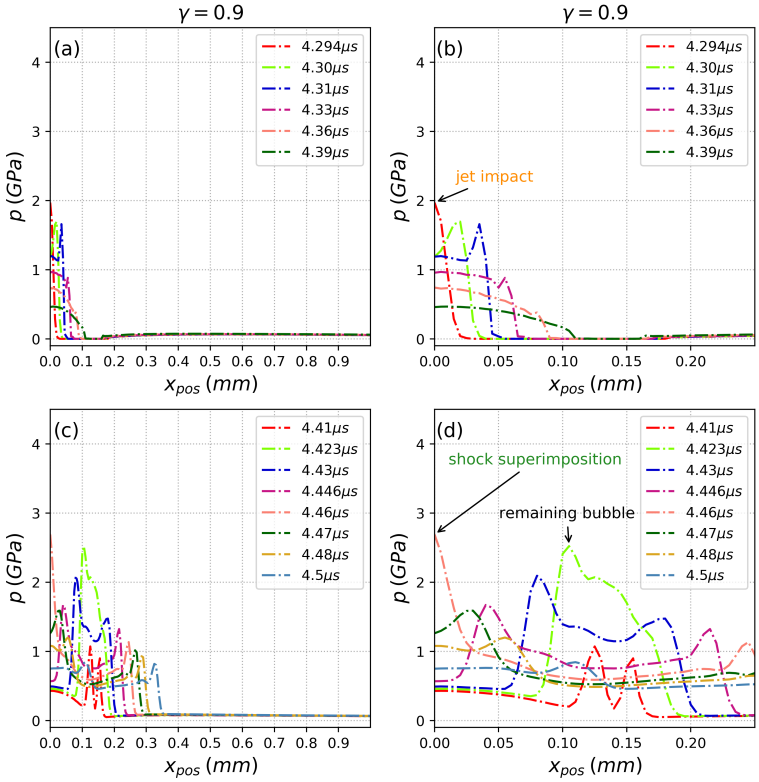

Figure 6.21 – 2D attached bubble: pressure plots on the solid wall between points $F00$ and $F10$ at different time instants, $\gamma = 0.9$, case $SH0.9$.

towards the bubble symmetry axis, giving the third pressure peak of 2.69 GPa at $t = 4.46\,\mu s$ from the superimposition of shock wave and strong compression of liquid in the center region. Finally, this shock wave from the bubble center travels radially along the wall and in the computational domain attenuating in magnitude with increasing distance from bubble center.

Few important observations can be made regarding the remaining bubble collapse taking place at an offset of 0.1 mm from the bubble symmetry axis. The remaining bubble collapse is driven by two mechanisms: firstly the inward-moving induced flow by the collapsing bubble which pushes the bubble surface towards the symmetry axis. The second mechanism is the outward liquid jet flow from the bubble center along with the propagating water hammer shock, which pushes the remaining bubble away from the symmetry axis. This can be seen in the velocity vectors shown in fig. 6.22. Once the remaining bubble collapses, a recirculation zone in the flow field is generated in the direction towards bubble symmetry axis. Such a recirculation flow field is sustained during the rest of the dynamical part when the shock wave compresses the liquid at the bubble center and travels towards domain boundary.

Secondly during the remaining bubble collapse, the importance of boundary layer development can be seen in fig. 6.23. The remaining bubble collapse is split into two parts by outward travelling liquid flow on the solid wall after the jet impact. Due to the development of boundary layer, the fluid flow very close to the solid wall moves at a slower velocity as compared to the rest of outward flowing liquid jet along the wall. A maximum flow velocity of $u_x = 900\,m/s$ (cell $Re_x = 4500$) is computed for

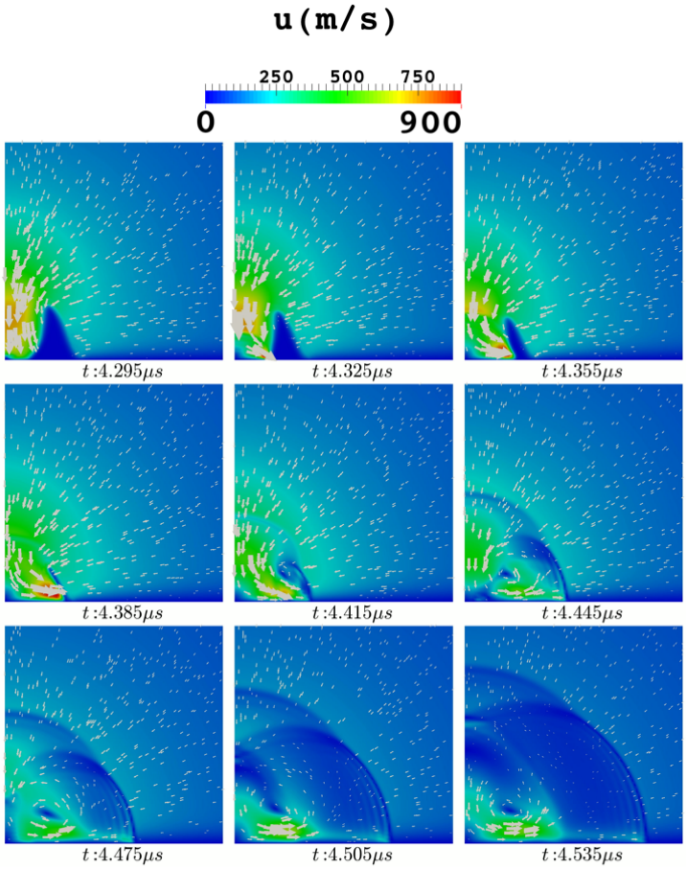

Figure 6.22 – Velocity vectors showing the flow field during the final stages of collapse near the solid wall, $\gamma = 0.9$, $R_{max} = 495\ \mu m$, $p = 0.1\ MPa$, $p_{shock} = 50\ MPa$, case $SH0.9$, frame size $= 500 \times 500\ \mu m^2$.

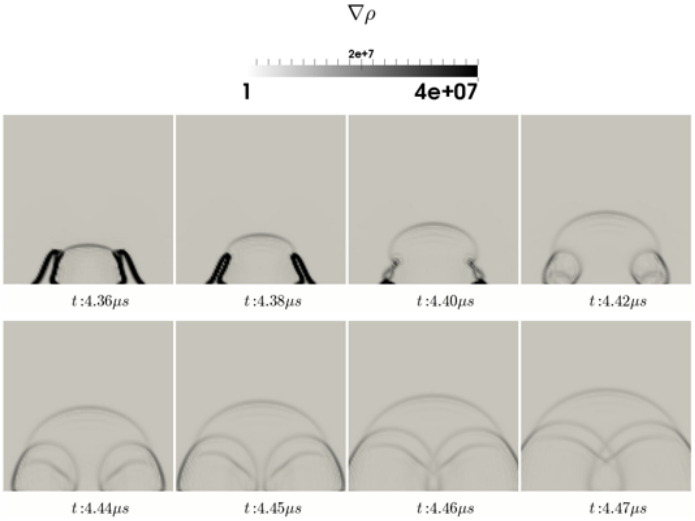

Figure 6.23 – Numerical Schlieren showing the sequence of events during the remaining bubble collapse-emission of primary and secondary shock, $\gamma = 0.9$, $R_{max} = 495\ \mu m$, $p = 0.1\ MPa$, $p_{shock} = 50\ MPa$, case $SH0.9$, frame size $= 500 \times 500\ \mu m^2$.

the outward flowing liquid jet. The fast-moving liquid flow on the wall surface splits the remaining bubble into two parts - a top part seen at $t = 4.40\,\mu s$ which collapses first with the emission of a primary shock wave. The rest of the remaining bubble attached to the solid collapses next giving out the secondary shock wave seen at $t = 4.42\,\mu s$. Both the primary and secondary shock wave travels radially outwards from the location of remaining bubble collapse. It is worth mentioning that in our investigation, the first grid point in the solid wall normal direction is located at a distance of $\Delta y = 5\,\mu m$. Therefore, the wall shear stress from the liquid jet flow has not been reported as it would require much finer mesh in the wall normal direction to resolve the boundary layers accurately. According to Zeng 2018, the wall shear stress is of the order of 100 KPa from the liquid jet flow along the solid wall for a bubble $R_{max} = 50\,\mu m$ at $\gamma = 1$, resolved with a much finer mesh of first grid point at $\Delta y = 0.1\,\mu m$.

Finally, comparing the bubble dynamics and pressure peaks on solid wall for shock-induced collapse and liquid pressure-induced collapse, we find qualitative agreement between the bubble dynamics. This in principle suggests that experimental observations of bubble dynamics at low ambient pressures are valid at high (technically relevant) ambient pressure-induced bubble collapse as well.

6.3.1.2 Detached Bubble ($\gamma = 1.4$)

In the case of detached cavity at $\gamma = 1.4$, the shock front is initially at a distance of $1.3\,mm$ from the bubble center and hits the bubble upper surface at $t = 0.51\,\mu s$. The bubble upper surface flattens and move towards the shock propagation direction i.e. towards the solid wall. The shock front used to induce the bubble collapse is reflected back from the solid wall and interacts once more with the collapsing bubble. This interaction happens at a relatively early stage of collapse and therefore, this reflected shock does not retard the formation of liquid jet in our simulation. During the final stages, the liquid jet is formed compressing the bubble upper surface along the symmetry axis. The evolving shape of the bubble matches well with the experimental observations shown in fig. 6.24 for $\gamma = 1.4$. The shock-induced bubble at $\gamma = 1.4$ will be referred here on as case $SH1.4$.

In the final stages, the liquid jet is pushing the bubble upper surface which collapses with the bubble lower surface resulting in the emission of a shock wave. The shock produced is a water hammer shock from the liquid jet travelling with the bubble upper surface collapsing on the bubble lower surface and the shock subsequently propagates towards the solid wall. Such generation of water hammer shock has been reported numerically by Johnsen 2009 and experimentally by Lindau 2003. The maximum liquid jet velocity is $750\,m/s$ at $t = 4.1\,\mu s$ which decelerate upon the collapse of bubble upper surface on lower surface. Along with the water hammer shock travelling towards the wall, another shock wave is also created which travels in the opposite direction. At $t = 4.20\,\mu s$ in fig. 6.25, the shock speed of the water hammer shock is $2400\,m/s$ which is travelling in a liquid almost at rest. At the same instant, the shock wave propagating in the wall opposite direction is travelling at $2600\,m/s$ in a flow field towards the wall induced by the high velocity liquid jet. The water hammer shock impacts the wall with peak pressure of $1.34\,GPa$ at $t = 4.26\,\mu s$ shown in fig. 6.26. The impacting shock is immediately reflected back from the wall and the duration of the impact is about $5\,ns$ at point p_{F00}. The reflected shock travels along the wall with the radial expansion of the impacting water-hammer shock and

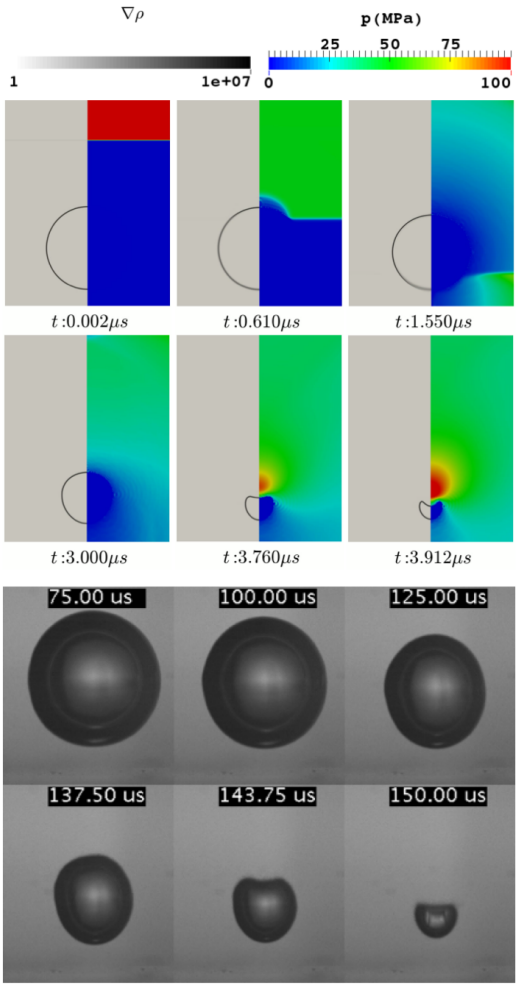

Figure 6.24 – 2D detached bubble: comparison of bubble shapes in (*top*) numerical simulation $\gamma = 1.4$, $R_{max} = 500\ \mu m$, $p = 0.1\ MPa$, $p_{shock} = 50\ MPa$, case $SH1.4$, (*bottom*) experimental images, $\gamma = 1.4$, $R_{max} = 730\ \mu m$.

the shock intensity decreasing with increasing wall distance from the symmetry axis.

Additionally, a detached low pressure cavity develops in the water as seen at $t = 4.40\,\mu s$ in fig. 6.25. Such a rebound of vapor structure can have additional effect on wall erosion and has been reported in Lauer 2012 for detached vapor bubble collapse as well. In our investigation, the effect of bubble rebound is not considered as no condensable gas or nucleation model has been implemented.

6.3.2 3D Single bubble collapse

The shock-induced bubble collapse case is extended to three dimensions for which a hexahedron domain of dimension $2 \times 2.5 \times 2\ mm^3$ is taken with $\Delta x = \Delta y = \Delta z = 10\ \mu m$ as shown in fig. B.9 of Appendix B. We will look into the dynamics of shock-induced 3D collapse for an attached bubble at $\gamma = 0.9$ and equivalent radius $R_{max} = 498\ \mu m$ followed by a detached bubble at $\gamma = 1.4$ with equivalent

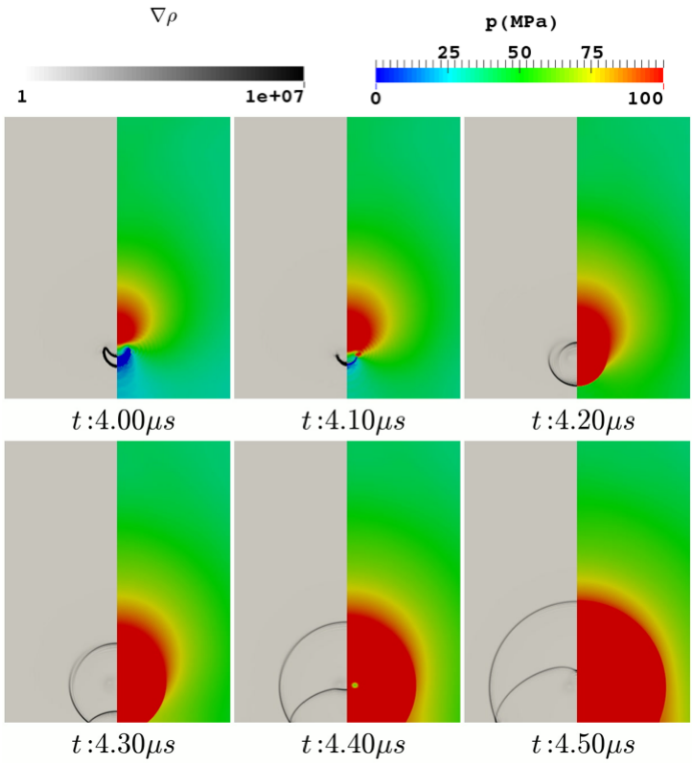

Figure 6.25 – 2D detached bubble: final stages of collapse showing shock propagation near the solid wall $\gamma = 1.4$, $R_{max} = 500\ \mu m$, $p = 0.1\ MPa$, $p_{shock} = 50\ MPa$, case $SH1.4$, frame size $= 1 \times 2.5\ mm^2$.

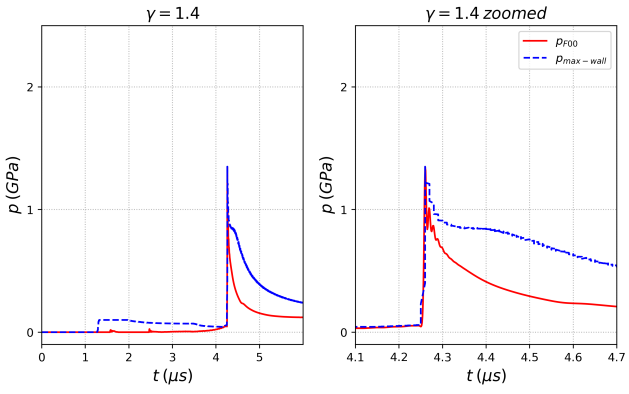

Figure 6.26 – 2D detached bubble: pressure peaks at p_{F00} and $p_{max-wall}$ on the solid wall for shock-induced collapse $\gamma = 1.4$, case $SH1.4$.

radius $R_{max} = 500\mu m$. The shock wave is initiated from a distance of 2 mm from the solid wall and hits the bubble upper surface with a front of 50 MPa. Taking advantage of two symmetric planes along x and y direction, only $\frac{1}{4}^{th}$ of the problem is resolved. The physical cavitation model and numerical parameters are similar to the 2D shock-induced bubble collapse. In fig. 6.27, we present the top and front view of the $\frac{3}{4}^{th}$ cut section of bubble iso-volume attached to the solid wall. The bubble is attached to the solid wall with no slip condition and cut by two symmetry planes on the side. The domain boundaries are treated as outlets equipped with NSCBC wave treatment.

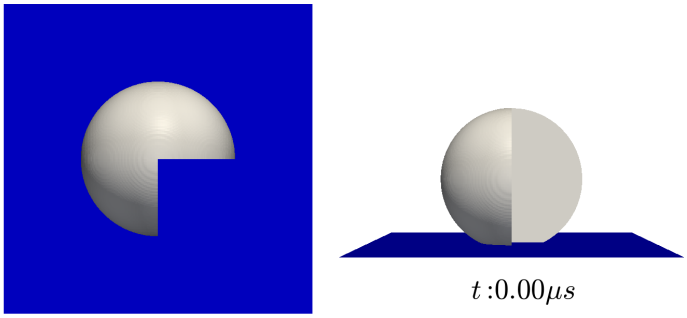

Figure 6.27 – Top and front view of $\frac{3}{4}^{th}$ cut section of bubble iso-volume attached on the solid wall, $\gamma = 0.9$, frame size $= 2 \times 2\, mm^2$.

The evolution of bubble collapse is shown in fig. 6.28 from the top view. The color contour on the bubble surface shows the evolution of fluid velocity at each time instant whereas the color map on the solid wall shows the evolution of surface pressure at each time instant. The evolving bubble shape is evident with the formation of liquid jet seen from $t = 3.0\,\mu s$ onwards with the jet velocity increasing as the liquid jet develops. Figure 6.29 shows the evolution of wall pressure at the bubble symmetry axis p_{F00} and maximum pressure evolution on the wall $p_{max-wall}$. The first and second peak of $8\,GPa$ at $t = 3.3\,\mu s$ and $5\,GPa$ at $t = 3.37\,\mu s$ represents the liquid jet collapse at the symmetry axis and bubble torus collapse at an offset from the wall. The liquid jet velocity in 3D is $1150\,m/s$ and local density at the moment of collapse is $\rho = 1580\,kg/m^3$. The third pressure peak of bubble torus collapse induced shock superimposition and liquid compression at the symmetry axis is of about $2\,GPa$. The decrease in the third pressure peak for attached case highlights faster attenuation of shock waves in 3D. The liquid jet collapses and the emitted shock wave seems to be the biggest source of pressure loading on the solid wall, evident from the 3D computations.

On the other hand, for a detached bubble at $\gamma = 1.4$, the dynamics is pretty similar to the 2D case. Figure 6.30 shows the velocity evolution on the bubble and pressure evolution on the solid wall. The maximum pressure load is of $1.58\,GPa$ at $t = 3.16\,\mu s$ from the water hammer shock due to the collapse of bubble upper surface on the bubble lower surface. The wall pressure is initially atmospheric and suddenly increases when the shock impacts and reflects off the wall at around $t = 3.15\,\mu s$. The impacting shock intensity decreases as $1/r$, where r is the radial distance from shock impact location shown in fig. 6.31.

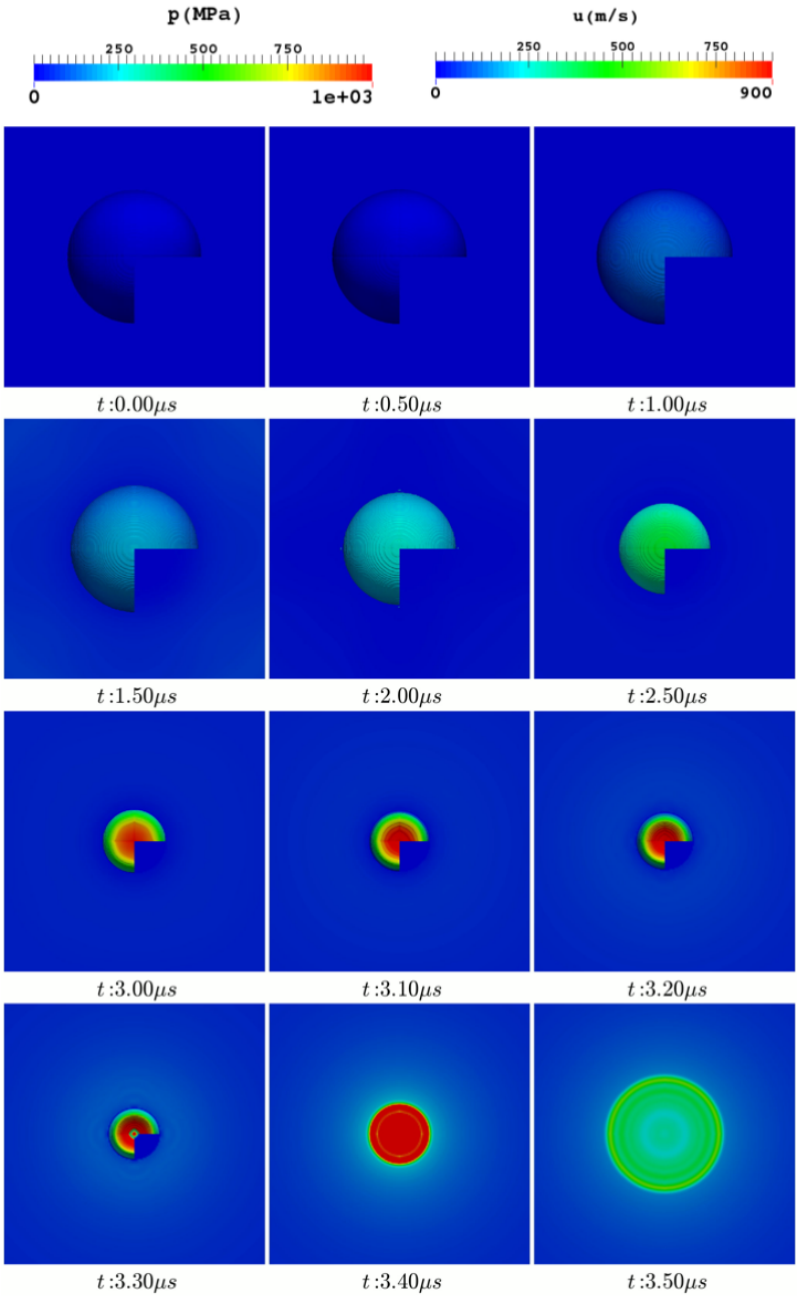

Figure 6.28 – 3D attached bubble: evolution of velocity on the iso-volume of attached bubble and pressure contour on solid wall, $\gamma = 0.9$, $R_{max} = 498\,\mu m$, $p = 0.1\,MPa$, $p_{shock} = 50M\,Pa$, frame size $= 2 \times 2\,mm^2$.

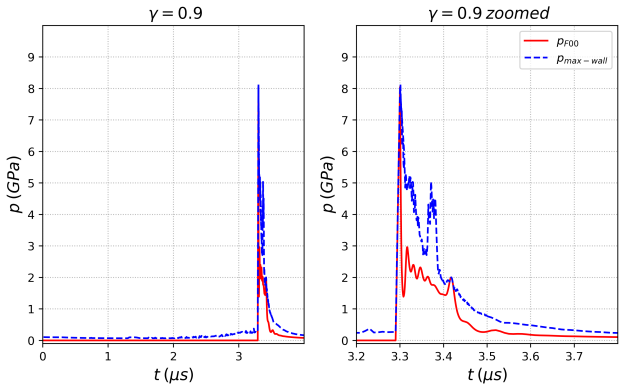

Figure 6.29 – 3D attached bubble: pressure peaks at p_{F00} and $p_{max-wall}$ on the solid wall for shock-induced collapse $\gamma = 0.9$.

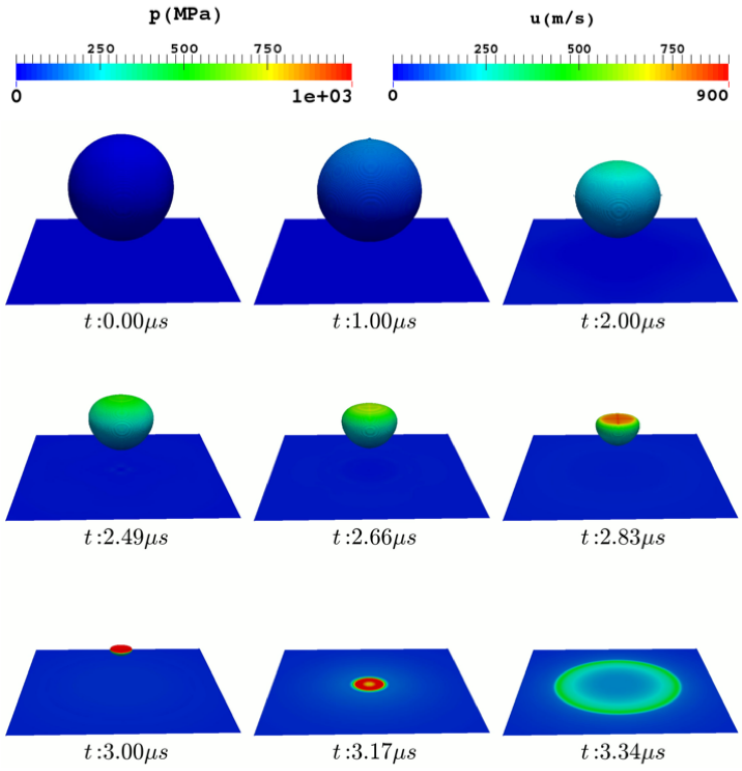

Figure 6.30 – 3D detached bubble: evolution of velocity on the iso-volume of attached bubble and pressure contour on solid wall, $\gamma = 1.4$, $R_{max} = 500\,\mu m$, $p = 0.1\,MPa$, $p_{shock} = 50M\,Pa$, frame size $= 2 \times 2\,mm^2$.

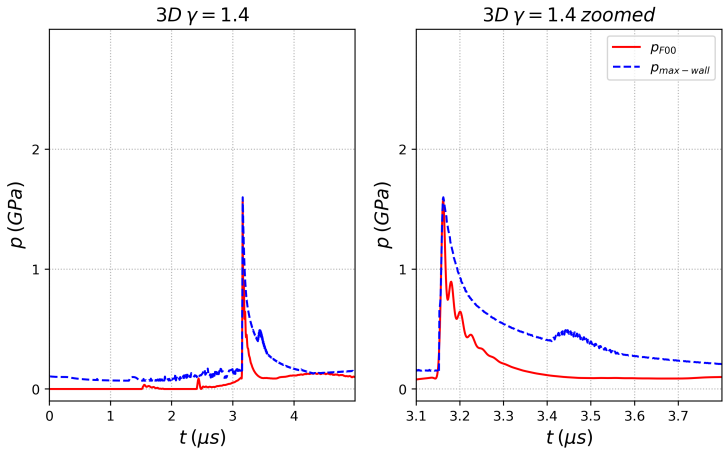

Figure 6.31 – 3D detached bubble: pressure peaks at p_{F00} and $p_{max-wall}$ on the solid wall for shock-induced collapse, $\gamma = 1.4$.

6.3.3 3D Bubble Cloud

Finally a 3D bubble planar cloud is considered to demonstrate and highlight the applicability of the methodology developed so far. We consider all the bubbles in the cloud have a radius $R_{max} = 250\,\mu m$ and arrange them in 5 columns. The middle column of 5 bubbles are at $\gamma = 0.8$, the two columns of bubbles next to the middle column on either side are at $\gamma = 1.2$, and the next two columns on either side are at $\gamma = 1.4$. A simple representation would be that the middle column of bubbles are attached to the solid wall and the other two columns are formed by detached bubbles with increasing γ as shown in fig. 6.32. The distance between bubble center is taken as $750\,\mu m$ in the lateral plane, so that the bubble surfaces are at a minimum distance of $250\,\mu m$ from each other. By taking advantage of the symmetry, we numerically simulate only $(1/4)^{th}$ of the computational domain.

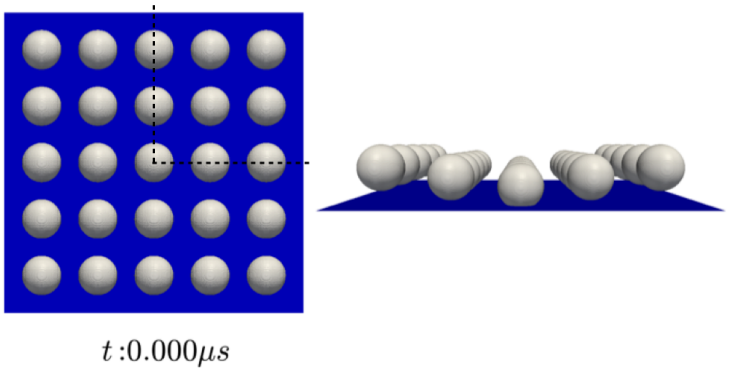

Figure 6.32 – Top view and front view showing the initial setup of planar 3D bubble cloud, frame size $= 4 \times 4\,mm^2$.

The final stages of 3D planar bubble cloud collapse is shown in fig. 6.33, which shows that the detached bubble collapses take place before the attached bubble collapses. The detached bubble column farthest from the solid wall collapses first with the emission of water-hammer shock which propagates and impacts the wall.

The attached bubble column in the middle collapses in the end with the formation of multiple liquid jets impacting on the solid wall. The surface pressure evolution from such collapses is a combination of multiple dynamical events happening at the same time and is a much more complex process. There are multiple shock-shock, shock-bubble interactions and localized liquid compression zones at different locations on the solid wall. The evolution of maximum pressure $p_{max-wall}$ on the solid from the bubble cloud collapse is presented in fig. 6.34, which shows many high pressure loading instances on the wall. It is difficult to characterize a bubble cloud and resulting surface pressure as the cloud composition and bubble dynamics is governed by many contributing factors. A much more elaborate study involving different bubble densities and composition in the cloud could be a way forward.

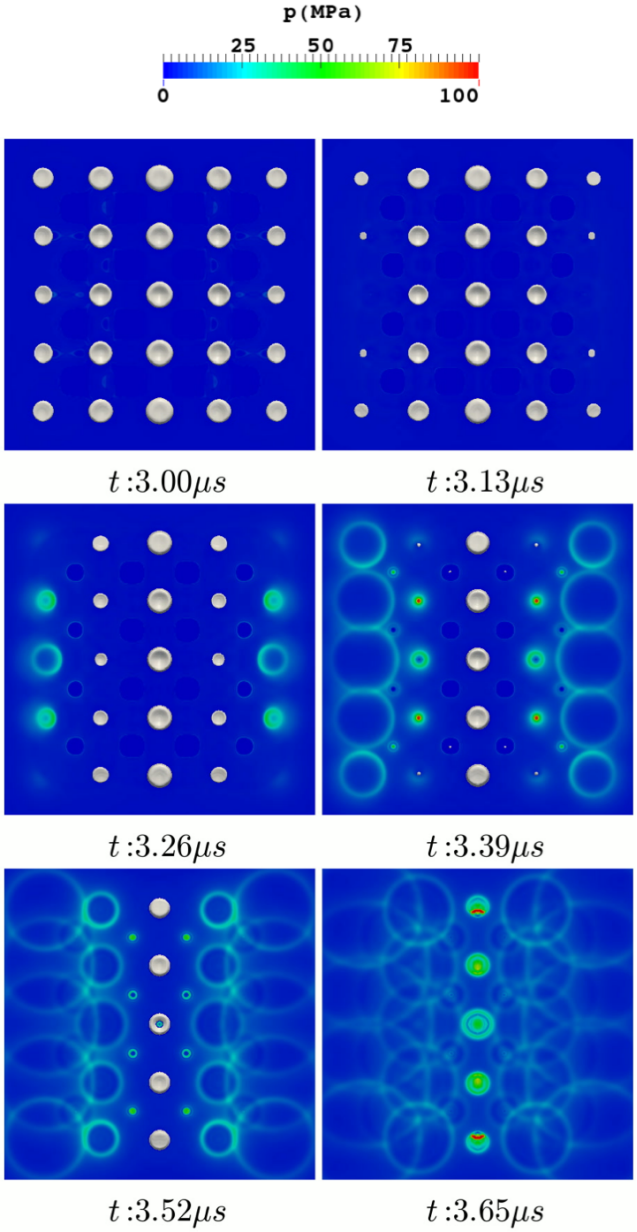

Figure 6.33 – Temporal evolution of bubble shapes and pressure on the solid wall from 3D collapsing cloud, $p = 0.1\,MPa$, $p_{shock} = 50M\,Pa$, frame size $= 4 \times 4\,mm^2$.

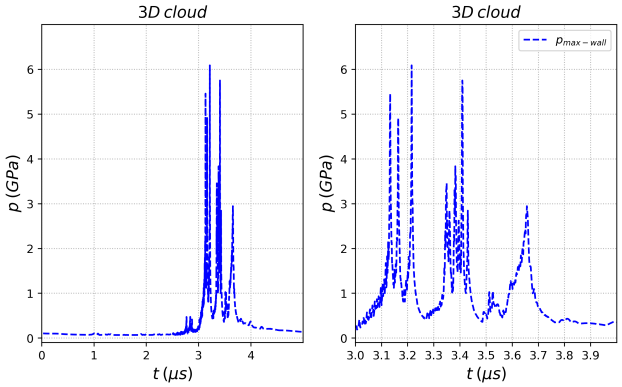

Figure 6.34 – Maximum pressure evolution $p_{max-wall}$ on solid wall from the 3D bubble cloud collapse.

6.4 Summary

The dynamics of the bubble collapse has been presented for liquid pressure-induced and shock-induced collapse. The attached bubble dynamics shows three major events - firstly the liquid jet impact on solid wall resulting in the water hammer pressure p_{wh}. Secondly the collapse of the remaining bubble (2D equivalent of 3D bubble torus) at an offset from the symmetry axis. Finally the strong compression of liquid at the symmetry axis from the superimposition of the shock waves emitted from the remaining bubble collapse. For a detached bubble, the water hammer shock emitted when the bubble upper surface collapses on the bubble lower surface is the source of pressure loading on solid wall. The 3D bubble collapse highlights the importance of liquid jet impact on the solid wall and the high pressure loading on the wall especially at smaller stand-off distances. Similarly, the pressure loading from the bubble cloud simulation highlights the complex nature of pressure loading on the wall which varies depending on the bubble cloud composition and density. Overall, the bubble dynamics has been captured quite accurately for the considered stand-off distances, matching well with the existing literature and experimental data. The magnitude of the pressure loading on the other hand vary depending on the mechanism driving the bubble collapse and the stand-off distances. These different estimates show that the pressure loading on the wall in cavitation strongly depends on the flow conditions. It would be interesting to perform a parametric study for a wider range of stand-off distances and driving pressure. The response of the solid material will be presented for the test cases $P0.9$, $SH0.9$ and $SH1.4$ in the next chapter.

Chapter 7

Material Response

7.1 Introduction

In order to better understand cavitation erosion, the response of the solid is characterized for attached and detached bubble collapse. First we will look into the response of solid in a one-way coupled approach where the pressure loads generated by the fluid are applied as boundary conditions on the solid, with no feedback to the fluid. It will be extended to a two-way coupled approach where the feedback of the solid surface displacement is taken into consideration in the fluid simulation. The main difference between the bubble collapse simulation presented so far and experiments lies in the fact that in the simulations we assume the wall to be rigid with infinite impedance. The solid wall perfectly reflects any incoming wave from the surface. In a two-way coupling, the finite acoustic impedance of the solid wall will play a role in the subsequent bubble dynamics.

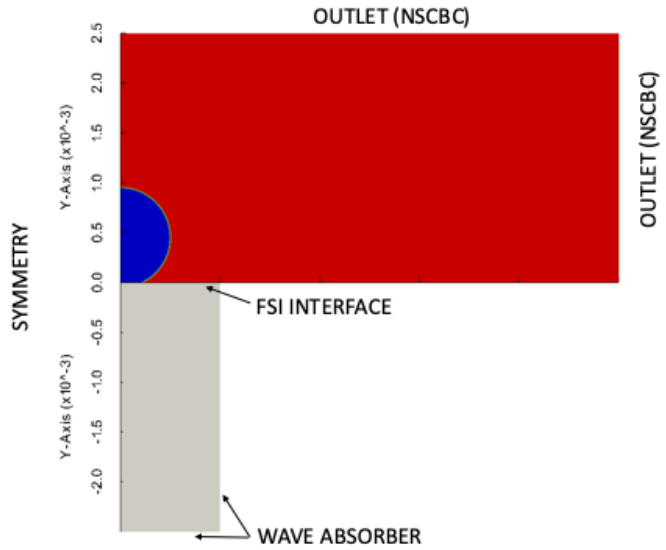

Figure 7.1 – FSI coupling domain and interface between the fluid and solid, max. bubble radius $R_{max} = 500\,\mu m$, (*bottom*) solid domain, size $= 1 \times 2.5\,mm^2$, (*top*) fluid domain, size $= 5 \times 2.5\,mm^2$.

To do so, we take into consideration a fluid and solid domain shown in fig. 7.1. The coupling interface between the fluid and solid domain is taken to be 1 mm from the bubble symmetry axis as most of the dynamical events take place in this region. The use of a much smaller solid computational domain is possible thanks to the use of wave absorbers on the bottom and right boundaries. We will present plots and contours of our 2D investigation for this one-half of the solid domain considered. To aid in our discussion, we will once again present the plots for constitutive law for Al-7075, NAB and St A-2205 in fig. 7.2. The constitutive law for the materials are discussed in section 4.3, the material properties are listed in table 4.1 and the boundary conditions for the solid domain are further discussed in section 4.5. To remind again, the yield strength of Al-7075, NAB and St A-2205 are 500 MPa, 300 MPa & 560 MPa respectively.

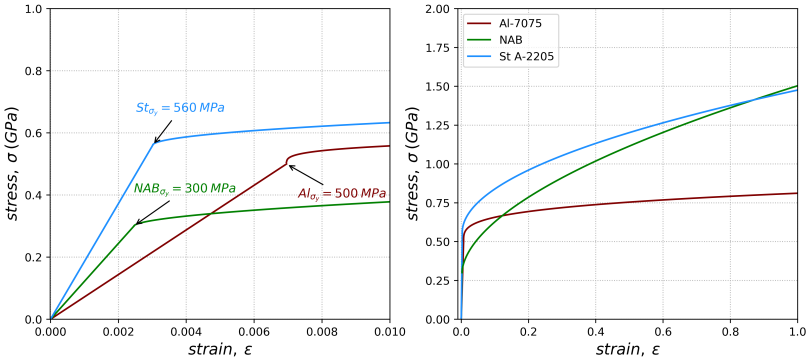

Figure 7.2 – Stress-strain curves for Al-7075, St A-2025 and NAB at strain rate 1.0 s^{-1}.

7.2 One-Way FSI results

First we look at the one-way uncoupled effects on the solid wall considering the test cases $P0.9$, $SH0.9$ and $SH1.4$ presented previously. To recall again our 2D fluid simulations, $P0.9$ is the bubble collapse at $\gamma = 0.9$ under the influence of ambient liquid pressure of $100 MPa$, whereas $SH0.9$ and $SH1.4$ are the shock-induced bubble collapse in atmospheric conditions located at $\gamma = 0.9$ and $\gamma = 1.4$ respectively. The fluid pressure is obtained on 201 nodes along the considered length of solid wall. On the other hand, the solid surface interface is resolved with 801 nodes and therefore the fluid pressures are integrated between the fluid-solid interface with non-matching mesh resolution. The FSI coupling time is $\Delta t_{FSI} = 5\, ns$ for the one-way coupling, which means fluid pressure is extracted at the rigid wall every Δt_{FSI} for the entire simulation duration and are applied at every Δt_{FSI} on the solid interface as time dependent boundary condition. This in turn means that the time step for our implicit solver PASAPAS in Cast3M for solid solution is $\Delta t = 5\, ns$. An example of fluid time step Δt is plotted in fig. 6.3 for the case $P0.9$ which ranges from 1 ns to 0.05 ns depending on the bubble dynamics. The solid is considered initially at rest without any loading at $t = 0\, s$ and therefore not in equilibrium with the initial fluid pressure. For ease of discussion, we identify certain points on the solid domain highlighted in fig. 7.3. The point $S00$ is the point on solid surface at the bubble

symmetry axis, corresponding to the fluid point $F00$. Similarly the point $S10$ is located on the other end of the solid wall corresponding to the point $F10$.

7.2.1 Attached Bubble ($\gamma = 0.9$)

The interface position for the three materials for the case $P0.9$ (for pressure evolution see fig. 6.6) is presented in fig. 7.4. This is the case of attached 2D bubble collapsing under ambient liquid pressure of 100 MPa. The solid interface initially undergoes an elastic displacement due to the ambient liquid pressure of $100MPa$ since the simulation is initialized at $t = 0s$ with an unloaded solid interface. Figure 7.4($left$) is the solid interface after the liquid jet impact at $t = 3.1\ \mu s$ where Al-7075 shows the maximum displacement of 5 μm followed by NAB and St A-2205. Up to this point, NAB and St A-2205 exhibit similar interface displacement except near the symmetry axis. At the end of collapse at $t = 6\mu s$, the maximum interface displacement reaches 23 μm for Al-7075. The displacement in solid wall from liquid jet impact and remaining bubble collapse can be seen distinctively in the plot of fig. 7.4($right$).

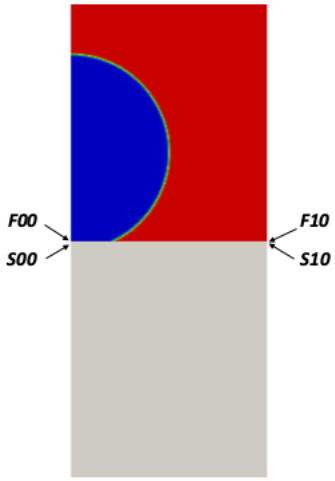

Figure 7.3 – Location of probe points in the solid domain, $S00(x, y) = (0, 0)$, $S10(x, y) = (0.001, 0)$.

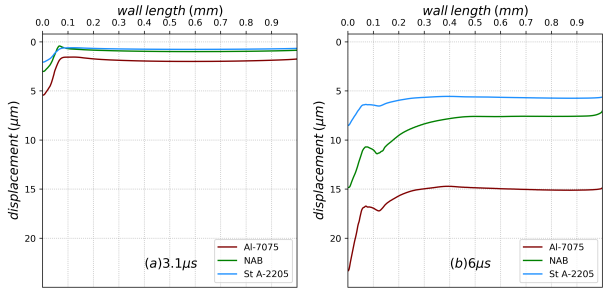

Figure 7.4 – Solid wall interface profile at (a) after liquid jet impact, (b) after entire simulation time $t = 6\ \mu s$, case $P0.9$.

The temporal evolution of displacement at the symmetry axis i.e. pt. $S00$ and pt. $S10$ is plotted in fig. 7.5 (a) & (b) respectively. At pt. $S10$, the elastic response of the solid interface to initial pressure field of 100 MPa can be seen as soon as the simulation starts between time $0 < t < 1\ \mu s$. The interface at pt. $S10$ recovers after initial compression and undergoes a relatively large displacement from the shock waves propagating on the solid wall after 3 μs.

We define a quantity called relative displacement, which is the difference in displacement at pt. $S00$ and at pt. $S10$. The assumption is that pt. $S00$ at the bubble symmetry axis sustains the high impact pressure loads from the bubble collapse and would undergo plastic deformation. On the other hand, pt. $S10$ at the

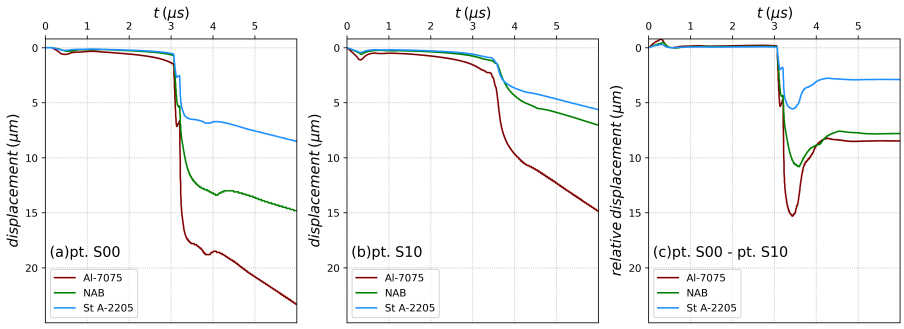

Figure 7.5 – Temporal evolution of surface displacement at (a) S00, (b) S10, (c) relative displacement, case $P0.9$.

outer end of the domain away from the bubble deforms mainly due to the propagation of shock waves, undergoing purely elastic deformation. The difference will help us to identify the permanent plastic deformation at the end of simulation. Figure 7.5(c) exhibits the relative displacement at the bubble symmetry axis where Al-7075 and NAB undergoes permanent deformation of about 8 μm whereas St A-2205 has a permanent deformation of 3 μm.

On the other hand, if we compare the case of attached 2D bubble at atmospheric condition collapsing under the influence of impacting 50 MPa shock wave, we can summarize the results in fig. 7.6 and fig. 7.7. This is case $SH0.9$ with pressure evolution on wall in fig. 6.20. The liquid jet produces considerably similar displacement at pt. $S00$ seen in fig. 7.6(a), a bit smaller owing to 10% decrease in liquid jet pressure for case $SH0.9$ in comparison to $P0.9$. The total displacement at the symmetry axis is also smaller for $SH0.9$, with maximum displacement of 15 μm for Al-7075. The

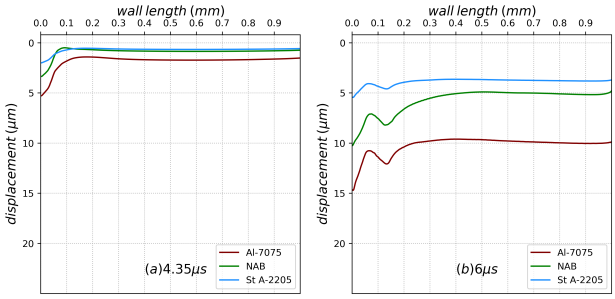

Figure 7.6 – Solid wall interface profile at (a) after liquid jet impact, (b) after entire simulation time $t = 6\ \mu s$, case $SH0.9$.

temporal evolution at different points is shown in fig. 7.7. As the bubble collapse is at atmospheric conditions within the liquid, there is no compression of the solid at the beginning of simulation. There is small observable displacement at pt. $S00$ and pt. $S10$ at around $t = 1.4\ \mu s$ which is from the propagation of elastic waves in the solid after the initial shock used to initiate the collapse has hit the solid surface. An interesting observation can be seen at the relative displacement plot in fig. 7.7(c) where the total plastic deformation is maximum for NAB in the shock-induced collapse case. In comparison, we find the total plastic deformation is maximum for Al-7075 in the pressure-induced collapse case $P0.9$.

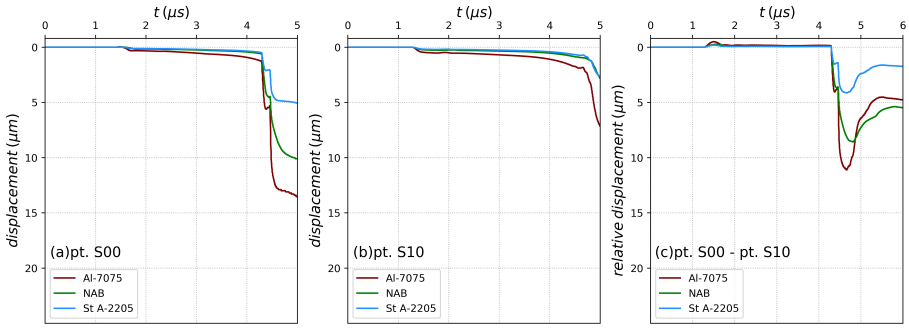

Figure 7.7 – Temporal evolution of surface displacement at (a) S00, (b) S10,(c) relative displacement, case $SH0.9$.

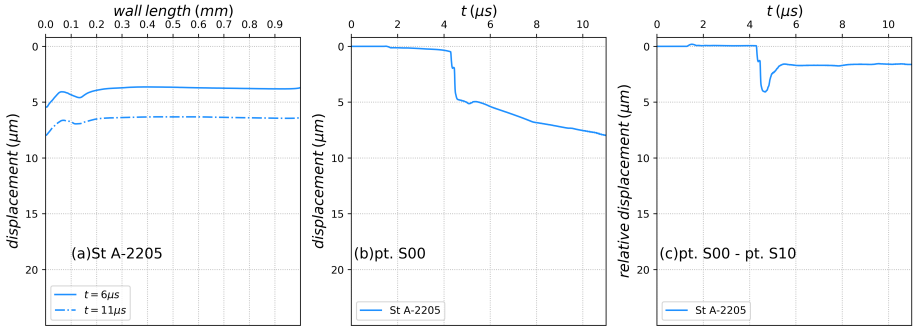

Figure 7.8 – Temporal convergence of relative displacement (a) interface profile at 6 μs and 11 μs, (b) total displacement at S00, (c) relative displacement at S00 for total time $t = 11$ μs, case $SH0.9$.

We looked into the temporal convergence of permanent plastic deformation at pt. $S00$ in fig. 7.8. The solid computational boundaries are treated with wave absorbing characteristic and the normal displacement in the wave absorbing boundaries are not constrained. It physically means that we numerically simulate only a small part of a very large solid material and no reflected elastic waves from the solid boundary reaches our computational domain. This assumption, in return, implies that the solid will be in a continuous state of elastic displacement or compression from the applied impact load and propagation of elastic waves in the solid. Figure 7.8(a) shows the interface position for St A-2205 at $t = 6\,\mu s$ presented previously and at an extended simulation time of $t = 11\,\mu s$. It clearly shows the elastic displacement that the solid interface undergoes even after the highly dynamical load has attenuated. The temporal evolution of displacement and relative displacement at pt. $S00$ shows beyond reasonable doubt that the permanent plastic deformation is converged in time in the simulations.

At this point, we summarize the observations for case $P0.9$ and $SH0.9$ before moving to the detached bubble case. The plastic deformation is higher for liquid pressure-induced collapse in comparison to shock-induced collapse for attached bubble, as the wall pressures are comparatively higher. The plastic response of Al-7075 and NAB are nearly similar whereas St A-2205 offers the maximum resistance to induced load. To quantify the plasticity developed in the solid, we will draw compar-

isons on maximum accumulated plastic strain $P_{\varepsilon_p}^{max}$ and surface area under plastic deformation A_{ε_p}. The surface area under plastic deformation A_{ε_p} is computed from the solid surface undergoing plastic strain of at least 0.5% and above. The values of $P_{\varepsilon_p}^{max}$ and A_{ε_p} for the case $P0.9$ are summarized in table 7.1. For the case $P0.9$,

Material	$P_{\varepsilon_p}^{max}$	A_{ε_p} (m^2)
Al-7075	0.265	7.786×10^{-8}
NAB	0.0904	1.339×10^{-7}
St A-2205	0.0818	2.110×10^{-8}

Table 7.1 – Maximum accumulated plastic strain $P_{\varepsilon_p}^{max}$ and area under plastic deformation A_{ε_p} at $t = 6\,\mu s$ for Al-7075, NAB and St A-2205, case $P0.9$.

the maximum accumulated plastic strain $P_{\varepsilon_p}^{max}$ for Al-7075, NAB and St A-2205 are 0.265, 0.0904 & 0.0818 whereas the area under plastic deformation A_{ε_p} are $7.786 \times 10^{-8}\,m^2$, $1.339 \times 10^{-7}\,m^2$ and $2.110 \times 10^{-8}\,m^2$ respectively. Although $P_{\varepsilon_p}^{max}$ is highest for Al-7075, the A_{ε_p} is highest for NAB. This can be attributed to lower yield strength σ_y of NAB in comparison Al-7075 which generates plasticity in much larger area for the same loading condition. St A-2205 has both the lowest $P_{\varepsilon_p}^{max}$ and A_{ε_p} of all the materials.

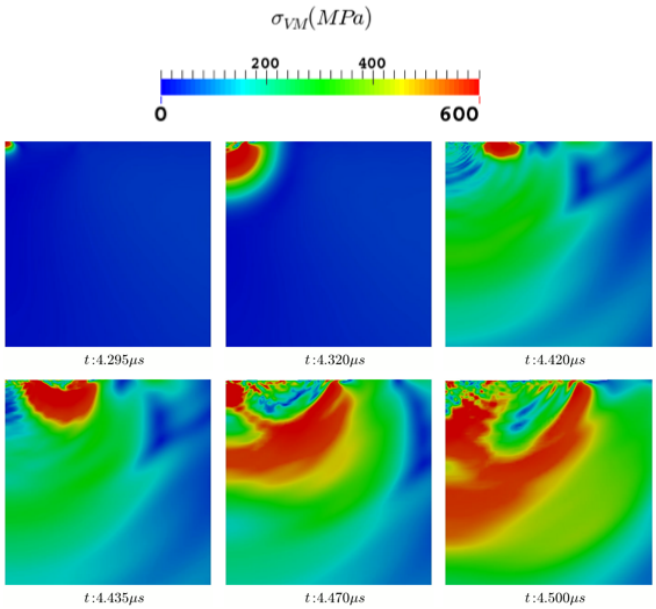

Figure 7.9 – von Mises stress σ_{VM} at different time instants during liquid jet impact ($t = 4.295\ \mu s$), remaining bubble collapse (2D equivalent of 3D bubble torus at $t = 4.420\,\mu s$) and subsequent shock wave superimposition at bubble symmetry axis ($t = 4.470\,\mu s$) for St A-2205, $R_{max} = 495\,\mu m$, case $SH0.9$, frame size $= 1 \times 1\,mm^2$.

The evolution of von Mises stress (σ_{VM}) in St A-2205 at different stages of the collapse for the case $SH0.9$ is presented in fig. 7.9. A value of σ_{VM} greater than the initial yield strength σ_y ($560\,MPa$ for St A-2205) indicates the region where the material have yield seen at $t = 4.295\ \mu s$, $4.420\ \mu s$, & $4.470\ \mu s$ for liquid jet impact, remaining bubble collapse at an offset and shock wave superimposition at the symmetry axis respectively.

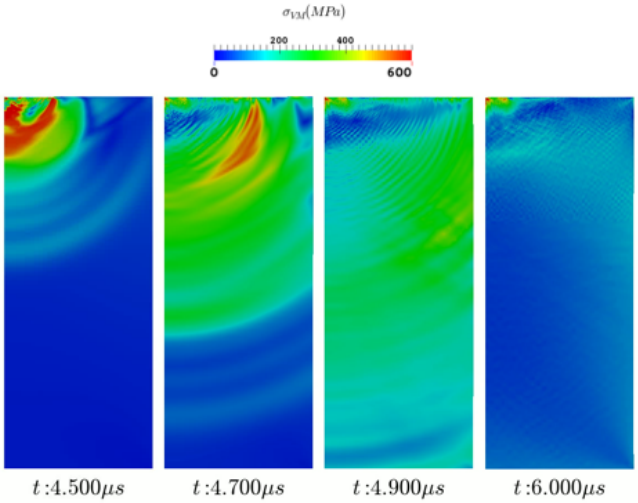

Figure 7.10 – von Mises stress σ_{VM} contour showing propagation of stress waves in the solid for St A-2205, $R_{max} = 495\,\mu m$, case $SH0.9$, frame size $= 1 \times 2.5\,mm^2$.

In the case of $SH0.9$, the maximum accumulated plastic strain $P_{\varepsilon_p}^{max}$ for Al-7075, NAB and St A-2205 are 0.255, 0.0972 & 0.0856 whereas the area under plastic deformation A_{ε_p} are $5.523\times10^{-8}m^2$, $9.816\times10^{-8}m^2$ and $2.052\times10^{-8}m^2$ respectively summarized in table 7.2. In general, we obtain a decrease in A_{ε_p} for the case $SH0.9$ in comparison to $P0.9$ which is expected. The induced pressure loads on the solid walls are higher in the case $P0.9$ due to higher pressure ratios driving the bubble collapse.

Material	$P_{\varepsilon_p}^{max}$	A_{ε_p} (m^2)
Al-7075	0.255	5.523×10^{-8}
NAB	0.0972	9.816×10^{-8}
St A-2205	0.0856	2.052×10^{-8}

Table 7.2 – Maximum accumulated plastic strain $P_{\varepsilon_p}^{max}$ and area under plastic deformation A_{ε_p} at $t = 6\,\mu s$ for Al-7075, NAB and St A-2205, case $SH0.9$.

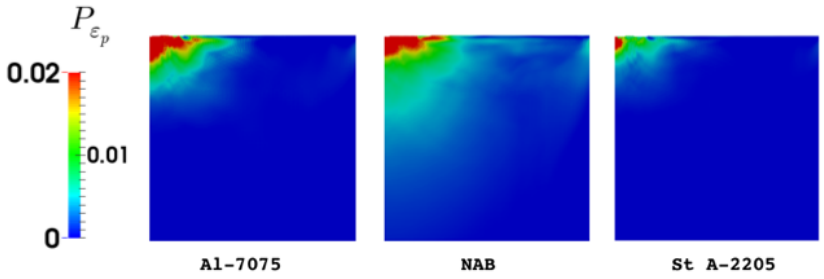

Figure 7.11 – Accumulated plastic strain P_{ε_p} for the three considered material at the end of simulation time $t = 6\,\mu s$, $R_{max} = 495\,\mu m$, case $SH0.9$, frame size$= 1\times1\,mm^2$.

The accumulated plastic strain P_{ε_p} contour at the end of the simulation (i.e

$t = 6\ \mu s$), for all the considered materials is shown in fig. 7.11. The maximum plastic deformation region is located near the bubble symmetry axis where most of the dynamical events takes place. Although the $P_{\varepsilon_p}^{max}$ in Al-7075 is 2.6 times higher than NAB, the A_{ε_p} is highest in NAB i.e. 1.77 times that of Al-7075. This again is related to the material properties considered where the yield strength of NAB is $\sigma_y = 300\,MPa$ whereas for Al-7075, it is $\sigma_y = 500\,MPa$. In addition to the plasticity at the bubble symmetry axis, the propagating shock waves on the solid wall leads to the generation of significant plasticity along the length of the solid wall.

7.2.2 Detached Bubble

In the case of detached bubble at $\gamma = 1.4$ i.e. the case $SH1.4$, the only impact pressure is the water-hammer shock impacting and travelling on the solid wall, discussed with the pressure plot in fig. 6.26. Since there is no bubble rebound

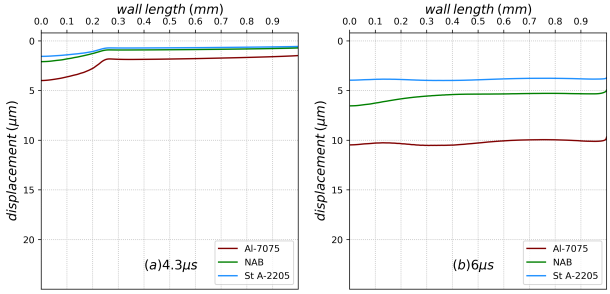

Figure 7.12 – Solid wall interface position (a) after water-hammer shock impact at symmetry axis, (b) after entire simulation time $t = 6\ \mu s$, case $SH1.4$.

considered, at no point does any part of the vapor bubble reaches the wall. The radially propagating shock wave hits near the symmetry axis and travels along the wall. The response of the considered material just after the shock wave hits the wall at $t = 4.3\ \mu s$ and after it has propagated along the wall at $t = 6\ \mu s$ is shown in fig. 7.12. The solid wall interface undergoes displacement all along the considered wall length, with the maximum displacement of about $10\,\mu m$ for Al-7075. At the end of the simulation, only NAB shows a kind of pit near the symmetry axis whereas the displacement for St A-2205 and Al-7075 demonstrates a wavy solid interface with maximum relative displacement at an offset from the symmetry axis. The region of maximum relative displacement corresponds to the region of maximum accumulated plastic strain $P_{\varepsilon_p}^{max}$ in the solid.

We can monitor the propagation of the shock in the interface by tracking the temporal evolution of interface for St A-2205 in fig. 7.13. The displacement of the interface with the passing shock wave and advancing time can be seen. So can be the elastic displacement of the interface long after the shock wave has passed between $t = 5\ \mu s$ and $t = 6\ \mu s$. A few points about the propagation of the shock wave could be explained with the help of fig. 7.15. First the temporal evolution of maximum pressure $p_{max-wall}$ on the wall in fig. 7.15(a) which looks almost planar in time after the shock impact. Comparing it with spatial evolution of pressure in fig. 7.15(b), we can essentially see the radially propagating shock wave with its maximum at different location on the wall at different time instant. Next we can look at the evolution of speed of sound c on the wall obtained from fluid calculations

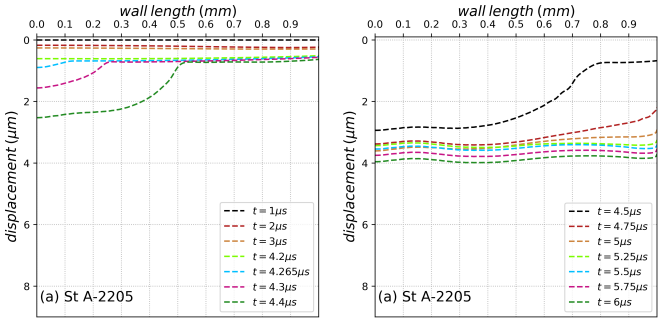

Figure 7.13 – Interface position at different time instant showing propagation of water-hammer shock on St A-2205, case $SH1.4$.

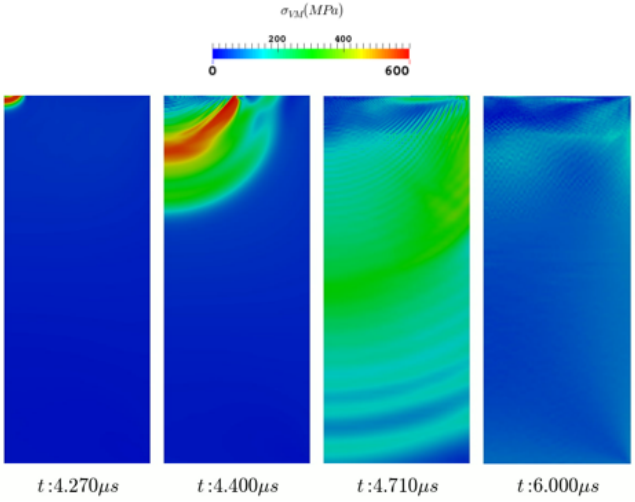

Figure 7.14 – von Mises stress σ_{VM} contour showing propagation of stress waves in the solid for St A-2205, $R_{max} = 500\,\mu m$, case $SH1.4$, frame size $= 1 \times 2.5\,mm^2$.

in fig. 7.15(c), which represents the shock propagating velocity on the solid wall. It can be seen that near the symmetry axis, the shock speed on the wall is very high whereas it starts decreasing as the shock moves along the wall after the impact. Finally we track the fluid velocity $\mathbf{u}_x$ parallel to the wall at a wall normal distance of $\Delta y = 5\,\mu m$ in our viscous fluid calculations. The velocity $\mathbf{u}_x$ increases as the shock travels away from the symmetry axis and such high wall parallel velocity along the interface would indicate high wall shear stresses near the center of the solid wall length considered. We do not try to quantify the wall shear stress as it needs to be resolved with much finer grid resolution in wall normal direction to capture the boundary layers accurately.

The accumulated plastic strain P_{ε_p} contour for a detached bubble collapse is shown in fig. 7.16. The region with maximum plasticity is at an offset distance from the bubble symmetry axis for all the three materials. The $P_{\varepsilon_p}^{max}$ in Al-7075 is 0.014 located at a distance of 450 μm from the symmetry axis and at a depth of 45 μm from the solid surface. Similarly $P_{\varepsilon_p}^{max}$ in NAB and St A-2205 is 0.0109 and 0.00539 respectively, located nearly in the same region in the solid as Al-7075. Using the same definition for area under plastic deformation A_{ε_p} as before, we find

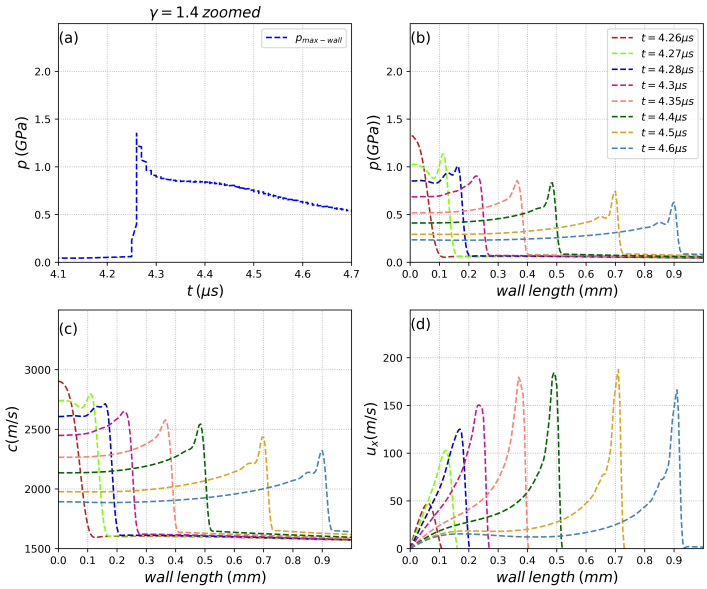

Figure 7.15 – Temporal evolution pressure, sound speed on the wall and fluid velocity u_x at $\Delta y = 5\,\mu m$ (wall parallel i.e. along x-direction from viscous fluid calculations) near solid wall for detached bubble collapse, case $SH1.4$.

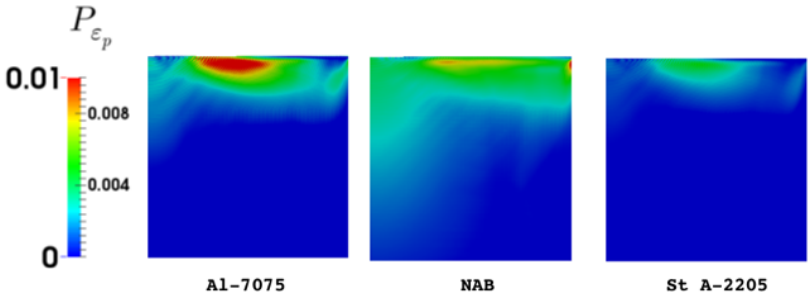

Figure 7.16 – Accumulated plastic strain P_{ε_p} for the considered material at $t = 6\,\mu s$, $R_{max} = 500\,\mu m$, case $SH1.4$, frame size= $1 \times 1\,mm^2$.

plastic surface area of $5.019 \times 10^{-8}\,m^2$, $3.681 \times 10^{-8}\,m^2$ and $6.243 \times 10^{-12}\,m^2$ for Al-7075, NAB and St A-2205 respectively. The values of $P_{\varepsilon_p}^{max}$ and A_{ε_p} for the case $SH1.4$ are summarized in table 7.6. A few observations can be made: the maximum

Material	$P_{\varepsilon_p}^{max}$	$A_{\varepsilon_p}\,(m^2)$
Al-7075	0.014	5.019×10^{-8}
NAB	0.0109	3.681×10^{-8}
St A-2205	0.00539	6.243×10^{-12}

Table 7.3 – Maximum accumulated plastic strain $P_{\varepsilon_p}^{max}$ and area under plastic deformation A_{ε_p} at $t = 6\,\mu s$ for Al-7075, NAB and St A-2205, case $SH1.4$.

plastic strain from the impacting shock wave is found for Al-7075. The maximum plastic strain is located at an offset from the bubble symmetry axis. Although the maximum plastic strain region is located at an offset, the propagating shock does

generate non negligible plasticity all along the length of solid wall. The A_{ε_p} is the highest for NAB similar to what was reported for attached bubble collapse.

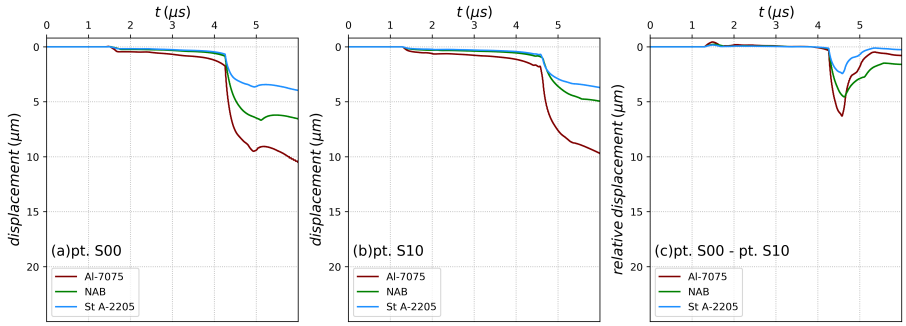

Figure 7.17 – Temporal evolution of displacement at (a) S00, (b) S10,(c) relative displacement, case $SH1.4$.

Such an offset in the maximum plastic strain region has been reported in the doctoral thesis of Paquette 2017 and more recently analyzed in Joshi 2018. The offset has been attributed to the inertial effects in the solid, where due to high shock speed on the solid surface near the symmetry axis the solid cannot respond, and the rate of plasticity increases at an offset with decreasing shock speed. The wall shear stress from the high fluid velocity in the wall parallel direction, possibly in the order of few hundred KPa based on literature, could possibly contribute further to the plastic strain at an offset on the solid wall. Although it must be highlighted that the wall shear stress would be many order smaller in magnitude than the propagating shock wave pressure along the wall. Finally, we present the displacement analysis for detached bubble collapse in fig. 7.17 where the relative displacement indicates the permanent plastic deformation on the material. As seen previously in the fig. 7.13, such plastic deformation takes place more or less everywhere on the solid interface. The maximum plastic deformation is of the order of $2\,\mu m$ for NAB whereas it is of the order of $1\,\mu m$ or less for Al-7075 and St A-2205. It is consistent with our observation where NAB absorbs much of the energy from the shock waves and plasticizes more. For a detached bubble collapse, the pit formation is near the symmetry axis for NAB whereas Al-7075 and St A-2205 undergoes pit formation at an offset from the symmetry axis. The overall pit depth in a detached bubble collapse is smaller in comparison to an attached bubble collapse.

7.3 Two-Way FSI results

Until now, we focused with the one-way coupling on the material response to hydrodynamic loads during cavitation bubble collapse. Such an approach is satisfactory if the solid wall displacement is sufficiently small. The behaviour of the solid wall can be assumed to be almost rigid and no significant attenuation of hydrodynamic loads are expected. On the other hand if the solid wall displacement is large, a two-way coupling approach is needed to account for the feedback of solid wall deformation into the fluid domain. Therefore based on the material response from one-way coupling, the need for a two-way coupled fluid-structure interaction can be evaluated in an extensive cavitation erosion study. In our investigation, we extend

the shock-induced attached bubble collapse i.e. case $SH0.9$ to perform two-way coupled FSI.

The approach for the two-way coupling is similar to the *step-wise coupled analysis* discussed in section 4.6.2. A first step is to perform a complete fluid simulation for bubble collapse assuming a rigid wall. The spatial and temporal evolution of the pressure on the solid wall is extracted every Δt_{FSI} for the entire simulation time. The time and space dependent pressure is applied as a time dependent boundary condition every Δt_{FSI} on the interface in the solid solver to calculate the first step of time dependent displacement of the wall, exactly as for one-way coupling. A second step of fluid simulation is then performed using the time dependent boundary displacement for calculating a second estimate of the pressure on the wall and subsequently followed by a second solid-solver step. A cubic spline interpolation is used to interpolate the computed boundary displacement on 801 nodes to 201 nodes used in fluid domain boundary. This step-wise fluid and solid simulations are performed separately until convergence of pressure and boundary displacement is reached between successive steps. In our analysis, four steps of fluid and solid simulations are performed with pressure and displacement exchanged at $\Delta t_{FSI} = 1\,ns$. The solution convergence is defined by the relative difference below 0.5% in the maximum pressure for CFD and in maximum displacement for CSM between two successive steps. We obtain convergence of pressure and displacement between the third and fourth step of the simulations. For example in the case of St A-2205 out of the total decrease in p_{wh} from liquid jet impact, there is a relative decrease of 81% in the second fluid step and about 19% in the third fluid step of the simulations. The relative difference between the third fluid step and fourth fluid step is 0.3% at which point a convergence of the numerical prediction is achieved. The dampening of pressure and convergence of wall pressure $p_{max-wall}$ after four steps in our FSI analysis for St A-2205 is shown in fig. 7.18.

A coupling has to be implemented between the fluid and solid domain by means of dynamic and kinematic interface conditions. The pressure and shear load from the fluid side has to be in equilibrium with the traction at the boundary of the solid at the fluid–solid interface (dynamic interface condition). As mentioned in the previous section, the order of magnitude of shear loads (based on estimations from literature) are much smaller in comparison to the normal pressure loads in our simulations, we neglect the shear loads at the interface boundary. In addition, the normal velocity of the solid must equal the fluid velocity at the fluid–solid interface (kinematic interface condition) and is achieved by solving the ALE form of the *Navier-Stokes* equations in the fluid solver. The deformation at the fluid interface is uniformly distributed in the rest of the fluid computational domain. The fluid interface velocity must match the velocity of the solid interface determined by the solid solver. At the opposite end of the fluid computational domain, the boundary displacement is zero. The node velocity anywhere else in the domain is evaluated by linear interpolation based on the node position between both ends of the computational boundary.

In a loosely coupled FSI methodology, the flow-induced pressure is transferred time step-wise to the solid as a normal stress at the fluid–solid interface inducing solid wall motion. Only one solution of solid and fluid problem is required per time step, making it appealing in terms of computational effort. In the absence of a convergence sub-iteration step, the solution of the fluid problem is always one step behind the solution of the solid problem. Such a scenario gives rise to time lag (or phase error) between fluid and solid computations. In strongly coupled methods like

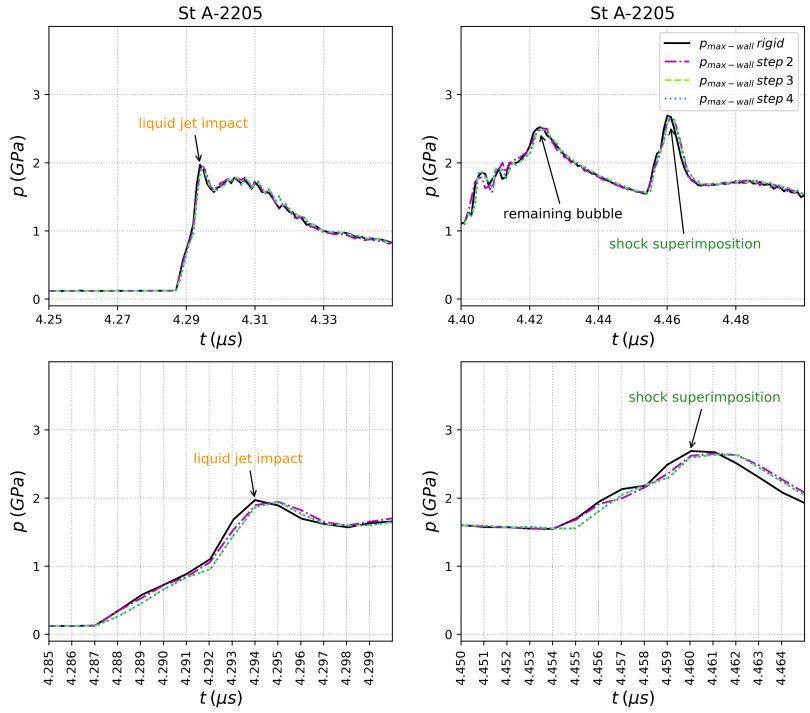

Figure 7.18 – Pressure dampening in *step-wise coupled* FSI showing convergence of pressure on St A-2205 in four steps, case $SH0.9$.

in Paquette 2017, convergence sub-iterations are used at each time step to obtain solution of the fully coupled system.

In our methodology, we reduce the time lag between fluid-solid domain by verifying the convergence between successive steps of fluid and solid computation in our step-wise analysis. The predicted wall displacement from a previous solid solver step allows fluid to evolve in response to the deforming wall and once convergence has been established between the solutions, the wall deformation and fluid pressure are in agreement. It is also important to specify that the time-dependent wall displacements are predicted from a previous solid step and the fluid evolves in response to the deforming wall in the subsequent fluid step. It is thus essential to use smaller Δt_{FSI} to avoid predicting wall displacement too much ahead of the evolving fluid and hence, a $\Delta t_{FSI} = 1\ ns$ is used for the two-way analysis.

We start the analysis of the results by first comparing the maximum wall pressure $p_{max-wall}$ from 2D bubble collapse in fig. 7.19. The temporal evolution of pressure on the rigid wall and deformable wall of Al-7075, NAB, St A-2205 are plotted. To recall the pressure peaks on rigid wall, the first peak of $1.97\ GPa$ at $4.294\ \mu s$ is the p_{wh} from the liquid jet impact at the bubble symmetry axis. The second peak of $2.52\ GPa$ at $4.423\ \mu s$ is the remaining bubble collapse at an offset of $0.1\ mm$ from the bubble symmetry axis. This remaining bubble collapse emits shock waves and the superimposition of the shock waves at the symmetry axis give rise to the third peak of $2.69\ GPa$ at $4.46\ \mu s$.

We will initially look into the first pressure peak from liquid jet impact shown in fig. 7.19. The maximum pressure recorded on a deformable Al-7075 wall at the bubble symmetry axis is $1.82\ GPa$ at $4.297\ \mu s$. Al-7075 is the softest of the three

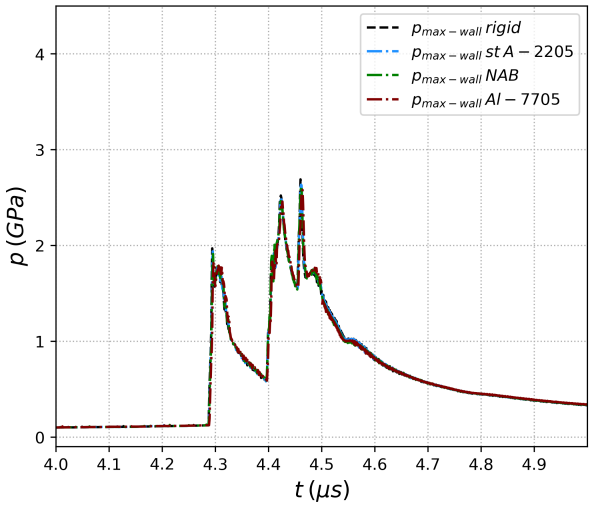

Figure 7.19 – Maximum pressure $p_{max-wall}$ evolution on rigid wall and on the deformable materials with two-way FSI, case $SH0.9$.

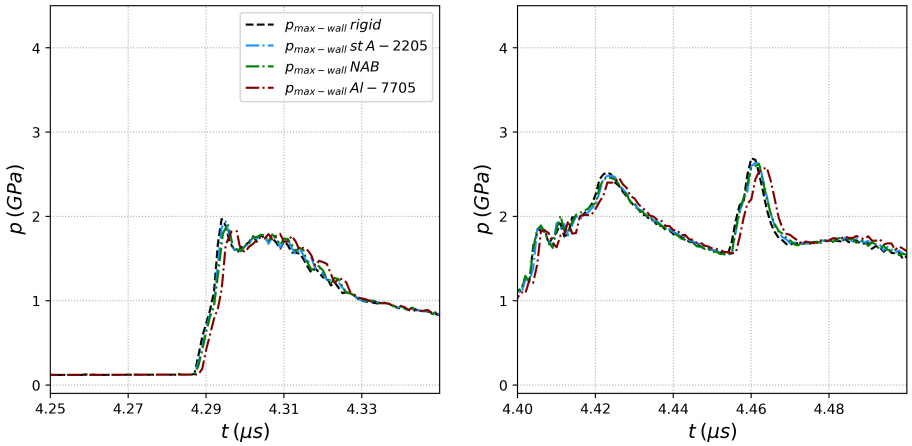

Figure 7.20 – Zoomed-in on maximum pressure $p_{max-wall}$ evolution on rigid wall and on the deformable materials with two-way FSI, case $SH0.9$.

materials and has the lowest slope in the elastic regime of the $\sigma - \varepsilon$ curve. It is expected to provide the maximum damping to the pressure load out of the three materials. The first pressure peak for deformable NAB and St A-2205 wall are 1.91 GPa and 1.94 GPa respectively with time shift due to damping of 1.5 ns and 1 ns. The pressure peak decreased about 8% in Al-7075 at the time of liquid jet impact in comparison to the rigid wall. Similarly the decrease in pressure peaks for NAB and St A-2205 are 3% and 1.5% respectively. We can compare the computed impact pressure of liquid jet for different materials with the theoretical expression of dampened pressure in eq. (7.1) which depends on the ratio of the liquid and the solid acoustic impedances ρc.

$$\Delta p = \frac{(\rho_l c_l v_l)}{1 + (\rho_l c_l / \rho_s c_s)} \tag{7.1}$$

The difference between the numerical results and theoretical estmation from eq. (7.1)

for Al-7075, NAB and St-A2205 are about $2\%, 1.5\% \,\&\, 2\%$ giving a reasonably good agreement. In comparison, Chahine 2015 reported a total dampening in pressure peaks of approximately 6% and 3% for Al-7075 and St A-2205 respectively, from a 3D bubble of $R_{max} = 2\,mm$ at $\gamma = 0.75$ collapsing at an ambient liquid pressure of $0.1\,MPa$. The comparisons for the pressure dampening has been summarized in table 7.4.

Material	Present study	Theoretical eq.(7.1)	Chahine 2015
Al-7075	8%	10%	6%
NAB	3%	4.5%	-
St A-2205	1.5%	3.5%	3%

Table 7.4 – Comparison of pressure dampening between the present study, theoretical estimation and existing literature.

We find the behaviour of NAB and St-A2205 much closer to each other in comparison to Al-7075 as can be seen in fig. 7.20. Similarly the second and third pressure peaks recorded for Al-7075 are $2.45\,GPa$ and $2.57\,GPa$, for NAB are $2.46\,GPa$ and $2.62\,GPa$ and for St A-2205 are $2.48\,GPa$ and $2.63\,GPa$ respectively. The estimated pressures for the three different dynamical peaks i.e. liquid jet collapse, remaining bubble ring collapse and shock wave superimposition during bubble collapse for the rigid wall and the considered materials has been summarized in table 7.5. The pressure decrease due to damping in Al-7075 is about 2.7% in the second pressure peak from remaining bubble collapse and of 4.5% in the third pressure peak from shock wave superimposition at the symmetry axis. The predicted pressure peaks during liquid jet impact, remaining bubble ring collapse and shock wave superimposition for the rigid wall and the considered materials has been summarized in table 7.5. The numerical Schlieren and accumulated plastic strain P_{ε_p} contour for St A-2205

	Peak 1	Peak 2	Peak 3
Material	Liquid jet	Remaining bubble collapse	Shock superimposition
	in GPa		
Rigid	1.97	2.52	2.69
Al-7075	1.82	2.45	2.57
NAB	1.91	2.46	2.62
St A-2205	1.94	2.48	2.63

Table 7.5 – Comparison of estimated pressure loads at different dynamical events during bubble collapse for the rigid wall and the considered materials.

presented in fig. 7.21 shows the different salient features of the two way coupling simulation in the final FSI iteration step. Data is mirrored in both the fluid and solid domain along the Y-axis for visualization. At $t = 4.320\,\mu s$ after the liquid jet impact on the wall, the first sign of plasticity near the bubble symmetry axis can be seen.

The water hammer shock formed at the liquid jet impact on the wall can be seen moving towards the liquid domain at $t = 4.320\,\mu s$ and $t = 4.365\,\mu s$. This shock wave also propagates along the wall with the compressing inner surface of the remaining bubble and generates plasticity along the wall. The fluid interface movement matches the solid surface deformation in the simulation, thus giving a conforming fluid-solid

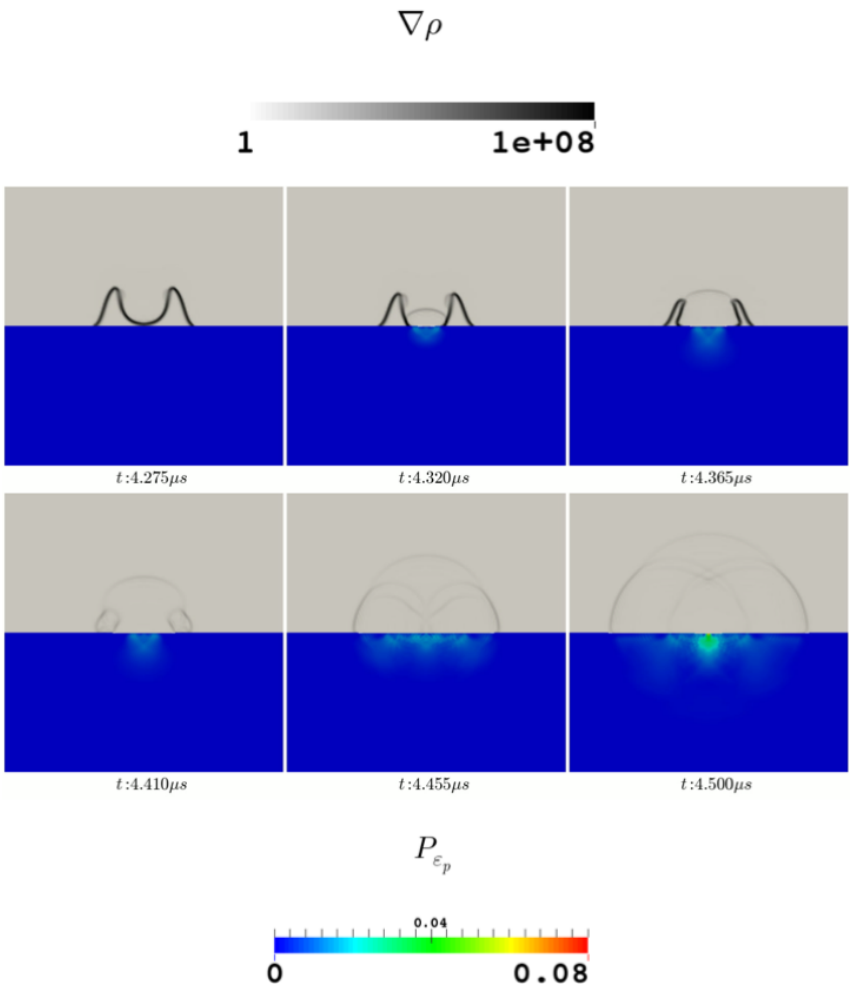

Figure 7.21 – Numerical Schlieren and accumulated plastic strain P_{ε_p} in two-way FSI for St A-2205 at different time instants showing the dynamical features of bubble collapse and corresponding generation of plasticity, $R_{max} = 495\ \mu m$, case $SH0.9$, frame size=$1 \times 1\ mm^2$.

physical domain with matching interface deformation. The relative error in the displacement of the fluid and solid interface is about 0.0023%. The next sequence is the collapse of remaining bubble at an offset of about $0.1mm$ from the symmetry axis, which is accompanied by the emission of another shock. This shock wave produced at an offset travels along the solid surface and the generation of plasticity from the propagating shock waves can be seen at $t = 4.455\ \mu s$. Finally the superimposition of the shocks at the symmetry axis triggers the final pit formation by generating additional plastic strain in the already plasticized area.

A comparison of the maximum accumulated plastic strain $P_{\varepsilon_p}^{max}$ and A_{ε_p} can be drawn between the two-way and one-way computations. Figure 7.22 shows the contours for accumulated plastic strain P_{ε_p} in the materials obtained with one-way and two-way FSI. The maximum plastic strain from two-way coupled simulation for Al-7075, NAB and St A-2205 are 0.191, 0.101 and 0.0608 respectively. If we

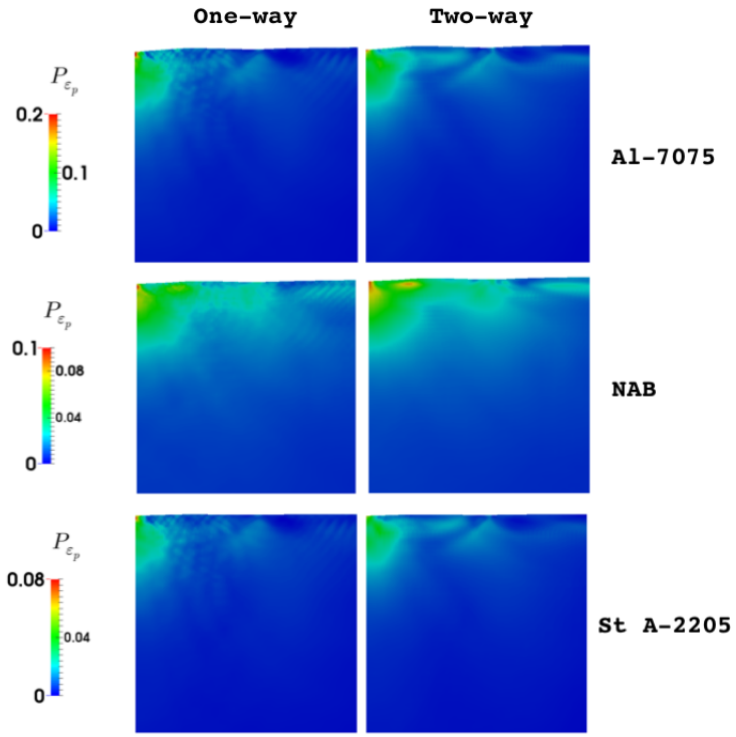

Figure 7.22 – Comparison of accumulated plasticity P_{ε_p} contour for one-way and two-way coupled FSI at $t = 6\mu s$, $R_{max} = 495\mu m$, case $SH0.9$, frame size=$250 \times 250\mu m^2$.

compare the decrease in different peak pressures and its effect on $P_{\varepsilon_p}^{max}$ for Al-7075, we find a decrease of the three peak pressures by 8%, 2.7% and 4.5% which gives a reduction of 25% in the $P_{\varepsilon_p}^{max}$. There is a decrease of 3.5% on A_{ε_p} which is $5.3291 \times 10^{-8}\, m^2$ for Al-7075 with two-way coupling. We obtain A_{ε_p} for NAB and St A-2205 of $9.2381 \times 10^{-8}\, m^2$ and $2.0062 \times 10^{-8}\, m^2$ which is a decrease of of 6% and 2.3% respectively. Similar to what we have seen before, NAB produces the maximum

Material	$P_{\varepsilon_p}^{max}$	$A_{\varepsilon_p}\ (m^2)$
Al-7075	0.191	5.3291×10^{-8}
NAB	0.101	9.2381×10^{-8}
St A-2205	0.0608	2.0062×10^{-8}

Table 7.6 – Maximum accumulated plastic strain $P_{\varepsilon_p}^{max}$ and surface area under plastic deformation A_{ε_p} at $t = 6\ \mu s$ for Al-7075, NAB and St A-2205 with two-way FSI coupling, case $SH0.9$.

plasticized area in comparison to other materials. The decrease in plasticized surface area is also highest in NAB, indicating its sensitivity in developing plastic strain due to low yield strength.

In our final analysis, we can draw comparisons of interface shape for the three materials at final simulation time of 6 μs presented in fig. 7.23. We find similar pit shapes in one-way and two-way simulation for the three materials. The relative difference in final interface position between one-way and two-way coupling is the maximum in Al-7075 followed by NAB and St A-2205 respectively. The highest

relative difference in final interface position for Al-7075 highlights the material behaviour of maximum damping the impact pressure loads. NAB, although allowing far less surface deformation and damping, responds with much larger plasticized surface area. The behaviour of St A-2205 is much similar to rigid wall, although it damps more shock wave pressure peak, about 2.3% in comparison to 1.5% of pressure from liquid jet impact.

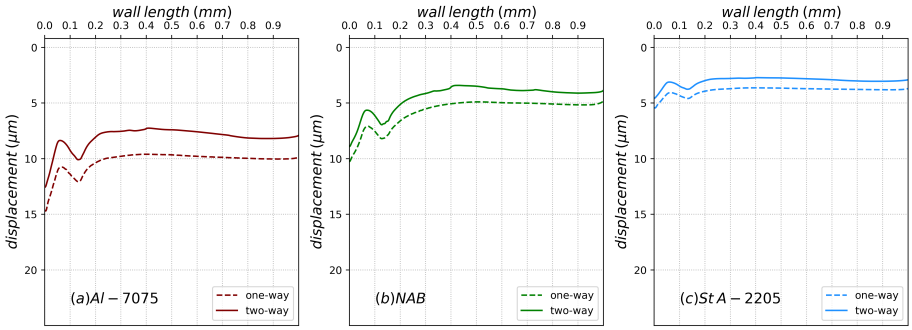

Figure 7.23 – Comparison of solid interface profile for one-way and two-way coupled FSI, case $SH0.9$.

We can draw comparisons of our observations with the two-way coupled analysis presented in Paquette 2017 for a shock-induced detached bubble collapse. A decrease in maximum pressure peak of 10% for $Al-7075$ was reported with a decrease of plasticized area by a factor of 2 in the simulations. We are in reasonable agreement with the magnitude of pressure damping from the deformed solid wall of Al-7075. The discrepancy in the magnitude of decrease in plasticized area can be explained with two major differences. The material properties considered in Paquette 2017 are at strain rate of 0.05 s^{-1} where the yield strength σ_y of Al-7075 is 335 MPa in comparison to 500 MPa at strain rate of 1.0 s^{-1} in our work. Therefore, behaviour of Al-7075 and NAB are reported to be closer in Paquette 2017 with yield strength σ_y of 335 MPa and 300 MPa respectively. Second is the difference in collapse dynamics and pressures from detached and attached bubble collapse. A detached bubble collapse is prominently the emission of shock wave at a distance and response of material to shock wave propagation on the wall. It is marked with very small plastic strain and surface displacement, also seen in our results. As we have highlighted throughout the course of this work, an attached bubble collapse is a much more complex dynamical event dominated by many interconnected physical features which determine the resultant pressures on the wall. There are multiple shock waves impacting and propagating on the solid wall, the magnitude of which are often many orders higher in comparison to detached bubble collapse. As a result, the decrease in $P_{\varepsilon_p}^{max}$ is considerable in two-way coupling in this work, for example about 30% in St A-2205. On the other hand, the area under plastic deformation A_{ε_p} decreases by about 3.5%, 6%, 2.3% for Al-7075, NAB and St A-2205 respectively.

7.4 Summary

In this chapter, we carried out a comparative study of material response for aluminum alloy Al-7075, nickle-aluminum bronze alloy (NAB) and duplex stain-

less steel (St A-2205). We first highlighted the difference in material behaviour for shock-induced and high ambient liquid pressure-induced collapse relevant in technical applications. The solid response predicted higher plastic deformation in liquid pressure-induced collapse owing to higher driving pressure for the collapse which generates high pressure loads in such applications. We then investigated the material response to attached and detached bubble collapse. The attached bubble collapse is found to cause maximum plastic deformation and pit formation at the bubble symmetry axis. For the considered attached bubble of $R_{max} = 495\ \mu m$ at $\gamma = 0.9$ (case SH0.9) in our one-way FSI analysis, we found a total displacement of $5\ \mu m$ in Al-7075 at the bubble symmetry axis from the impacting liquid jet. In comparison, the remaining bubble collapse (2D equivalent of bubble torus collapse) produced a total displacement of $9\ \mu m$ in Al-7075. In all the materials, we found the remaining bubble collapse produces higher surface deformation in comparison to the liquid jet for the attached bubble at $\gamma = 0.9$.

The plastic deformation in detached bubble collapse is at an offset from the symmetry axis due to inertial effects in the solid. Overall we found higher plastic deformation and pit formation on the solid from a collapsing attached bubble. Next, we presented a two-way coupled investigation where we examined the effect of surface deformation on the resulting pressure peaks. The two-way coupled simulations provides a more reasonable predictions of pressure loading on deformable solid walls as well as the plasticity generated due to loading in the solid.

We can also draw qualitative comparisons of our results with the recent findings in Dular 2019, especially on the observed mechanism of damage in experimental investigations of the collapsing bubble of $R_{max} = 3.3\ mm$. Surface damage was recorded with high-speed visualisations on a $9\ \mu m$ aluminium foil attached to a $1\ mm$ thick microscopic glass by an optically clear $50\ \mu m$ thick adhesive tape. For $\gamma = 0.9$, the liquid jet produced a pit depth of $15\ \mu m$ whereas the bubble ring (or torus) collapse had a pronounced effect on the pit depth, which was reported to be in the order of $35\ \mu m$. The material damage volume as a function of stand-distance γ reported in Dular 2019 is shown in fig. 7.24, which shows that the pit formation by liquid jet is pronounced at very small values of γ whereas at $\gamma = 0.9$, the bubble ring collapse is the cause for the resulting pit formation.

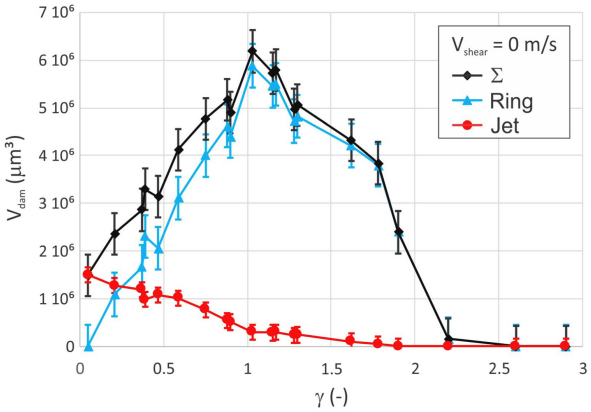

Figure 7.24 – Surface damage as a function of distance from the wall (Dular 2019)

Part IV

Final Remarks

Chapter 8

Conclusions and Perspective

8.1 Conclusions

In the course of this thesis, investigation on the mechanism of cavitation erosion on the fundamental scale of bubble collapse is carried out. The broader objective is to model the dynamics of collapsing bubbles near rigid and deforming materials and characterize the material response by coupling the fluid and solid mechanics. A Compressible Cavitation Solver (*CCS*) has been developed in YALES2 for CFD simulation of liquid water and two-phase cavitating flows in 2D and 3D. The compressible *Navier-Stokes* equations are solved together with the equations of state defining all the fluid phases to model small scale as well as large scale cavitating structures efficiently. The solver takes compressibility and viscous effects into account and is capable of resolving highly instantaneous pressure loads from violent collapses of cavitating structures inside the flow field. The improvement in solver algorithm for cavitation modelling, the advantages of NSCBC characteristics boundary conditions and strategies to reduce numerical oscillations have been highlighted for two-phase compressible flows. This has been extended to the Arbitrary Lagrangian-Eulerian (ALE) formulation for computational mesh movement in the Cavitation ALE Solver (*CLE*) required for coupled fluid-structure interaction studies. The developed solver algorithm is verified through a series of single-phase shock tube and two-phase analytical Rayleigh-Plesset test cases. The solid mechanics simulations have been performed with the finite-element solver Cast3M solver to predict the dynamical behaviour of the materials. The elastic-plastic response of aluminum (Al-7075) alloy, nickel-aluminum-bronze (NAB) alloy and duplex stainless steel (St A-2205), following a power law relationship between stress and strain in the plastic regime, has been studied and compared for different cases. A step-wise coupling approach has been employed to realize one-way and two-way fluid structure interaction simulation. Such a methodology has been demonstrated to be capable of coupling fluid and solid physical domains with minimal code development.

In our numerical study on bubble collapse, higher pressure loading on the material surface is obtained for smaller stand-off distances where the bubble is attached to the wall in comparison to detached bubble away from the wall. In attached bubble collapse, the pressure loading is due to the liquid-jet impact and collapse of the remaining bubble ring (or bubble torus) which emits high-intensity shock waves near the solid wall. The high pressure loading results in generation of plastic strain at

the bubble symmetry axis as well as along the material surface due to shock wave propagation in the domain. Permanent plastic deformation in the shape of pits in the material surface is formed at the symmetry axis for all the materials.

For higher stand-off distances where the bubble is detached and away from the wall, the shock waves emitted on bubble collapse hit the wall and propagate along the material surface. The high pressure loading results in high stress waves propagating radially from loading location and maximum plastic strain is generated under the material surface at an offset from the bubble symmetry axis. For a detached bubble collapse, the pit formation for NAB is found to be near the symmetry axis whereas for Al-7075 and St A-2205, the pit formation takes place at an offset from the symmetry axis on the region of maximum plastic strain. The relative pit depth for detached bubble collapse is found to be smaller in comparison to attached bubble collapse.

In our investigation, the maximum accumulated plastic strain and surface area under plastic deformation in the solid is found to be higher for attached bubble collapse in comparison to detached bubble collapse. The high plastic deformation is related to the observation of high pressure loading in attached bubbles in comparison to detached bubbles. The 3D bubble collapse results also demonstrate a more concentrated pressure loading on the material surface for attached bubbles with the liquid-jet impact and subsequent pressure loading when the bubble ring collapses very close to the material surface. Such concentrated pressure loading is indicative of resulting pit on the material surface from liquid-jet impact on bubble collapse.

Two-way coupled fluid-structure interaction simulation shows that the pressure load is damped on the material with surface deformation. The decrease in pressure loads are higher when the surface deformation is high due to increased energy absorption. The impact pressure from liquid jet impact on Al-7075 decreases by 8% whereas the decrease in pressure peak during remaining bubble ring collapse and shock wave superimposition is 2.7% and 4.5%. In comparison to one-way coupled prediction of material response, decrease in pressure peaks in two-way coupling resulted in decrease of 25% in the maximum accumulated plastic strain and 3.5% of total plasticized area in Al-7075. On the other hand, the behaviour of duplex stainless steel is very close to that of a rigid surface. This is consistent with the observation of delay in pressure peaks and lower magnitude of impact pressures on compliant coatings.

The experimental investigations provided deeper insight into bubble shapes and dynamics at different stand-off distances γ. When the bubble nucleation is closer to the wall, at $\gamma = 0.55$, the bubble grows and collapses attached to the wall and indentation pits are formed on the material surface. For $0.8 \leq \gamma \leq 1.2$, the bubble cavity is pushed away from the material surface due to the *splash* effect. No surface damage was observed for the range of stand-off distances where the bubble cavity rises up with the "splash" and collapses away from the material surface.

At $\gamma = 1.4$, the bubble undergoes the first collapse away from the material, and a shock wave is emitted towards the surface. Numerical simulations neglecting the rebound have shown that the shock wave cause accumulation of plastic strain at an offset distance from the bubble symmetry axis. The maximum plastic strain is approximately at an offset distance of the initial bubble radius from the symmetry axis. In comparison, the experimental dynamics shows that the rebounding bubble torus collapses on the material surface and disintegrates into tiny micro-bubbles. The collapsing micro-bubbles formed by the breakup of the main bubble cavity, produces pitting like damage along a circular ring on the material surface. Based

on these observations, it can be suggested that shock waves alone are not sufficient to cause surface pitting like damage on material surface. The shock waves from the first collapse of detached bubble produces significant plasticity in the material. The pitting like damages are caused either by the liquid-jet from the micro-bubbles or very localized shock waves produced when the micro-bubble collapses close enough to the material surface. From the perspective of single cavitation bubble, it can be concluded that the maximum damage takes place when the bubble is attached or is very close to the material surface.

8.2 Perspective and Future Work

The developed solvers and methodology can be extended to predict cavitation dynamics in complex flow applications. As the solvers are developed in a modular and structured basis following the guidelines for YALES2, extensions and modifications can be implemented easily. A parametric study for different bubble size, stand-off distances and collapse driving pressure on the dynamics of single bubble and bubble-bubble interaction can be carried out in 2D and 3D. The representation of the cavitation behaviour can be improved by including the effect of non-condensable gas into the two-phase flow model by employing a multi-component homogeneous mixture model ($p_{vapor} = p - p_{gas}$), where p_{vapor} is the vapor pressure, p is the pressure inside the bubble & p_{gas} is the non-condensable gas pressure. This can be further extended to study bubble cloud behaviours where the interaction between bubbles influences the resulting pressure loads on the material. A classification of bubble cloud characteristics and its effects on resulting surface damages deserves further investigations.

On the material side, accounting for the strain rate sensitivity of the material would provide more realistic behaviour. Subsequently, the work can be extended to include fracture and damage model to account for actual mass loss observed in experimental studies. A 3D extension of the fluid-structure interaction model for single bubble and bubble cloud collapse would provide substantial amount of information on the missing links between fluid and solid mechanics. The FSI methodology can be optimized by using larger time step size for exchanging information between fluid and solid domains, when the dynamics does not change much and pressure loads are insignificant. An extension to strongly coupled FSI with MPI for information exchange between domains would automatize the methodology but would require substantial amount of work.

Part V

Appendix

Appendix A

Numerics

A.1 Method of Characteristics

The 1D Euler equations can be used to derive the analytical solution for wave propagation in compressible flows. The equations of conservation of mass and momentum can be expressed as eq. (A.1):

$$\begin{aligned} \frac{\partial \rho}{\partial t} + \frac{\partial (\rho u)}{\partial x} &= 0 \\ \frac{\partial \rho u}{\partial t} + \frac{\partial (\rho u^2 + p)}{\partial x} &= 0 \end{aligned} \tag{A.1}$$

The system can be written in vector-matrix form in eq. (A.2), (A.3) & (A.4):

$$\frac{\partial \bar{W}}{\partial t} + \bar{\bar{A}}(\bar{W}) \frac{\partial \bar{W}}{\partial x} = 0 \tag{A.2}$$

$$\bar{W} = \begin{pmatrix} w_1 \\ w_2 \end{pmatrix} = \begin{pmatrix} \rho \\ \rho u \end{pmatrix} \tag{A.3}$$

$$\bar{F} = \begin{pmatrix} \rho u \\ \rho u^2 + p \end{pmatrix} \tag{A.4}$$

$\bar{\bar{A}}(\bar{W})$ means $\bar{\bar{A}}$ is a function (component) of $\bar{W}$ in eq. (A.5).

$$\bar{\bar{A}}(\bar{W}) = \frac{\partial \bar{F}}{\partial \bar{W}} = \begin{pmatrix} \frac{\partial \rho u}{\partial \rho} & \frac{\partial \rho u}{\partial \rho u} \\ \frac{\partial (\rho u^2 + p)}{\partial \rho} & \frac{\partial (\rho u^2 + p)}{\partial \rho u} \end{pmatrix} \tag{A.5}$$

The equation of state and speed of sound c for liquid water are given in eq. (A.6) & (A.7):

$$p = (p_{sat} + B) \left(\frac{\rho}{\rho_{sat,l}} \right)^N - B \tag{A.6}$$

$$\frac{\partial p}{\partial \rho} = c^2 = (p_{sat} + B)\ N\ \frac{(\rho)^{N-1}}{(\rho_{sat,l})^N} \tag{A.7}$$

The components of $\bar{\bar{A}}(\bar{W})$ can be expressed as eq. (A.8), (A.9), (A.10) & (A.11):

$$\frac{\partial \rho u}{\partial \rho} = \frac{\partial w_2}{\partial w_1} = 0 \tag{A.8}$$

$$\frac{\partial \rho u}{\partial \rho u} = \frac{\partial w_2}{\partial w_2} = 1 \tag{A.9}$$

$$\begin{aligned} \frac{\partial \rho u^2 + p}{\partial \rho} &= \frac{\partial \rho u^2}{\partial \rho} + \frac{\partial p}{\partial \rho} \\ \frac{\partial (w_2^2/w_1)}{\partial w_1} + \frac{\partial p}{\partial \rho} &= -u^2 + c^2 \end{aligned} \tag{A.10}$$

$$\begin{aligned} \frac{\partial \rho u^2 + p}{\partial \rho u} &= \frac{\partial \rho u^2}{\partial \rho u} + \frac{\partial p}{\partial \rho u} \\ \frac{\partial (w_2^2/w_1)}{\partial w_2} + \frac{\partial p}{\partial \rho u} &= 2u \end{aligned} \tag{A.11}$$

Therefore, the eigenvalues of $\bar{\bar{A}}$ are:

$$\begin{aligned} det\left(\bar{\bar{A}} - \lambda \bar{\bar{\mathcal{I}}}\right) &= 0 \\ det\begin{pmatrix} -\lambda & 1 \\ -u^2 + c^2 & 2u - \lambda \end{pmatrix} &= 0 \end{aligned} \tag{A.12}$$

$$\begin{aligned} -\lambda\left(2u - \lambda\right) - \left(C^2 - U^2\right) &= 0 \\ \lambda^2 - 2u\lambda + \left(u^2 - c^2\right) &= 0 \end{aligned} \tag{A.13}$$

the roots are:

$$\begin{aligned} \lambda &= \frac{2u \pm \sqrt{4u^2 - 4\left(u^2 - c^2\right)}}{2} \\ \lambda &= u \pm c \end{aligned} \tag{A.14}$$

The eigenvalues along with the fluid velocity u define the trajectories for information propagation in 1D called the *"characteristics curve"* given in eq. (A.15).

$$\begin{aligned} \frac{dx}{dt} &= \lambda_1 = u - c \\ \frac{dx}{dt} &= \lambda_2 = u \\ \frac{dx}{dt} &= \lambda_3 = u + c \end{aligned} \tag{A.15}$$

A.2 Integral theorems

For any arbitrary closed volume Ω with its boundary surface $\partial\Omega$, the identities for a scalar ϕ and vector field F are:

$$\int_\Omega \nabla \phi dV = \oint_{\partial\Omega} \phi dS \tag{A.16}$$

$$\int_\Omega \nabla \cdot F dV = \oint_{\partial\Omega} F \cdot dS \tag{A.17}$$

$$\int_\Omega \nabla \times F dV = \oint_{\partial\Omega} F \times dS \tag{A.18}$$

A.3 Vector identities

The vector identities for any scalar ϕ and vector field F are:

$$\nabla \times \nabla\phi = 0 \tag{A.19}$$

$$\nabla \cdot (\nabla \times F) = 0 \tag{A.20}$$

$$\nabla \cdot (\phi F) = F \cdot (\nabla\phi) + \phi\,(\nabla \cdot F) \tag{A.21}$$

$$\nabla \times (\phi F) = \phi \nabla \times F + (\nabla\phi) \times F \tag{A.22}$$

$$\nabla\,(\nabla \cdot F) = \nabla^2 F + \nabla \times (\nabla \times F) \tag{A.23}$$

Appendix B

Computational domain and mesh

The computational domain and mesh used for all numerical simulations are presented below. A good quality mesh is essential for improving the solution accuracy and reduce numerical oscillations in computation. Mesh quality can be expressed in terms of skewness.

Skewness is one of the primary quality measures for a mesh determining how close a mesh element is to the ideal equilateral element, defined as eq. (B.1):

$$E_{sk} = \frac{S_{eq} - S}{S_{eq}} \tag{B.1}$$

Here, S is the area (in 2D) or the volume (in 3D) of the considered mesh element and S_{eq} is the maximum area (in 2D) or volume (in 3D) of an equilateral cell circumscribing the same radius as the considered mesh element. A value close to 0 describes an equilateral element and a value close to 1 describes a degenerated element.

The computational mesh has been generated in Ansys GAMBIT software except the 3D full domain for Rayleigh Plesset validation which has been generated in Ansys ICEM-CFD. The 2D, 3D cartesian mesh for bubble collapse and FEM mesh has been generated in the solver YALES2 and CAST3M solver respectively.

B.1 2D Rayleigh Collapse

The computational domains used for 2D Rayleigh validation test case presented in Chapter 5 are shown below. A full domain in fig. B.1 and $(\frac{1}{4})^{th}$ symmetrical domain in fig. B.3 are compared. Uniform quad elements are used in the center of the domain with $\Delta x = \Delta y = 5\ \mu m$ while the exterior domain is meshed with tri elements and a growth ratio in cell size of 1.05. The smooth transition in cell size between the quad elements in the domain center and tri elements in the farfield is shown in fig. B.2.

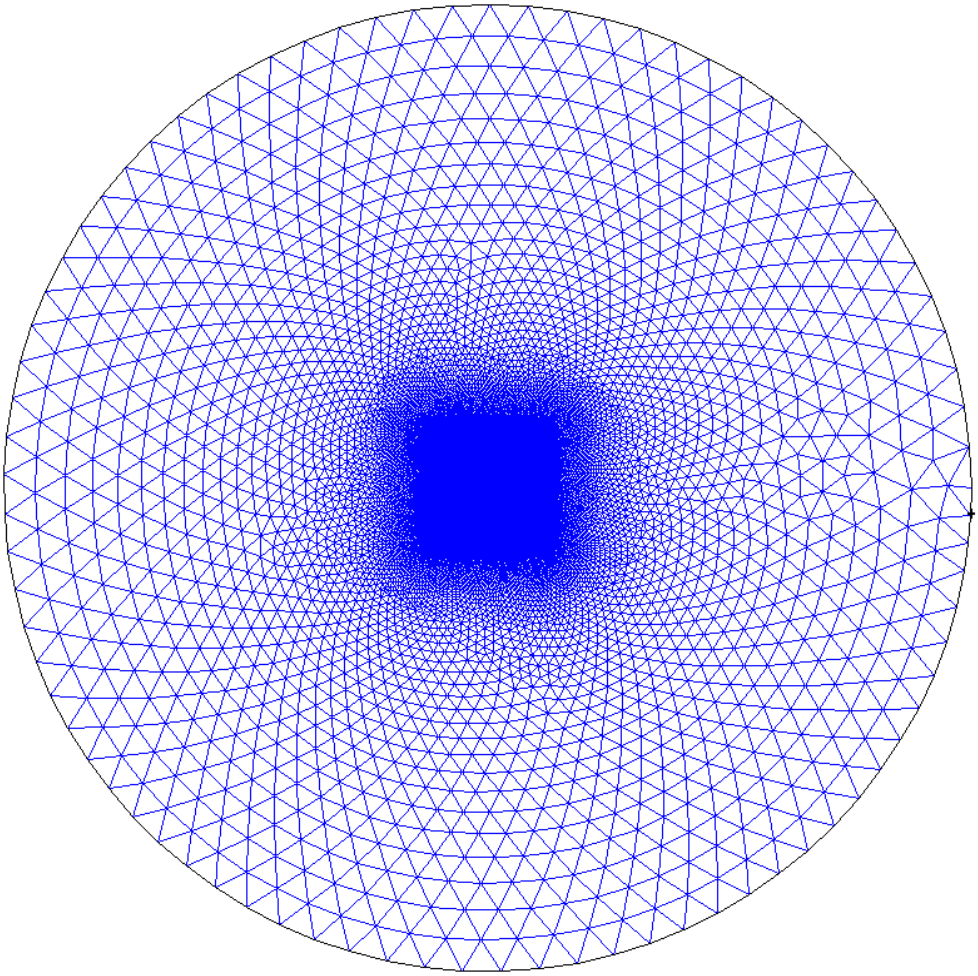

Figure B.1 – Computational domain for full 2D Rayleigh collapse case, $R_{max} = 8.5\,mm$, $N_{cells} = 205648$, max. skewness=0.47.

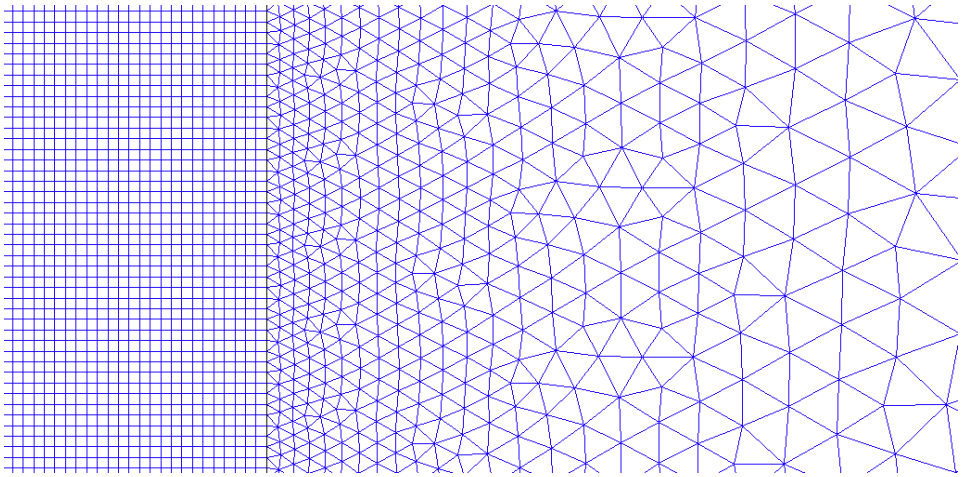

Figure B.2 – Cell size transition between the uniform quad-elements and surrounding tri-elements, growth ratio= 1.05.

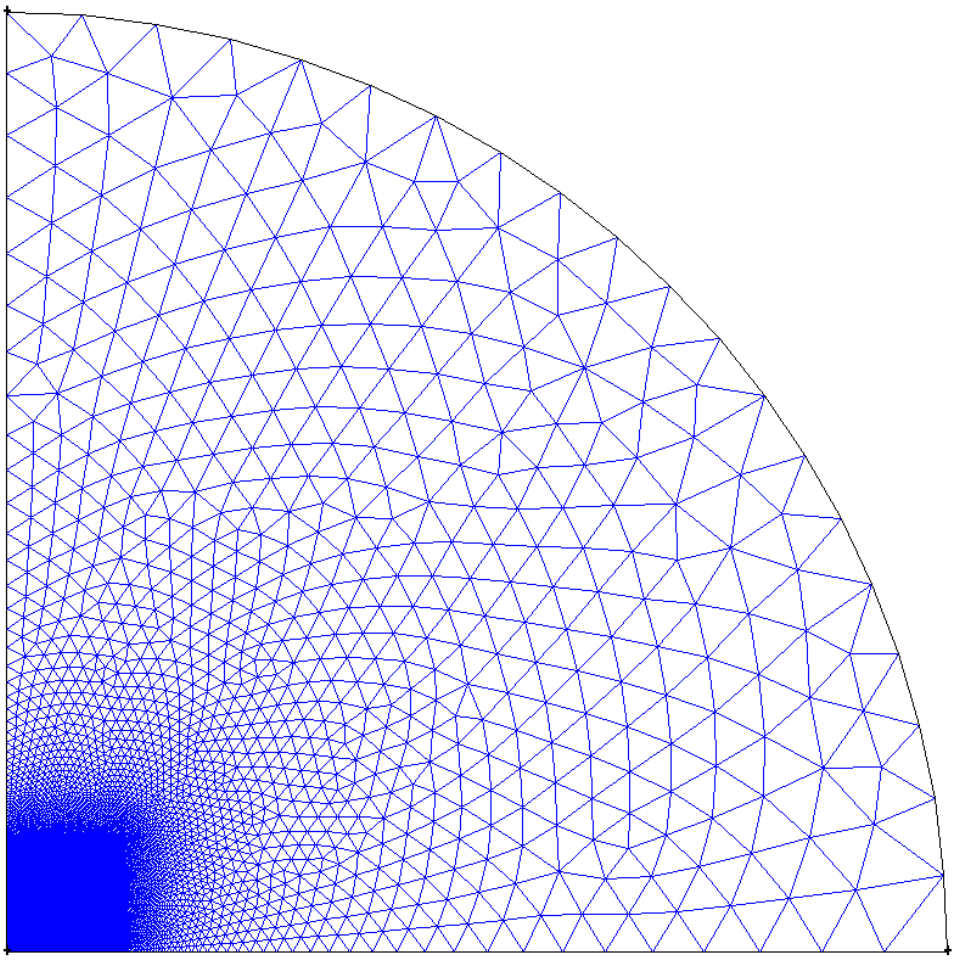

Figure B.3 – Computational domain for $(\frac{1}{4})^{th}$ symmetrical computation of 2D Rayleigh collapse case, $R_{max} = 8.5\,mm$, $N_{cells} = 50992$, max. skewness=0.4.

B.2 3D Rayleigh-Plesset

For a 3D Rayleigh-Plesset validation presented in Chapter 5, a full 3D domain in fig. B.4 and a $(\frac{1}{8})^{th}$ symmetrical domain in fig. B.5 are used. The full 3D domain of size $10 \times 10 \times 10\,mm^3$ is meshed with hexahedral cells of $\Delta x = \Delta y = \Delta z = 5\,\mu m$ at the domain center to have uniform spaced mesh along the bubble radius. The farfield domain is meshed with hexahedral cells of uniformly increasing size towards the domain boundary with a growth ratio of 1.1.

In the $(\frac{1}{8})^{th}$ symmetrical domain, bubble is resolved with uniformly spaced hexahedral cells with $\Delta x = \Delta y = \Delta z = 5\,\mu m$ whereas the farfield domain is meshed with tetrahedral cells and a growth ratio of 1.1.

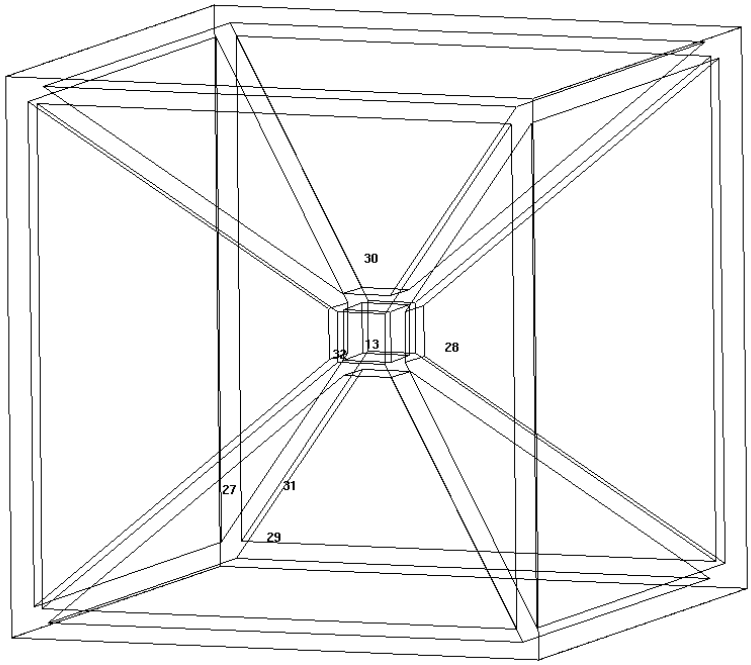

Figure B.4 – Full domain for 3D Rayleigh-Plesset validation, domain size $10 \times 10 \times 10\, mm^3$, $N_{cells} = 14771173$, max. skewness=0.5.

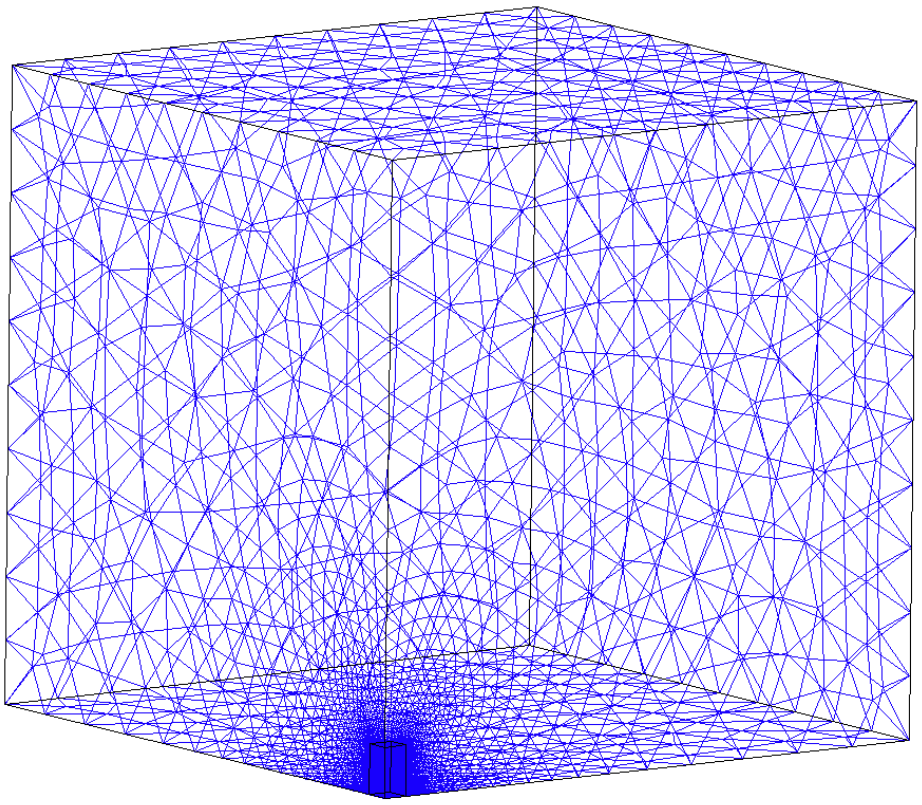

Figure B.5 – $(\frac{1}{8})^{th}$ symmetrical domain for 3D Rayleigh-Plesset validation, domain size $20 \times 20 \times 20\, mm^3$, $N_{cells} = 6117566$, max. skewness=0.68.

B.3 Bubble collapse

The 2D bubble collapse near solid boundary has been investigated for two boundary configurations - domain boundary at $40R_0$ in fig. B.6 and domain boundary at $10R_0$ in fig. B.8. In $40R_0$ the bubble is resolved in within a region of uniformly spaced quad cells with $\Delta x = \Delta y = 5\ \mu m$ whereas the exterior domain has unstructured quadrilateral cells with growth ratio of 1.05. This value has been used keeping in mind the transition between the mesh cells shown in fig. B.7. A higher growth ratio increases the possibility of numerical oscillations in the interface between the two meshed domains.

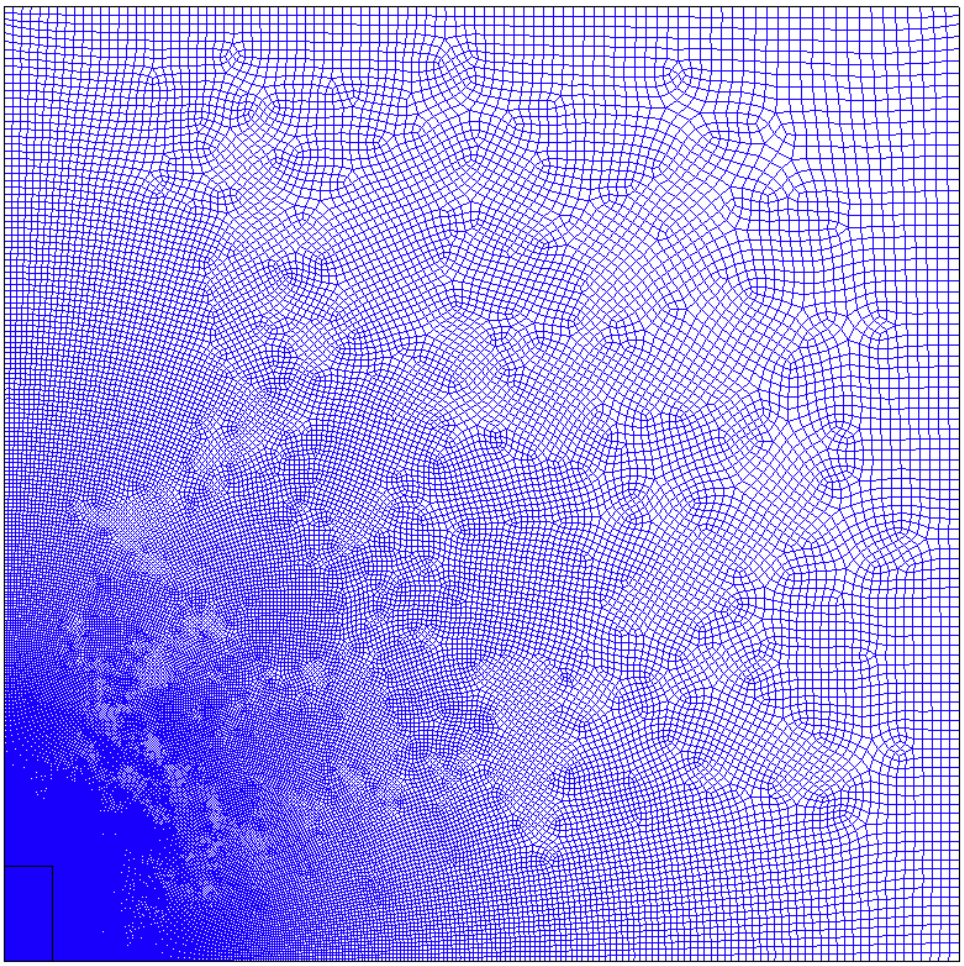

Figure B.6 – Computational domain for 2D bubble collapse near a solid wall - domain $40R_0$, size $20 \times 20\ mm^2$, $N_{cells} = 176058$, max. skewness=0.64.

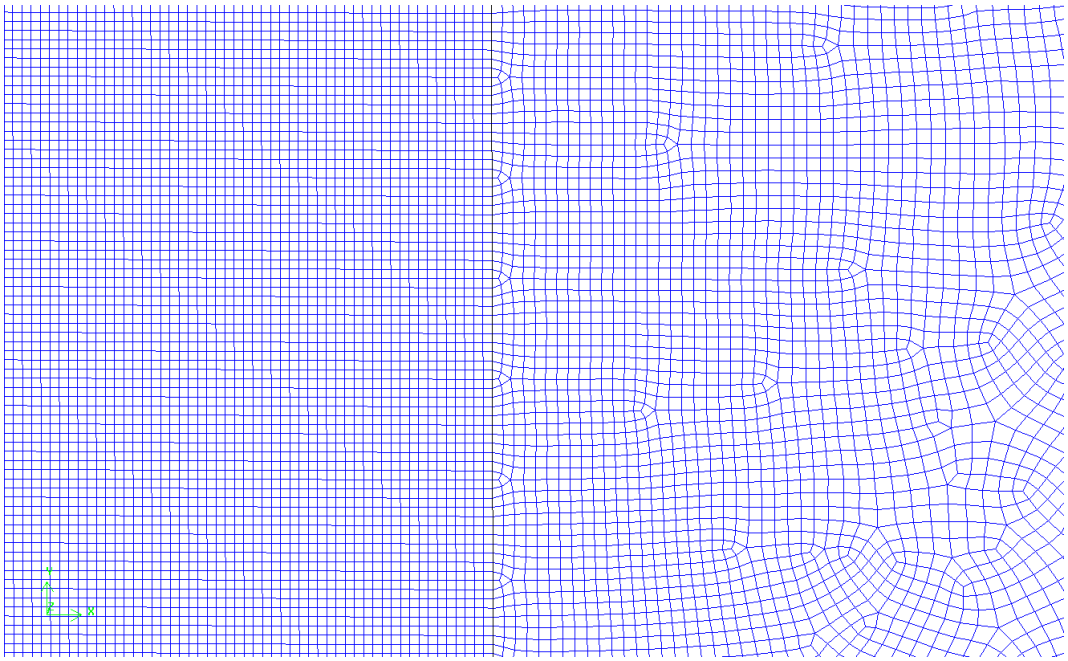

Figure B.7 – Cell size transition between the two meshed domains - domain $40R_0$.

A 2D and 3D cartesian domain with smaller domain size shown in fig. B.8 and fig. B.9 has been found ideal for bubble collapse and FSI problems. The computational domain and mesh are generated with the YALES2 solver using the input file.

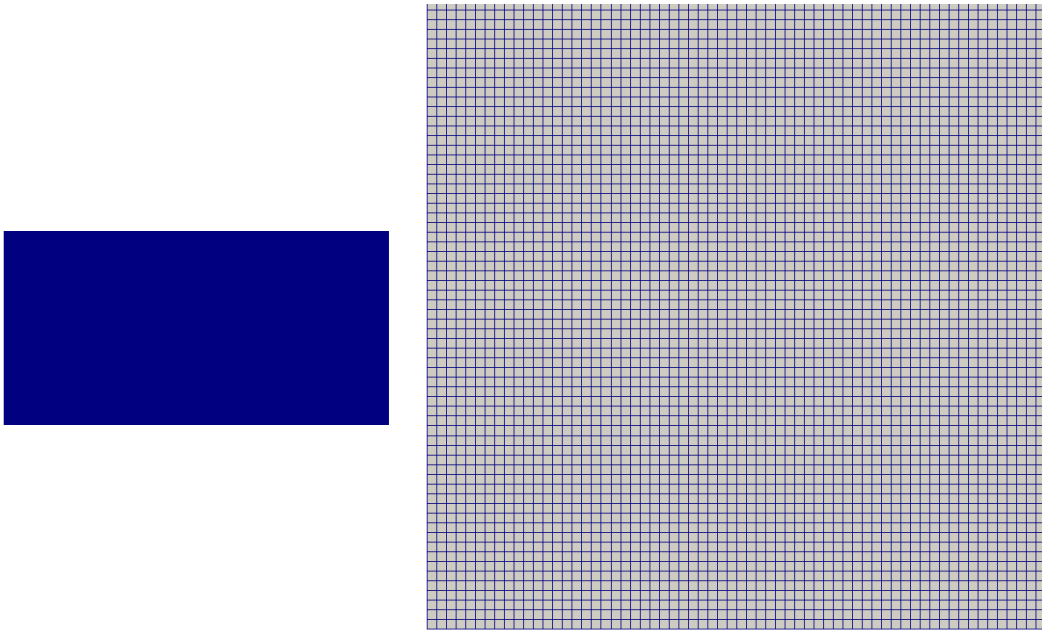

Figure B.8 – 2D bubble collapse near a solid wall with cartesian mesh - boundary $40R_0$, domain size $5 \times 2.5\,mm^2$, computational cells 500×500, $N_{cells} = 250000$, max. skewness=0 - domain $10R_0$.

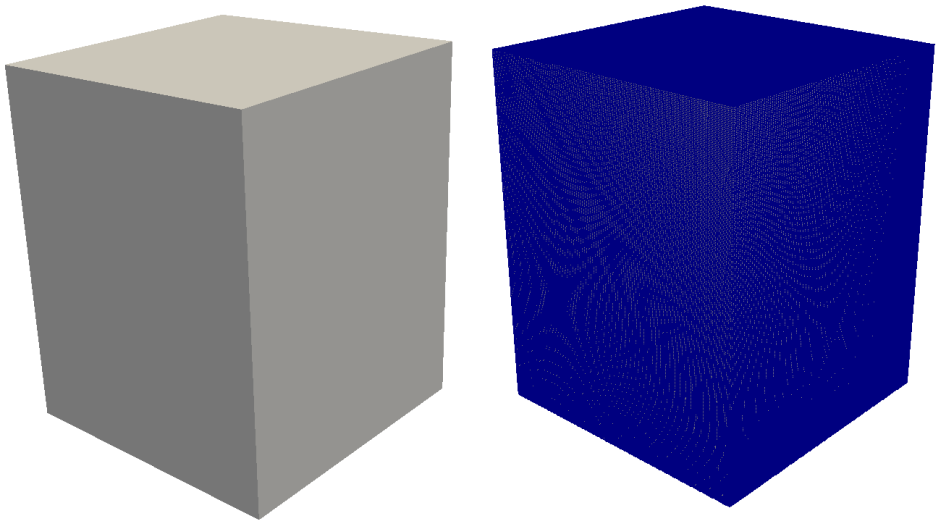

Figure B.9 – Computational domain for 3D bubble collapse near solid wall with cartesian mesh - domain size $2 \times 2.5 \times 2\ mm^3$, computational cells $200 \times 250 \times 200$, $N_{cells} = 10000000$, max. skewness=0.

B.4 FEM domain

The FEM mesh used for the prediction of material response is shown in fig. B.10. The mesh has been generated in CAST3M by specifying the parameters in the input file.

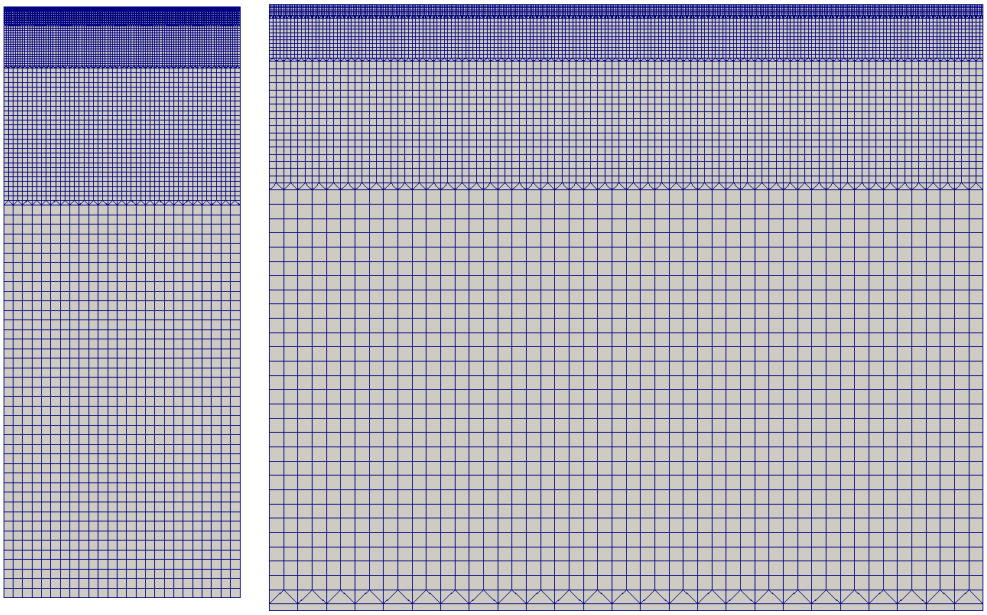

Figure B.10 – Computational domain and mesh for FEM simulation - domain size $= 1 \times 2.5\ mm^2$, $N_{elements} = 9850$, $N_{nodes} = 29065$.

Appendix C

Computational Time

The computational time needed to perform CFD and FEM simulations are detailed. All simulations are performed on the DELL cluster (*Kareline*) of MoST team at LEGI, Univ. Grenoble Alpes. CFD simulations are performed on the nodes of DELL powered C6320 machine, consisting of 400 cores interconnected by the infiniband network. Each server node of 20 cores has a peak clock speed of 3 GHz and 64 GB of memory. The FEM simulations are performed on the interactive nodes of the cluster, powered with Dell PowerEdge C6100 of 48 cores, having a peak clock speed of 3 GHz and 48 GB of memory. Post-processing were performed on the interactive cluster *Charlie*, a DELL R730 server equipped with GPU's.

The computational time has been presented in table C.1, in terms of Wall-Clock Time (WCT) and Reduced Computational Time (RCT), defined in eq. (C.1) where N_{core} is the number of CPU cores, N_{iter} is the number of iterations and N_{CV} is the number of control volumes.

$$RCT = (WCT \times N_{core})/(N_{iter} \times N_{CV}) \tag{C.1}$$

Case	N_{CV}	WCT	RCT (μs)
2D Rayleigh Full	182866	25min	6.03
2D Rayleigh $(\frac{1}{4})^{th}$	45757	316sec	5.83
3D Rayleigh Full	14,890,632	16h24min	26.44
3D Rayleigh $(\frac{1}{8})^{th}$	4,431,786	11h11min	33.04
2D bubble-wall $40R_0$	176,804	1h14min	8.06
2D bubble-wall $10R_0$	501,501	2h52min	5.61
3D Cartesian	10,140,651	17h2min	16.12
FEM $\Delta t_{FSI} = 5\,ns$	9850	120 min	-

Table C.1 – WCT and RCT for different computations.

List of Figures

List of Tables

Bibliography

Beattie D.R.H., Whalley-P.B. (1982). "A simple two-phase frictional pressure drop calculation method". In: *International journal of multiphase flow* 8.1, pp. 83–87.

Benjamin T.B., Ellis-A.T. (1966). "The collapse of cavitation bubbles and the pressures thereby produced against solid boundaries". In: *Philosophical Transactions for the Royal Society of London. Series A, Mathematical and Physical Sciences*, pp. 221–240.

Best J.P., Kucera-A. (1992). "A numerical investigation of non-spherical rebounding bubbles". In: *Journal of fluid mechanics* 245, pp. 137–154.

Blake J.R., Gibson-D.C. (1987). "Cavitation bubbles near boundaries". In: *Annual Review of Fluid Mechanics* 19.1, pp. 99–123.

Blake J.R., Tomita Y. Tong R.P. (1998). "The art, craft and science of modelling jet impact in a collapsing cavitation bubble". In: *In Fascination of Fluid Dynamics*. Springer, pp. 77–90.

Bremond N., Arora M. Dammer S.M. Lohse D. (2006). "Interaction of cavitation bubbles on a wall". In: *Physics of fluids* 18.12, p. 121505.

Brennen, C.E. (1995). *Cavitation and bubble dynamics*. Oxford University Press.

Briançon-Marjollet L., Franc J.-P. Michel J.-M. (1990). "Transient bubbles interacting with an attached cavity and the boundary layer". In: *Journal of Fluid Mechanics* 218, pp. 355–376.

Brujan, E.-A. (2011). *Cavitation in Non-Newtonian Fluids: With Biomedical and Bioengineering Applications*. Springer.

Brujan E.-A., Nahen K.-Schmidt P. Vogel-A. (2001). "Dynamics of laser-induced cavitation bubbles near an elastic boundary". In: *Journal of Fluid Mechanics* 433, pp. 251–281.

Chahine G.L., Hsiao C.-T. (2015). "Modelling cavitation erosion using fluid-material interaction simulations". In: *Interface Focus* 5. ISSN: 2042-8898. DOI: 10.1098/rsfs.2015.0016.

Chahine G.L., Kapahi A.-Choi-J.-K. Hsiao-C.-T. (2016). "Modeling of surface cleaning by cavitation bubble dynamics and collapse". In: *Ultrasonics sonochemistry* 29, pp. 528–549.

Chnafa C., Mendez S.-Nicoud-F. (2014). "Image-based large-eddy simulation in a realistic left heart". In: *Computers & Fluids* 94, pp. 173–187.

Choi J.-K., Chahine-G.L. (2016). "Relationship between material pitting and cavitation field impulsive pressures". In: *WEAR* 352-353, 42–53. ISSN: 0043-1648. DOI: {10.1016/j.wear.2016.01.019}.

Chorin, A.J. (1968). "Numerical solution of the Navier-Stokes equations". In: *Mathematics of computation* 22.104, pp. 745–762.

Cook A.W., Cabot W.H. (2004). "A high-wavenumber viscosity for high-resolution numerical methods". In: *Journal of Computational Physics* 195.2, pp. 594–601.

Di Paola F., Guerin-C.-Berthinier-C. Paredes-R. (2017a). *Starting with Cast3M thermo-mechanical calculations - Training manual*.

— (2017b). *PASAPAS procedure and the users procedures - Training Manual*.

Donea J., Huerta A.-Ponthot-J.-Ph. Rodríguez-Ferran-A. (2004). "Arbitrary Lagrangian–Eulerian Methods". In: *Encyclopedia of Computational Mechanics*. American Cancer Society. Chap. 14. DOI: 10.1002/0470091355.ecm009. URL: https://onlinelibrary.wiley.com/doi/abs/10.1002/0470091355.ecm009.

Dular, M. (2006). "Experimental and numerical modeling of cavitation erosion". In: *Sixth International Symposium on Cavitation, CAV2006*.

Dular M., Pozar T.-Zevnik-J.-Petkovsek R. (2019). "High speed observation of damage created by a collapse of a single cavitation bubble". In: *Wear* 418-419, pp. 13–23. ISSN: 0043-1648. URL: https://doi.org/10.1016/j.wear.2018.11.004.

Egerer C., Hickel S.-Schmidt-S.-Adams N.A. (2013). "LES of Turbulent Cavitating Shear Layers". In: *High Performance Computing in Science and Engineering '13*. Springer, pp. 349–359.

Fivel M., Franc J.-P.-Roy-S.C. (2015). "Towards numerical prediction of cavitation erosion". In: *Interface focus* 5.5, p. 20150013.

Fortes-Patella R., Reboud-J.L.-Briancon-Marjollet L. (2004). "A phenomenological and numerical model for scaling the flow aggressiveness in cavitation erosion". In: *EROCAV Workshop, Val de Reuil, France*. Vol. 11, pp. 283–290.

Franc, J.-P. (2009). "Incubation time and cavitation erosion rate of work-hardening materials". In: *Journal of Fluids Engineering* 131.2, p. 021303.

Franc J.-P., Michel J.-M. (2006). *Fundamentals of cavitation*. Vol. 76. Springer Science & Business Media.

Franc J.-P., Riondet M.-Karimi-A. Chahine-G.L. (2012). "Material and velocity effects on cavitation erosion pitting". In: *Wear* 274, pp. 248–259.

Fujikawa S., Akamatsu T. (1980). "Effects of the non-equilibrium condensation of vapour on the pressure wave produced by the collapse of a bubble in a liquid". In: *Journal of Fluid Mechanics* 97.3, pp. 481–512.

Gibson D.C., Blake J.R. (1980). "Growth and collapse of cavitation bubbles near flexible boundaries". In: *7th Australasian Conference on Hydraulics and Fluid Mechanics*. Institution of Engineers, Australia, p. 283.

— (1982). "The growth and collapse of bubbles near deformable surfaces". In: *Applied Scientific Research* 38.1, pp. 215–224.

Gibson, D.C. (1968). "Cavitation adjacent to plane boundaries". In: *Proc. 3rd Australasian Conf. on Hydraulics and Fluid Mechanics*. Sydney, pp. 210–214.

Goncalves E., Patella R. F. (2009). "Numerical simulation of cavitating flows with homogeneous models". In: *Computers & Fluids* 38.9, pp. 1682–1696.

— (2010). "Numerical study of cavitating flows with thermodynamic effect". In: *Computers & Fluids* 39.1, pp. 99–113.

Hawker N.A., Ventikos Y. (2012). "Interaction of a strong shockwave with a gas bubble in a liquid medium: a numerical study". In: *Journal of Fluid Mechanics* 701, pp. 59–97.

Hickling R., Plesset M. S. (1964). "Collapse and rebound of a spherical bubble in water". In: *The Physics of Fluids* 7.1, pp. 7–14.

Hirt C.W., Amsden A.A. Cook-J.L. (1974). "An arbitrary Lagrangian-Eulerian computing method for all flow speeds". In: *Journal of computational physics* 14.3, pp. 227–253.

Hsiao C.-T., Jayaprakash A.-Kapahi-A. Choi-J.-K. Chahine G.L. (2014). "Modelling of material pitting from cavitation bubble collapse". In: *Journal of Fluid Mechanics* 755. ISSN: 0022-1120. DOI: 10.1017/jfm.2014.394.

Johnsen E., Colonius T. (2008). "Shock-induced collapse of a gas bubble in shockwave lithotripsy". In: *Journal of the Acoustical Society of America* 124, pp. 2011–2020. ISSN: 0001-4966. DOI: 10.1121/1.2973229.

— (2009). "Numerical simulations of non-spherical bubble collapse". In: *Journal of fluid mechanics* 629, pp. 231–262.

Joshi, S. (2018). "Modelling cavitation erosion using Smoothed Particle Hydrodynamics". PhD thesis. Université Grenoble Alpes.

Kim J., Moin P. (1985). "Application of a fractional-step method to incompressible Navier-Stokes equations". In: *Journal of computational physics* 59.2, pp. 308–323.

Kraushaar, M. (2011). "Application of the compressible and low-Mach number approaches to Large-Eddy Simulation of turbulent flows in aero-engines". PhD thesis. Institut National Polytechnique de Toulouse-INPT.

Lauer E., Hu X.Y. Hickel-S.-Adams N.A. (2012). "Numerical modelling and investigation of symmetric and asymmetric cavitation bubble dynamics". In: *Computers and Fluids*.

Lauterborn W., Ohl C.-D. (1997). "Cavitation bubble dynamics". In: *Ultrasonics sonochemistry* 4.2, pp. 65–75.

Lauterborn W., Vogel A. (2013). "Shock wave emission by laser generated bubbles". In: *Bubble dynamics and shock waves*. Springer, pp. 67–103.

Lewis R.W., Nithiarasu P.-Seetharamu-K.N. (2004). *Fundamentals of the finite element method for heat and fluid flow*. John Wiley & Sons.

Lindau O., Lauterborn W. (2003). "Cinematographic observation of the collapse and rebound of a laser-produced cavitation bubble near a wall". In: *Journal of Fluid Mechanics* 479, pp. 327–348.

Malandain, M. (2013). "Simulation massivement parallèle des écoulements turbulents à faible nombre de Mach". PhD thesis. INSA de Rouen.

Moureau V., Bérat C.-Pitsch-H. (2007). "An efficient semi-implicit compressible solver for large-eddy simulations". In: *Journal of Computational Physics* 226.2, pp. 1256–1270.

Moureau V., Domingo P.-Vervisch-L. (2011). "Design of a massively parallel CFD code for complex geometries". In: *Comptes Rendus Mécanique* 339.2-3, pp. 141–148.

Müller S., Helluy P.-Ballmann-J. (2010). "Numerical simulation of a single bubble by compressible two-phase fluids". In: *International Journal for Numerical Methods in Fluids* 62.6, pp. 591–631.

Naude C.F., Ellis A.T. (1961). "On the mechanism of cavitation damage by non-hemispherical cavities collapsing in contact with a solid boundary". In: *Journal of Basic Engineering* 83.4, pp. 648–656.

Obreschkow D., Tinguely M. Dorsaz-N.-Kobel P.-De Bosset A. Farhat M. (2011). "Universal scaling law for jets of collapsing bubbles". In: *Physical review letters* 107.20, p. 204501.

Ohl C.-D., Kurz T.-Geisler-R. Lindau-O. Lauterborn W. (1999). "Bubble dynamics, shock waves and sonoluminescence". In: *Philosophical Transactions of the Royal Society of London A: Mathematical, Physical and Engineering Sciences* 357.1751, pp. 269–294.

Paquette, Y. (2017). "Interaction Fluide-Structure et Érosion de Cavitation". PhD thesis. Université Grenoble Alpes.

Philipp A., Lauterborn W. (1998). "Cavitation erosion by single laser-produced bubbles". In: *Journal of Fluid Mechanics* 361, pp. 75–116. ISSN: 0022-1120. DOI: 10.1017/S0022112098008738.

Plesset M.S., Chapman R.B. (1971). "Collapse of an initially spherical vapour cavity in the neighbourhood of a solid boundary". In: *Journal of Fluid Mechanics* 47.2, pp. 283–290.

Plesset, M.S (1954). "On the stability of fluid flows with spherical symmetry". In: *Journal of Applied Physics* 25, p. 9.

Pöhl F., Mottyll S. Skoda-R.-Huth S. (2015). "Evaluation of cavitation-induced pressure loads applied to material surfaces by finite-element-assisted pit analysis and numerical investigation of the elasto-plastic deformation of metallic materials". In: *Wear* 330, pp. 618–628.

Poinsot T.J., Lele S.K. (1992). "Boundary conditions for direct simulations of compressible viscous flows". In: *Journal of computational physics* 101.1, pp. 104–129.

Popinet S., Zaleski S. (2002). "Bubble collapse near a solid boundary: a numerical study of the influence of viscosity". In: *Journal of Fluid Mechanics* 464, pp. 137–163.

Prosperetti, A. (1987). "The equation of bubble dynamics in a compressible liquid". In: *Physics of Fluids* 30.11, pp. 3626–3628.

Quartapelle L., Selmin V. (1993). "High-order Taylor-Galerkin methods for nonlinear multidimensional problems". In: *Finite Elements in Fluids* 76.90, p. 46.

Rayleigh, L. (1917). "On the pressure developed in a liquid during the collapse of a spherical cavity". In: *Philosophical Magazine Series 6* 34, pp. 94–98.

Reuter F., Gonzalez-Avila S.R.-Mettin-R. Ohl-C.-D. (2017). "Flow fields and vortex dynamics of bubbles collapsing near a solid boundary". In: *Physical Review Fluids* 2.6. ISSN: 2469-990X. DOI: 10.1103/PhysRevFluids.2.064202.

Reynolds, O. (1894). "Experiments showing the boiling of water in an open tube at ordinary temperatures". In: *Scientific Papers on Mechanical and Physical Subject* 2, pp. 1900–1903.

Roger T., Lartigue-G. Moureau-V. (2016). "An asymptotic-preserving and semi-implicit pressure-based compressible solver for flows at all Mach numbers". In: *ERCOFTAC ETMM11 international conference*. Sicily, Italy.

Roy S.C., Franc-J.-P.-Fivel-M. (2015c). "Cavitation erosion: Using the target material as a pressure sensor". In: *Journal of Applied Physics* 118.16, p. 164905.

Roy S.C., Franc-J.-P.-Pellone-C. Fivel-M. (2015a). "Determination of cavitation load spectra-Part 1: Static finite element approach". In: *Wear* 344, pp. 110–119.

Roy S.C., Franc-J.-P.-Ranc-N. Fivel-M. (2015b). "Determination of cavitation load spectra—Part 2: Dynamic finite element approach". In: *Wear* 344, pp. 120–129.

Shaw S.J., Schiffers-W.P.-Emmony-D.C. (2001). "Experimental observations of the stress experienced by a solid surface when a laser-created bubble oscillates in its vicinity". In: *The Journal of the Acoustical Society of America* 110.4, pp. 1822–1827.

Shaw S.J., Schiffers-W.P.-Gentry-T.P.-Emmony D.C. (2000). "The interaction of a laser-generated cavity with a solid boundary". In: *The Journal of the Acoustical Society of America* 107.6, pp. 3065–3072.

Silverrad, D. (1912). "Propeller Erosion". In: *Engineering* 33.

Sod, G.A. (1978). "A survey of several finite difference methods for systems of non-linear hyperbolic conservation laws". In: *Journal of computational physics* 27.1, pp. 1–31.

Song W.D., Hong-M.H-Lukyanchuk-B.-Chong T.C. (2004). "Laser-induced cavitation bubbles for cleaning of solid surfaces". In: *Journal of applied physics* 95.6, pp. 2952–2956.

Tinguely, M. (2013). "The effect of pressure gradient on the collapse of cavitation bubbles in normal and reduced gravity". PhD thesis. Laboratoire de Machines Hydrauliques.

Tomita Y., Robinson P.B.-Tong-R.P.-Blake J.R. (2002). "Growth and collapse of cavitation bubbles near a curved rigid boundary". In: *Journal of Fluid Mechanics* 466, pp. 259–283.

Tong R.P., Schiffers W.P.-Shaw-S.J.-Blake J.R.-Emmony-D.C. (1999). "The role of 'splashing' in the collapse of a laser-generated cavity near a rigid boundary". In: *Journal of Fluid Mechanics* 380, pp. 339–361. ISSN: 0022-1120. DOI: 10.1017/S0022112098003589.

Van Terwisga T.J.C., Ziru-L.-Fitzsimmons-P.A. Foeth-E.J. (2009). "Cavitation erosion-a review of physical mechanisms and erosion risk models". In: *7th International Symposium on Cavitation CAV2009*.

Vantieghem, S. (2011). "Numerical simulations of quasi-static magnetohydrodynamics using an unstructured finite-volume solver: development and applications". PhD thesis. Universite Libre de Bruxelle.

Vogel A., Lauterborn W.-Timm-R. (1989). "Optical and acoustic investigations of the dynamics of laser-produced cavitation bubbles near a solid boundary". In: *Journal of Fluid Mechanics* 206, pp. 299–338.

Wang Q.X., Blake J.R. (2010). "Non-spherical bubble dynamics in a compressible liquid. Part 1. Travelling acoustic wave". In: *Journal of Fluid Mechanics* 659, pp. 191–224.

Zeng Q., Gonzalez-Avila-S.R.-Dijkink-R. Koukouvinis-P.-Gavaises M. Ohl C.-D. (2018). "Wall shear stress from jetting cavitation bubbles". In: *Journal of Fluid Mechanics* 846, pp. 341–355. ISSN: 0022-1120. DOI: 10.1017/jfm.2018.286.

Zhang Z.-Y., Zhang-H.-S. (2004). "Surface tension effects on the behavior of a cavity growing, collapsing, and rebounding near a rigid wall". In: *Physical Review E* 70.5, p. 056310.